Titre: Title:	Enabling Real-Time Terahertz Imaging With Advanced Optics and Computational Imaging
Auteur: Author:	Hichem Guerboukha
Date:	2019
Type:	Mémoire ou thèse / Dissertation or Thesis
Référence: Citation:	Guerboukha, H. (2019). Enabling Real-Time Terahertz Imaging With Advanced Optics and Computational Imaging [Thèse de doctorat, Polytechnique Montréal]. PolyPublie. https://publications.polymtl.ca/4090/

URL de PolyPublie: PolyPublie URL:	https://publications.polymtl.ca/4090/
Directeurs de recherche: Advisors:	Maksim A. Skorobogatiy
Programme: Program:	Génie physique

POLYTECHNIQUE MONTRÉAL
affiliée à l'Université de Montréal

Enabling real-time terahertz imaging with advanced optics and computational imaging

HICHEM GUERBOUKHA
Département de génie physique

Thèse présentée en vue de l'obtention du diplôme de *Philosophiæ Doctor*
Génie physique

Décembre 2019

POLYTECHNIQUE MONTRÉAL
affiliée à l'Université de Montréal

Cette thèse intitulée :

Enabling real-time terahertz imaging with advanced optics and computational imaging

présentée par **Hichem GUERBOUKHA**
en vue de l'obtention du diplôme de *Philosophiæ Doctor*
a été dûment acceptée par le jury d'examen constitué de :

Nicolas GODBOUT, président
Maksim SKOROBOGATIY, membre et directeur de recherche
Christophe CALOZ, membre
François BLANCHARD, membre externe

DEDICATION

To you who reminded us that with every hardship comes ease.

ACKNOWLEDGEMENTS

This thesis would not have been possible without the support of many people.

I would like to thank Prof. Maksim Skorobogatiy for all the years I passed under his supervision. These years have been full of challenges and discoveries. I learned from him to always push beyond the first experiment, and most importantly the rigorous ways of theoretical thinking. I also want to thank Prof. Nicolas Godbout, Prof. Christophe Caloz and Prof. François Blanchard for accepting to judge and comment this thesis.

I want to acknowledge all the people involved in the completion of this thesis, in particular my co-authors Kathirvel Nallappan, Yang Cao, Dr. Mohamed Seghilani and Prof. José Azaña. I am grateful to the meticulous and professional technical assistance of Francis Boutet, Jean-Paul Lévesque, Evgueni Babian, Mikaël Leduc and Yves Leblanc. I also want to thank all my friends in the office and in the lab for all the memorable everyday moments.

I am grateful to the Fonds de Recherche du Québec en Nature et Technologies and the Natural Sciences and Engineering Research Council of Canada who made this thesis possible through their repeated trust and generous financial support.

Finally, I dedicate this thesis to my family. To my parents who taught me the importance of education and hard work. To my brother, to my sisters, to their families, to my in-laws, to the extended family, to the little ones. And to my wife who encouraged me to start this PhD and was always there through the years. May all of you share with me the joys of a completed thesis.

RÉSUMÉ

La bande des térahertz est une région particulière du spectre électromagnétique comprenant les fréquences entre 0.1 THz à 10 THz, pour des longueurs d'onde respectives de 3 mm à 30 μm. Malgré tout l'intérêt que cette région a suscité au cours de la dernière décennie, de grands obstacles demeurent pour une application plus généralisée de la radiation THz dans les applications d'imagerie. Cette thèse aborde le problème du temps d'acquisition d'une image THz. Notre objectif principal sera de développer des technologies et techniques pour permettre l'imagerie THz en temps réel.

Nous débutons cette thèse avec une revue de littérature approfondie sur le sujet de l'imagerie THz en temps réel. Cette revue commence par énumérer plusieurs sources et détecteurs THz qui peuvent immédiatement être utilisés en imagerie THz. Nous détaillons par la suite plusieurs modalités d'imagerie développés au cours des dernières années : 1) Imagerie THz en transmission, en réflexion et de conductivité, 2) imagerie THz pulsée, 3) imagerie THz par tomographie computationnelle et 4) imagerie THz en champ proche. Nous discutons par la suite plus en détail à propos de technologies habilitantes pour l'imagerie THz en temps réel. Pour cela, nous couvrons trois différents axes de recherche développés en littérature : 1) Imagerie en temps réel de spectroscopie THz dans le domaine du temps, 2) caméras THz et 3) imagerie en temps réel avec détecteur à pixel unique.

Nous présentons ensuite le système d'imagerie que nous avons développé pour les démonstrations expérimentales de cette thèse. Ce système est basé sur la spectroscopie THz en temps réel et permet donc d'obtenir des images hyperspectrales en amplitude et en phase. Il utilise des antennes photoconductrices pour l'émission et la détection de la radiation THz. En outre, le détecteur est fibré, ce qui permet de le déplacer spatialement pour construire des images. Nous couvrons aussi brièvement plusieurs techniques de fabrication avancées que nous avons utilisées : impression 3D par filament, stéréolithographie, machinage CNC, gravure/découpe laser et transfert de métal par toner.

Nous portons ensuite notre attention à l'objectif principal de cette thèse à travers trois démonstrations distinctes.

Premièrement, nous concevons des composants THz à faibles pertes en utilisant des matériaux poreux. L'absence de détecteurs THz ultra-sensibles implique que les pertes encourues dans un système d'imagerie sont hautement indésirables. En effet, un moyennage temporel est généralement fait pour extraire de faibles signaux THz sévèrement enfouis sous le bruit technique. Ceci a pour impact de diminuer le nombre d'images à la seconde. Nous proposons

donc d'utiliser des inclusions de dimensions sous-longueurs d'onde de faible indice (trous d'air) dans un matériau diélectrique solide pour fabriquer des composants optiques. Nous montrons que ces composants ont des pertes inférieures à des mêmes composants fabriqués en variant l'épaisseur du même matériau tout-solide. Nous fabriquons des lentilles planaires et poreuses ainsi qu'un transformateur de moment angulaire. Nous utilisons notre système d'imagerie pour caractériser l'effet de ces composants sur le faisceau THz.

Deuxièmement, nous démontrons une technique d'encodage spectral qui permet de réduire considérablement le nombre de mesures requis pour reconstruire une image THz. Cette réduction du nombre de points réduit du même coup le temps d'acquisition d'une image THz. En utilisant l'optique de Fourier, une simple lentille sphérique et la relation linéaire entre la fréquence spatiale et la fréquence THZ, nous montrons qu'il est possible de construire l'espace-k avec un chemin circulaire de mesure dans le plan de Fourier. Nous démontrons par la suite comment reconstruire des objets d'amplitude et de phase en utilisant une transformée de Fourier inverse. Nos expériences ont démontré qu'un objet pouvait être reconstruit en utilisant aussi peu que 20 mesures spectrales.

Troisièmement, nous développons une technique de super-résolution pour la microscopie THz en temps réel. L'imagerie THz sous-longueur d'onde est un domaine de recherche en évolution dans lequel la radiation THz est confinée dans un volume restreint pour résoudre des détails au-delà de la limite de diffraction. Alors que les techniques actuelles offrent des gains impressionnant en termes de résolution spatiale, elles ont des longs temps d'acquisition en raison de la nécessité de construire une image pixel par pixel. Entre-temps, des techniques de microscopie de super-résolution ont été développées dans le visible pour reconstruire une image de haute résolution en utilisant les propriétés statistiques et de localisation des fluorophores. Nous adaptons une de ces techniques pour les THz. Puisqu'il n'y a pas de fluorophore THz naturel, nous proposons d'utiliser une modulation spatiale de la phase et l'amplitude à une échelle sous-longueur d'onde. De plus, parce que nous contrôlons directement la forme de la modulation, nous montrons que nous pouvons concevoir une image de super-résolution en utilisant très peu de masques de modulation. Notre théorie étant simplement basée sur l'équation des systèmes d'imagerie linéaire, notre méthode peut directement être appliquée aux caméras THz, mais aussi à l'imagerie avec détecteur de pixel unique.

ABSTRACT

The terahertz band is a region of the electromagnetic spectrum comprising frequencies between 0.1 THz to 10 THz for respective wavelengths of 3 mm to 30 μm. Despite all the interest and potential generated in the past decade for applications of this spectral band, there are still major hurdles impeding a wider use of THz radiation for imaging. This thesis addresses the problem of image acquisition time. Our main objective is to develop technologies and techniques to achieve real-time THz imaging.

We start this thesis with a comprehensive review of the scientific literature on the topic of real-time THz imaging. This review begins by listing some off-the-shelf THz sources and detectors that could be readily used in THz imaging. We then detail some key imaging modalities developed in the past years: 1) THz transmission, reflection and conductivity imaging, 2) THz pulsed imaging, 3) THz computed tomography, and 4) THz near-field imaging. We then discuss practical enabling technologies for real-time THz imaging: 1) Real-time THz time-domain spectroscopy imaging, 2) THz cameras, and 3) real-time THz single-pixel imaging.

We then present our fiber-coupled THz time-domain spectroscopy imaging setup. This system is used throughout the thesis for experimental demonstrations. We also briefly overview many advanced fabrication techniques that we have used, namely fused deposition modeling, stereolithography, CNC machining, laser cutting/engraving and metal transfer using toner.

We then turn to the main objective of this thesis with three distinct demonstrations.

First, we design low-loss THz components using porous media. The losses incurred in the imaging system are highly undesirable due to the lack of sensitive THz detectors. Indeed, time averaging is generally performed in order to retrieve THz signals severely buried under noise, which in return reduce the framerate. We propose to use low-refractive index subwavelength inclusions (air holes) in a solid dielectric material to build optical components. We show that these components have smaller losses than their all-solid counterparts with otherwise identical properties. We fabricate a planar porous lens and an orbital angular momentum phase plate, and we use our imaging system to characterize their effects on the THz beam.

Second, we demonstrate a spectral encoding technique to significantly reduce the required number of measurements to reconstruct a THz image in a single-pixel detection scheme. This reduction in the number of measurements directly impacts the overall image acquisition time. Using Fourier optics, a simple spherical lens and the linear relationship between the spatial frequency and the THz frequency, we show that we can construct the k-space with a circular

measurement path in the Fourier plane. We then demonstrate how this k-space can be used to reconstruct both amplitude and phase objects. Our experiments show that the object can be constructed using as few as 20 spectral measurements.

Third, we develop a super-resolution technique aimed at achieving real-time THz microscopy. THz subwavelength imaging is an on-going research topic in which THz radiation is confined in a very limited volume in order to resolve spatial features beyond the diffraction limit. While current techniques offer impressive gains in terms of spatial resolution, they inherently have long acquisition times, due to the necessity of pixel-by-pixel raster scanning. In the meantime, super-resolution optical microscopy techniques have been developed in the visible range to reconstruct a high resolution image from a collection of frames using the statistical and localization properties of fluorophores. We adapt one of this technique for the THz range. Since there are no natural THz fluorophores, we propose to use subwavelength phase and amplitude modulation. Since we directly control the form of the modulation, we show that we can design efficient super-resolution images using very few modulating frames. Simply based on the equation of linear imaging systems, this technique could then be directly applied with THz cameras, but also with single-pixel imaging.

TABLE OF CONTENTS

LIST OF TABLES

LIST OF FIGURES

LIST OF SYMBOLS AND ACRONYMS

ABCD	Air-biased-coherence-detection
CCD	Charge-coupled device
CMOS	Complementary metal-oxide-semiconductor
CNC	Computer numerical control
CT	Computed tomography
CW	Continuous wave
DMD	Digital micromirror device
DLP	Digital light processing
EOS	Electro-optic sampling
FDM	Fused deposition modeling
FET	Field-effect transistor
FWHM	Full width at half maximum
HDPE	High-density polyethylene
LTEM	Laser terahertz emission microscopy
NEP	Noise-equivalent power
PCA	Photoconductive antenna
PSF	Point spread function
PSK	Phase-shift keying
QAM	Quadrature amplitude modulation
RI	Refractive index
SLA	Stereolithography
SLM	Spatial light modulator
SNR	Signal-to-noise ratio
STEAM	Serial time-encoded amplified
TFISH	THz field-induced second harmonic
THz	Terahertz
THz-TDS	Terahertz time-domain spectroscopy
THz-QTDS	Terahertz quasi-time-domain spectroscopy
TOF	Terahertz time-of-flight imaging
TRTS	Time-resolved THz spectroscopy
TPI	Terahertz pulsed imaging

LIST OF APPENDICES

CHAPTER 1 INTRODUCTION

Science and technology have considerably evolved in the past century to a point where it is now possible to see beyond the visible range of the spectrum. Today, it is well understood that light is an electromagnetic wave. In fact, what we call visible light is a very narrow portion of the electromagnetic spectrum with wavelengths ranging from several kilometers to dimensions below the atom. And in this spectrum, some regions have yet to be completely unfolded.

One of these regions is the terahertz band that covers the frequencies from 0.1 to 10 THz, corresponding to respective wavelengths of 3 mm to 30 μm. Located between microwaves and infrared, this portion of the spectrum was called the THz gap for many decades, due to the practical difficulties of generating and detecting radiation at these frequencies. In the 1990s, with the development of ultrafast lasers, technologies to do so rapidly emerged and spread around laboratories throughout the world. A new field of THz science and technology was born.

Today, a large part of the research efforts in the THz technological field is oriented toward applications [1, 2], and imaging is a very promising area [3]. Indeed, the THz band has a number of relevant, sometimes unique, benefits when applied to imaging. Like microwaves, THz can penetrate most dielectric materials with different attenuation levels, revealing inner structures with meaningful contrast. In contrast to microwaves however, the THz wavelengths are sufficiently small to also provide high resolution images applicable in many day-to-day practical scenarios. Moreover, many molecular species have unique spectral fingerprints in the THz range, opening a path to spectroscopic imaging. Finally, owing to their low photon energies, the THz do not induce harmful photoionization in biological tissues, as it the case with X-rays for example.

In the past two decades, many applications of THz imaging have been demonstrated in various areas: industrial environments [4, 5], pharmaceutical and biomedical sectors [6, 7], agri-food industry [8–10], defense and security [11,12], art conservation [13,14], etc. However, despite all the interest and potential, this research has yet to be transferred from academic to industrial environments.

Context and Challenges

One of the principal technological reason that explain why THz imaging is still underused is the image acquisition time. Even today, it is common to come across scientific articles where images are reportedly captured in several minutes, if not hours. Of course, this is a major hurdle impeding a wider use of THz imaging.

In **Chapter 2** of this thesis, we provide an extensive review of the literature on the topic of real-time THz imaging. This chapter is a transcription of a review article published in *Advances in Optics and Photonics* entitled *Toward real-time terahertz imaging* (2018) [15]. With more than 400 referenced research documents, this article offers an in-depth overview of the state-of-the-art in THz imaging, with an emphasis on the technologies enabling real-time operation. It explains more in detail why THz images are slow to acquire. In it, we identified three research directions that are currently pursued by the scientific community. For the purpose of this introduction, we would like to briefly overview these directions.

Historically, the first THz image was obtained using THz time-domain spectroscopy (THz-TDS) [77]. To this day, THz-TDS is very popular due to its ability to provide spectral amplitude and phase images. However, because it uses a single-pixel detector, a lengthy two-dimensional raster scanning is needed to obtain an image. *The first research direction* aims at improving the THz-TDS experimental setup in order to achieve real-time imaging (Section 2.3).

Unlike other parts of the spectrum, one of the fundamental problems in THz imaging is the difficulty of fabricating sensitive multipixel THz cameras. While in conventional charged-coupled device (CCD) cameras, visible photons allows for electrons to cross the semiconductor bandgap, the energy carried by the THz photon is simply not sufficient. Therefore, *the second research direction* is dedicated to the development of sensitive THz cameras (Section 2.4). For that, two major candidates are emerging: thermal cameras and field-effect transistor (FET)-based cameras.

The lack of THz cameras did not prevent the development of many ingenious imaging techniques with single-pixel detectors. Indeed, as counterintuitive as it may seem, *the third research direction* use single-pixel detectors to rapidly obtain THz images (Section 2.5). On one hand, special instrumentation such as f-theta lenses, Gregorian reflector systems and conveyor belts are used to achieve real-time operation in practical industrial environments. On the other hand, images are reconstructed using few measurements and computational imaging techniques such as compressive sensing, advanced spatial modulation and temporal/spectral encoding.

As we show in the review, these three research directions are not in competition with one another, nor are they mutually exclusive. Many of the ideas developed in one area can be easily transferred to another.

Moreover, THz subwavelength imaging is another active field where all three research directions have made notable contributions. As we discuss in more details in Section 2.2.5 and throughout the review, this research topic aims at developing THz microscopes able to resolve spatial features beyond the diffraction limit. To do so, one of the preferred approaches is to use optical elements (apertures, metallic tips, etc.) to confine the THz radiation in a very limited volume. While this technique offers impressive gains in spatial resolution, it inherently has long acquisition times, due to the necessity of slow pixel-by-pixel raster scan.

Objectives and Structure of the Thesis

The main objective of this thesis is to develop technologies and techniques to achieve real-time THz imaging. After the literature review, the remaining of the thesis is divided in five chapters.

Chapter 3 presents the general methodology of this thesis. As we will see, it was important for us to always ground our approach in deep theoretical understanding, but also back it with experimental results as much as possible. In this chapter, we begin by describing the first major accomplishment of this thesis: the design and assembly of a fiber-coupled THz-TDS imaging system. As the first imaging system in our lab, it acts as a unifier for the experimental results shown after. In this chapter, we also describe various innovative fabrication techniques that we used throughout the thesis. These techniques are usually not even considered for optical applications, but become interesting for large THz wavelengths.

The three following chapters are the core of the thesis as they present our original contributions to the field. They address three distinct sub-objectives all aimed at reducing THz image acquisition times:

1) Developing low-loss THz components. The lack of sensitive detectors implies that the losses incurred in the imaging system itself are highly undesirable, since they would result in longer averaging times, preventing real-time operation. Meanwhile, THz components such as lenses are made of dielectric materials that have quadratic dependence of the losses with frequency. Thus, there is a real need for low-loss optical components that would help achieve real-time imaging. This need is addressed in **Chapter 4** which is a transcription of a research article published in *Advanced Optical Materials* entitled *Planar porous components for low-loss terahertz optics* (2019) [16]. Using porous media, we show that porous lenses

can be fabricated with overall lower losses than their all-solid counterparts. This article was selected to appear in the December 2019 Year in Optics issue of *Optics & Photonics News* which *highlights the most exciting optics research to emerge in the preceding 12 months.* Appendix A reproduces the Supplementary material related to this publication

2) Reducing the number of measurements in spectral THz imaging. As we discussed earlier, THz-TDS is a common system that can provide spectral amplitude and phase imaging. However, common THz-TDS detectors are single-pixel. In this sub-objective, we aim at using computational imaging and spectral encoding to reduce the number of required measurements. **Chapter 5** is a transcription of a research article published in *Optica* entitled *Exploiting k-space/frequency duality toward real-time terahertz imaging* (2018) [17]. Using Fourier optics and a simple lens, we demonstrate that it is possible to reconstruct amplitude and phase objects using as little as 20 spectral measurements, by encoding the spatial frequencies in the spectrum. Appendix B reproduces the Supplementary material related to this publication

3) Implementing super-resolution for real-time subwavelength THz imaging. Super-resolution optical microscopy techniques are diverse computational techniques developed in the visible range to reconstruct images of higher resolution from a collection of frames. These techniques could be used with multipixel THz cameras to achieve real-time imaging with setups similar to what exists in optical microscopy. **Chapter 6** presents our most recent work on the development of a super-resolution technique for the THz range. Since there are no fluorophores in the THz range, we propose to use amplitude and phase modulation to modify, on a subwavelength scale, the THz wave incident on the object. Because we directly control the form of the modulation, rather than relying on statistics of a large number of frames, we can design efficient super-resolution modulation masks of very few frames, thereby improving framerates in real-time imaging.

Finally, in **Chapter 7**, we discuss complementary details about the previous chapters and how they can be related to the main objective of this thesis. We further comment on the potential of porous lenses to reduce the internal losses of THz imaging systems. We show how the spectral encoding technique can be modified to work with cylindrical lenses and conveyor belts. Finally, we discuss the applicability of the super-resolution technique when using incoherent measurements obtained with a THz camera for example.

CHAPTER 2 LITERATURE REVIEW - ARTICLE 1: TOWARD REAL-TIME TERAHERTZ IMAGING

Hichem Guerboukha[1], Kathirvel Nallappan[1,2], and Maksim Skorobogatiy[1]
[1]Génie physique, Polytechnique Montréal
[2]Génie électrique, Polytechnique Montréal
Advances in Optics and Photonics, vol. 10, no. 4, pp. 843-938 (2018)

Abstract: Terahertz (THz) science and technology have greatly progressed over the past two decades to a point where the THz region of the electromagnetic spectrum is now a mature research area with many fundamental and practical applications. Furthermore, THz imaging is positioned to play a key role in many industrial applications, as THz technology is steadily shifting from university-grade instrumentation to commercial systems. In this context, the objective of this review is to discuss recent advances in THz imaging with an emphasis on the modalities that could enable real-time high-resolution imaging. To this end, we first discuss several key imaging modalities developed over the years: THz transmission, reflection, and conductivity imaging; THz pulsed imaging; THz computed tomography; and THz near-field imaging. Then, we discuss several enabling technologies for real-time THz imaging within the time-domain spectroscopy paradigm: fast optical delay lines, photoconductive antenna arrays, and electro-optic sampling with cameras. Next, we discuss the advances in THz cameras, particularly THz thermal cameras and THz field-effect transistor cameras. Finally, we overview the most recent techniques that enable fast THz imaging with single-pixel detectors: mechanical beam-steering, compressive sensing, spectral encoding, and fast Fourier optics. We believe that this critical and comprehensive review of enabling hardware, instrumentation, algorithms, and potential applications in real-time high-resolution THz imaging can serve a diverse community of fundamental and applied scientists.

2.1 Introduction

Science and technology behind modern day imaging have come a long way since the invention of the photography in the 1800s. In the same century, many great minds devoted their energy to comprehend the nature of light, culminating in the famous theory of electromagnetism summarized in Maxwell's equations. Today, it is taken for granted that light is an electromagnetic wave, and that visible light constitutes only a very small portion of the electromagnetic spectrum. In the 20th century, imaging moved far beyond the visible spectral range, resulting in the development of many novel imaging techniques, from x-ray

radiography that uses waves of subatomic size to radars that employ waves as large as several meters.

Currently, many parts of the electromagnetic spectrum are being widely used for countless applications. This review is dedicated to only a small part of the electromagnetic spectrum in rapid development—the terahertz (THz) range. While there is no unique definition of the THz band, it is generally considered to cover the range of frequencies from 0.1 to 10 THz, having respective wavelengths from 3 mm down to 30 μm (Fig. 2.1). Today, research in application of THz waves constitutes a very dynamic and multidisciplinary field in rapid development, with many fundamental discoveries being made and practical applications identified [1,2]. At the junction between microwaves and infrared, the THz range shares many of their properties and potential applications. For example, as a natural extension of microwaves, it is seen by many as the next frontier in wireless communications, promising higher data transmission rates to answer the ever-increasing demand for information transfer capacity [18–22].

In the field of sensing and imaging, THz radiation offers unique means to interrogate matter [3]. Like microwaves, THz is capable of penetrating most dielectric materials, revealing inner structures with meaningful contrast. However, different from microwaves, the THz wavelength is sufficiently small to also provide much higher image resolution. Furthermore, many molecular species have unique spectral fingerprints in the THz range. Already, these advantages have been used in multiple fields: industrial environments [4, 5]; the pharmaceutical [6, 7] and biomedical [23–26] sectors; the agri-food industry [8–10]; defense and security [11, 12]; art conservation [13, 14]; etc.

We start our review by summarizing in Table 1 some of the most promising commercial sources of THz radiation. For real-time imaging, an intense THz source is clearly beneficial when active illumination of the sample is required. The wavelength of the source is also an important factor as image spatial resolution is directly related to the wavelength of light used in illumination.

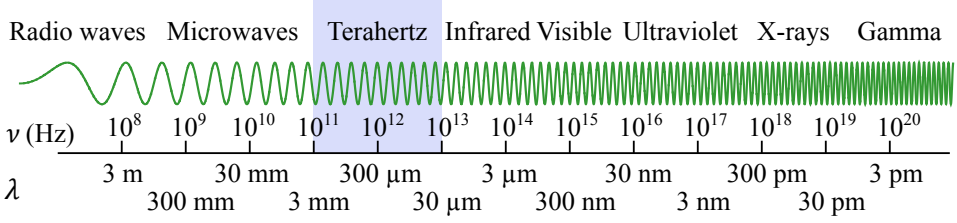

Figure 2.1 Terahertz range in the electromagnetic spectrum

Similarly, there are many choices today for detection of THz radiation. Such detectors range widely in their physical operation principles and sensitivities, ranging from thermal bolometers to solid-state transistors. At the same time, with few exceptions, most commercially available detectors, particularly those offering coherent detection, currently come as single-pixel devices. Furthermore, some achieve exceptional sensitivities, at the cost of cryogenic cooling. In the context of THz imaging, important research effort is currently concentrated toward the development of sensitive multipixel THz cameras operating at room temperatures (see Table 2 for a list of uncooled detectors). While coherent detection is probably too much to hope for in the short term, we nevertheless foresee considerable improvement of the sensitivities and the frame rates of THz cameras, taking advantage of existing microfabrication technology to enable scalability and lower fabrication costs. For more detailed reviews of THz detectors, we suggest several recent publications on this subject [27–29].

As surprising as it may seem, the lack of THz cameras did not impede the development of many ingenious relatively fast and high-resolution THz imaging modalities. In fact, many such imaging techniques cannot be realized using existing THz cameras as they rely on frequency-/time-resolved and field-resolved measurements. The most obvious example is imaging using a THz time-domain spectroscopy system (THz-TDS) that measures directly the electric field of a short THz pulse in time domain. In fact, historically, the first THz image was obtained using THz-TDS [77]. The principal strength of this method comes from the fact that it provides a broadband spectral image with both amplitude and phase information (Fig. 2.2). The principal disadvantage of a classic THz-TDS approach is the necessity of a lengthy two-dimensional (2D) raster scanning in order to obtain an image. This is in clear contrast with THz cameras, which are fast, but limited to the measurement of some spectrally averaged power distribution.

This review is dedicated to the means of achieving real-time THz imaging. The paper is structured as follows. In Section 2.2, we first review many important THz imaging modalities developed so far: THz transmission, reflection, and conductivity imaging; THz pulsed imaging; THz computed tomography; and THz near-field imaging. In addition to the presentation of those modalities, we also discuss their specific challenges toward real-time image acquisition. Then, in the following sections, we detail various practical realizations of real-time THz imaging systems. In Section 2.3,we begin by reviewing the fundamentals of THz-TDS and discuss several enabling technologies for real-time imaging: fast optical delay lines, photoconductive antennas arrays, and electro-optic sampling with cameras. In Section 2.4, we review two major candidates for real-time high-resolution imaging THz cameras. Particularly we review recent progress in THz thermal cameras and THz field-effect transistor (FET)-based cameras. Finally, in Section 2.5, we overview several promising techniques that enable fast THz

Table 2.1 Typical THz Sources for Off-the-shelf Imaging Applications

Source and emission principle	Mode	Frequency	Power	Refs.
Diode-based frequency multiplier				
Frequency multiplication of microwave source (e.g. Gunn/IMPATT diodes) with Schottky diode	CW tunable	<2 THz	++	[30]
Backward wave oscillator				
Backward acceleration of an electron beam in a corrugated traveling wave-tube under vacuum	CW tunable	<1 THz	+++	[31–33]
Quantum cascade laser				
Cascade of electrons in intersubband transitions by engineered quantum well heterostructures	CW/pulsed	1-10 THz	++	[34–37]
Photomixer				
Frequency difference through beating of two optical frequencies in a semiconductor	CW tunable	<3 THz	+	[38–40]
Difference frequency generation				
Nonlinear polarization at the difference frequency of two optical pump beams in a nonlinear crystal	CW tunable	<4 THz	+++	[41]
Parametric amplification and injection seeding				
Second-order nonlinear conversion of a pump pulse into two photons of lower energies (signal and idler)	CW tunable	<3 THz	+++	[42–45]
Photoconductive antenna (THz-TDS)				
Ultrafast photoexcitation of charge carriers in a biased semiconductor gap	Pulsed	<3 THz	++	[46–52]
Optical rectification (THz-TDS)				
Time-varying polarization proportional to the picosecond envelope of a pumping ultrafast optical pulse in a nonlinear crystal	Pulsed	<6 THz	++	[53–57]

Table 2.2 Typical THz Detectors/Cameras Operating at Room Temperature

Detector	Detection principle	NEP* $pW/\sqrt{Hz}$	Array	Refs.
Thermal				
Microbolometer	Resistive change by thermal excitation	10-100	Possible (Section 2.4.1)	[58–60]
Pyroelectric detector	Polarization change by thermal excitation of a pyroelectric crystal	10-1000	Possible (Section 2.4.1)	[61–63]
Golay cell	Pressure change by thermal excitation of an encapsulated gas	100-1000	Single-pixel	[64]
Mixer				
Schottky-barrier diode	High-frequency detection enabled by fast switching speeds in metal/semiconductor junction	10-100	Possible	[65, 66]
Plasmonic detector				
Field-effect transistor	Plasmonic excitation of electronic charge densities in transistor channels	10-100	Possible (Section 2.4.2)	[67–69]
Optically triggered (THz-TDS)				
Photoconductive antenna	Ultrafast photoexcitation of charge carriers in a semiconductor gap	-	Possible (Section 2.3.3)	[46–52]
Electro-optic sampling	Birefringence-induced by THz pulse in nonlinear media	-	Possible (Section 2.3.4)	[70–74]
Air-biased-coherence-detection (ABCD)	THz field-induced second harmonic (TFISH) in plasma gas	-	Single-pixel	[75, 76]

*The noise-equivalent power (NEP) is defined as the input power that gives a signal-to-noise ratio of 1 with a 1 Hz output bandwidth. It is a measure of the minimum detectable power, and a lower NEP indicates a more sensitive detector.‖

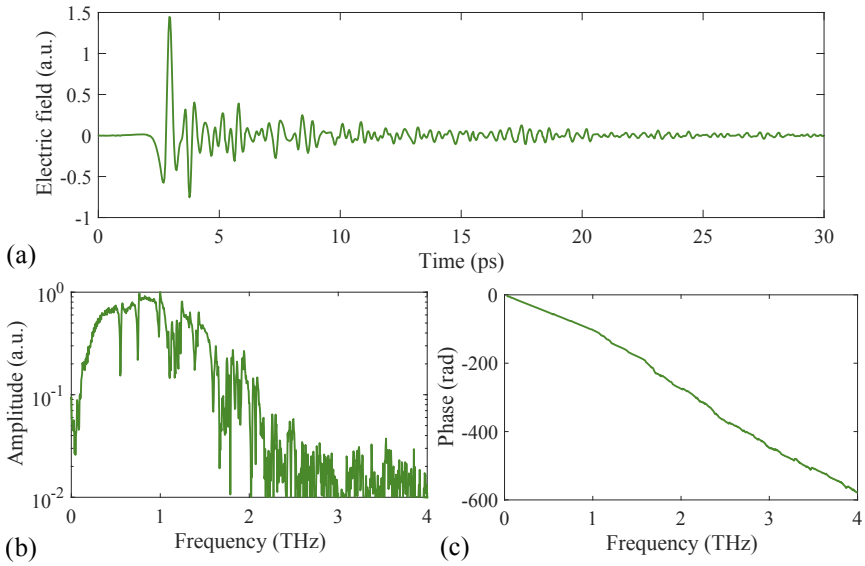

Figure 2.2 THz-TDS measurement. (a) A THz pulse in the time domain. (b) The corresponding Fourier transform amplitude and (c) phase. The dips in the spectrum correspond to absorption in water vapor.

imaging with single-pixel detectors: mechanical beam-steering, compressive sensing, spectral encoding, and fast Fourier optics. We believe that this critical and comprehensive review of enabling hardware, instrumentation, mathematical algorithms, and potential applications in real-time high-resolution THz imaging can serve a diverse community of fundamental and applied scientists.

2.2 Terahertz Imaging: Methods and Applications

In this section, we review several classical THz imaging techniques developed over the past two decades. These techniques serve as a benchmark to the novel THz imaging methods that we will detail in the following chapters. Particularly, we discuss the following THz imaging modalities: (1) Imaging with a THz-TDS; (2) THz transmission, reflection, and conductivity imaging; (3) THz pulsed imaging; (4) THz computed tomography; and (5) THz near-field imaging. In the context of this review, our objective is to explain the relevant principles of image reconstruction and identify various potential applications of THz imaging. We will also discuss their specific challenges to achieve real-time image acquisition. Since each of the abovementioned techniques has already been a subject of in-depth reviews in the past, we also refer the reader to these publications.

2.2.1 Imaging with a THz Time-Domain Spectroscopy System

Historically, the THz time-domain spectroscopy system (THz-TDS) was one of the first ways to measure THz radiation. In THz-TDS, broadband THz pulses are generated and detected using photoconductive antenna or nonlinear optical methods. The generation and detection of THz pulses is detailed in Section 2.3.1. The strength of the THz-TDS technique is in its ability to measure the amplitude and the phase of the THz electric field in time domain.

We first discuss a classic way of obtaining an image using THz-TDS. As an example, we use a THz-TDS in transmission mode and image a triangle made of high-density polyethylene (HDPE), a star made of paper, and a metallic washer [Fig. 2.3(a)]. The three samples are placed on top of a paper sheet surrounded by a metallic aperture made of aluminum foil.

To obtain a 2D image, the sample is raster-scanned and individual traces are recorded point by point in the focal plane of a pair of lenses or parabolic mirror that focuses a pre-collimated THz beam [Fig. 2.3(b)]. The result is a three-dimensional (3D) data cube with the third dimension being time. A Fourier transform is performed on the third dimension to obtain a hyperspectral image, i.e., an image per THz frequency. To extract useful information and to create an image, a certain normalization must be used to convert the raw one-dimensional (1D) time or frequency data into physically significant values [78–80]. The normalization is chosen to enhance the image contrast and is generally application dependent. It can also involve a reference measurement, for example, a measurement through an empty system or an uncovered substrate. Different examples of normalizations are presented in Fig. 2.4 (time domain) and Fig. 2.5 (frequency domain).

In Fig. 2.4(a), typical THz pulses are shown for different positions in the sample. When interacting with the sample, the THz pulse can be attenuated, delayed, or broadened. In Visualization 1, we present an example of a 3D cube image as a function of time, while in

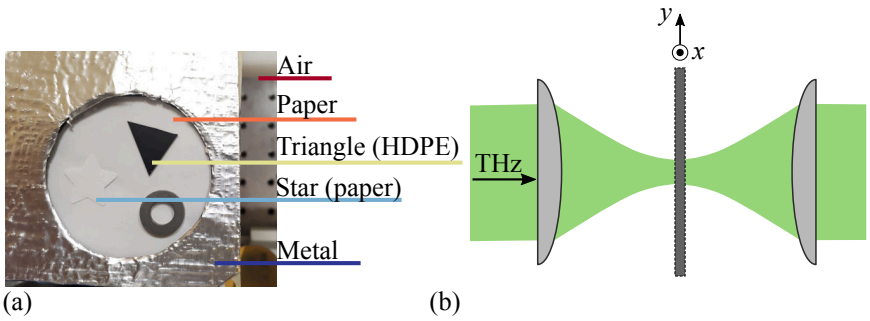

Figure 2.3 (a) Photograph of the sample. (b) The sample was mechanically moved in the (x, y) focal plane of a pair of lenses.

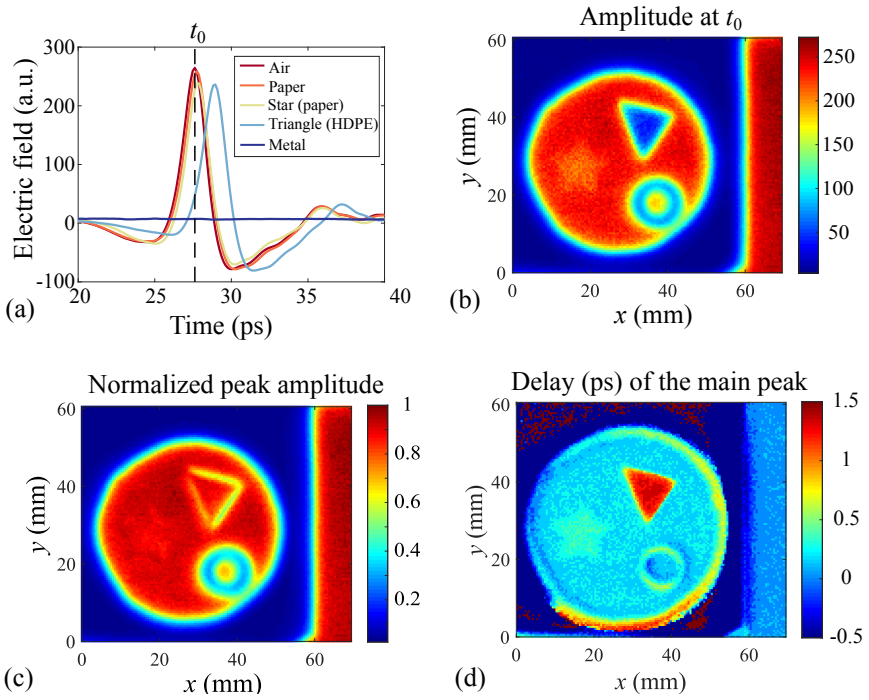

Figure 2.4 (a) Example of typical THz traces acquired at different positions across the sample in Fig. 2.3(a). (b) Amplitude of the electric field at $t_0 = 27.6$ ps: $E_{x,y}(t_0)$. (c) Normalized amplitude of the main peak: $\max\{|E_{x,y}(t)|\}/\max\{|E_{ref}(t)|\}$. (d) Delay of the main peak relative to a reference peak: $t\{\max[|E_{x,y}(t)|]\} - t\{\max[|E_{ref}(t)|]\}$

Fig. 2.4(b), we present a slice of this cube at $t_0 = 27.6$ ps. Visualizing the electric field as a function of time reveals the irradiation dynamics at the picosecond scale. A second common way of creating a THz image is to look at the maximum peak in time domain, normalized by the maximum peak of a reference function [Fig. 2.4(c)]. Here, the reference is taken as the THz pulse measured in air. The result is an image that provides information about the absorption, reflection, or scattering losses in the material. For example, scattering losses are clearly observable at the borders of the HDPE triangle. A third image can be obtained by mapping the time delay of the main peak with respect to the reference measurement [Fig. 2.4(d)]. This allows us to map the optical path change $\Delta(x, y) = n(x, y)d(x, y)$ across the sample, which can then provide material/thickness contrast. The temporal cross correlation of the two THz waveforms (with and without the sample) can also be used to visualize the optical path change [81].

By applying a Fourier transform on the third dimension of the data cube, one gets the amplitude [Fig. 2.5(a)] and the phase [Fig. 2.5(b)] of the spectrum. The amplitude gives a general indication of the losses, which, in general, increase with the frequency. The phase is related to the optical path (the refractive index/thickness). When necessary, it must be carefully

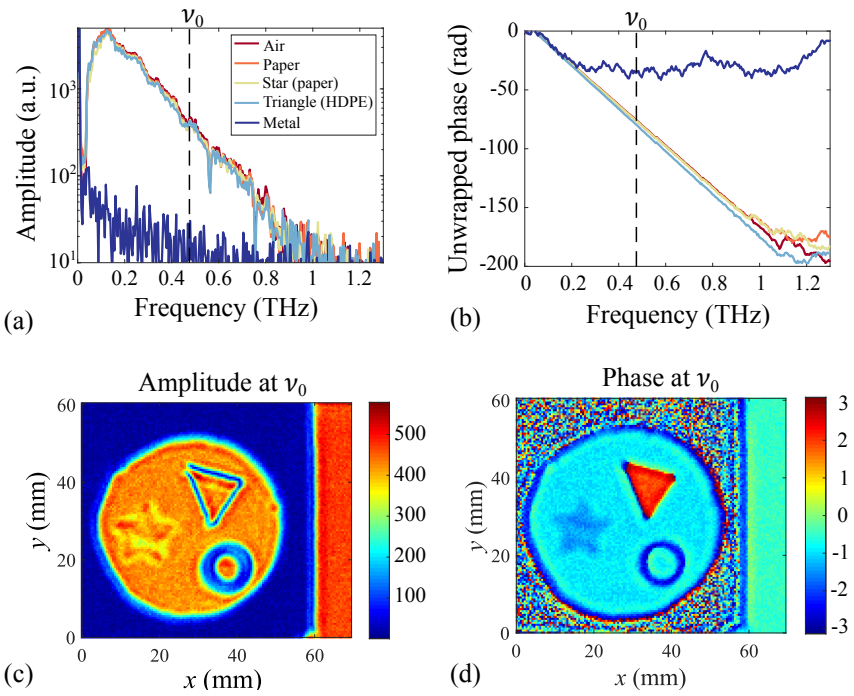

Figure 2.5 (a) Amplitude and (b) unwrapped phase of the spectrum at different positions across the sample in Fig. 2.3(a). (c) Amplitude and (d) phase images at $\nu_0 = 0.475$ THz.

unwrapped in regions of adequate signal-to-noise ratios (SNRs) to avoid numerical artifacts. In Visualization 2, we present an example of a 3D data cube as a function of frequency. In particular, the spatial resolution increases with the THz frequency. In Fig. 2.5(c), we plot the amplitude at 0.475 THz, while the phase (wrapped into a $-\pi$ to π interval) is shown in Fig. 2.5(d). The amplitude image shows the losses in the material, which are maximal for the propagation through the metallic washer. Again, scattering losses are observable at the borders of the HDPE triangle. Inside the star paper and the HDPE triangle, the phase image offers more contrast than the amplitude image. This is because, although the losses are similar in those materials, the refractive index is sufficiently different to provide a meaningful contrast. In general, phase imaging inherently possesses a 2π ambiguity that can be removed using a multiwavelength approach [82] or an interferometric scheme [83]. In Section 2.2.2,we show how to further analyze the THz-TDS measurement to extract the complex refractive index of a material.

Regarding the real-time operation of THz-TDS imaging systems, there are two major problems when using classical THz-TDS setups (see Section 2.3 for more technical details). The first problem is the need to use an optical delay line to obtain the temporal/spectral dimension. Common to many pump–probe optical experiments, the optical delay line usually comes

in the form of a pair of mirrors mounted on a micropositioning stage. The linear mechanical movement of the delay line becomes a hurdle for real-time operation. In Section 2.3.2, we present alternative solutions for fast optical delay lines that can provide acquisition time in the millisecond scale. The second problem is that one typically employs single-pixel THz detectors due to their wide commercial availability. This means that to obtain an image, one needs to mechanically scan the sample point by point. As an alternative to this slow imaging technique, in Section 2.3.3, we detail the technical realization of 2D THz-TDS photoconductive antenna arrays, while in Section 2.3.3, we discuss 2D electro-optic sampling (EOS) in the context of THz-TDS imaging.

2.2.2 THz Transmission, Reflection and Conductivity imaging

In THz-TDS measurements, both the amplitude and the phase of a THz waveform can be extracted. With appropriate numerical treatment, one can then obtain the complex refractive index using the Fresnel coefficients expressed in terms of the relevant material refractive indices. Consider, for example, an interface between media 1 and 2, each medium characterized with its own complex refractive index $\tilde{n}_{1,2} = n_{1,2} - ik_{1,2}$. Assuming that a THz parallel beam is transiting from medium 1 into medium 2, then the corresponding transmission and reflection coefficients can be written as

$$\begin{aligned} &\text{Transmission coefficient:} \quad t_{12} = \frac{2\tilde{n}_1}{\tilde{n}_1 + \tilde{n}_2} \\ &\text{Reflection coefficient:} \qquad r_{12} = \frac{\tilde{n}_1 - \tilde{n}_2}{\tilde{n}_1 + \tilde{n}_2} \end{aligned} \tag{2.1}$$

By fitting experimentally measured transmission and refraction coefficients with the corresponding analytical expressions [Eqs. 2.1], one can extract the material complex refractive indices, thus opening a way for direct imaging of the material refractive index distribution across the sample. In this example, we assume a collimated THz beam, while classical imaging is normally done via point-by-point raster scanning with a THz beam focused at the plane of a sample. In that case, one can still use the method described above; however, expressions for the Fresnel coefficients have to be somewhat modified to account for the non-planar wavefront of the probing beam [84, 85].

In the following subsections, we detail several common imaging modalities that allow imaging complex refractive index distribution at the interface between dissimilar media: THz transmission, reflection, and conductivity imaging.

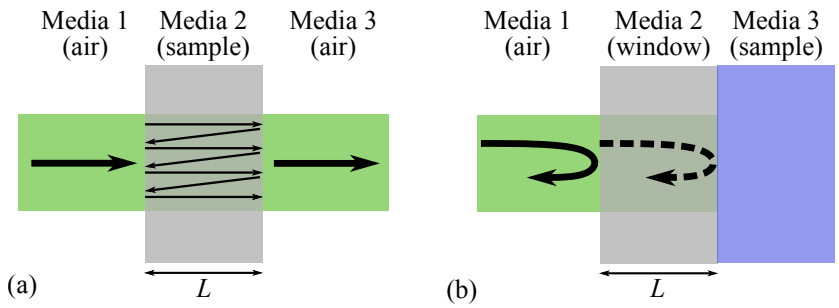

Figure 2.6 (a) Schematic of the transmission and (b) reflection setups for the experimental measurement of the transmission and reflection coefficients.

2.2.2.1 Transmission Spectroscopy

First, we present a more in-depth review on interpreting complex transmission data to extract the sample complex refractive index. In what follows, we suppose a collimated THz beam, while, as mentioned earlier, the same algorithm with minor modifications can also be used in the case of focused THz beams for point-by-point imaging. Following [86], consider a sample in the form of a plate of thickness L (medium 2) and complex refractive index $\tilde{n}_2$, located between two media, media 1 and 3, having complex refractive indices $\tilde{n}_2$ and $\tilde{n}_3$, respectively. In what follows we assume normal incidence of the probing THz wave [Fig. 2.6(a)]. To obtain the normalized transmission function $S_t(\omega)$ for a collimated THz beam, one performs two measurements: one is THz transmission through the sample $E_s(\omega)$, while another (reference measurement) is THz transmission through an empty system (sample removed and replaced with medium 1) $E_{\text{ref}}(\omega)$. Then, the normalized transmission function at the angular frequency ω can be written as

$$\begin{aligned} S_t(\omega) &= \frac{E_s(\omega)}{E_{\text{ref}}(\omega)} = \frac{t_{12}t_{23}\exp(i\tilde{n}_2\omega L/c)}{t_{13}\exp(i\tilde{n}_1\omega L/c)} \cdot \text{FP}(L,\omega) \\ &= \frac{2\tilde{n}_2(\tilde{n}_1+\tilde{n}_3)}{(\tilde{n}_1+\tilde{n}_2)(\tilde{n}_2+\tilde{n}_3)} \cdot \exp\left[i(\tilde{n}_2-\tilde{n}_1)\frac{\omega L}{c}\right] \cdot \text{FP}(L,\omega) \end{aligned} \tag{2.2}$$

where

$$\text{FP}(L,\omega) = \sum_{k=0}^{\infty}\left[r_{23}r_{21}\exp\left(\frac{i2\tilde{n}_2\omega L}{c}\right)\right]^k = \frac{1}{1-\left(\frac{\tilde{n}_2-\tilde{n}_1}{\tilde{n}_2+\tilde{n}_1}\right)\left(\frac{\tilde{n}_2-\tilde{n}_3}{\tilde{n}_2+\tilde{n}_3}\right)\cdot\exp(i2\tilde{n}_2\omega L/c)} \tag{2.3}$$

is the Fabry–Perot term that accounts for multiple reflections inside the sample. This term becomes important when characterizing thin films [87], but it can be neglected ($\text{FP}(L,\omega)=1$) if the sample under consideration is optically thick. In a THz-TDS measurement, a sample

can be considered optically thick if the echoes (multiple reflections) are well separated in time, and only the directly transmitted wave ($k = 0$ term in the sum of Eq. 2.3 is sampled during the time-domain measurement) [86]. Alternatively, a sample can be considered optically thick when the sample material loss is high enough, $2 \cdot \mathrm{Im}(\tilde{n}_2)\omega L/c \gg 1$, so that multiple reflected waves in Eq. 2.3 are so small in amplitude that they can be disregarded. A generalization of Eq. 2.2 for non-normal incidence is provided in Ref. [88].

Several methods can be used to solve Eq. 2.2 [86,88–93]. For example, if the sample ($\tilde{n}_2 = \tilde{n} = n - ik$) is in air ($\tilde{n}_1 = \tilde{n}_3 = \tilde{n}_{\mathrm{air}} = 1$) and if the Fabry–Perot term is neglected ($\mathrm{FP}(L, \omega) = 1$), Eq. 2.2 becomes

$$S_t(\omega) = \frac{4\tilde{n}}{(\tilde{n}+1)^2} \cdot \exp\left[-k\frac{\omega L}{c}\right] \exp\left[i(n-1)\frac{\omega L}{c}\right] \tag{2.4}$$

and can be rearranged to

$$n(\omega) = \frac{c}{\omega L} \arg\left[\frac{(\tilde{n}+1)^2}{4\tilde{n}} S_t(\omega)\right] + 1 \tag{2.5}$$

$$k(\omega) = -\frac{c}{\omega L} \ln\left|\frac{(\tilde{n}+1)^2}{4\tilde{n}} S_t(\omega)\right| \tag{2.6}$$

where $\arg[z]$ is the phase of the complex number z. A fixed-point algorithm can be used to get $n(\omega)$ and $k(\omega)$ [89, 91, 93]. In this algorithm, initial values of $n_0(\omega)$ and $k_0(\omega)$ are injected into Eqs. 2.4 and 2.6 to give new values of $n(\omega)$ and $k(\omega)$.By repeating this process iteratively, a fixed point is found, for which the values of $n(\omega)$ and $k(\omega)$ converge. As an initial guess for $n_0(\omega)$ and $k_0(\omega)$, one can assume that $4\tilde{n}/(\tilde{n}+1)^2 = 1$ [91]. Then,

$$n_0(\omega) = \frac{c}{\omega L} \arg\left[S_t(\omega)\right] + 1 \tag{2.7}$$

$$k(\omega) = -\frac{c}{\omega L} \ln\left|S_t(\omega)\right| \tag{2.8}$$

This approximation becomes almost exact if the material losses are small, i.e., $k \ll n$ [94].

For optically thick samples, the cut-back method can also be used to measure the sample complex refractive index. This is an adaptation of the waveguide characterization technique detailed in Refs. [95–99], and it can also be applied to planar uniform samples. Within this method, transmission measurements are performed for two sample lengths, L_1 and L_2. The main advantage of this technique is that the complex refractive index can be analytically obtained without resorting to iterative algorithms. Indeed, assuming that Fabry–Perot terms do not contribute $\mathrm{FP}(L_1, \omega) = \mathrm{FP}(L_2, \omega) = 1$, the relative transmission function does not

include any Fresnel coefficients:

$$\begin{aligned} S_t(\omega) = \frac{E_2(\omega)}{E_1(\omega)} &= \frac{t_{12}t_{23}\exp(i\tilde{n}\omega L_2/c)}{t_{13}\exp(i\tilde{n}\omega L_1/c)} = \exp\left[\frac{in\omega}{c}(L_2 - L_1)\right] \\ &= \exp\left[-\frac{k\omega}{c}(L_2 - L_1)\right]\exp\left[\frac{in\omega}{c}(L_2 - L_1)\right] \end{aligned} \tag{2.9}$$

From this, the complex refractive index $\tilde{n} = n + ik$ can be computed analytically:

$$n(\omega) = \frac{c}{\omega(L_2 - L_1)}\arg\left[S_t(\omega)\right] \tag{2.10}$$

$$k(\omega) = \frac{c}{\omega(L_2 - L_1)}\ln\left|S_t(\omega)\right| \tag{2.11}$$

This method can be used to rapidly retrieve the complex refractive index without relying on iterative algorithms.

2.2.2.2 Reflection Spectroscopy

Complementary to the transmission spectroscopy covered in the previous subsection, one can also interrogate materials in the reflection mode. In this subsection, we review interpretation of the complex reflection data to extract the sample complex refractive index. Thus, using analytical expressions for the generalized Fresnel coefficients [Eq. 2.1], equations can be derived for the normalized reflection function, which depends on both the collimated THz beam polarization and incidence angle (see Ref. [100] for a comprehensive formulation).

A common experimental setup for reflection spectroscopy is depicted in Fig. 2.6(b).The sample under study (medium 3) is placed behind a window of thickness L (medium 2), which, in turn, is placed in air (medium 1). As an example, we assume normal incidence of the THz beam, and we also assume that both THz emitter and detector are on the same side (transceiver configuration). This configuration, for example, was used to characterize liquids inside plastic bottles [100–104]. If the window is sufficiently thick, so that one could separate in time domain the traces coming from the air/window reflection $E_{\mathrm{ref}}(\omega)$ and the window/sample reflection $E_s(\omega)$, and if we can disregard the Fabry–Perot effect in the window, then the normalized reflection function can be written as

$$S_r(\omega) = \frac{E_s(\omega)}{E_{\mathrm{ref}}(\omega)} = \frac{t_{12}r_{23}t_{21}}{r_{12}}\exp\left(-\frac{i\tilde{n}_2\omega L}{c}\right) = \frac{4\tilde{n}_1\tilde{n}_2}{\tilde{n}_1^2 - \tilde{n}_2^2}\exp\left(-\frac{i\tilde{n}_2\omega L}{c}\right)\frac{\tilde{n}_2 - \tilde{n}_3}{\tilde{n}_2 + \tilde{n}_3} \tag{2.12}$$

If we assume that medium 1 is air ($\tilde{n}_1 = 1$) and medium 2 is a window of a known refractive

index ($\tilde{n}_2 = \tilde{n}_w$), Eq. 2.12 can be written as

$$C = \frac{E_s(\omega)}{E_{\text{ref}}(\omega)} \frac{1 - \tilde{n}_w^2}{4\tilde{n}_w} \exp\left(\frac{i\tilde{n}_w \omega L}{c}\right) = \frac{\tilde{n}_w - \tilde{n}_3}{\tilde{n}_w + \tilde{n}_3} \tag{2.13}$$

Then, $\tilde{n}_3(\omega)$ can be found analytically as

$$\tilde{n}_3(\omega) = \left(\frac{1 - C}{1 + C}\right) \tilde{n}_w(\omega) \tag{2.14}$$

When the sample is strongly absorbing, reflection geometry is clearly superior to the transmission spectroscopy as it does not rely on transmission through absorbing samples. Indeed, transmission spectroscopy is limited by the maximal dynamic range of the THz-TDS system, defined as the frequency-dependent maximal signal amplitude relative to the noise floor. When a sample is strongly absorbing, the noise floor is quickly reached for a short length of the sample. On the other hand, reflection spectroscopy does not rely on transmission through the sample, but rather on the amplitude and phase accuracy of the reflected signal. Therefore, the maximal absorbing coefficient depends on the SNR, defined as the average signal divided by its standard deviation [103, 105]. For example, since liquid water is strongly absorbing in the THz spectral range, many biomedical applications of THz waves are performed in reflection geometry [24, 106].

2.2.2.3 Conductivity imaging

In this subsection, we detail how to extract the electrical properties of a material from the complex refractive index. In many important physics problems, one needs to accurately determine the complex permittivity to electrically characterize a material. THz-TDS gives an almost direct experimental contactless measurement of the complex permittivity without resorting to the Kramers–Kronig relations, as is often done in Fourier-transform infrared spectroscopy (FTIR), for example. Indeed, from the refractive index calculated using the methods described in Sections 2.2.2.1 and 2.2.2.2, the complex permittivity $\tilde{\varepsilon}(\omega)$ can be obtained with [107, 108]

$$\begin{aligned} \tilde{\varepsilon}(\omega) &= \varepsilon_1(\omega) + i\varepsilon_2(\omega) = 1 + i\frac{\tilde{\sigma}}{\varepsilon_0 \omega} \\ \varepsilon_1(\omega) &= n(\omega)^2 - k(\omega)^2 \\ \varepsilon_2(\omega) &= 2 \cdot n(\omega)k(\omega) \end{aligned} \tag{2.15}$$

The complex permittivity is also related to the complex conductivity $\tilde{\sigma}(\omega)$ through $\tilde{\varepsilon} = 1 + i\tilde{\sigma}(\omega)/\varepsilon_0\omega$, with ε_0 the vacuum permittivity. Therefore,

$$\begin{aligned} \tilde{\sigma}(\omega) &= \sigma_1(\omega) + i\sigma_2(\omega) \\ \sigma_1(\omega) &= \varepsilon_0\varepsilon_2(\omega)\omega \\ \sigma_2(\omega) &= -[\varepsilon_1(\omega) - 1]\varepsilon_0(\omega) \end{aligned} \tag{2.16}$$

Insights about the nature of the conductivity can be obtained by fitting the frequency-dependent conductivity with a conductivity model. For example, in the Drude model, the conductivity can be fitted to

$$\begin{aligned} \tilde{\sigma}(\omega) &= \frac{\sigma_{\mathrm{DC}}}{1 - i\omega\tau} \\ \sigma_{\mathrm{DC}} &= ne\mu = \frac{ne^2\tau}{m} = \varepsilon_0\omega_p^2\tau \end{aligned} \tag{2.17}$$

where n is the charge-carrier density, e the elementary charge, μ the mobility, m the mass of the carrier, τ the Drude scattering time, and ω_p the plasma frequency.

Furthermore, the THz pulse can provide insights into the charge-carrier dynamics at the picosecond time scale. Time-resolved THz spectroscopy (TRTS), also known as optical-pump–THz-probe spectroscopy, is a technique derived from THz-TDS in which an optical pump is used to photoexcite the charge carrier in a material under study. By using an optical delay line, the transient conductivity is then probed with the THz pulse. This method is often used to study conductive materials [107–111]. In Section 2.2.5.2, we will see an application of this method in the context of THz near-field imaging.

As an example of THz conductivity imaging, we now discuss contactless mapping of the electrical properties of graphene using THz-TDS. Graphene is a unique bidimensional material with many extraordinary properties that has attracted significant attention due to its potential applications in many fundamental and applied fields [113–115]. With the upcoming integration of graphene into a variety of commercial products comes the need for a rapid, non-destructive, and accurate electrical characterization of this material on an industrial scale [116]. In this context, THz-TDS offers a contactless solution to such a need [117–120].

In Ref. [116], Bøggild *et al.* presented a comparative analysis of three techniques for large-area mapping of the graphene electrical properties. The dry laser lithography first transforms a graphene wafer into multiple electrode devices in 1–2 h before using an automated probe station to extract the relevant parameters using the field-effect or Hall-effect measurement (minutes per measurement point). The need to pattern individual electrode devices makes

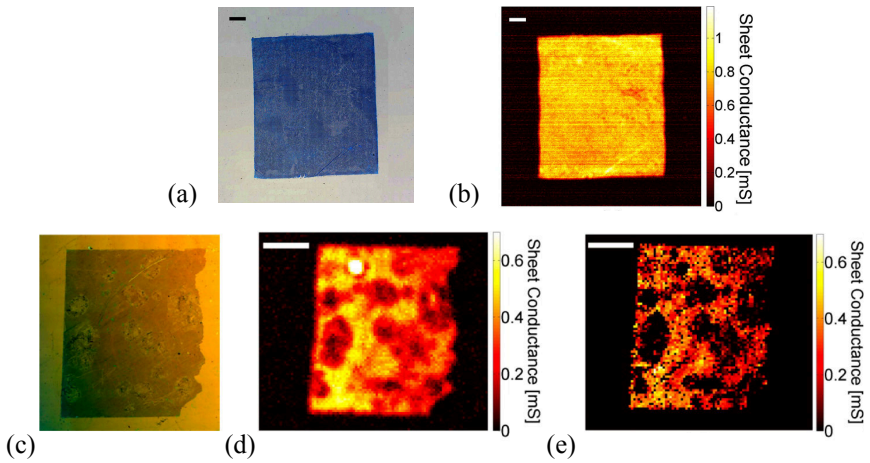

Figure 2.7 (a) Photograph of the graphene sheet and (b) corresponding sheet conductance map obtained using THz-TDS. (c) Damaged graphene sheet and (d) corresponding conductance mapped using THz-TDS and (e) M4PP. Reprinted with permission from Buron *et al.*, Nano Lett. **12**, 5074-5081 (2012) [112]. Copyright 2012 American Chemical Society.

this method destructive by nature. The micro four-point probes (M4PP) use metal-coated silicon microcantilevers to scan across the graphene sheet and obtain the electrical properties using the field-effect measurement (∼1 min per measurement point). This technique is non-destructive since it requires no sample preparation. However, contamination can occur because the tips and the graphene sheet are in contact. In comparison, THz-TDS imaging is non-contact and non-destructive. Furthermore, the acquisition time for a measurement point is limited by the mechanical scanning speed of the detector and the need to use an optical delay line to sample the temporal dimension (∼millisecond per measurement point).

In Ref. [112], Buron *et al.* demonstrated the conductance mapping of graphene with THz-TDS. Large-area graphene thin films were first grown using the chemical vapor deposition technique, before being transferred onto silicon substrates [Fig. 2.7(a)]. Then, the prepared samples were scanned in transmission geometry using a focused THz beam. By using the Fresnel coefficient in transmission geometry, the complex conductance could be determined in the thin film limit. The conductance was found to be virtually constant across the whole THz range, with an imaginary part close to zero and a real part near its DC value [Fig. 2.7(b)]. The real part of the conductance was (0.768 ± 0.077) mS comparable to (0.64 ± 0.13) mS measured with a contact-based M4PP. Next, to demonstrate nonuniform imaging, a damaged graphene sample [photograph in Fig. 2.7(c)] was imaged using THz-TDS [see Fig. 2.7(d)]. Again, the sheet conductance results agree with the M4PP measurement in Fig. 2.7(e).In Ref. [121], the same group used a gate voltage on the graphene sheet to map the carrier mobility, while in Ref. [122] the carrier mobility, carrier density and carrier scattering time

were obtained by fitting the Drude model to the conductance spectra.

In general, the challenges of real-time THz spectroscopy and conductivity imaging are similar to those of the THz-TDS imaging system. To speed up image acquisition, the spectrum needs to be rapidly obtained using a fast optical delay line (see Section 2.3.2) and the detector needs to be a 2D array (see Sections 2.3.3 and 2.3.4). Furthermore, to determine the complex refractive index, one may need to use iterative algorithms, which can be problematic for real-time operation. However, in some cases, analytical solutions can be found. For example, in transmission spectroscopy, if the material losses are small (i.e., $k \ll n$), Eqs. 2.7 and 2.8 can be directly used, while the cut-back method provides an analytical solution [Eqs. 2.10 and 2.11]. As for conductivity imaging, similar iterative algorithms must be used to obtain acceptable fits of the frequency-dependent permittivity with conductivity models. Ideally, the calculation times could be improved by using graphical processing units (GPUs).

2.2.3 THz Pulsed Imaging

THz pulsed imaging (TPI) also known as THz time-of-flight imaging (TOF) refers to mapping the arrival times of the THz pulses to the detector. The measurement is performed in reflection geometry using a THz-TDS configuration. The temporal delay between the reflected pulses reveals the internal structure of the sample.

Already in the early days of THz imaging, TPI was demonstrated by imaging the internal structure of a 3.5 inch floppy disk [124]. In a TOF measurement, the optical path travelled by the pulse is directly related to the pulse temporal delay Δt. Assuming a constant refractive index n over the relevant THz frequency range (associated with the pulse Fourier transform), one can use the time delay between the pulse reflected by the sample surface and the pulse reflected by the sample internal interface to measure the distance d from the sample surface to such internal interface:

$$d = \frac{c\Delta t}{2n} \tag{2.18}$$

One of the practical applications of the TPI technique was demonstrated in the pharmaceutical industry [7, 125–127]. There, an important problem is quality control of medicinal tablet coatings during their fabrication. Unlike in the visible/infrared regions of the spectrum, the majority of dry tablets are semi-transparent to THz radiation, thus enabling non-destructive imaging at high penetration depth [128, 129]. In [123], for example, May *et al.* developed an inline sensor to monitor the tablet coating thickness in real time. The THz radiation was focused on a commercial perforated tablet coater [Figs. 2.8(a)–(c)]. With a prior knowledge of the coating refractive index, Eq. 2.18 was used to measure the tablet coating thickness

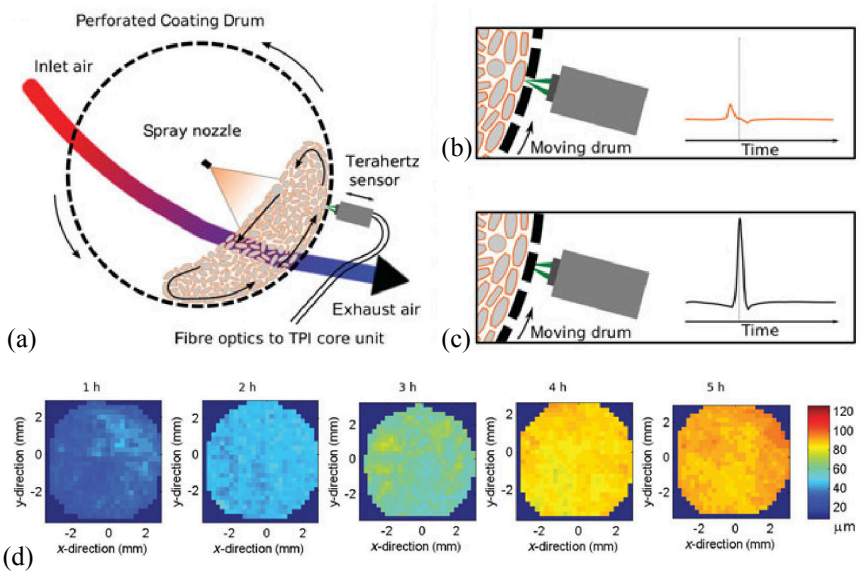

Figure 2.8 (a) Schematic of the tablet coating monitoring using THz-TDS in reflection geometry. (b) Time-domain measurement of the coating thickness and (c) reference measurement. (d) TPI of a tablet during the coating process and corresponding thickness evaluation. Reprinted from J. Pharm. Sci. **100**, May *et al.*, "Terahertz in-line sensor for direct coating thickness measurement of individual tablets during film coating in real-time," 1535–1544 (2011) [123]. Copyright 2011, with permission from Elsevier.

during the coating process [Fig. 2.8(d)]. The general concept behind TPI was also used to assess the hardness, density [130], and porosity [131] of the pharmaceutical tablets, as well as thickness uniformity of automobile exterior coatings [132].

Moreover, in the field of art conservation, TPI was used as a non-destructive method to study the paint layers of ancient masterpieces [14, 134–137]. Thus, in Ref. [133], by using TPI in reflection mode, a hidden portrait has been revealed in an 18th century easel painting by the Danish painter Nicolai Abildgaard. While the visible image portrays an old woman [Fig. 2.9(a)], the x-ray image revealed a portrait of a man underneath the top paint layer [Fig. 2.9(b)]. However, x-ray radiation, due to its ionizing property, can be hazardous to paint and it can compromise radiometric dating. Moreover, while x-ray essentially probes the losses in the paint, TPI can provide supplementary information, such as the paint thickness.

To create a THz image, the authors first deconvoluted the reflected THz signal using a plane metal surface placed at the position of the paint as a reference. Various paint layers were then identified by looking for the distinct reflected pulses in the timedomain data [Fig. 2.9(c)]. Additionally, the authors used spectral integration over certain frequency ranges to reveal

various details of the internal painting:

$$M = \int_{\nu_1}^{\nu_2} |\mathrm{FFT}\{E(t_1 < t < t_0)\}|\, \mathrm{d}\nu \tag{2.19}$$

where the time intervals t_0 and t_1 correspond to the beginning and the end (in time domain) of a particular reflected pulse. For example, by integrating over the whole frequency range for the reflected pulse that defines the second paint layer, they observed the hidden portrait [Fig. 2.9(d)], while by integrating over the 0.55–0.62 THz range, finer details were observed around the nose and the mouth of the subject [Fig. 2.9(e)]. In Fig. 2.9(f), a false color image was realized by superimposing various frequency-averaged THz images obtained using different frequency integration intervals. The color differences in the composite image can be interpreted by noting that different paint pigments have distinct spectral optical properties.

In Ref. [138], TPI imaging was combined with computational imaging techniques to extract, in a fully automated manner, information about the sample layered structure. In particular, by using a THz-TDS setup in reflection geometry [Fig. 2.10(a)], RedoSanchez *et al.* demonstrated an automatized reading of the roman characters written on pages pressed together

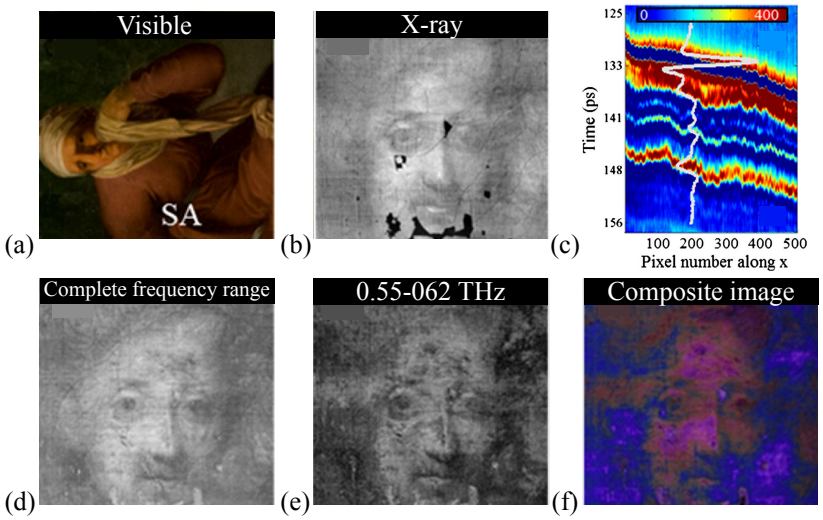

Figure 2.9 (a) Visible image of the painting. (b) X-ray image reveals the hidden paint. (c) Timedomain data shows several distinct layers of paint. (d) THz image obtained by integrating over the full frequency range of the reflected pulse that defines the second paint layer. (e) THz image as in (d) but with spectral data integrated over the 0.55–0.62 THz range. It reveals sharper details around the mouth and the nose. (f) THz false color image obtained by superimposing various frequency-averaged images (blue, 0.22–0.36 THz; red, 0.36–048 THz; and green, 0.48–055 THz). It reveals that several distinct pigments have been used in the painting. Adapted with permission from [133].

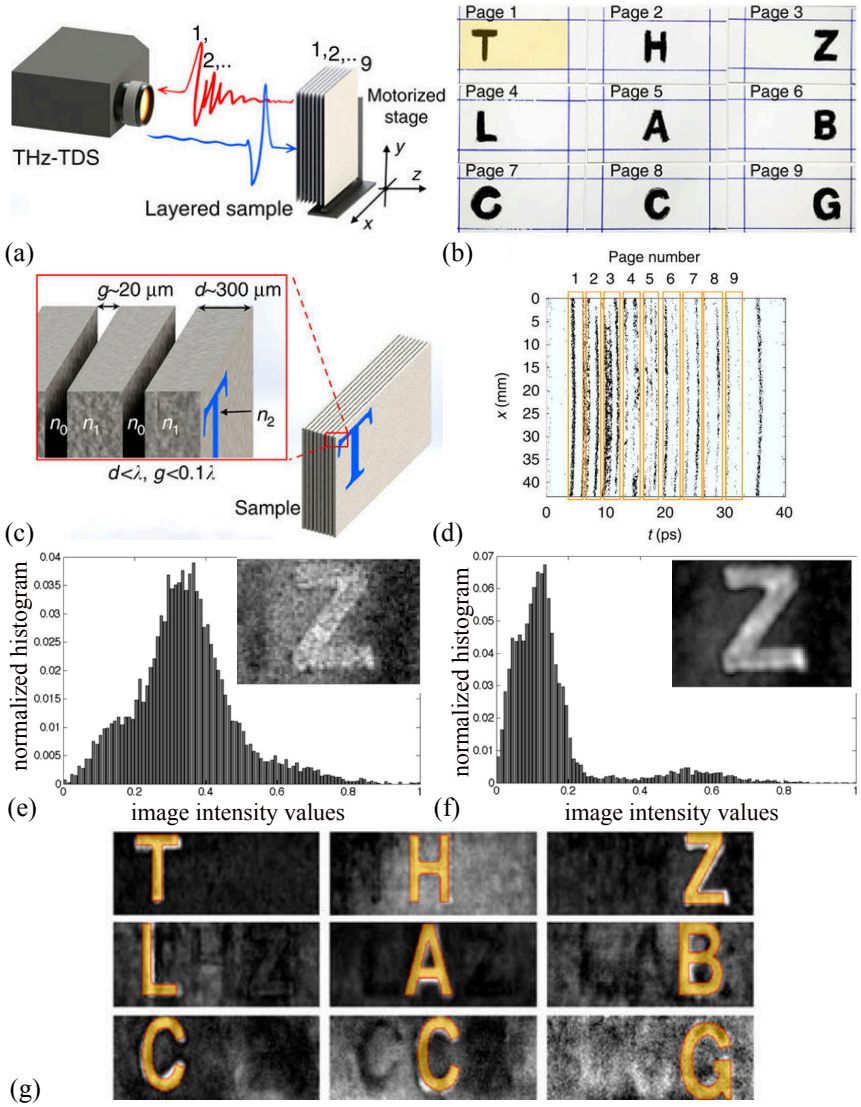

Figure 2.10 (a) Experimental setup featuring a THz-TDS setup in reflection mode. (b) Images of different pages in the visible spectral range and (c) schematic of the book pages. (d) Page number identification using the PPEX algorithm. (e) Pixel intensity histogram for a THz frequency image with a low kurtosis and (f) a high kurtosis. (g) Automatic character recognition by using the CCSC optimization algorithm. Adapted from [138] under the terms of the Creative Commons Attribution 4.0 License. With copyright permission.

to mimic a closed book [Figs. 2.10(b) and (c)]. First, using a -probabilistic pulse extraction (PPEX) algorithm developed by the authors, they identified the presence of different pages by recognizing (numbering) the temporal intervals containing distinct reflected THz pulses [Fig. 2.10(d)]. Next, they performed Fourier transforms of the individual reflected pulses in order to obtain spectrally resolved images of distinct pages. To select the frequency image with the highest contrast, they analyzed the kurtosis of the pixel intensity histograms, as-

suming that kurtosis is higher for higher image contrasts [Figs. 2.10(e) and (f)]. In those selected images, the characters can then be easily recognized in the first paper layers, but the character recognition becomes challenging as the depth increases due to decreased contrast and the presence of phantom images from other layers. To address this issue, the authors used a convex cardinal shape composition (CCSC) optimization algorithm [139] to automatically recognize the letters. The CCSC algorithm works essentially by comparing the regions of high intensity to a set of letters at different positions and orientations.

As for real-time imaging using the TPI technique, the optical delay line is a crucial component (see Section 2.3.2) in such systems, since the method relies on the detection of the reflected echoes obtained in the temporal data of the THz-TDS system. Furthermore, to speed acquisition, 2D arrays can be used to avoid mechanical movement of the sample (Sections 2.3.3 and 2.3.4). Alternatively, single-pixel detection combined with compressive sensing techniques can be employed (see Ref. [140] and Section 2.4.2). Moreover, TPI measurements usually involve multiple reflections for a sample with multiple layers. Therefore, manual intervention is necessary to identify the temporal intervals corresponding to the distinct reflected echoes. To avoid human involvement in the data acquisition process and to speed up the image construction, artificial intelligence or other algorithms can be developed to automatically distinguish the temporal intervals (see, for example, the PPEX algorithm detailed in Ref. [138]).

2.2.4 THz Computed Tomography

Since many materials are relatively transparent to THz radiation, developing 3D THz imaging modalities that can reveal the material's internal structure constitutes an active research field. Extensive reviews of various reconstruction methods for 3D imaging are provided in [80, 142, 143]. As an example, here we detail the THz computed tomography (THz-CT) technique. First demonstrated in the THz spectral range in Refs. [144, 145], the technique derives from the x-ray CT commonly used in the biomedical field.

A typical setup for THz-CT is presented in Fig. 2.11(a). A parallel THz beam is incident onto a sample having, for example, local optical losses distributed according to $\alpha(x, y)$. Here, we define an auxiliary function $f(x, y) = -\alpha(x, y)$, where (x, y) are the coordinates in the local coordinate system associated with the sample. A sample is then placed onto a rotational stage with an instant position characterized by the rotation angle θ. The sample is then rotated, while the detector (or the sample) is moved along a fixed line by distance t to construct the sinogram $P(\theta, t)$ [Fig. 2.11(b)]. In this particular example, the auxiliary function $P(\theta, t)$ is defined as the natural logarithm of the measured THz intensity distribution

$P(\theta, t) = \ln(I(\theta, t))$. Therefore, in this example, the sinogram physically corresponds to some measure of the cumulative optical loss due to transmission through the sample along a certain straight line $L(\theta, t)$ defined by the stage rotation angle and the detector position [141]:

$$P(\theta, t) = \int_{L(\theta,t)} f(x, y)\mathrm{d}l \tag{2.20}$$

The mathematical operation in Eq. 2.20 is known as the Radon transform. It corresponds to the line integral over $L(\theta, t)$. The detector or sample is moved laterally (variable t) and rotated (variable θ) and the sinogram $P(\theta, t)$ is measured. Therefore, to reconstruct the original object $f(x, y)$ (for example the optical loss distribution), the inverse Radon transform is computed through the filtered backprojection (FBP) algorithm [146] or using iterative algorithms, such as the simultaneous algebraic reconstruction technique (SART) and the ordered subsets expectations maximization (OSEM) [147].

In Ref. [141], Brahm *et al.* used the broadband information provided by THz-TDS to identify chemical contents. A sample made of glucose and lactose in a polystyrene holder [Fig. 2.11(c)] was measured at different angles. To create the sinogram, the measurements were normalized by reference measurements of lactose and glucose. In the resulting sinogram, the amplitude

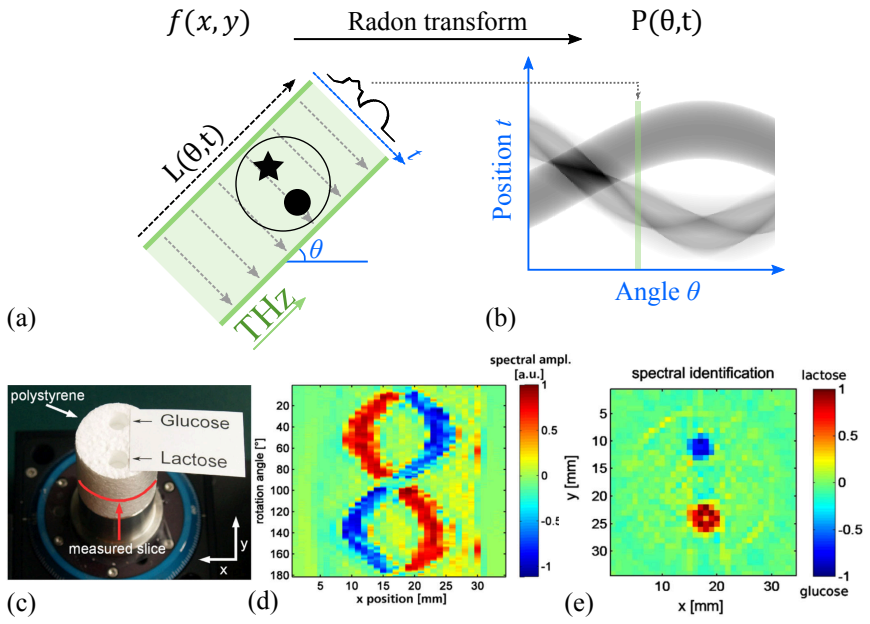

Figure 2.11 (a) THz-CT in the transmission geometry. (b) A typical sinogram from THz-CT. (c) Photograph of the sample with glucose and lactose, (d) corresponding sinogram, and (e) reconstructed material's distribution of the slice in (c). Reprinted with permission from Brahm *et al.*, Appl. Phys. B **100**, 151–158 (2010) [141]. Copyright 2010 AIP Publishing LLC.

values varied between −1 and +1 to indicate the presence of lactose and glucose, respectively [Fig. 2.11(d)]. Then, the FPB algorithm was used to reconstruct the slice of the object [Fig. 2.11(e)]. In [148], the identification and localization were refined by using a wavelet-based method.

THz-CT measures a slice of the object. To obtain the information about the third dimension, instead of measuring along a unidimensional line [axis t in Fig. 2.11(a)], a 2D image per angle θ must be acquired. In Ref. [149], Bessou *et al.* performed THz-CT on dried human bones. In Fig. 2.12(a)–(c), a photograph, an x-ray radiograph, and a THz transmission image of a right human coxal bone are presented. As can be seen from Fig. 2.12(b), the wing of the ilium is transparent to the x rays, while the inferior part is opaque. The THz image

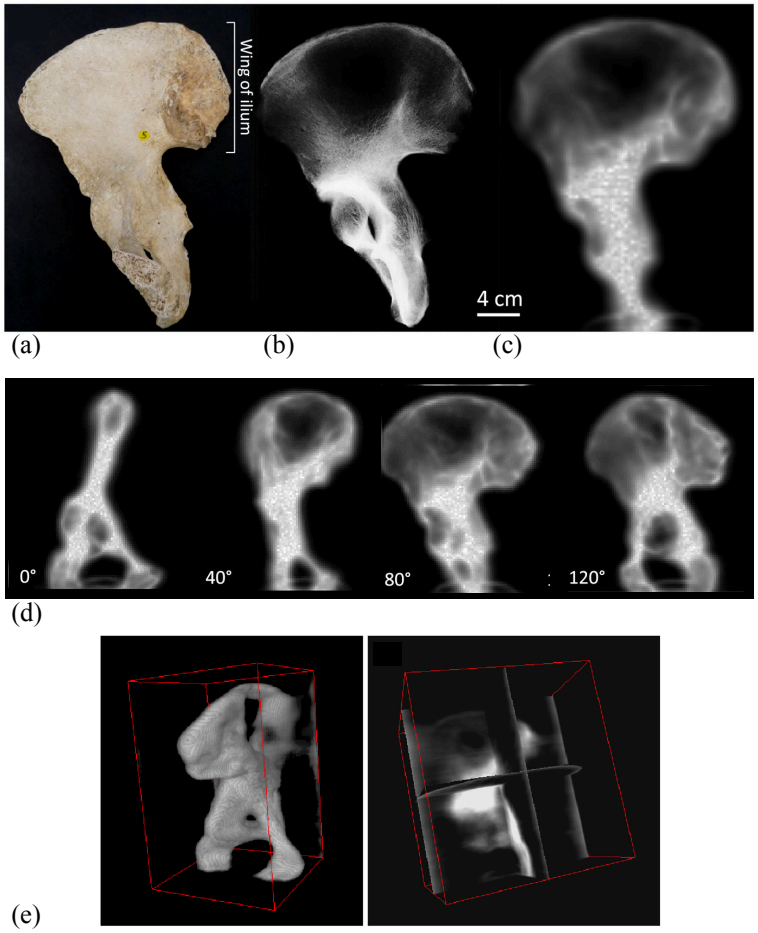

Figure 2.12 (a) Photograph, (b) x-ray, and (c) THz transmission image of a dried right human coxal bone. (d) THz-CT for four different orientations of the bone. (e) 3D reconstruction and (f) internal structure revealed by THz-CT. Reprinted with permission from [149]. Copyright 2012 Optical Society of America.

[Fig. 2.12(c)] presents similar characteristics despite a lower spatial resolution. In Fig. 2.12(d), angular slices of the reconstructed bone are presented, while the 3D reconstruction is shown in Fig. 2.12(e).

In x-ray CT, since the relative size of the wavelength (∼nanometers) is much smaller than that of the object (∼millimeters), one can ignore the illuminating beam selfdiffraction and consider it strictly parallel. On the other hand, in THz-CT, the beam size is limited by the size of the focusing optics, which is typically no larger than ∼10 cm in diameter, while the wavelength of THz light can be as large as several millimeters. Thus, in the THz regime, parallel beam approximation might not be adequate and should be replaced by a Gaussian beam approximation. To obtain better reconstructions, the Gaussian beam intensity profile was introduced into the propagation model in Ref. [150]. In Ref. [151], a statistical reconstruction method called maximum likelihood for transmission (ML-TR) initially developed for x-ray CT was modified to include the Gaussian beam propagation. Alternatively, a nondiffractive Bessel THz beam was shown to improve the quality of the reconstruction in Ref. [152].

Furthermore, while in x-ray CT, only the absorption losses are measured, in THz-CT, reflection and refraction losses become important for non-uniform samples with large refractive index. In Ref. [153], Abraham *et al.* used a multipeak averaging procedure coupled to the algorithm to reduce the effect of the refraction losses on image quality, while in Refs. [154, 155], the Fresnel reflection and refraction losses were evaluated and eliminated using a ray-tracing method. Among successful applications of THz-CT, we note in particular, a study of the internal content of a 18th Dynasty Egyptian sealed pottery reported in Refs. [156–158]. In Ref. [159], polymer additive manufacturing objects from the aerospace and medical industries were successfully imaged in 3D using THz-CT.

Real-time THz-CT is particularly challenging since a third dimension (the angular rotation of the sample) must be measured. However, THz-CT does not require the time-domain/spectral information to reconstruct an object's internal structure. In fact, schemes involving only the transmitted amplitude/intensity THz radiation can be used. For example, in Ref. [160], silicon-based CMOS emitter and detector were used at a frequency of 490 GHz. Other CW THz-CT works involved the use of a doubleheterojunction bipolar transistor at 350 and 650 GHz [161], a gas laser at 2.52 THz [162], a superconducting intrinsic Josephson junction oscillator at 440 GHz [163], and injection-seeded parametric emitter and detector [164]. This opens the possibility of using THz cameras (Section 2.4) to simultaneously obtain two spatial dimensions. For example, in Ref. [165], a pyroelectric camera was used to obtain a 3D image of a straw. Furthermore, if one uses THz-TDS for THz-CT, in addition to the need of array detectors (Sections 2.3.3 and 2.3.4), one also needs to use fast optical delay lines

(Section 2.3.2). In particular, in Section 2.3.4.2, we review the work of Jewariya *et al.* [166] who demonstrated THz-CT acquisition in only 6 min using EOS and a CCD camera. Finally, if one wants to avoid the use of array detectors, a single-pixel detector can also be used for THz-CT, either with fast beam-steering optics [167] or with compressive sensing [168] (Sections 2.5.1.1 and 2.5.1.2).

2.2.5 THz Near-Field Imaging

The imaging systems that we have discussed so far operate in the far-field regime, and, thus, feature resolutions that are limited by diffraction of the THz beam on the elements of the optical system. For example, light from a point source positioned near the microscope objective focal plane and passing through a circular lens produces a diffraction pattern in the shape of concentric rings (Airy disk). The spatial resolution in the object plane is generally defined using the Rayleigh criterion [169], where the minimal resolvable feature δx is defined as the minimal distance between a point source central maximum and the second point source first minimum. This can be written as

$$\delta x = 1.22\frac{\lambda F}{D} \tag{2.21}$$

where F and D are the focal length and diameter of the lens, respectively. This corresponds to the size, in the object plane, of the smallest object that the lens can resolve and also the radius of the smallest spot to which a collimated beam of light can be focused. Therefore, according to Eq. 2.21, the smallest resolvable feature is normally comparable to or larger than the wavelength of the THz light.

To resolve the object's subwavelength features, one needs to detect the evanescent fields, which exist only at short distances from the object (near-field region). This type of imaging is known as THz near-field imaging. Prior reviews of this topic are found in Refs. [170–173]. Several techniques have been explored to enable subwavelength THz imaging. In the following, we first briefly overview some recent subwavelength imaging techniques, before focusing on two major types of techniques that have attracted the most attention in the literature, namely, aperture-based and scattering-based near-field imaging.

The confocal THz near-field imaging technique, as its name suggests, derives from the confocal microscopy at optical wavelengths. It consists of using a pair of apertures (pinholes) that act as spatial filters to block THz radiation propagating outside the cone of light, thus resulting in increased lateral and depth resolution [174–177]. For example, in Ref. [176], using a quantum cascade laser at 2.9 THz, the authors demonstrated lateral and axial resolutions

of 70 μm ($\lambda/1.4$) and 400 μm. In Ref. [177], medieval manuscripts were imaged with confocal THz imaging at 0.3 THz with a lateral resolution of 0.5 mm ($\lambda/2$). In confocal microscopy, the lateral resolution is improved by reducing the pinhole diameter. However, the diameter cannot be reduced below a certain threshold for which no signal is collected at all, therefore requiring powerful sources.

In comparison, the solid-lens immersion approach allows for more throughput light intensities. The idea here is to use a specially designed lens that generates a spot size smaller than the diffraction limit in the evanescent field region following the lens. For example, the lens can be a cube [178, 179] or a sphere [180]. In Ref. [181], a combination of an aspheric lens and a truncated sphere was used to achieve a resolution of $\lambda/3.1$ (at 0.5 THz), better than the resolution of an aspheric lens alone ($\lambda/1.2$). In this case, however, the spatial resolution (although subwavelength) is fundamentally limited by the material properties of the immersion lens (specifically its refractive index). In Ref. [182], a similar setup was used to image soft biological tissues with a resolution of $\lambda/6.7$ at 0.6 THz.

In the direct-contact method, the sample is placed in direct contact with a subwavelength detector. This approach is generally employed with EOS using THz-TDS (Section 2.3.1.1). In this case, the detector is a femtosecond optical beam (the size of which is smaller than the THz wavelength) that probes the polarization change in a nonlinear crystal. The sample is then in direct contact with the crystal, leading to a direct measurement of the THz electric field in the near-field region. For example, in Ref. [183], Adam *et al.* demonstrated a 20 μm resolution by imaging various metal structures deposited onto an electro-optic GaP crystal. In Ref. [184], Seo *et al.* measured the 2D time-domain THz electric field behind the slit arrays, from which the magnetic and Poynting fields were reconstructed. Because of the possibility of using cameras operating in the visible/ infrared range, the direct-contact EOS technique is a serious candidate for real-time near-field THz imaging. This will be reviewed in Section 2.3.4.2. Very recently, an additional approach using SiGe heterojunction bipolar transistor technology has emerged for direct-contact near-field imaging [185]. Fabricated with 130 nmBiCMOS process technology, the sensor operating at 0.55 THz both generated and detected THz radiation. The close on-chip proximity of the emitter and the detector allowed the demonstration of a lateral resolution of 10–12 μm ($\lambda/55$).

Among other THz near-field imaging techniques, we note the deconvolution from the image of the point-spread function, mathematically modeled using the Gaussian beam theory and variables such as the beam divergence, depth of focus, and absorption coefficient of the object [186, 187].

Realizing real-time near-field imaging is not trivial since most of the techniques rely on the

mechanical scanning of subwavelength apertures/tips. Therefore, the parallel acquisition of multiple images becomes difficult. In that context, the direct-contact THz near-field imaging technique distinguishes itself as it allows acquiring 2D images. Furthermore, spectroscopic features being rich at the subwavelength scale, there is great interest in combining THz-TDS with near-field THz imaging. This combination is realized in EOS with crystals and it is the subject of Section 2.3.4.2.

2.2.5.1 THz Aperture Near-Field Optical Microscopy

The most direct way of enabling a near-field imaging system is to use a subwavelength-size aperture in the near field. In the visible/infrared this approach is also known as scanning near-field optical microscopy (SNOM). The resolution of this method scales with the size of the aperture, however, the sensitivity of the method decreases rapidly (superlinearly) with smaller aperture sizes [188]. The aperture can also be a tapered metal cone tip [189], a dynamically moving aperture produced by optically pumping a semiconductor wafer [190]. We mention that, in principle, apertureless subwavelength dielectric probes can be designed using a solid immersion lens approach, which can provide much higher throughput light intensities than aperture-based methods [181]. In this case, however, the spatial resolution (although subwavelength) is fundamentally limited by the material properties of the immersion lens, which is not the case for aperture-based near-field imaging.

In more detail, in Ref. [188], the detector (a photoconductive antenna) was placed at a subwavelength distance from a near-field rectangular aperture probe to detect the exponentially decaying evanescent THz field [193]. In this arrangement, the spatial resolution is determined by the aperture size [194]; however, following Bethe's study of diffraction by a circular hole [195, 196], the transmitted electric field decreases with the third power of the aperture size, thus rendering the transmission through deeply subwavelength apertures extremely small. To increase the optical transmission through subwavelength apertures, in Ref. [197], Ishihara *et al.* inscribed concentric periodic grooves onto a metallic substrate around the aperture. In this bull's-eye structure, the incident THz wave excites surface waves that increase the electric field values in the subwavelength aperture 20-fold. In Ref. [198], the circular aperture was replaced by a bow-tie aperture to increase the transmission by 3 and enable a resolution of 12 μm ($\lambda/17$ at 1.45 THz).

Recently, the near-field probe and the THz photoconductive antenna were integrated on a single chip. In Ref. [191], Macfaden *et al.* placed the aperture probe at a 1 μm distance from the THz antenna, which resulted in a sub-1-μm thickness of the GaAs semiconductor active layer, which is a key enabling element of the antenna. The problem with such a

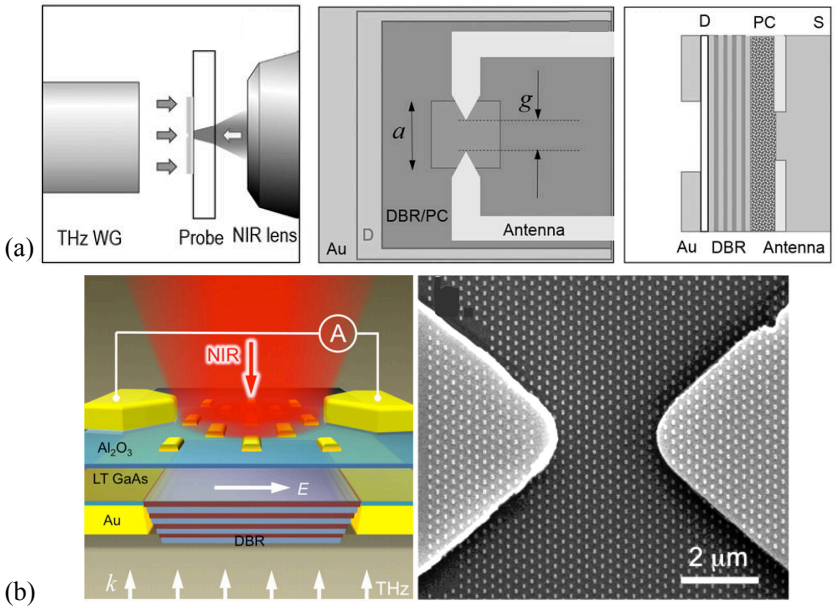

Figure 2.13 (a) Integrated subwavelength aperture/THz-PCA in a single chip separated by a distributed Bragg reflector. Adapted from Macfaden *et al.*, Appl. Phys. Lett. **104**, 01110 (2014) [191]. Copyright 2014 AIP Publishing LLC. (b) Integrated chip enhanced with a plasmonic nanoarray. Adapted with permission from Mitrofanov *et al.*, ACS Photon **2**, 1763–1768 (2015) [192]. Copyright 2015 American Chemical Society.

small thickness of the GaAs layer is that it is much smaller than the characteristic optical absorption length (1.4 μm) at the wavelength (800 nm) used for photoexcitation (infrared pump beam) of the antenna. This means that few charge carriers are generated by the pump beam within the GaAs layer of the PCA and, consequently, sensitivity of the THz detection is reduced. To increase the detection efficiency, the authors introduced a distributed Bragg reflector between the semiconductor layer and the subwavelength aperture [Fig. 2.13(a)]. The purpose of this reflector was twofold. First, it behaved as a resonator that enhanced the optical field of the pumping infrared beam at the position of the antenna gap. Second, it provided optical isolation of the sample under study from the pumping optical pulse, which is important when imaging light-sensitive materials such as semiconductors. As a result, with the integrated chip, a spatial resolution of 3 μm ($\lambda/100$ at 1 THz) was demonstrated. In Ref. [192]], to increase the sensitivity of the antenna even further, a gold nanoantenna array was added in the vicinity of the active layer of the antenna [Fig. 2.13(b)]. The array was designed to have a plasmonic resonance at 800 nm and the experimental spectra showed that 80% of the pump light was absorbed. With this structure, a spatial resolution of 2 μm was demonstrated ($\lambda/150$ at 1 THz).

2.2.5.2 THz Scattering Near-Field Optical Microscopy

A second class of THz near-field systems is known as THz scattering near-field optical microscopy. In those systems, the THz radiation is focused on a metallic tip that confines strongly the THz radiation in a small region. When brought close to a sample, the tip scatters in the far field the THz radiation that has interacted with the sample in the near field. To distinguish the scattered field from the background noise, the tip is mechanically modulated at a certain fixed frequency that enables THz detection with a lock-in amplifier.

In the early demonstrations of the scattering-type THz near-field imaging, spatial resolutions of 18 μm (λ/110 at 0.15 THz) [199] and 150 nm (λ/1000 at 2 THz) [200] were achieved. Those resolutions were essentially determined by the size of the tip apex. One of the main advantages of the scattering-type THz near-field imaging is that the THz system can be coupled with existing imaging techniques that use vibrating probing tips. For example, in Ref. [201], THz illumination and detection were combined with the vibrating cantilever of an atomic force microscope (AFM) to map the charge-carrier concentration of a transistor at the nanometer scale with 40 nm resolution (λ/3000 at 2.54 THz).

Laser THz emission microscopy (LTEM) is a near-field imaging technique initially proposed for non-destructive inspection of electrical failures in circuits [202]. Within this method, upon femtosecond illumination of a sample, charge carriers are accelerated, and THz pulses are emitted. In LTEM, the spatial resolution is determined by the femtosecond pulse spot size, leading to a spatial resolution of 3 μm (λ/2000 at 0.05 THz) in Ref. [202]. Very recently, nanoscale LTEM was proposed by focusing the infrared femtosecond pulse on a commercial AFM metal tip and a semiconductor substrate [203]. Dipole oscillations of the charges are the source of THz pulses in the region of the tip apex. Nanoscale imaging can then be performed by detecting the THz pulses that have interacted with a sample brought close to the metal tip. In [203], a tipsize-limited spatial resolution of 20 nm was achieved and allowed the THz imaging of a single gold nanorod.

In Ref. [204], THz-TDS was coupled to a scanning tunneling microscope (STM) to combine the nanometer spatial resolution of the STM with the subpicosecond time resolution of the THz-TDS. Without modifying the STM design, the THz pulse was focused onto the probe tip to produce a subpicosecond voltage transient that drove electrons across the junction [Fig. 2.14(a)]. Since the measured current is localized in the tunnel junction, the spatial resolution is defined by the size of the tip apex, which was measured to be 2 nm (λ/150000 at 1 THz) in Ref. [204]. To demonstrate the potential of the THz-STM in measuring ultrafast carrier dynamics, Cocker *et al.* [204] optically pumped a sample of InAs nanodots grown on GaAs. Then, they measured both the STM topography and the THz-STM images. By

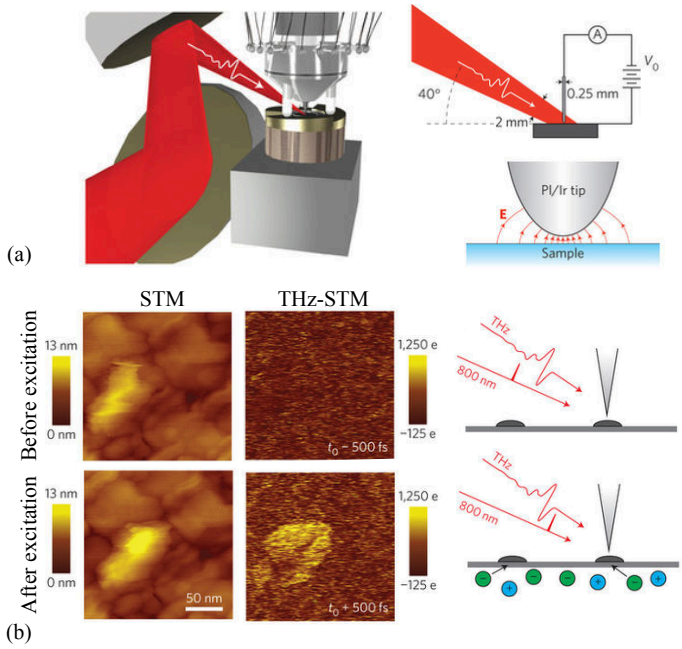

Figure 2.14 (a) Schematic of the THz-STM. (b) STM image, THz-STM image and schematic before and after optical excitation. Reprinted by permission from Macmillan Publishers Ltd.: Cocker *et al.*, Nat. Photonics **7**, 620–625 (2013) [204]. Copyright 2013.

varying the time delay between the optical pulse and the THz pulse, clear contrast in the THz-STM images was observed [Fig. 2.14(b)]. In Ref. [205], by using THz-STM, the authors imaged the dynamics of the orbital structure of a pentacene molecule.

2.3 Enabling Real-Time THz-TDS Imaging

Many of the imaging techniques we reviewed in Section 2.2 use the THz-TDS setup. In this section, we have a closer look at THz-TDS, as well as at various techniques that can speed up acquisition of the THz pulses and enable real-time imaging.

Fig. 2.15 depicts two classical experimental setups for THz-TDS in transmission and reflection modalities. An ultrafast laser beam is divided and sent along two optical paths. THz pulses are generated in the emission arm and then they travel to a sample placed at the focal plane of the focusing optics. After interacting with the sample, the THz pulses are coherently detected in the detection line arm, using an optical delay line to induce a temporal difference between the optical pump and the probe pulses.

There are two main methods to generate and detect THz pulses: (1) using photoconductive antennas (PCA) and (2) using optical rectification and EOS in nonlinear crystals. In this

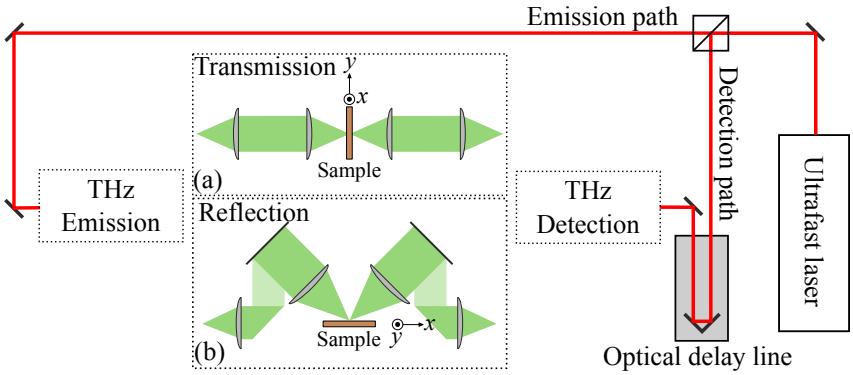

Figure 2.15 Schematic of a THz time-domain spectroscopy system in (a) transmission and (b) reflection geometries. The emission and detection hardware are described in Section 2.3.1.

section, we begin by detailing the emission and detection principles using the abovementioned technologies (Section 2.3.1). For real-time imaging, the predominance of the relatively slow optical delay lines presents one of the main challenges. Therefore, in Section 2.3.2, we review several novel optical delay line designs that speed up pulse acquisition. Typically, both PCA and EOS are single-pixel detectors, which complicates the acquisition of high-resolution THz images. Therefore, in Section 2.3.3, we overview some of the recent works aimed at fabricating PCA arrays, while in Section 2.3.4, we detail the use of cameras to perform EOS.

2.3.1 Coherent THz Generation and Detection THz-TDS

2.3.1.1 Photoconductive Antenna

A photoconductive antenna (PCA) can be used to generate and detect THz pulses [46–52]. The PCA is made of two metal electrodes deposited onto a semiconductor substrate. Photoexcited carriers are created in the gap between the electrodes by optical excitation (typically using ultrafast infrared pump laser beams). The PCA is essentially a photoswitch, where, for THz generation and detection, both the switch-on and switch-off times must be subpicosecond [206]. The switch-on is determined by the pump pulse duration of the optical excitation (typically < 100 fs), while the switch-off time is dictated mainly by the carrier lifetime.

To generate THz, the antenna gap is voltage-biased and illuminated with a femtosecond laser pulse [Fig. 2.16(a)]. Excited photocarriers are then accelerated on a subpicosecond time scale. This rapid rise and fall of the transient photocurrent is the source of a THz electromagnetic field irradiated away from the antenna. The process of transient photocurrent switching can generate broadband THz pulses with bandwidths up to 15 THz [207], the limitation

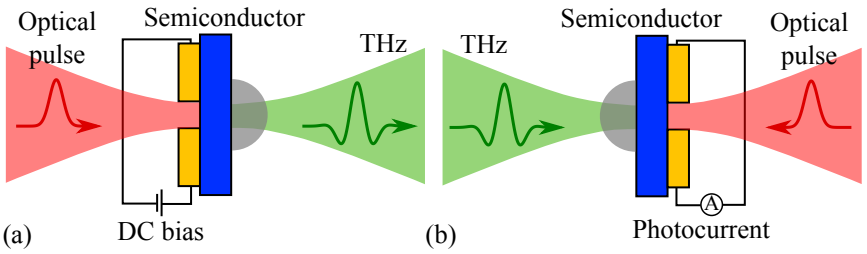

Figure 2.16 Schematic of the photoconductive antenna operation to (a) generate and (b) detect THz pulses.

being the carrier lifetime. Recently, average THz power levels as high as 3.8 mW (with 240 mW optical pumping) were achieved, by using a large-area PCAwith embedded plasmonic contact electrode gratings [208, 209], while most THz-TDS systems operate with THz pulses of ∼1–100 μW average power. To improve the SNR, the emitter antenna is typically biased with an alternating voltage and lock-in amplification is used.

For THz detection, no bias voltage is applied between the electrodes [Fig. 2.16(b)], while the excited photocarriers are accelerated by the incoming THz radiation. This results in a time-varying photocurrent $J(\omega)$ between the antenna electrodes, which is proportional to the field amplitude of the THz radiation $E_{\mathrm{THz}}(\omega)$:

$$J(\omega) \propto [I(\omega)R(\omega)]E_{\mathrm{THz}}(\omega) \tag{2.22}$$

where $I(\omega)$ is the spectrum of the optical source, and $R(\omega)$ is the Fourier transform of the time response of the semiconductor photocarriers, which includes the trapping and recombination times [210,211]. The term $[I(\omega)R(\omega)]$ is the spectral sensitivity of the PCA, and it can be seen as a low-pass filter function applied to the incident THz pulse $E_{\mathrm{THz}}(\omega)$. Consequently, the detected THz bandwidth can be improved by pumping the PCA detector with temporarily shorter optical pulses (larger bandwidth) or by tuning the charge-carrier lifetimes. In Refs. [212, 213], significant improvement in the THz detection sensitivity was reported by using nanostructured plasmonic contact electrodes that effectively reduce the average transport path length of the photocarriers. Consequently, an increased number of carriers reached the contact electrodes, leading to higher photocurrent and increased sensitivities.

Finally, we note that the classic PCA is a single-pixel detector, which is problematic for real-time high-resolution THz imaging due to the necessity of slow raster scanning of the sample. Recently, there were several reports of designing arrays of PCA detectors, which can be beneficial for imaging applications. We detail these advancements in Section 2.3.3.

2.3.1.2 Optical Rectification and Electro-Optic Sampling

Optical rectification is a second-order nonlinear process commonly used to generate pulsed THz radiation [54,55,214] [Fig. 2.17(a)]. An ultrafast optical pulse $E_(\omega)$ propagating inside a nonlinear electro-optic crystal is the source of a time-varying second-order polarization term that can be expressed as [206]

$$P_i^{(2)}(0) = \sum_{j,k} \varepsilon_0 \chi_{ijk}^{(2)}(0, \omega, -\omega) E_j(\omega) E_k^*(\omega) \tag{2.23}$$

where the indices i, j, and k correspond to the Cartesian components of the field, and $\chi_{ijk}^{(2)}$ is the second-order susceptibility tensor element for the crystal. Eq. 2.23 indicates that, when the optical electric field $E(\omega)$ is correctly oriented relative to the crystal axis, the induced second-order polarization is roughly proportional to its square $|\vec{P}^{(2)}| \propto |E(\omega)|^2$. For THz generation, the optical field is a time-dependent femtosecond pulse, for example, a Gaussian distribution with a width related to a [215]:

$$E(t) \propto E_0 e^{at^2} e^{i\omega t} \tag{2.24}$$

Therefore, the induced polarization is also time dependent and proportional to the envelope of the optical pulse:

$$|P^{(2)}| \propto E_0 e^{-2at^2} \tag{2.25}$$

Furthermore, this induced polarization is the source of a THz electric field $\vec{E}_{\mathrm{THz}}(\omega)$ through the wave equation

$$\nabla^2 \vec{E}_{\mathrm{THz}} - \frac{n_{\mathrm{THz}}}{c^2} \frac{\partial \vec{E}_{\mathrm{THz}}}{\partial t^2} = \frac{1}{\varepsilon_0 c^2} \frac{\partial^2 \vec{P}^{(2)}}{\partial t^2} \tag{2.26}$$

where n_{THz} is the crystal's refractive index at THz frequencies. Thus, in principle, the THz pulse spectral bandwidth can be increased by reducing the optical pump pulse duration. In practice, the phase-matching condition, which includes the crystal dispersion at optical and THz frequencies [216], bounds the interaction length (walk-off length) and limits the efficiency of the THz generation. ZnTe is the most commonly used crystal for THz generation. A second popular choice is the $LiNbO_3$ crystal, which has a larger nonlinear coefficient, but that requires a tilted-pulse-front excitation for efficient generation [217–219]. With this method, single-cycle THz pulses with amplitudes exceeding 1 MV/cm can be generated [220]. Recently, nonlinear organic crystals have also been successfully used to generate THz pulses through optical rectification [56]. In Ref. [57], Vicario *et al.* used a Cr:forsterite laser at 1.25 μm to pump organic crystals DAST, OH1, and DSTMS, generating THz pulses with peak

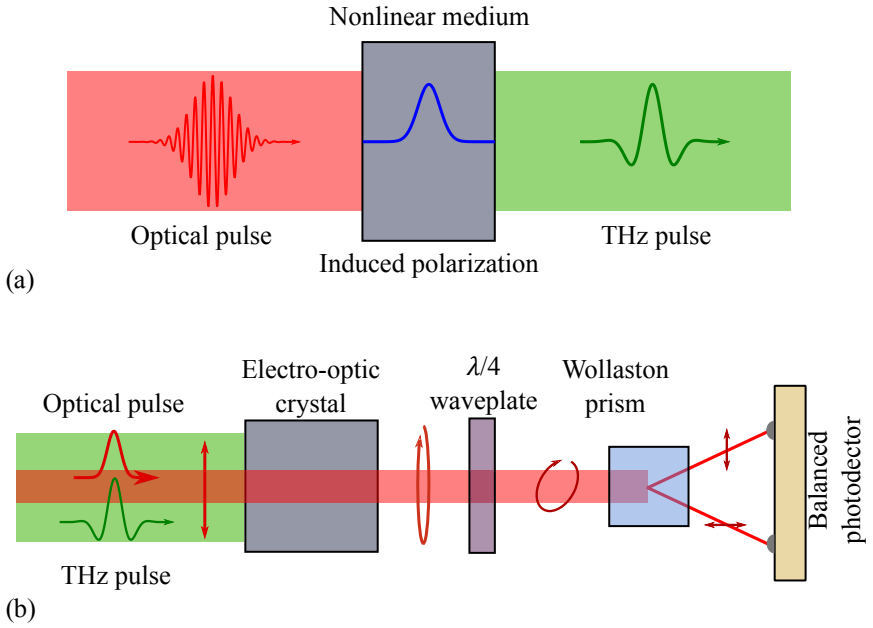

Figure 2.17 (a) THz generation using optical rectification and (b) THz detection using EOS.

electric fields of 6.2, 9.9, and 18 MV/cm, respectively. We also mention the generation of THz pulses with tight focus of ultrafast optical pulses to generate gas plasma (for example, in air) and THz radiation through a four-wave mixing process involving third-order nonlinear susceptibility [75]. The reciprocal nonlinear process can also be used to coherently measure the THz pulse from the THz field-induced second harmonic (TFISH). This technique is known as the THz air-biased coherent detection technique (THz-ABCD). Compared to the generation/detection with optical rectification in a crystal, THz-ABCD provides a very large spectral bandwidth (from 0.2 THz to >30 THz), limited primarily by the optical pulse duration [76].

Using nonlinear crystals, the detection is based on electro-optic sampling (EOS), which is conceptually the opposite of optical rectification [70–74, 216]. Under the Pockels effect, the THz electric field modulates the birefringence of a $\chi^{(2)}$ crystal. Therefore, by probing the birefringence with a femtosecond optical beam, the THz electric field can be coherently measured. Fig. 2.17(b) shows a typical experimental setup for detecting THz pulses using EOS. The optical probe beam and the THz pulse interact inside the crystal. The linearly polarized optical beam will have a slightly elliptical polarization at the output of the crystal. Then, a polarization control system is used to extract from the elliptical polarization its two orthogonal linear components for balanced detection. For example, a quarter-wave plate can be used to convert the optical probe beam polarization into an almost-circular polarization. Then, a Wollaston prism can be used to divide the almost-circular polarization into two

orthogonal components. Finally, a balanced photodetector measures the intensity difference between the two orthogonal components, which is proportional to the applied THz electric field.

Since EOS measures the state of polarization of a probing optical beam, conventional visible/infrared cameras can be used to provide real-time THz images (see Section 2.3.4 for details). We mention that the nonlinear parametric upconversion process [45, 221, 222] has also been used to demonstrate CW THz imaging with infrared cameras [164, 223, 224].

2.3.2 Fast Optical Delay Line

In THz-TDS, an optical delay line is used to scan and measure the THz pulse in time domain. The pulse spectrum is then retrieved using Fourier transform. In a classic THz-TDS setup, a linear reflective optical delay line positioned either in the emission or detection side is used. Such delay lines are realized by mounting a retroreflective prism onto a linear mechanical micropositioning stage. Thus, when the delay line travels a distance Δz, the time delay between the probe and pump pulses is modified to $\Delta t = 2\Delta z/c$. In this expression, the factor 2 expresses the fact that the optical beam travels twice the distance (back and forth) in the delay line. As a typical THz pulse has $\sim$1 ps duration, one normally uses $\delta t = 0.01$ ps sampling resolution to correctly resolve the THz pulse. This, in turn, imposes restriction on the precision of the micropositioning stage $\delta z = c\delta t/2 \sim 1.5$ μm, which is readily achievable with high-quality commercial micro-positioning mechanical stages.

The THz spectrum is obtained by taking the Fourier transform of the temporal pulse. From the properties of the Fourier transform, it follows that the pulse maximal frequency $\nu_{\max}$ and the frequency resolution δnu are given by

$$\nu_{\max} = \frac{1}{2\delta t} = \frac{c}{4\delta z} \tag{2.27}$$

$$\delta\nu = \frac{1}{\Delta t_{\max}} = \frac{c}{2\Delta z_{\max}} \tag{2.28}$$

where δt and $\Delta t_{\max}$ are the temporal sampling resolution and the total temporal delay used in the pulse acquisition, respectively, while δz and $\Delta z_{\max}$ are the positional increment and the total movement of the delay line, respectively. For example, a $\delta z = 30$ μm positioning step size and a total delay line displacement of $\Delta z_{\max} = 30$ mm gives a spectrum with a maximal frequency of 2.5 THz and a resolution of 5 GHz.

For real-time imaging applications, the raster scanning of a sample is too timeconsuming mostly due to the limited scanning speed of the optical delay lines, which typically do not

exceed 1 Hz, thus resulting in ∼1 s per pixel acquisition rates. The limited speed of traditional optical delay lines that use mechanical micropositioning stages is essentially due to their interrupted back-and-forth linear displacement. From a mechanical point of view, rotary movements enable uninterrupted displacements with higher speeds, which prompted significant research into the development of rotary delay lines. In the following, we begin by reviewing two major types of mechanical rotary delay lines that are based on rotary reflectors (Section 2.3.2.1) or rotary prisms (Section 2.3.2.2). Finally, in Section 2.3.2.3 we focus our attention on non-mechanical delay lines.

Here, it is important to note that even if infinitely fast optical delay lines would become available in the future, one still has to be aware of the fundamental signal acquisition delay per pixel, which is related to the averaging time constant of the lock-in amplifier used to increase the SNR of the detected signal. As more powerful THz emitters become available in the future, the averaging times could become shorter. A typical lock-in averaging time used in the current low-power THz-TDS systems is larger than $\delta t_{av} = 1$ ms. Ideally, lock-in averaging has to be done for every position of the delay line, thus resulting in a total acquisition time for a single THz pulse (single pixel) of $\delta t_{av}\Delta t_{\max}/\delta t = \delta t_{av}\Delta z_{\max}/\delta z \sim 1$ s in the case of $\delta t_{av} = 1$ ms, $\Delta z_{\max} = 30$ mm, and $\delta z = 30$ μm discussed above, which is a an example of a typical high-resolution THz scan.

2.3.2.1 Rotary Reflectors

Rotary delay lines can feature planar or curvilinear mirrors that are mounted directly or otherwise actuated by a rotating motor shaft. Rotary reflector lines were typically placed in the path of an optical pump beam, but they could be placed in the THz beam path.

Rotary optical delay lines were originally developed for optical coherence tomography (OCT) (notably multiple-pass cavity delay lines [225,226]), and they generally feature a combination of rotating curved and planar mirrors [227, 228], which can even include turbines in place of motors for faster rotation speeds. Although optical delay lines for OCT enable very high scanning rates of up to several tens of kilohertz, such delay lines show small optical delays (∼20 ps) that are insufficient for THz-TDS applications.

To increase the maximal optimal delay, retroreflectors coupled to a galvanometer were proposed for ultrafast optical measurements [229]. Such a system achieved an optical delay of 300 ps with a scanning rate of 30 Hz. However, since the linear movement of the mirror induced by the rotating galvanometer was sinusoidal in time, an additional calibration step was needed to recover the instant value of the linear optical delay as a function of time.

Curvilinear reflective surfaces designed to provide linear optical delay as a function of the reflector rotation angle were first reported in Refs. [230–234]. In Ref. [232], Kim *et al.* mounted six reflectors onto a servo motor and demonstrated acquisition of the THz pulses with a net scanning rate of 400 Hz and a maximal optical delay of 70 ps. However, in their design, the incident beam and the reflected beam were collinear. Therefore, a beam splitter was needed to separate the incident and reflected beams, thus leading to a significant loss of optical power. The importance of this design is in its linear dependence on the reflector rotation angle. Thus, by using a motor with a fixed and stable angular rotation frequency, a linear optical delay as a function of time is assured, and no additional calibration steps are needed.

In Ref. [233], Skorobogatiy developed a comprehensive mathematical theory for the design of rotary delay lines that feature up to three rotating and stationary curvilinear reflectors. Analytical and semi-analytical expressions for the reflector shapes were given for four classes of rotary delay lines that included linear dependence of the optical delay on the reflector rotation angle. Thus, the work analyzed (1) a single rotating reflector, (2) a single rotating reflector and a single stationary reflector, (3) two rotating reflectors, and (4) two rotating reflectors and a single stationary reflector. In the case of two rotating reflectors, the author showed that it is possible to separate the incoming and outgoing beams, while still keeping a linear relationship between the delay and the rotation angle.

In the follow-up work [234]], a linear rotary delay line featuring two rotating reflectors was realized experimentally and employed in a THz-TDS setup designed for spectroscopy of dynamic processes. Particularly, four pairs of curvilinear reflectors were fabricated using computer numerical control (CNC) machining on the same rotary disk [Fig. 2.18(a)]. The acquisition of THz pulses was demonstrated with a speed of up to 48 Hz per blade (192 Hz with four blades), with a maximal optical delay of ∼80 ps [Fig. 2.18(b)]. The input and output beams were physically separated in space, thus avoiding the use of a beam splitter. To record THz traces with such high acquisition rates, the authors replaced the lock-in amplifier with a low-noise transimpedance amplifier. They showed that the bandwidth of the detected signal decreased as the rotation speed increased, and they related this to the acquisition electronics [Fig. 2.18(c)]. As for practical applications of such a system, the authors monitored the time dynamics of a spray painting process by observing the amplitude and temporal position evolution of the main THz peak during paint deposition and drying [Figs. 2.18(d) and (e)]. They also demonstrated detection of thickness of free-falling polyethylene samples (moving speeds of up to 1 m/s) by monitoring in real time the optical delay of the THz pulse [Figs. 2.18(f) and (g)] with and without a sample. The results were shown to be on par with manual micrometer measurements of the sample thickness.

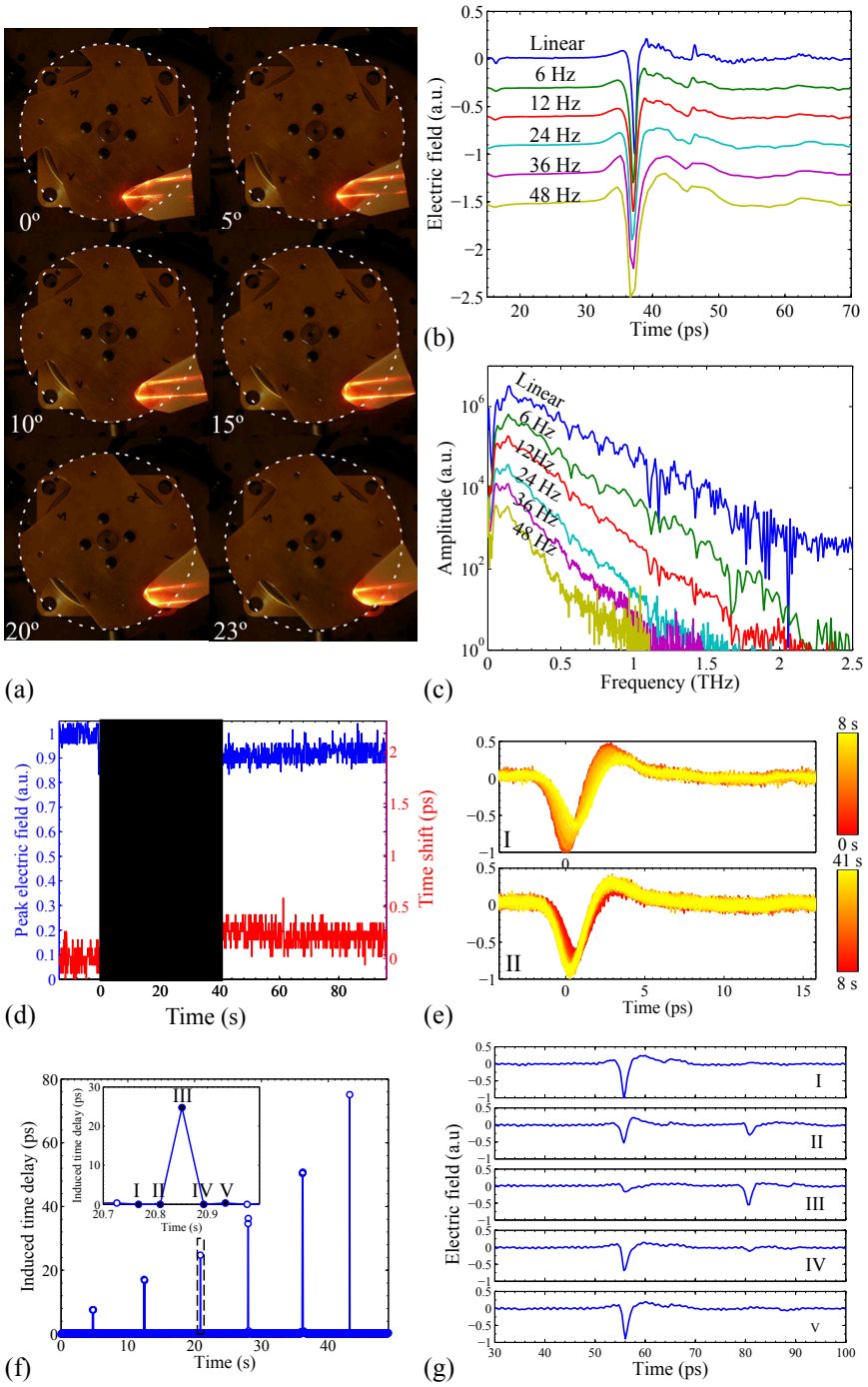

Figure 2.18 (a) Experimental realization of a linear rotary delay line featuring four pairs of the curvilinear reflectors. (b) Time-domain THz pulses and (c) corresponding spectra for different angular rotation speeds. (d) Real-time monitoring of the spray-painting process. Amplitude (blue top) and temporal position (red bottom) of the THz peak that passes through a sprayed-on layer of paint. (e) Time-domain THz pulses during spraying action (region I) and during paint layer drying (region II). (f) Thickness evaluation of free-falling polyethylene samples. Induced time delay due to passing of polyethylene samples of different thicknesses. Inset: passing of a 14.72 mm sample and (g) corresponding time traces. © 2015 IEEE. Reprinted, with permission, from Guerboukha *et al.*, IEEE Trans. Terahertz Sci. Technol. **5**, 564–572 (2015) [234].

However, the curvilinear reflectors developed in Refs. [36, 230–233] were essentially designed with ray optics, assuming infinitely thin laser beams. Therefore, distortion of the wavefront was important and, consequently, the parallel incident beam was distorted after reflection. This results in a less efficient generation or detection of THz radiation.

2.3.2.2 Rotary Prisms

Rotary delay lines can also feature rotating prisms. In such systems, the variable optical delay is generated by rotating a prism in the path of the optical pump or the THz beams. In Ref. [235], Ballif *et al.* used a rapidly rotating BK7 glass cube ($n = 1.5$ at 850 nm) to realize such a delay line. They showed that the optical delay as a function of the angle had 20% deviation from a linear curve. In Ref. [236], they demonstrated a high repetition rate of 28.6 kHz with a maximal optical delay of 6.67 ps. However, this delay is too small to be useful for applications in THz-TDS. By increasing the size of the cube, the total optical delay can be increased. Thus, with a cube size of 50 mm, the same authors demonstrated a total optical delay of up to 215 ps [235]. However, with large cubes, when placed in the path of a pump beam, group velocity dispersion (GVD) becomes important, which leads to broadening of the femtosecond pulse, lower THz generation efficiency, and reduced THz pulse bandwidth.

The abovementioned rotary delay line was designed for an infrared pump of nanometer-size wavelength. Therefore, complex alignment and precise manufacturing was required, with prism surface roughness smaller than $\lambda/10$. To circumvent these complexities, in Ref. [237], Probst *et al.* used an 80 mm cube of high-density polyethylene ($n = 1.53$) in the path of a THz beam to generate the optical delay [Fig. 2.19(a)]. This cost-effective method was relatively simple to implement. However, it provided a highly nonlinear dependence of the time delay on the rotation angle [Figs. 2.19(b) and (c)], thus requiring an additional calibration step. A complete rotation of the cube generated eight THz pulses with maximal optical delay of 40 ps each. The authors demonstrated acquisition rates of up to 800 Hz, the main limitations being the acquisition electronics, the induced air turbulence at high rotation speeds, relatively small time delay, and THz signal attenuation due to absorption in the prism material [Figs. 2.19(d) and (e)]. Furthermore, the authors used their delay line to image a floppy disk (100 mm $\times$ 100 mm) in less than 3 min, limited by the raster scanning of the sample and the acquisition electronics [Figs. 2.19(f) and (g)].

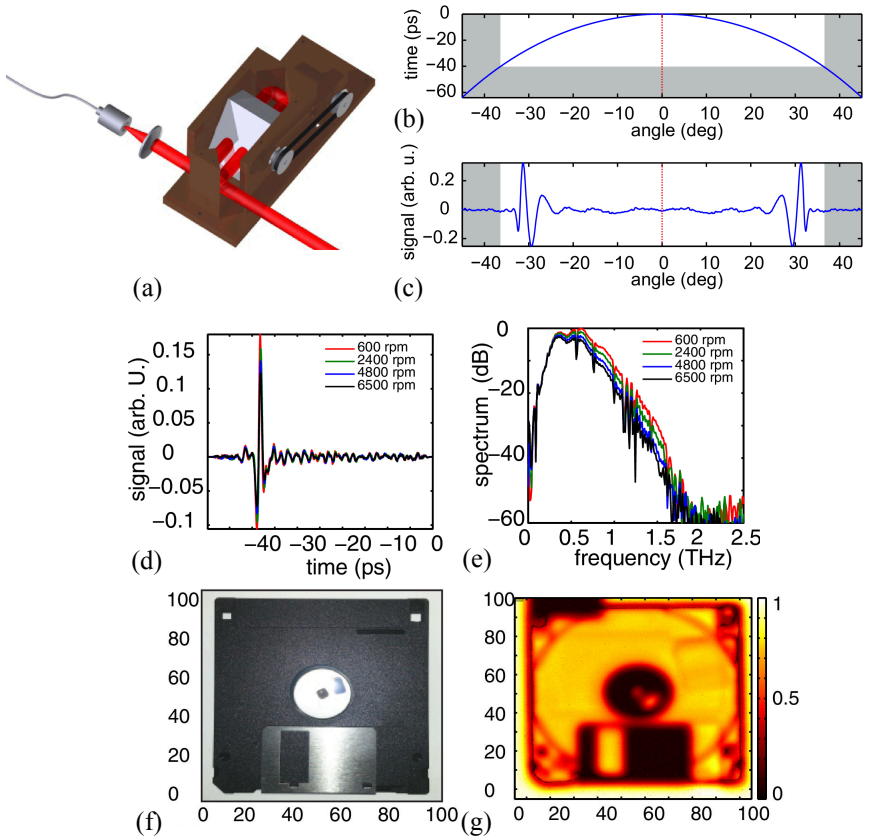

Figure 2.19 (a) Rotary optical delay line featuring a rotating HDPE cubic prism. (b) Nonlinear time delay as a function of the angle of rotation. (c) Raw THz traces for different rotation speeds of a prism. (d) Calibrated time traces and (e) corresponding spectra for different rotation speeds. (f) Photograph and (g) THz transmission image of a 3.5 inch floppy disk. Reprinted with permission from [237]. Copyright 2014 Optical Society of America

2.3.2.3 Non-Mechanical Time-Domain Sampling

To avoid mechanical sampling of the time delay, methods based on modifying the laser repetition rate of the femtosecond laser can be used. Asynchronous optical sampling (ASOPS) was introduced in the pump–probe scheme to detect molecular species concentrations in flames [238, 239]. It was first implemented in the THzTDS configuration in Refs. [240, 241]. In this technique, scanning of the time delay is obtained by using two femtosecond lasers (one laser is placed in the emission line, another in the detection line) featuring two slightly different pulse repetition rates f_1, f_2. Consequently, the relative time delay between the two pulse trains will mimic a linear ramp from 0 to $\Delta t = 1/f_1$ (assuming $f_2 > f_1$), while the scan rate will be determined by the beat frequency between the two lasers $\Delta f = f_2 - f_1$ [Fig. 2.20(a)].

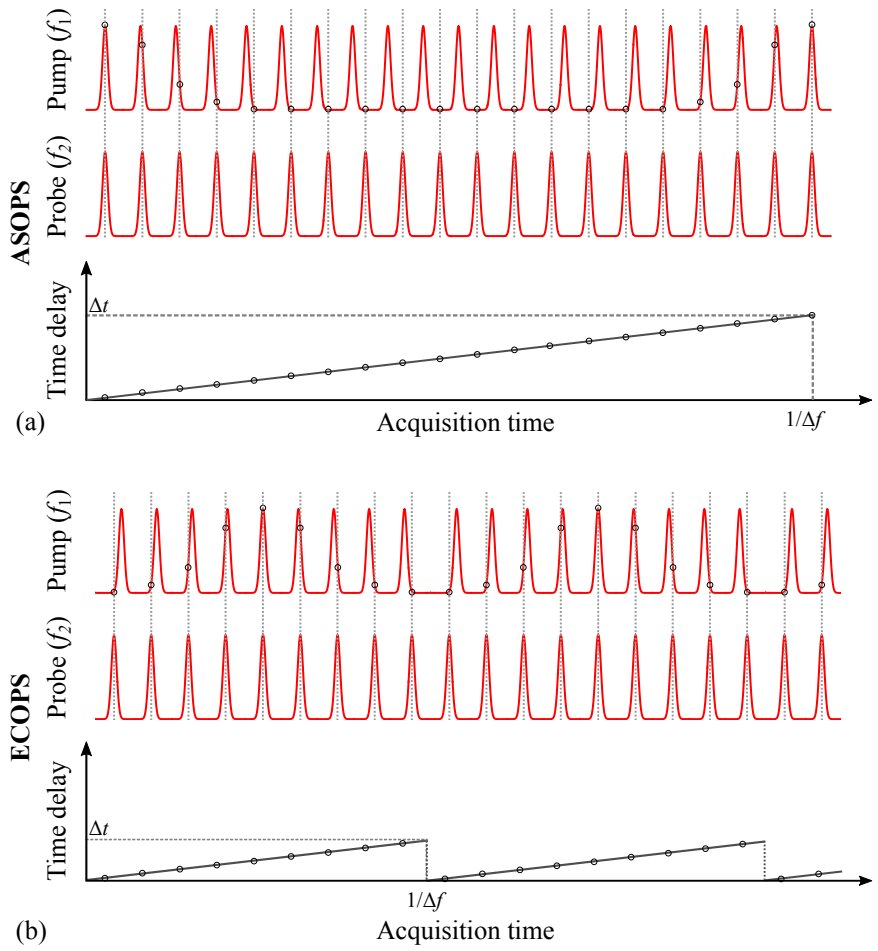

Figure 2.20 Schematic description of the (a) ASOPS and (b) ECOPS technique. In ASOPS, the pump and probe pulses have slightly different repetition rates, leading to a continuous scan of the time delay between consecutive pulses. In ECOPS, the repetition rate of the pump is modulated to avoid wasting the temporal window between consecutive pulses.

In Ref. [242], Bartels *et al.* used two mode-locked Ti:sapphire femtosecond lasers with repetition rates close to 1 GHz and an offset frequency of $\Delta f = 10$ kHz.As a result, a temporal 1000 ps scan was performed with a scan rate of 10 kHz (acquisition time per single THz pulse trace of 100 μs). By reducing the temporal window, one can furthermore increase the scan rate. For example, in Ref. [243], 100 ps total delay has been demonstrated at a repetition rate of 100 kHz. However, to obtain such performance, unconventional lasers with 10 GHz repetition rate were used.

As ASOPS constantly scans the entire time interval between two consecutive pulses, this might be wasteful if the size of the scanned temporal window (say ∼1000 ps) exceeds greatly the time duration of a typical broadened THz pulse (10–100 ps). To reduce the size of

the scanned temporal window, electronically controlled optical sampling (ECOPS) has been developed as an alternative to ASOPS [244–246]. In ECOPS, the repetition rate of one of the lasers is precisely controlled by electronically modulating the cavity length of one of the lasers. Consequently, the scan range can be correctly adjusted to the time of the THz pulse [Fig. 2.20(b)]. As a result, in Ref. [245], a 77 ps time delay window is scanned at a scan rate of 1 kHz, an improvement of 50 times compared to the conventional ASOPS, using the same parameters. In Ref. [247], for versatility, both the ASOPS and ECOPS techniques were implemented in the same fiber-based laser system.

ASOPS and ECOPS techniques have many benefits. The absence of moving parts allows for faster scanning rates, eliminates the positional instabilities of the laser beam, and removes the electronic noise caused by motor movement. However, its main disadvantage is the need to use two ultrafast lasers, which essentially doubles the cost of the THz-TDS system.

The optical sampling by laser cavity tuning (OSCAT) technique simplifies the system by using a single femtosecond laser [52,248,249]. Instead of having balanced optical paths in the emitter and detector sides, OSCAT uses the pulse i and the successive pulse $(i+a)$ in the same pulse train. Consider a laser emitting a train of optical pulses with a repetition rate of f that can be tuned by Δf [Fig. 2.21]. The pulse i and the pulse $(i+a)$ have unbalanced optical paths, where the pulse $(i+a)$ has travelled the additional optical path length:

$$l_a = \frac{ac}{nf} \tag{2.29}$$

with c the speed of light and n the refractive index of the propagation medium for the pulse $(i+a)$, for example, an optical fiber. With such unbalanced optical paths, the optical delay between the pulse i and the pulse $(i+a)$ is a function of the laser repetition rate f and its

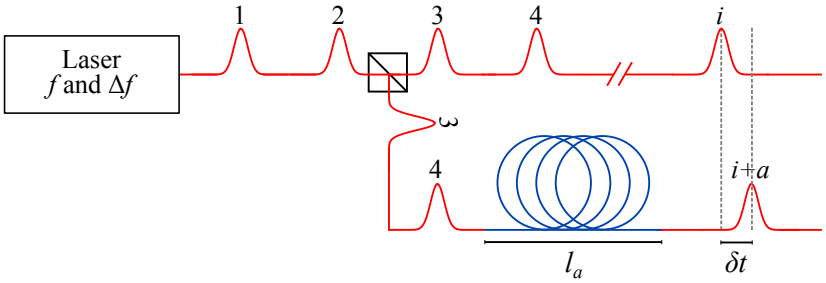

Figure 2.21 Schematic description of the OSCAT technique.

tuning Δf through the following relation:

$$\delta = a\left(\frac{1}{f} - \frac{1}{f+\Delta f}\right) \tag{2.30}$$

Therefore, by dynamically changing the tuning Δf, the temporal window between two optical pulses can be scanned.

OSCAT was first introduced and demonstrated in cross-correlation measurements in Refs. [248, 249]. In Ref. [250], the OSCAT technique was implemented for THz-TDS, with a 1550 nm fiber-coupled laser with a repetition rate of $f = 250$ MHz that could be tuned over $\Delta f = 2.5$ MHz using a precise intracavity stepper motor in the laser cavity. Therefore, to use the maximal delay between two adjacent pulses ($\Delta f = 1/f = 4$ ns), $a = 101st$ consecutive pulse must be used. This results in an additional optical path of $l_a = 121$ m in free space for the pulse $(i + a)$. Since this distance is impractical for compact THz-TDS systems, a combination of a standard single-mode fiber and a telecom dispersion fiber of a total length of 80 m was used. The same system was also operated in a rapid scan regime using a 3.5 kHz piezoactuator in the laser cavity to demonstrate over 5 ps optical delay at a scan rate of 100 Hz. Today, using the OSCAT technology, commercial systems achieve up to 40 ps total delay at scanning rates of 200 Hz.

2.3.3 Photoconductive Antenna Arrays

Integration of several PCAs into imaging arrays is an interesting proposition for real-time THz-TDS imaging. In this section, we overview some attempts to fabricate arrays of PCAs. In Ref. [214], Pradarutti *et al.* fabricated an array of 15 antennas with an inter-antenna distance of 1 mm packaged into a single photoconductive chip. Each antenna featured a gap of 30 μm by 5 μm. By using a telescope system and cylindrical lenses, they focused a 350 mW optical beam into an array of 15 PCA detectors [Fig. 2.22(a)]. A multichannel lock-in amplifier was used to improve the SNR [251]. The measured THz traces [Fig. 2.22(b)] demonstrate a lateral variation of the amplitude that was related to the incident THz nonuniform profile. Then, they imaged a metallic Siemens star of 60 mm $\times$ 50 mm [Fig. 2.22(c)] by moving the PCA array. The image was acquired in $\sim 10\%$ of the time required to measure it with a single-pixel PCA. However, the area covered by the optical beam on the multiarray PCA (10,000 μm $\times$ 10,000 μm) was significantly larger than the effective gap area of the PCA (75 μm $\times$ 75 μm). Consequently, only about 2.6 mW illuminated each gap, while the remaining increased the overall noise level. In Ref. [252], a microlens array was used to focus the optical beam into the gaps. In Ref. [253], the authors proposed and experimentally ex-

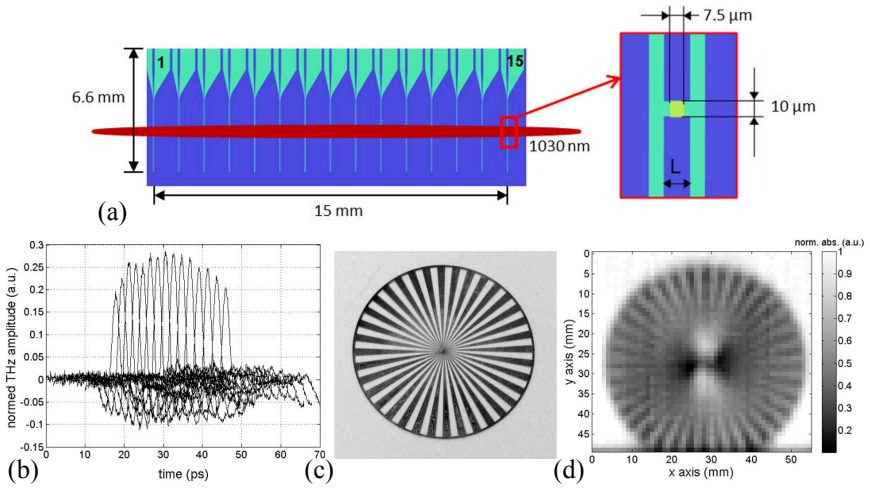

Figure 2.22 (a) Schematic and geometry of the linear array of PCA with 15 detectors used in Ref. [214]. (b) Simultaneously recorded THz pulses. (c) Photograph and (d) imaging of a metallic Siemens star. Reprinted with permission from [214]. Copyright 2014 Optical Society of America.

plored a concept of dynamically reconfigurable THz-PCA arrays. Such arrays feature several wide-gap THz antennas placed in parallel to each other that were dynamically interrogated by steering a multifocused optical pump beam along the antenna gaps. The pump beam was formed and steered using a spatial light modulator.

Designing and using PCA arrays, although very attractive, presents many challenges. Considering that the efficiency of a single PCA is relatively low, simultaneous interrogation of multiple PCAs requires powerful probe beams. For example, a 10 × 10 array using 10 mW per channel would require a 1 W femtosecond laser. Additionally, the focusing optics are complicated to manufacture, and dense integration on multiple antennas on the same chip is problematic due to crosstalk or interference between them. These practical difficulties currently confine almost exclusively the use of PCAs as coherent single-pixel detectors for imaging (see Section 2.3.5).

2.3.4 EOS with Visible/Infrared Cameras

2.3.4.1 Dynamic Subtraction and Balanced Electro-Optic Detection in a Camera

Within the EOS modality, since it is an optical beam in the visible/infrared region that is detected, conventional charge-coupled device (CCD) or complementary metaloxide semiconductor (CMOS) visible/infrared cameras can be used to obtain a 2D THz image. However,

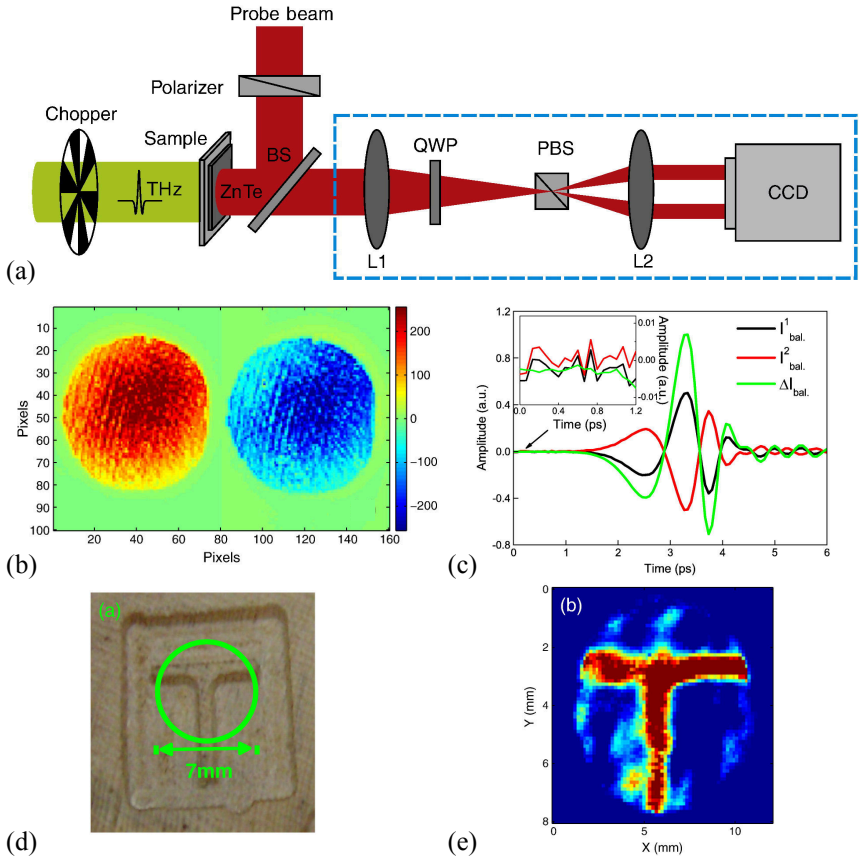

Figure 2.23 (a) Experimental setup for EOS with a CCD camera. (b) Both polarizations measured spatially by the CCD and (c) as a function of time with the delay line. (d) Photograph of the letter T engraved in wood and (e) reconstructed THz image by subtracting corresponding pixels in the CCD. Reprinted from Opt. Commun. **283**, Wang *et al.*, "Terahertz real-time imaging with balanced electro-optic detection," 4626–4632 [257]. Copyright 2010, with permission from Elsevier.

unlike single-pixel detection schemes, the use of unfocused beams decreases the local amplitude of the detected signal, approaching it to the noise level. Furthermore, the SNR of an EOS-based THz imager suffers from the limited ability of directly using lock-in detection with the CCD and CMOS devices. In the following, we highlight some techniques developed in the literature to increase the SNR when using CCD/CMOS cameras with EOS.

Already in 1996, Wu *et al.* demonstrated EOS imaging with a ZnTe crystal and a thermoelectrically cooled CCD camera [73]. However, unlike in the case of single-pixel EOS, the THz beam is spread over a larger surface and no lock-in amplifier can be directly used with the CCD. This resulted in a poor SNR that required the use of a thermoelectrically cooled camera. The dynamic subtraction technique was introduced in Refs. [254–256] to improve the sensitivity. The technique essentially consists of subtracting a reference frame (without

THz) from a signal frame (with THz) to dynamically remove the background noise.

To increase the sensitivity even further, in Ref. [258], Pradarutti *et al.* demonstrated balanced electro-optic detection using a linear array consisting of eight pairs of InGaAs photodiodes in conjunction with a Wollaston prism. Although their approach combined lock-in amplification to enable high SNR, raster scanning was still necessary to scan along the second dimension. In Ref. [257], both dynamic subtraction and balanced electro-optic signals were used to increase the SNR. A Wollaston prism divided the optical probe beam into two mutually orthogonal polarizations that were detected simultaneously by a CCD [Fig. 2.23(a)]. As expected [259], the two measured polarizations had opposite values such that their difference increased the signal by a factor of 2 [Figs. 2.23(b) and (c)]. An algorithm was designed to perform the subtraction of the two images and reduce the misalignment errors. Furthermore, dynamic subtraction was performed by subtracting one frame (with THz signal) from a reference frame (without THz). An example of a THz image is given in Figs. 2.23(d) and (e). In Ref. [260], the authors added a half-wave plate in the probe beam to perform real-time THz polarization imaging.

2.3.4.2 Real-Time Near-Field EOS Imaging

Real-time near-field imaging using EOS is possible by placing the sample in direct contact with the nonlinear EOS crystal. In Ref. [261], Blanchard *et al.* imaged an area of 370 μm $\times$ 420 μm at 35 frames per second with a spatial resolution of 14 μm ($\lambda/30$ at the center frequency of 0.7 THz). To achieve such performance, the authors generated a THz pulse with a peak electric field of 200 kV/cm by optical rectification in $LiNbO_3$ using a tilted-pulse-front excitation. For detection, the THz pulse was focused on a LiNbO3 crystal with a thickness of 20 μm [Fig. 2.24(a)]. On the opposite side, the 800 nm probe light interacted with the crystal and was reflected into a balanced imaging setup using a CCD camera. As in Ref. [257], corresponding pixels of the orthogonal polarizations were subtracted to increase the SNR. To obtain high spatial resolution, a very thin electro-optic crystal has to be used. At the same time, a powerful THz source was necessary to compensate for the small interaction length between the THz and the optical probe. To demonstrate the ability of their THz microscope in imaging near-field structures, a metallic dipole antenna of subwavelength dimensions was directly deposited on top of the $LiNbO_3$ crystal [Fig. 2.24(b)]. By displacing the delay line, the reemitted THz radiation from the dipole could then be imaged at the picosecond scale [Fig. 2.24(c)].

In Ref. [263], to demonstrate biomolecule probing, free induction decay of a tyrosine crystal was observed in the near field, while in Ref. [264], resonant modes of a split ring resonator

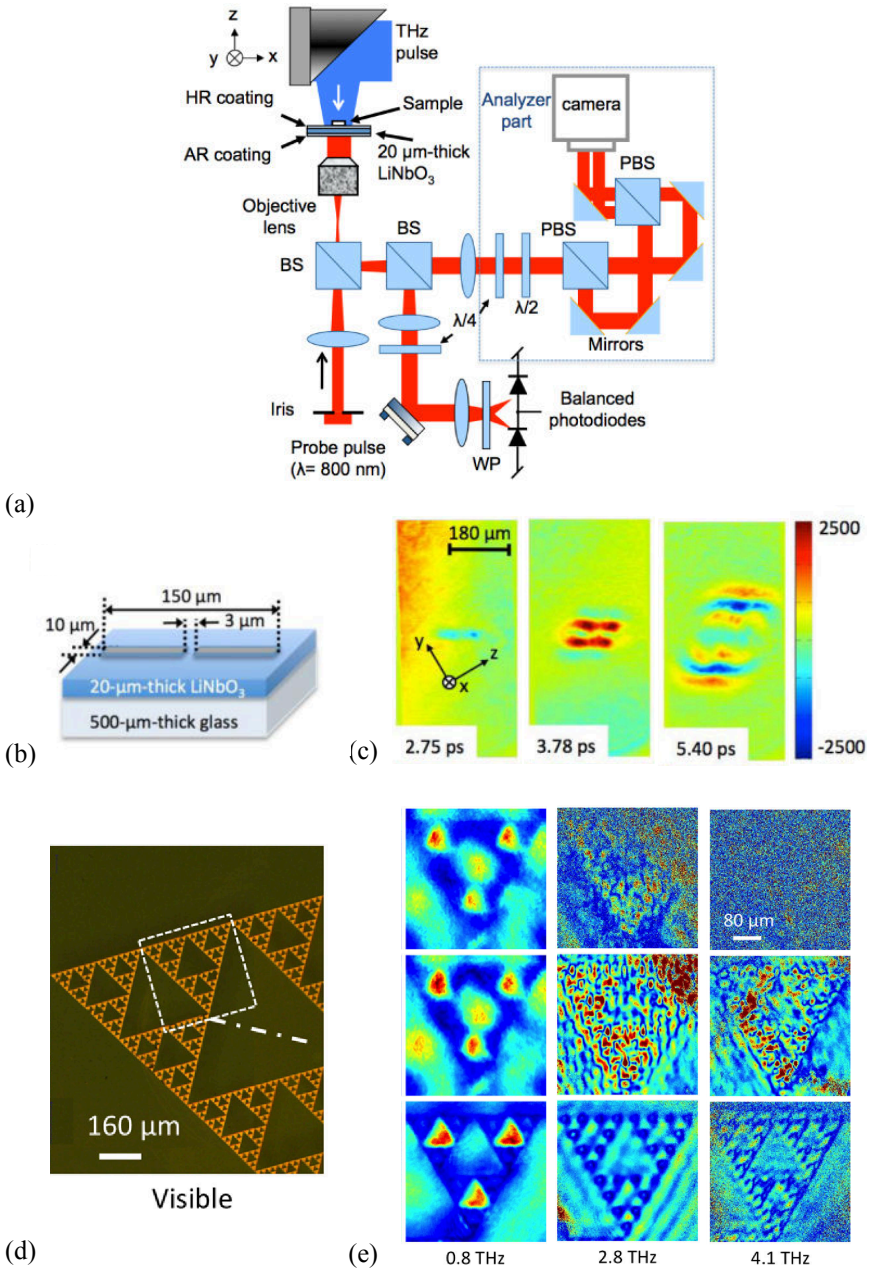

Figure 2.24 (a) Experimental setup of the EOS THz microscope with a CCD camera. (b), (c) Near-field imaging of a metallic antenna in the process of re-irradiating the incident THz pulse. Reprinted with permission [261]. Copyright 2011 Optical Society of America. (d) Demonstration of improved spatial resolution by imaging a Sierpinski fractal (e) without spectral filtering and a 10 μm crystal (top), with spectral filtering and a 10 μm crystal (middle), and with spectral filtering and a 1 μm crystal (bottom). Reprinted with permission from [262]. Copyright 2016 Optical Society of America.

were imaged. Since then, many methods have been considered to further increase the spatial resolution [173, 262, 265]. In Ref. [262], spatial resolution up to $\lambda/600$ at 100 GHz has been demonstrated. To achieve such performance, the $LiNbO_3$ crystal thickness has been reduced to 1 μm, the optical probe was spectrally filtered, and a 10× objective lens was used. A 100 nm thick gold Sierpinski fractal was patterned on top of 10 μm and 1 μm crystals [Fig. 2.24(d)] and imaged in Fig. 2.24(e).By reducing the crystal thickness and by using spectral filtering, the spatial resolution was increased. To enable real-time near-field EOS imaging, a detailed description of the needed components is reviewed in Ref. [173].

2.3.4.3 Temporal Encoding in the Camera

To record the complete THz temporal waveform, an optical delay line is still necessary. In principle, one could use the methods described in Section 2.3.2. However, for EOS sampling, one of the spatial dimensions of the camera can be used to encode the temporal dimension of the waveform. This idea was first demonstrated in Refs. [266–268] by using a chirped optical probe beam. Since distinct wavelengths travel with different speeds inside the EOS crystal, their polarizations are differently affected by the THz radiation through the Pockels effect. This essentially encodes temporal information about the THz waveform into the spectrum of the optical probe. Therefore, by using a grating to disperse the optical spectrum into a linear detector array, the THz temporal waveform can be sampled without the use of an optical delay line.

In Ref. [269], Shan *et al.* demonstrated single shot measurement of the temporal waveform by introducing an angle between the optical probe beam and the THz pulse. Thus, different points in the transverse spatial profile of the optical probe beam experienced different temporal positions of the THz electric field. Again, a linear array of detectors was used to resolve the THz waveform in a single shot. In Ref. [270], Yasuda *et al.* used a similar non-collinear geometry with a CCD camera [Fig. 2.25(a)]. One dimension was used to encode the temporal THz waveform, while the second was used to image one spatial dimension [Fig. 2.25(b)]. In [166], 3D imaging using THz-CT (Section 2.2.4) was demonstrated by imaging a pharmaceutical tablet in only 6 min [Fig. 2.25(c)]. To obtain a 2D image, the sample can be moved in the second dimension [271]. This approach is attractive for many industrial applications where a conveyer belt is used. This was demonstrated for biomedical applications in Ref. [272]. There, pharmaceutical tablets moving on a conveyer belt were imaged. Furthermore, spectroscopic identification of the crystallinity of dental tissue was demonstrated, along with observation of the drying process of wet hair.

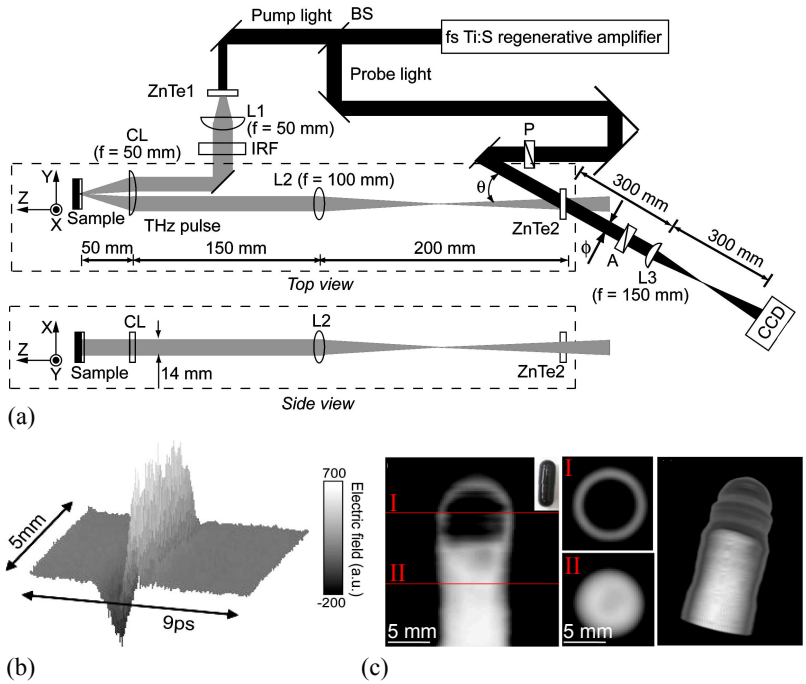

Figure 2.25 (a) EOS imaging setup using a non-collinear geometry and a CCD camera. (b) One dimension of a CCD camera records the temporal waveform, while the second one measures spatial information along one dimension. Reprinted from Opt. Commun. **267**, Yasuda *et al.*, "Real-time two-dimensional terahertz tomography of moving objects," 128–136 [270]. Copyright 2006, with permission from Elsevier. (c) 3D imaging of a pharmaceutical tablet acquired in 6 min using a THz-CT. Reprinted with permission from [166]. Copyright 2013 Optical Society of America.

2.3.5 Section Summary and Future Directions

Even though THz cameras are in rapid development (see Section 2.4), the development of THz-TDS-based imaging systems is still of great importance, since they can provide additional/complementary spectroscopic information to reconstruct an image (Section 2.2.1). Furthermore, they feature outstanding SNR due to the lock-in technique. The ability of THz-TDS to measure both the amplitude and the phase of the THz pulse electric field allows for unique imaging modalities that simply cannot be achieved with conventional intensity-based THz cameras. For example, THz-TDS imaging can be used to map the complex refractive index and the conductivity of a sample, even at a subwavelength scale (near-field imaging).

As we saw in this section, the technical challenges to enable real-time THz-TDS imaging are intrinsically related to the THz-TDS setup. First, the mechanical linear optical delay line must be replaced to enable the acquisition of multiple THz pulses per second. Rotary optical delay lines in the form of curved mirrors in the optical path or prisms in the THz

path are simple and cost-effective solutions. Ultimately, their speed is still limited by the motor or turbine rotation speeds and air turbulence, as well as by the need for costly high-speed electronics for signal processing. At the same time, non-mechanical solutions such as ASOPS, ECOPS, and OSCAT are attractive since they can provide acquisition rates in the kilohertz range. Some of them are already commercially available, but ASOPS and ECOPS require the use of two synchronized femtosecond lasers, which essentially doubles the cost of the THz-TDS systems. In comparison, the OSCAT technique needs only one laser, at the expense of using dispersive fibers to generate the optical path differential.

The second problem that impedes real-time imaging is the fact that classical THz-TDS systems are built with single-pixel detectors. There are two major technologies to detect THz pulses: photoconductive antennas and EOS. For now, it seems that photoconductive antennas, while having a very high SNR, do not constitute the preferred approach for real-time THz imaging due to the necessity of slow raster scanning. So far, dense integration of multiple antennas on a single chip has proven to be problematic due to the electromagnetic crosstalk between them and the necessity of using multichannel lock-in systems (one lock-in per pixel). Additionally, interrogating multiple antennas at the same time also requires a powerful probe laser and intricate micro-optics for laser focusing. While several works demonstrated the fabrication of arrays of photoconductive antennas, we believe that the main application of photoconductive antennas will remain in the context of single-pixel imaging (Section 2.5) using beam-steering optics (Section 2.5.1), compressive sensing (Section 2.5.2), spectral encoding methods (Section 5.3), or other computational imaging techniques.

In comparison, EOS has recently attracted much attention in the context of 2D realtime THz-TDS imaging. The fact that the technique records visible/infrared light means that conventional visible/infrared CMOS/CCD cameras can be used. EOS-based imaging still lacks in SNR compared to a photoconductive antenna detector with a lock-in amplifier, so further noise management within this technique is required. Moreover, there is a real interest in near-field EOS imaging since the crystals used to generate the EOS signal can also be used as sample substrates (contact-based near-field imaging). This interest is certainly driven by the recent development of efficient generation techniques with optical rectification and tilted-pulse excitation that allow reduction of crystal thickness, and, therefore, increase spatial resolution. In this context, EOS THz-TDS microscopes are within reach.

Finally, we would like to discuss two research directions that have emerged recently that may have important impact on THz-TDS systems in general, and THz-TDS imaging in particular. These are (1) THz quasi-time-domain spectroscopy systems (THz-QTDSs) and (2) CMOS-based electronic generation and detection of THz pulses. The THz-QTDS aims

at replacing an expensive ultrafast laser by less expensive multimode laser diodes [273–275]. In short, a multimode laser beam comprising equally spaced spectral lines is focused onto a photoconductive antenna. In time domain, the result is a THz pulse train with a repetition rate that is determined by the mode spectral spacing [276]. In Ref. [277], imaging with a THz-QTDS system was demonstrated by using a 100 mW multimode laser diode at 662 nm, with mode spacing of 25 GHz and spectral emission bandwidths of 3 nm. In Ref. [278], a compact and cost-effective THz-QTDS system was proposed by mounting the laser diode directly onto a mechanical delay line extracted from a DVD drive. This prototype was fully controlled by a Raspberry Pi single-board computer with a sound card that fed the emitter antenna with a reference voltage, detected the current for digital software lock-in amplification, and controlled the stepper motor. In Ref. [279], a fiber-coupled THz-QTDS system was demonstrated using conventional telecom technology at 1550 nm. All these prototypes may pave the way for extremely affordable THz spectroscopy systems. However, the challenges for imaging applications using THz-QTDS are similar to those based on THz photoconductive antenna technology, namely, those related to the single-pixel nature of the detection device.

A second emerging idea for THz spectroscopy is the electronic generation and detection of THz pulses. Here, the main advantage is to completely avoid the use of lasers for THz pulse generation. These recent developments are based on CMOS processing technology, which may be beneficial toward mass fabrication of THz spectroscopy systems at lower costs. Two avenues are being considered for electronic generation of THz pulses. The first idea uses a technique similar to mode-locking in femtosecond lasers to dynamically shape pulses [280]. Using oscillatory CW sources on silicon, picosecond pulses are emitted by carefully controlling the amplitude and phase of the fundamental frequency and the multiple harmonics. The second idea is inspired by the spark gap transmitter, where an electromagnetic pulse is emitted by an antenna following a fast-rising/falling current switching [281]. Initially, an antenna stores a DC current in the form of magnetic energy, and, when the current is turned OFF, the antenna converts the energy into a radiated picosecond pulse. Similarly, an impulse is emitted following an ON switch. For now, the detection of these picosecond pulses has been demonstrated using a conventional THz-TDS system or using horn antenna detectors. Interestingly, in Ref. [282], an on-chip THz spectral detector is realized by measuring the scattered current density on a multiport antenna. The general concept is that different scattering modes are excited on the antenna depending on the excitation frequency. Therefore, the spectrum can be reconstituted by measuring the spatial current density and by using a one-time calibration procedure. For now, these ideas of emission and detection of THz pulses using electronic means are limited to the sub-THz region.

2.4 THz Cameras

Over the past decade, intensive research has been conducted to develop THz cameras similar to those available in the visible region of the spectrum. THz cameras must satisfy a number of requirements before deployment in industrial applications. First, they must operate at room temperatures while still retaining high sensitivity, thus forgoing the complexity associated with cumbersome and expensive cryogenic cooling systems. Second, to reduce the cost, the fabrication process of the THz cameras should be compatible with modern fabrication techniques, such as the CMOS process technology, which also allows scaling into high-resolution imaging arrays. Third, the size and weight of a THz camera along with its total power consumption should be small enough to facilitate the integration into industrial imaging systems. Finally, a THz camera should be sensitive enough to allow recording of THz videos at a high frame rate. This is especially important since powerful THz sources (particularly broadband sources) are still sparse. Ideally, the detector should be sensitive enough to record a THz image in passive imaging, i.e., without an active THz source. Ideally, THz cameras should be able to detect complex electric fields, while, for now, most THz cameras can detect only intensity. This, and the fact that cheap, high-power THz sources are still lacking, drive the competition between imaging using single point detection versus imaging using multipixel arrays.

In general, the performance of THz detectors can be characterized with two important figures of merit: the responsivity and the noise-equivalent power (NEP). The responsivity is the direct detector response (either in volts or amperes) to the incident THz power (in watts). It can be expressed in V/W or A/W, with the majority of THz imaging arrays employing voltage to characterize the THz signal. To measure the responsivity, one typically measures the total incident power using an etalon technique. In the case of THz cameras, assuming that the imaging array captures all the incident THz power, the responsivity per pixel can be assessed by summing the voltages of all the pixels and then dividing it by the total incident power. In general, higher responsivity is an indication of a better performing detector.

The NEP is a measure of the minimum detectable power. It is defined as the input power that results in a signal equal to the noise (SNR = 1) with a 1 Hz bandwidth output. It is measured in $\mathrm{W}/\sqrt{\mathrm{Hz}}$, and a lower NEP indicates a more sensitive detector. However, due to specific data acquisition conditions when using a camera, the minimum detectable power (in W) is often a better quantity to characterize the video mode operation. It corresponds to the lowest power that can be measured by a single pixel in a single frame. Clearly, this parameter depends on the frame rate, and a reduced frame rate can generally detect lower THz powers.

In this section, we review the two main classes of THz cameras that have been reported in the modern literature: THz thermal cameras and THz FET cameras.

2.4.1 THz Thermal Cameras

THz thermal cameras detect the heat generated by incident THz radiation. Depending on the detection principle of the heat, one usually distinguishes three types of thermal detectors of THz radiation: 1) Golay cells, 2) pyroelectric sensors, and 3) bolometers. In an imaging setup, they are commonly used with a modulated source, which is produced using an optical chopper, for example. While this allows reducing the ambient noise, it reduces the overall maximum frame rate that can be obtained at room temperature. The main advantage of thermal detectors is that they have very broad spectral range of operation, something that is typically not obtainable with photon detectors.

In Golay cells, the generated heat is transferred to an expanding gas cell. The increased pressure is then optically measured by moving mirrors [64]. Since they rely on the mechanical movement of a membrane, Golay cells are slow detectors. Nevertheless, due to their simple operating principle, they are widely used to measure THz power. However, they are difficult to integrate into dense arrays of detectors. Consequently, THz imaging with Golay cells is often done in a single-pixel detection scheme [283]. Values for the NEP in Golay cells range between 0.1 and 10 nW/$\sqrt{\text{Hz}}$.

Pyroelectric sensors detect changes in the electrical polarizability of certain crystals caused by increase in the temperature. When an absorbing layer transfers the heat to the crystal, a temporary voltage is generated. Common pyroelectric crystals are triglycine sulfate (TGS), deuterated triglycine sulfate (DTGS), lithium tantalate ($LiTaO_3$), and barium titanate ($BaTiO_3$). Among these, TGS and DTGS have the highest sensitivities at THz frequencies [284], with typical responsivity and NEP of $\sim$1 kV/W and 1 nW/$\sqrt{\text{Hz}}$, respectively, at a modulation frequency of $\sim$10 Hz. Unlike Golay cells, pyroelectric detectors are commercially available as array cameras. For example, in Ref. [285], Yang *et al.* used a 124 $\times$ 124 pixel pyroelectric commercial camera to demonstrate THz imaging with a gas laser source at 1.89 THz (70 mW average power). Sensitivity of the pyroelectric detectors can be improved by reducing the crystal thickness and by increasing THz absorption in the crystal coating layer. Typical minimum detectable power for commercial pyroelectric cameras is in the range of 50-100 nW.

Another type of THz camera uses thermal bolometers as individual pixels. Because of the relatively high sensitivity and established fabrication technology, bolometer imaging arrays are currently considered prime candidates for real-time THz imaging.

The bolometer pixel operates by measuring changes in a temperature-dependent resistance. In Fig. 2.26(a), we have summarized the main constituents of a bolometer as described by Richards [286]. The radiation power P_{THz} from the THz beam is incident onto an absorbing element (heat capacity C_A) connected via a thermal link (conductance G_L) to a heat sink (reservoir at temperature T_S). The temperature of the absorbing element T_A rises at a rate $dT_A/dt = P_{\mathrm{THz}}/C_A$ to the limiting value $T_A = T_S + P_{\mathrm{THz}}/G_L$, with the thermal time constant $\tau = C_A = G_L$. When the illumination is turned off, the temperature T_A relaxes back to T_S with the same time constant [Fig. 2.26(b)]. This temperature change is measured with a resistive thermometer (typically amorphous silicon or vanadium oxide) connected to the absorbing element.

Microbolometers are arrays of bolometers mounted onto readout integrated circuits (fabricated with CMOS process technology) for focal-plane camera operation. As the operation principle of microbolometers is not wavelength specific, commercial microbolometers designed for infrared radiation were first used for real-time THz imaging [288–291]. For example, in Ref. [289], Lee *et al.* used a commercial 320 × 240 pixel uncooled vanadium oxide (VO_x) microbolometer focal-plane array camera designed for 7.5–14 μm wavelengths. They used a quantum cascade laser at 4.3 THz (50 mW peak power) as a source to image the contents of a closed envelope. Since the camera was sensitive to both THz and infrared background radiation, three frames were necessary to obtain a THz image. The third frame (infrared signal only) was subtracted from the first frame (both infrared and THz signals), while the second frame was used as a buffer for the temperature to decay in the bolometer. This resulted in an overall frame rate of 20 frames per second (fps). In their following work, the authors also demonstrated stand-off real-time THz imaging at a distance of 25 m [292].

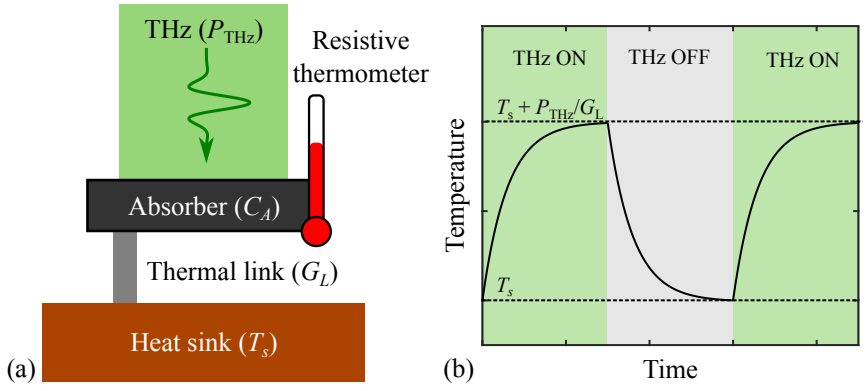

Figure 2.26 (a) Schematic representing the main components of the bolometer. (b) Rise and fall of the temperature in the absorber as a function of time.

In more recent years, microbolometers were specifically designed to operate in the THz range. When cooled at cryogenic temperatures to remove background thermal noise, they can achieve remarkable NEP in the range of 10^{-16} W/$\sqrt{\text{Hz}}$ [27]. However, with proper design modifications, even at room temperatures, microbolometers can demonstrate high enough sensitivities to be suitable for a variety of industrial imaging applications. In Refs. [58, 293], the authors at NEC corporation proposed to use a cavity structure to increase the sensitivity of a microbolometer THz camera of 320 × 240 pixels. Their device is schematically presented in Fig. 2.27(a) [287]. A thin metallic layer of TiAlV absorbed the THz radiation and induced changes in the resistance of the thermometer (VO_x film). Under the THz absorber layer, a thick metallic layer was placed, which reflects the unabsorbed THz radiation back into the bolometer. This geometry represents a resonating Fabry–Perot cavity between the bolometer and the reflector. A SiN_x layer was added to ensure the mechanical stability of the device and to match the effective cavity length with the THz wavelength. This addition led to an increase in the sensitivity in the sub-THz region, where the microbolometers are generally underperforming. They reported a minimum detectable power of 100 pW at 1 THz. Using optical rectification with tilted-pulse-front excitation in $LiNbO_3$, they demonstrated THz

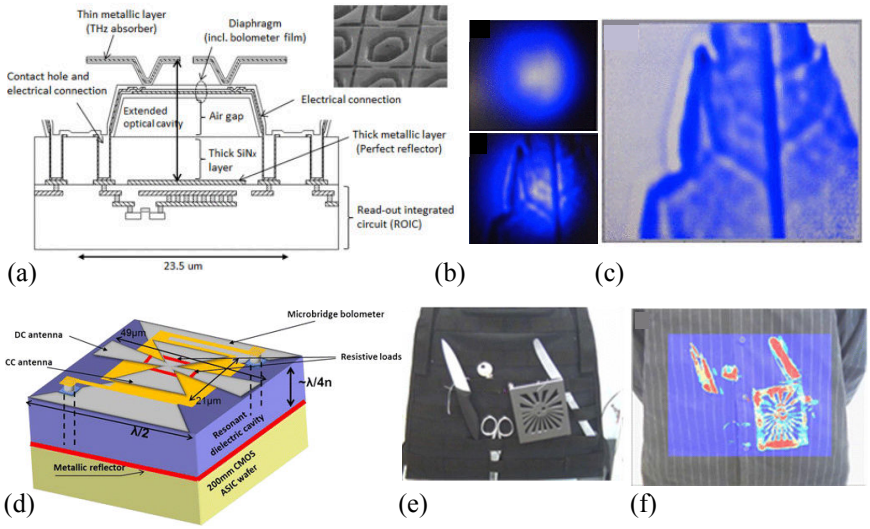

Figure 2.27 (a) Schematic representation of the cavity microbolometer developed in Ref. [287] (inset: micrograph). (b) Raw images without (top) and with (bottom) the dry leaf. (c) Corrected image for the non-uniform THz beam profile. © 2016 IEEE. Reprinted, with permission, from Nemoto *et al.*, IEEE Trans. Terahertz Sci. Technol. **6**, 175–182 (2016) [287]. (d) Schematic representation of the antennacoupled bolometer developed in Ref. [60]. (e) Photograph of objects under a shirt that were (f) imaged with THz. Reprinted with permission from Simoens *et al.*, J. Infrared Millim. Terahertz Waves **36**, 961–985 (2015) [60]. Copyright 2015 Springer.

imaging of a dry leaf [Fig. 2.27(b)]. In Ref. [294], they used the microbolometer in conjunction with a diffraction grating to develop a real-time spectrometer that could operate at 15 fps.

In Refs. [60,295,296], the authors, affiliated with CEA-LETI, used an antenna to increase coupling of THz radiation to the amorphous silicon-based transducer in a bolometer [Fig. 2.27(c)]. Crossed bow-tie antennas were placed on top of a microbridge bolometer membrane. Both THz radiation polarizations were coupled through the dissipative currents in the load resistances located in the center of a bolometer. The antenna-coupled bolometer membrane was suspended on an 11 μm thick SiO_2 layer deposited over a metallic reflector to create a resonant cavity. In principle, the dimensions of the antenna and the cavity length can be tailored to any THz frequency. They achieved a minimum detectable power of 30 pW at 2.5 THz [quantum cascade laser (QCL) source]. Hidden objects under a shirt were imaged, and the field of view was increased with fast scanning optics [Fig. 2.27(d)].

Metamaterials have been investigated to increase the absorption of THz radiation [297–300]. In Ref. [301], Carranza *et al.* fabricated a 64 $\times$ 64 focal-plane array with metamaterial absorbers using a 180 nm CMOS process. Their main motivation was to exploit as much of the CMOS process technology as possible, thereby avoiding costly postprocessing fabrication techniques. Thus, they integrated the readout electronics and the metamaterial absorber in the CMOS process. The metamaterial was designed to provide a broadband response centered around 2.5 THz. As for the sensor, they investigated two types of resistive thermometer. First, they patterned a VO_x sensor using postprocessing techniques, and they achieved a minimum NEP of 108 pW/$\sqrt{\text{Hz}}$ and a responsivity of 59 kV/W. Their second prototype used a silicon p-n diode as the sensor. Although the diode is less sensitive to temperature changes, it can be patterned directly with the CMOS process. They obtained NEP of 10.4 nW/$\sqrt{\text{Hz}}$ and a responsivity of 274 V/W.

2.4.2 THz Field-Effect Transistor-Based Cameras

Rectification in the field-effect transistor (FET) is the second technological trend in THz cameras. Previous reviews on the topic can be found in Refs. [68,302–304]. The general idea is to use plasma wave excitations to enable response at frequencies considerably higher than the maximal transistor operation frequency (cut-off frequency). In the 1990s, using a direct analogy between the electron transport equation in 2D gated material and the hydrodynamic equations in shallow water, Dyakonov and Shur theoretically demonstrated that plasma waves in the FET channel could be used for THz detection [305]. Fig. 2.28(a) schematically represents their proposed FET for THz detection. A DC voltage U_0 is applied between the gate and the source, while the incident THz radiation causes an alternating voltage U_a. Because of

the asymmetry of the boundary conditions and due to the nonlinear properties of the plasma waves, a constant drain-to-source voltage $\Delta U \propto U_a^2$ is generated.

They predicted resonant (frequency-specific) and non-resonant (broadband) detection mechanisms, depending on the electron momentum relaxation time τ that defines the conductivity in the channel $\sigma = ne^2\tau/m$ (n, e, and m are the electron density, charge, and mass, respectively). Given an incident THz radiation at frequency ω, the resonant case occurs when $\omega\tau > 1$, that is to say, when the channel conductivity is large. In this case, provided that the channel length L is sufficiently small, the plasma waves reach the drain side of the channel, are reflected back, and create a standing wave. A wavelength-specific DC voltage is then developed between the drain and the source [305]:

$$\Delta U^R = \frac{e\tau^2}{L^2 m}\left[\frac{U_a^2}{4(\omega - m\omega_0)^2\tau^2 + 1}\right] \tag{2.31}$$

where $m = 1, 3, 5, 7, ...$ Experimental evidence of THz detection in the resonant regime was demonstrated with a III–V high-electron mobility transistor in Ref. [306].

In the non-resonant regime (when $\omega\tau < 1$), the plasma waves are overdamped and cannot fully reach the other side of the transistor channel. In this case, a DC photoresponse between the drain and the source still exists in the form of an exponential decay [303]:

$$\Delta U^{NR}(x) = \frac{U_a^2}{4U_0}[1 - \exp(-2x/l_c)] \tag{2.32}$$

where x is the distance from the source and l_c is the characteristic decay length (typically a few tens of nanometers [307]). This type of broadband detection occurs in silicon FETs.

The seminal work by Dyakonov and Shur sparked a series of experimental demonstrations of THz detection in FETs, first with III–V semiconductors [310–314], then, more recently, with InAs nanowire [315], graphene [316], and black phosphorus [317]. However, in the short

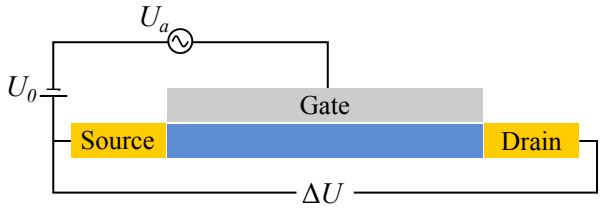

Figure 2.28 Schematic representation of the field-effect transistor used for THz detection. A DC voltage U_0 is applied between the gate and the source, while the incident THz radiation causes an alternating voltage U_a.

term, the work on silicon-based FETs will probably have more impact on development of THz cameras thanks to the compatibility of silicon material with the standard CMOS-foundry process, thus enabling large scale array fabrication at lower costs.

THz detection with silicon FETs was first experimentally demonstrated in Refs. [318, 319]. Their behavior was explained by using the non-resonant broadband detection mechanism of Dyakonov and Shur. In Ref. [67], it was shown that the NEP of silicon FETs (100 pW/$\sqrt{\text{Hz}}$) was comparable to conventional THz detectors operating at room temperature (such as thermal detectors). In Ref. [308], using circuit theory, the authors described the non-resonant FET detection mechanism with the distributed resistive self-mixing concept, where the channel was modeled as a nonlinear resistance–capacitance (RC) transmission line [320]. This theoretical framework helped them to design an efficient 3 × 5 pixel array of FET detectors using 250 nm CMOS process technology [Fig. 2.29(a)]. Each pixel consisted of a patch antenna designed for 0.65 THz coupled to a FET detector and a voltage amplifier, achieving a minimal NEP value of 300 pW/$\sqrt{\text{Hz}}$. Using lock-in amplification, they imaged the inside of an envelope [Fig. 2.29(b)]. In Ref. [309], the same group demonstrated improvement in the image contrast by using a heterodyne detection scheme in transmission mode [Fig. 2.29(c)]. A reference THz source (local oscillator) was combined to the transmitted THz beam to image details of the inside of a tablet [Fig. 2.29(d)]. In Ref. [321], a similar heterodyne scheme was used in both transmission and reflection modalities with an antenna-coupled FET fabricated on 150 nm CMOS process technology [322].

In Ref. [307], Schuster *et al.* studied the performance of several THz FET detectors fabricated using 130 nm Si CMOS, with embedded bow-tie antennas of different geometries and configurations. They obtained record NEP (<10 pW/$\sqrt{\text{Hz}}$) and responsivity (>5 kV/W, without amplification) at 0.3 THz by reducing the size of a silicon substrate (to reduce absorption losses), by using a shorter channel length and by connecting the antenna to the gate and source (to avoid parasitic THz collection on the drain side). They also demonstrated imaging up to a frequency of 1.05 THz. In Ref. [323], multispectral THz imaging was demonstrated with silicon FETs fabricated using a commercial 90 nm CMOS process. A record high frequency of 4.25 THz with a NEP of 110 pW/$\sqrt{\text{Hz}}$ was measured.

In the works reviewed above, the THz images were still obtained by mechanically scanning the sample, limiting the image acquisition time. However, the main advantage of using silicon FET is its compatibility with mainstream CMOS processing, which also enables on-chip integration with read-out electronics for mass fabrication of imaging arrays. Thus, in Refs. [69, 324], Al Hadi and co-workers fabricated an array of 32 × 32 pixels using 65 nm CMOS process technology [Fig. 2.30(a)]. In addition to the ring antenna and the FET

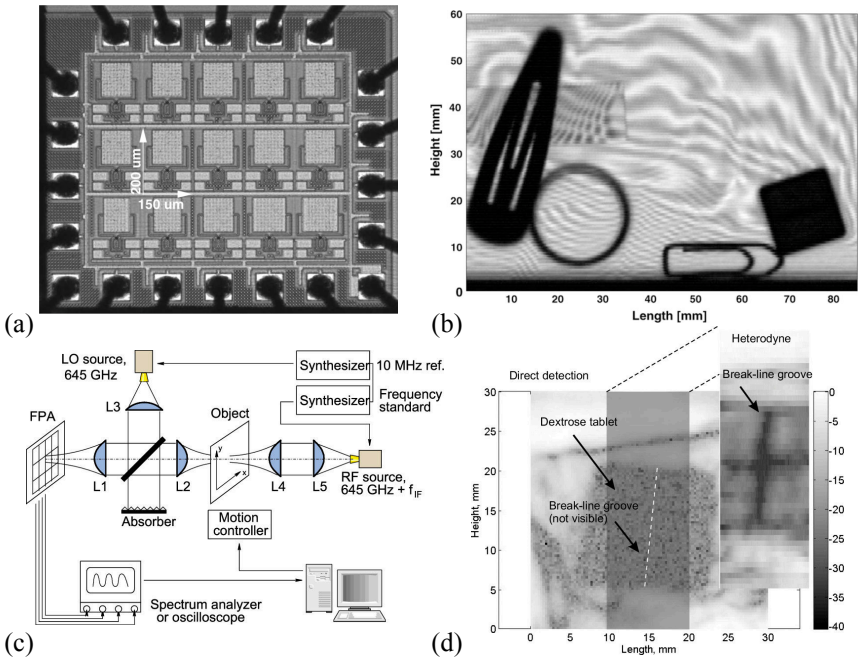

Figure 2.29 (a) Micrograph of the 3 × 5 array of FET developed in Ref. [308]. (b) THz radiation revealing the inside of an envelope. © 2009 IEEE. Reprinted, with permission, from Ojefors *et al.*, IEEE J. Solid-State Circuits **44**, 1968–1976 (2009) [308]. (c) Heterodyne detection scheme using a second source as a local oscillator [309]. (d) Image of a dextrose tablet wrapped in polyethylene foils. When compared to the direct detection mode, the heterodyne mode provides more contrast. Reprinted with permission from Glaab *et al.*, Appl. Phys. Lett. **96**, 042106 (2010) [309]. Copyright 2010 AIP Publishing LLC.

detector, each pixel included a reset circuit to clear the accumulated charges, an integration capacitor, and a differential amplifier. Each row was biased one at a time and the columns were consecutively selected with an external programmable logic device located inside the camera. The THz camera was packaged in a metal box with an integrated silicon lens for compact handheld applications [Fig. 2.30(b)]. The authors demonstrated 0.65 THz video recording using a focal-plane array configuration [Fig. 30(c)]. A digital still taken from the 24 fps video recording is presented in Fig. 30(e). The authors measured a minimum detectable power of 20 nW. Recently, Zdanevičius *et al.* were able to measure a minimal power of 1.4 nW at 30 fps [325]. The noise was reduced by using a parallel read-out architecture to simultaneously interrogate 48 pixels of their 24 × 24 pixel array.

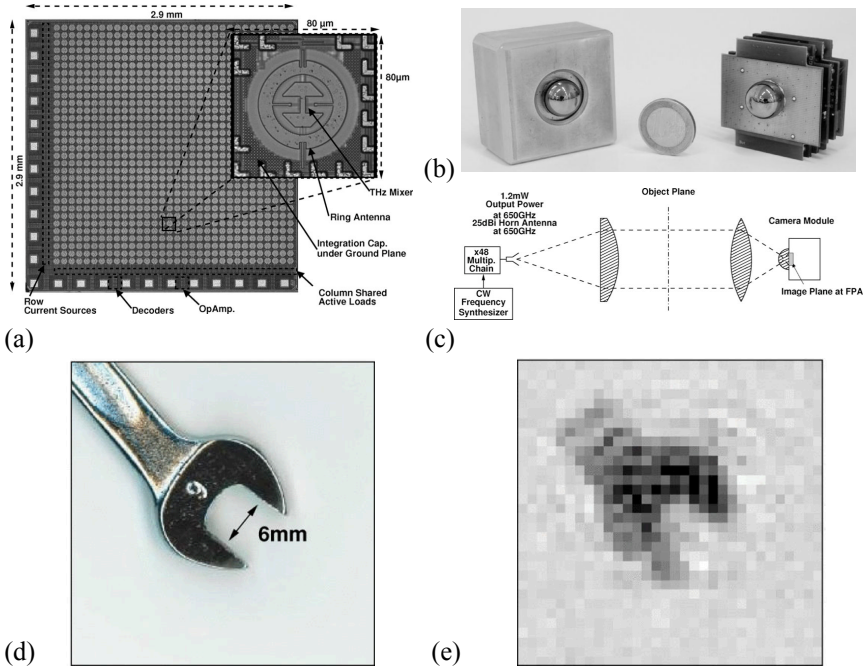

Figure 2.30 (a) Micrograph of the 32 × 32 focal-plane array developed in Ref. [69]. (b) Photograph of the THz camera device. (c) Transmission mode imaging setup in a focal-plane array configuration. (d) Photograph of a 6 mm wrench and (e) THz still image obtained from a 25 fps video stream at 650 GHz. © 2012 IEEE. Reprinted, with permission, from Hadi *et al.*, IEEE J. Solid-State Circuits **47**, 2999–3012 (2012) [69].

2.4.3 Section Summary and Future Directions

As we saw in this section, several requirements are necessary to enable mass deployment of THz cameras in various applications. They must operate at room temperature, without the need of cryogenic cooling. Their fabrication must be compatible with modern standard process technologies, such as the CMOS process technology. Their size, their weight, and their power consumption should be relatively small for easy integration into optical systems. Finally, they should be sensitive enough to allow recording of a THz signal at high frame rate, eventually without any active THz source. In the past decade, two major types of THz cameras have attracted attention: THz thermal cameras and THz FET-based cameras.

The first demonstrated THz cameras recorded an image based on the heat generated by THz radiation. There are three types of thermal detectors. The Golay cell measures the pressure change induced by the thermal expansion of a gas. Because of their simple operating principle, they are routinely used to measure THz powers. However, they are difficult to integrate into dense arrays of detectors and do not constitute a valid choice for THz cameras. Pyroelectric sensors detect the generated electrical polarizability of certain crystals when they are heated.

Unlike Golay cells, pyroelectric cameras are commercially available. However, their low sensitivity makes them less attractive for THz imaging.

Bolometers detect the change in a temperature-dependent resistance. The main components of a bolometer are the absorber that generates the heat, the resistive thermometer that outputs the voltage, and the thermal link that dissipates the heat to the heat sink. Microbolometers are arrays of bolometers mounted onto a read-out integrated circuit for focal-plane camera operation. Microbolometers can reach impressive sensitivities when cryogenically cooled due to the suppression of background thermal noise. However, room temperature operation with remarkable sensitivities (minimum detectable power of 100 pW) has been achieved thanks to recent advances in the design, such as the inclusion of a Fabry–Perot cavity, antennas, and metamaterials to increase the absorbed THz radiation.

THz FET-based cameras measure a rectified voltage after interaction of the THz radiation with a plasma wave in a transistor channel. The theoretical work predicted resonant (frequency-specific) and nonresonant (broadband) detection mechanisms. There were numerous demonstrations of THz FET-based detectors, using a variety of materials ranging from III–V semiconductors to graphene layers. However, in the short term, silicon-based FETs will probably have more impact on the development of THz cameras thanks to the compatibility of silicon material with the standard CMOS-foundry process. This key advantage could enable large-scale array fabrication at reduced costs. The behavior of silicon FET can be explained using the nonresonant broadband detection mechanism, as well as the distributed self-mixing concept where the channel is modeled as an RC transmission line. Record NEP in the range of $\mathrm{pW}/\sqrt{\mathrm{Hz}}$ was obtained by using a bow-tie antenna to couple the incident THz radiation at 0.3 THz, while broadband detection was used to measure frequencies up to 4.25 THz with an NEP of 100 $\mathrm{pW}/\sqrt{\mathrm{Hz}}$. As for camera operation, minimal detectable power in the range of 1–20 nW has been reported with up to 1024 pixels.

In addition to silicon-based FET cameras, future research directions include the development of a THz emitter on a silicon platform. This would enable all-silicon THz imaging systems attractive toward imager implementation at reduced costs. Several silicon-based THz sources have already been demonstrated in the literature: 0.19 mW at 0.28 THz [326], 0.81 mW at 0.34 THz [327], 1 mW at 0.53 THz [328], and 2 mW at 0.32 THz [329]. We expect increase in the power outputs and operation at higher THz frequencies. For THz imaging, there are several important advantages of using such sources. These types of sources can be used as local oscillators in heterodyne detection schemes for coherent imaging [329], therefore increasing the image contrast. They could also allow fabrication of on-chip transceivers, where the close proximity of the emitter and detector allows subwavelength imaging in the

near-field region [185]. Finally, distributed arrays of silicon emitters could allow dynamic electronic THz beam steering to increase the field of view of an imaging system [326].

We would like now to discuss on the potential of THz cameras and compare it with THz-TDS imaging systems. Although the development of THz cameras is crucial for many applications, we believe that it is not directly competing with THz-TDS imaging systems. While THz cameras provide non-discriminatory intensity-based imaging, we expect that amplitude-based THz-TDS imaging systems will develop into niche sectors, where the application will drive the system design. Indeed, as we saw in Section 2.2, the ability of THz-TDS to provide spectroscopic information in addition to THz imaging proves to be useful in various applications, for example, in quality control of large-area graphene or pharmaceutical applications.

2.5 THz Imaging with Single-Pixel Detectors

Historically, due to high cost and difficulty of manufacturing multipixel THz cameras/ arrays, many techniques have been proposed to enable real-time THz imaging using single-pixel detectors. Such techniques are mature and can be used to build costeffective industrial imaging systems. Additionally, they have a large modernization potential, as they could be greatly improved when substituting a single-pixel detector with 1D or 2D THz pixel arrays (when they would become commercially available). Finally, single-pixel imaging is often phase sensitive, allowing measurement of both amplitude and phase information of the electric field with very high SNR, which is one of its key advantages over intensity-only imaging using multipixel THz arrays. Therefore, even with an advent of multipixel THz arrays, further development of single-pixel techniques remains highly pertinent. In this section, we review the three most prominent single-pixel imaging techniques: 1) mechanical beam steering, 2) single-pixel imaging and compressive sensing, and 3) spectral/temporal encoding and Fourier optics.

2.5.1 Mechanical Beam Steering

In a conventional THz imaging system, the sample is positioned at the focal point of focusing optics. Then, using a single-pixel detector, the THz image is constructed by physically moving the sample in the focal plane (see Fig. 2.15). However, in many situations, sample displacement is not desirable or even possible. Instead of moving the sample, one can steer the THz beam over the sample. In principle, one could use spatial light modulation [330–333], special THz generation techniques [334–336], or a distributed array of THz emitters [326, 337] to accomplish this task. However, most of the demonstrated applications for real-time

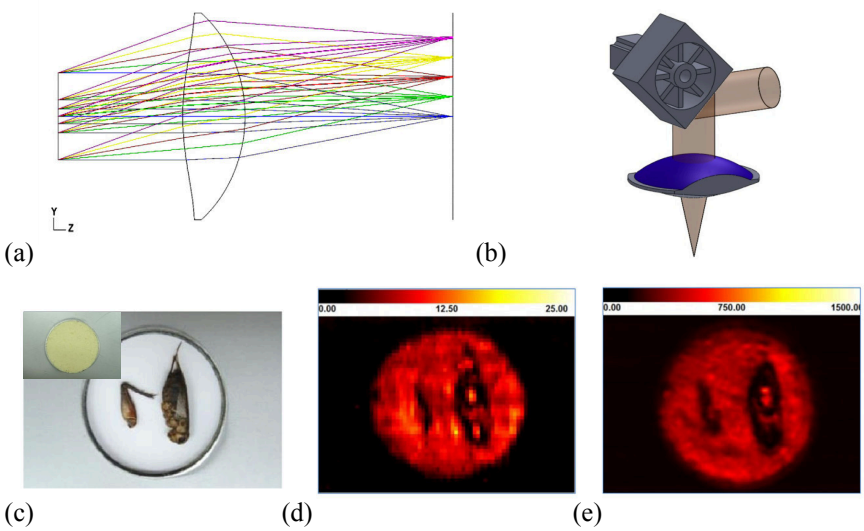

Figure 2.31 (a) f-theta scanning lens used in Ref. [338]. The colored lines correspond to an input angle and are focused on a single point in the focal plane. Adapted with permission from [338]. (b) Polygonal mirror used in Ref. [339] to replace the galvanometer. (c) Photographs of the crickets. Inset shows the crickets buried under the noodle flour. (d) Transmission image obtained in 3.13 s with the f-theta lens and the polygonal mirror and (e) obtained in 42 min with a conventional raster-scan. Adapted with permission from [339].

THz imaging use mechanical beam steering. In the following, we review two main types of mechanical devices: (1) the oscillating mirror with an f-theta scanning lens and (2) the Gregorian reflector system.

2.5.1.1 Oscillating Mirror with an f-Theta Scanning Lens

The f-theta lens is a specially designed lens that provides a flat image plane for a range of input angles [338–341]. Also known as a scanning lens, the f-theta lens is often used along with galvanometers to convert an incident angle into a linear position in the focal plane [Fig. 2.31(a)]. In Ref. [340], Katletz *et al.* combined flat mirrors mounted on a two-axis galvanometer and a rotationally symmetric f-theta scanning lens to steer the THz beam in two dimensions. A maximal scanning area of 100 mm × 100 mm was collected in 1–2 min at the rate of 1 line/s, mainly limited by the speed of the galvanometer. However, since the system was based on THz-TDS, the movement of the delay line was still necessary. In Ref. [341], Yee *et al.* used similar beam steering with ECOPS to obtain the temporal dimension (see Section 2.3.2.3). A time delay window of 52 ps was acquired in 1 ms, which led to the acquisition of 100 mm × 100 mm in 40 s. The authors also demonstrated 3D THz TOF imaging.

To avoid the need for a delay line, in Refs. [338,339], Ok *et al.* used a 210 GHz source with an output power of 75 mW to demonstrate applications in food quality inspection. In Ref. [338], a combination of a single-axis galvanometer and an f-theta lens were used to get the first spatial dimension, while the second was obtained with a linear translation stage (conveyer belt configuration). A 100 mm × 150 mm image was acquired in 15 s, limited again by the galvanometer speed. To further increase the acquisition rate, in Ref. [339], a polygonal mirror was designed and fabricated to replace the galvanometer [Fig. 2.31(b)]. With its four faces, one line can be acquired at 80 Hz, 4 times the rotor speed. To demonstrate food inspection, the authors buried crickets in noodle flour [Fig. 2.31(c)]. A transmission image of 288 mm × 207 mm was acquired in only 3.13 s [Fig. 2.31(d)] and compared with a conventional raster-scan image obtained in 42 min [Fig. 2.31(e)].

In Refs. [167,342], a fast two-axis scanning mirror was used to steer a 2.5 THz beam emitted from a THz QCL. The mirror could tilt in two directions and was placed at a focal length from a high-density polyethylene lens. The THz beam was scanned over a 40 mm diameter region by spiral scanning of the mirror. An image with 0.5 mm resolution was acquired in 1.1 s. THz computed tomography was demonstrated in 87 s by rotating the object by 180 deg in steps of 3 deg.

2.5.1.2 Gregorian Reflector System

Security and defense are potential applications of THz imaging that has attracted much of attention recently. Since many textiles are transparent to THz, concealed objects can be detected without exposure to ionizing radiation. In the f-theta lens that we previously described, the field of view and the distance between the imaging optics and the sample were limited to a few centimeters, which is not sufficient for stand-off security applications. In this subsection, we review the Gregorian reflector system that addresses this problem.

Llombart and co-workers proposed in Refs. [343–345] to use a confocal ellipsoidal reflector system in reflection geometry to mechanically scan a sample with a THz beam. Their transceiver system was based on a previously developed frequencymodulated continuous wave (FMCW) radar at 675 GHz [346,347]. The scanning optics included two paraboloid reflectors sharing a common focal point, similar to a Gregorian telescope. Between the two reflectors, a planar mirror with a diameter of 13 cm was rotated by ±2.5 deg in elevation and azimuth direction [Fig. 2.32(a)]. The mirror rotation allowed scanning of the sample on a 50 cm × 50 cm area. The paraboloid reflectors' characteristics were chosen to provide a 25 m stand-off distance for which the beam spot size was 1 cm. Imaging at 1 fps is enabled by a rotary mirror oscillating at 31.25 Hz. Imaging of hidden PVC pipes behind a subject's jacket was

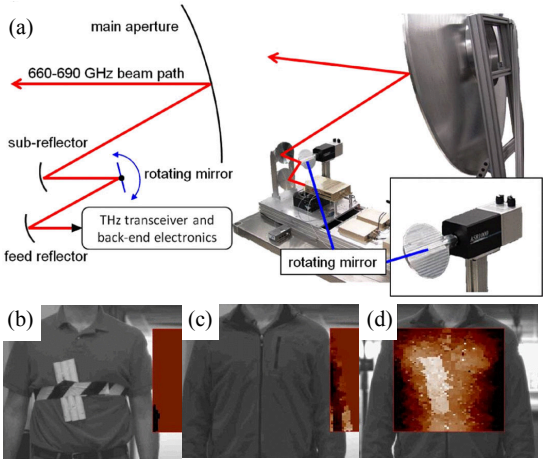

Figure 2.32 (a) Gregorian reflector system with a rotating mirror to scan the subject positioned at 25 m. (b), (c) Photograph of the hidden PVC pipes inside the subject's jacket. (d) THz image obtained in 1 s with the FMCW radar at 675 GHz. © 2011 IEEE. Reprinted, with permission, from Cooper *et al.*, IEEE Trans. Terahertz Sci. Technol. **1**, 169–182 (2011) [343].

demonstrated [Figs. 2.32(b)–(d)]. In Ref. [348], a bifocal Gregorian reflector system was proposed to increase the field of view without impacting the beam quality or imaging speed. Geometrical optics calculations were used to substitute the ellipsoidal reflectors by specially designed shaped surfaces, which were able to increase the field of view by 50%. Finally, most recently, similar opto-mechanical devices are combined with THz cameras to provide meter-scale field of view at 25 fps [349, 350].

2.5.2 Single-Pixel Imaging and Compressive Sensing

In the past, computational imaging techniques have been developed to enable imaging with single-pixel detectors. One such technique is compressive sensing. There, instead of directly imaging a sample, the detector performs a series of measurements of the transmitted intensity through a sample covered with different pixelated masks [Fig. 2.33(a)]. The measured data set can be mathematically described by using matrix–vector multiplication [351]:

$$\bar{y} = \Phi \bar{x} \tag{2.33}$$

where $\bar{x}$ is the vectorized version of a sample (local sample transmission), $\bar{y}$ is the corresponding vector of measured intensities by a detector, and the matrix Φ contains the information about the concatenated collection of the vectorized masks.

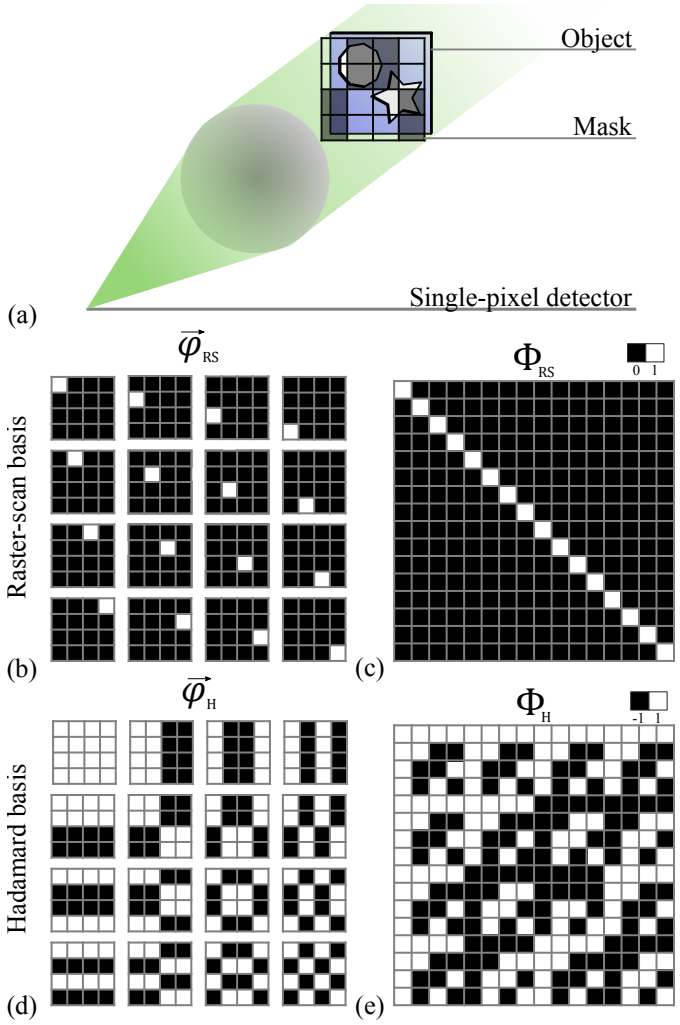

Figure 2.33 (a) Experimental setup for imaging with a single pixel using a mask aperture. (b) Raster-scan basis and set of 16 masks (ϕ^i_{RS}) for a 4 × 4 sample. (c) Measurement matrix Φ_{RS} constructed by concatenating the vectorized versions of the masks ϕ^i_{RS}. (d) Hadamard basis and set of 16 masks (ϕ^i_H) and (e) corresponding measurement matrix Φ_H

For example, to mimic a raster-scan, an aperture can be moved in the object plane. Every position of the aperture can be described by a mask. In Fig. 2.33(b), we present 16 masks for a sample of 4 × 4 pixels. For each mask, a vectorized version of the aperture (ϕ_{RS}) is constructed with values of 0 and 1 corresponding to opaque or transparent regions of the mask, respectively. The matrix Φ_{RS} is then constructed by stacking the vectors ϕ_{RS}. For the raster-scan, the measurement matrix is simply an identity matrix [Fig. 2.33(c)]. However, the identity matrix corresponds to a very poor choice of Φ since the aperture blocks most of the light, and therefore the useful signal is buried in noise.

In fact, there are more judicious choices for the matrix Φ. One of the most commonly used

sets of masks is derived from the Hadamard basis, which was shown to provide the best SNR [352]. In Fig. 2.33(d), we present the 16 Hadamard masks, while the corresponding Hadamard matrix is shown in Fig. 2.33(e). Other possible choices of Φ include the Fourier or wavelet basis.

In the measurement process within single-pixel imaging, Φ is predetermined and $\bar{y}$ is measured. The sample image $\bar{x}$ can then be recovered by performing the matrix inverse $\bar{x} = \Phi^{-1}\bar{y}$. Mathematically, the matrix inversion requires that the number of masks must be equal to the number of pixels in the object.

The compressive sensing theory proposes to use a number of masks smaller than the number of pixels, while employing a pseudo-inversion in place of a true matrix inversion. In general, images are compressible (sparse) under certain representations. In fact, this compression property is commonly used to reduce the size of images in computers. For example, JPEG compression uses the discrete cosine transform, which takes advantage of the difficulty of the human visual perception system to distinguish features with high spatial frequency components [353]. In JPEG compression, those frequencies are equated to zero in postprocessing *after* the image is taken with a digital camera.

In compressive sensing, the image is compressed directly *during* the measurement step [354, 355], and it essentially allows reconstruction of an image with a number of measurements that is smaller than the number of pixels [356], which at first glance seems to defy the Nyquist requirement. In compressive sensing imaging, while Eq. 2.33 becomes under-determined and an infinite number of solutions is possible, the pseudo-inverse can still be defined, for example, in the least square sense so as to minimize the norm of the difference between the right and left parts of Eq. 2.33 [357].

In more detail, compressive sensing theory indicates that it is possible to recover an approximation of $\bar{x}$ from a number of measurements smaller than the image size, given that the signal $\bar{x}$ is sparse under a certain representation [351]. To ensure robust signal recovery even when noise is introduced in the measurements, the sensing matrix Φ must respect the restricted isometry property [358]. This property ensures that column vectors taken from arbitrary subsets of a representation basis are almost orthogonal. For example, the measurement matrix Φ can take the form of random subsets of the Fourier, Hadamard, or wavelet basis. Remarkably, even random binary apertures derived from a Bernoulli distribution give satisfactory reconstruction results in most cases [354]. Furthermore, if Φ respects the restricted isometry property, then the object $\bar{x}$ can be reconstructed with high probability using just $M \geq \mathrm{O}(K \log(N/K))$ random measurements, where K is the number of nonzero coefficients.

Then, if the measurement $\bar{y}$ originates from a highly sparse object $\bar{x}$, the compressive sensing

problem can be formulated as searching for the sparsest signal $\bar{x}$ that produces $\bar{y}$. This leads to a minimization formulation with the l_0-norm:

$$\text{minimize } \|\bar{x}\|_0 \text{ subject to } \bar{y} = \Phi\bar{x} \tag{2.34}$$

where $\|\bar{x}\|_0$ is the l_0-norm, i.e., the number of non-zeros in $\bar{x}$. However, such a minimization problem is NP-hard in general and, therefore, is computationally prohibitive [359]. A common alternative is to use the l_1-norm, for which tractable programming is possible:

$$\text{minimize } \|\bar{x}\|_1 \text{ subject to } \bar{y} = \Phi\bar{x} \tag{2.35}$$

It can be shown that, if Φ satisfies the restricted isometry property, then Eq. 2.35 (l_1-norm) shares similar solutions with Eq. 2.34(l_0-norm). This type of minimization is known as the basis pursuit [354, 355, 360]. Among the other types of optimization algorithms, we note the basis pursuit with inequality constraints, where a bound is added in the constraint to include additive noise:

$$\text{minimize } \|\bar{x}\|_1 \text{ subject to } \|\bar{y} - \Phi\bar{x}\| < \varepsilon \tag{2.36}$$

The greedy algorithms are alternatives to the optimization-based algorithms [361]. In these methods, the solution $\bar{x}$ is constructed iteratively by selecting columns of Φ depending on their correlation with the measurements $\bar{y}$. For example, in the orthogonal matching pursuit [362], the solution is found by selecting the column of Φ that is most correlated to a residual, defined by subtracting a partial estimate to the measurements $\bar{y}$. The CoSamp algorithm is also a commonly used greedy algorithm [363]. We note that many other types of algorithms can be used to solve the compressive sensing problem. Readers may find excellent reviews on this topic in Refs. [358, 361, 364].

In the following, we review compressive sensing in the context of THz imaging. Apart from assuming sparsity of the imaged object, the compressive sensing theory does not specify the nature of the measurement. The measured data can be amplitude, phase, intensity, and so on. Therefore, compressive sensing can also be used with incoherent measurements as is commonly done in the visible range. In the following, some works used incoherent measurements in the THz range (for example [365–367]). Others used the broadband amplitude and phase measurement obtained from a THz-TDS system to reconstruct an image per THz frequency (hyperspectral imaging) or used the complex spectral information to improve image quality.

2.5.2.1 THz Imaging with Compressive Sensing

Chan *et al.* were the firsts to propose using compressive sensing theory for THz imaging [368, 369]. In their first implementation [370], the measurements were performed in the Fourier plane, and the image was reconstructed using a 2D spatial inverse Fourier transform. The object mask was placed in the front focal plane of a lens and the detector was scanned in the back focal plane [Fig. 2.34(a)]. Using THz-TDS, both amplitude and phase at 0.2 THz were measured over an area of 64 × 64 mm, at 1 mm intervals (4096 pixels). Then, assuming sparsity of the image, they used the compressive sensing theory to select random points in the Fourier plane, therefore using a random subset of the Fourier basis function. Using the spectrally projected gradient algorithm [360], they demonstrated successful image reconstruction that used only 12% (500 pixels) of the original data points [Figs. 2.34(b) and (c)].

In the first experimental approach, it was still necessary to mechanically move a single-pixel detector in the Fourier plane. In their second experiment [369], the authors used a set of random binary metal masks in the object plane and a fixed single-pixel detector at the center of the Fourier plane [Fig. 2.34(d)]. The binary masks formed a basis from which a 1024 pixel

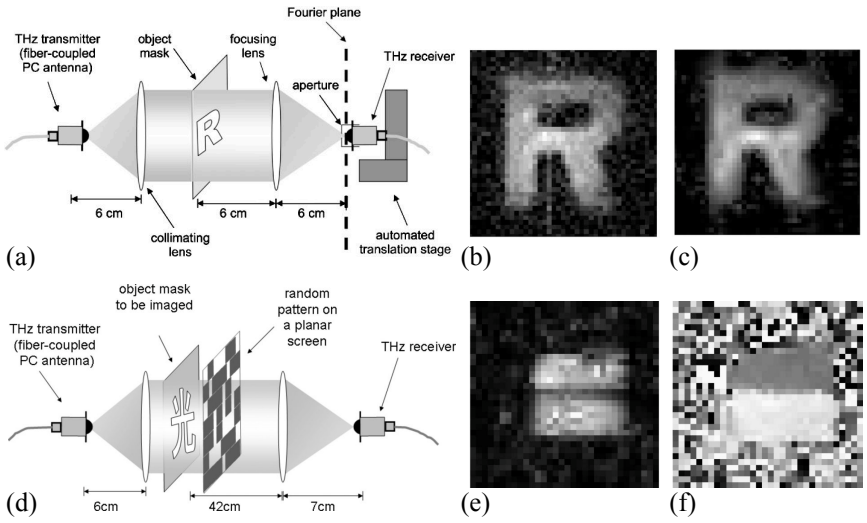

Figure 2.34 (a) Experimental setup for the Fourier transform compressive sensing reconstruction. (b) Reconstruction using 4096 measurements (100%) and (c) 500 measurements (12%) using compressive sensing. Reprinted with permission from [368]. Copyright 2008 Optical Society of America. (d) Experimental setup for the random binary masks compressive sensing reconstruction. Complex reconstruction of a 1024 pixels objects using 400 measurements (39%): (e) amplitude and (f) phase. Reprinted with permission from Chan *et al.*, Appl. Phys. Lett. **93**, 121105 (2008) [369]. Copyright 2008 AIP Publishing LLC.

image was reconstructed using as little as 300 (29%) measurements at a frequency of 0.1 THz. Thanks to the ability of THz-TDS to measure both the amplitude and the phase of the THz electric field [371], the authors also demonstrated phase contrast imaging of a rectangular hole half-covered with transparent plastic tape. While the amplitude of the reconstructed image shows no difference between the plastic and the air regions [Fig. 2.34(e)], the phase image clearly demonstrates contrast between the two regions [Fig. 2.34(f)].

The prospect of reducing the number of measurements by using only a single-pixel detection scheme resulted in a spurt of activity in compressive sensing applied to THz imaging. In Ref. [373], instead of random binary metal masks, Shen *et al.* used a set of optimized masks calculated to approximate the Karhunen–Loeve transform [374]. They showed that, using the same number of masks, the optimized masks gave better images than random masks. Also, using a broadband THz spectrum, they demonstrated spectroscopic contrast of lactose monohydrate power and polyethylene, owing to the fact that lactose has absorption peaks at 0.54 and 1.38 THz.

In Ref. [375], the authors used additional constraints in the optimization algorithm to obtain images of better quality. Thus, they used the assumption that the phase is generally a piecewise slow-varying function in the object plane and that the object is piecewise homogeneous with a uniform thickness. Additionally, using the information across all the THz frequencies, they showed improvement in the quality of the reconstructed image.

In the abovementioned works, the metallic masks were manually placed in the object plane. In Ref. [372], Shen *et al.* used a spinning metallic disk with holes as a mask set [Figs. 2.35(a) and (b)]. They used a THz-TDS setup and they fixed the delay line to the position of the main peak in time domain. They showed reconstruction of a THz image in 80 s by continuously rotating the mask at a speed of 5 deg/s [Figs. 2.35(c) and (d)]. They noted that the limitation in the acquisition speed was the SNR.

Three-dimensional imaging is also possible using single-pixel imaging. In Ref. [376], Jin *et al.* demonstrate pulse-echo reflectance tomography using compressive sensing applied to the scattering equation derived from the scalar wave equation [142]. In Ref. [168], THz-CT was performed using compressive sensing and the SART algorithm with Hadamard masks. In Ref. [140], Cho *et al.* demonstrated TPI using blockbased compressed sensing. The general idea of the block-based approach, developed in Ref. [377], is to divide the original object into several regions and to simultaneously apply the same binary operator in each region. This results in a reduction of the computational burden associated with the conventional compressive sensing, which allows computation of the image directly during the acquisition.

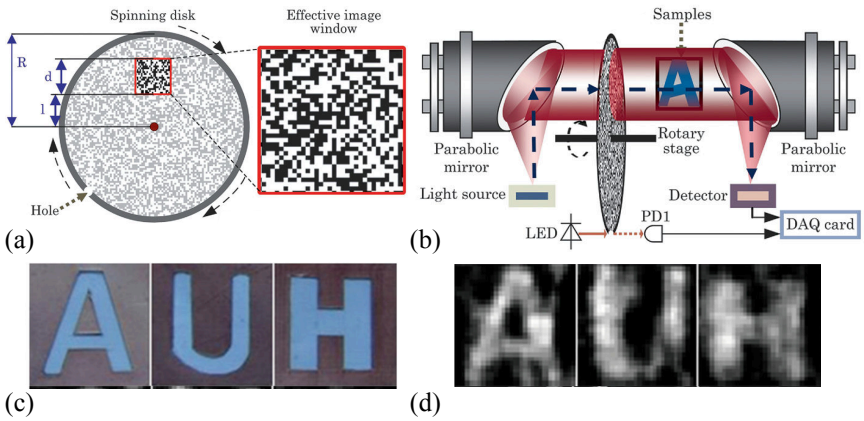

Figure 2.35 Real-time THz compressive sensing with a spinning disk. (a) Schematic of the spinning disk and (b) experimental setup. (c) Photograph of the sample and (d) reconstruction of a 32×32 pixel image using 160 measurements. Reprinted with permission from [372]. Copyright 2012 Optical Society of America.

2.5.2.2 Optical Spatial Light Modulation and Near-Field Imaging

To forgo completely the use of mechanically moving parts, the current trend in THz imaging within compressive sensing modality is to use spatial light modulation (SLM). There are many methods to spatially modulate the THz beam, and intensive research on this subject is still ongoing (see, for example, reviews on THz modulation in Refs. [378–381]). The general idea is to modulate the amplitude/phase of the transmitted or reflected THz beam, thus simulating the action of a mask.

Optically based modulation for compressive sensing THz imaging has been reported in Ref. [34]. There, the THz beam was spatially modulated with an optically controlled SLM made of a computer controlled digital light processing (DLP) projector that redirected light from an incoherent 8 W mercury arc lamp onto a photosensitive semiconductor material. In particular, apertures were optically inscribed onto a highresistive silicon wafer with a thickness of 500 μm. Within the silicon, the free carriers induced by the absorbed photons increase the conductivity and, hence, the absorption coefficient [383]. In Ref. [331], the reconstruction was made by raster-scanning a single aperture, which is not the efficient type of mask for compressive sensing imaging. In Refs. [384–386], the authors optically pumped Hadamard masks in the silicon wafer, while in Ref. [387], random masks were used on a germanium wafer. In Ref. [367], using only intensity measurements, phase-sensitive imaging at 690 GHz was demonstrated with the PhaseLift algorithm presented in Ref. [388].

In Ref. [382], Stantchev *et al.* performed single-pixel near-field imaging using optically based

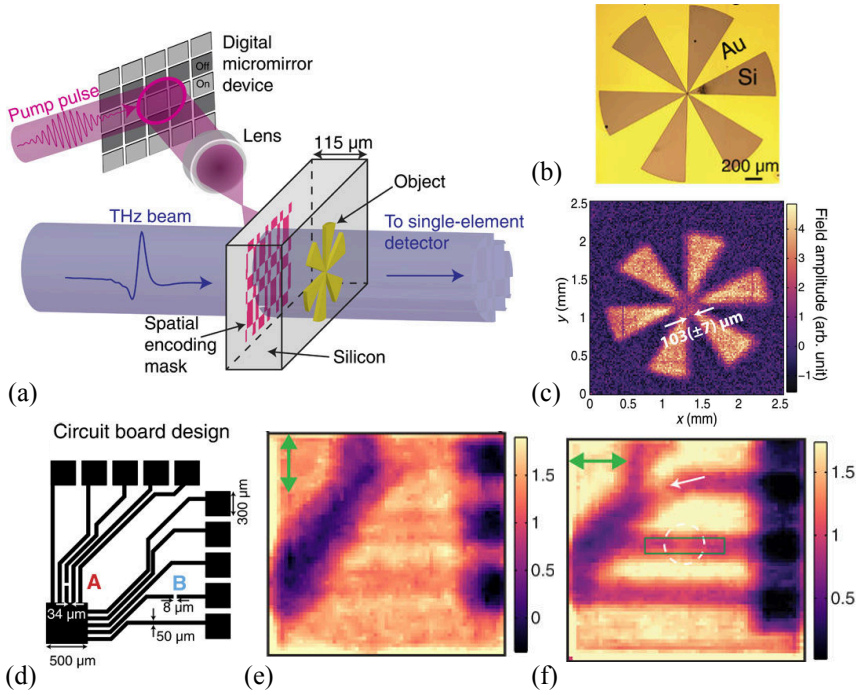

Figure 2.36 (a) Experimental setup using a silicon wafer and a digital micromirror device to generate the binary patterns. (b) Optical image of a metallic star and (c) reconstruction using Hadamard masks. (d) Schematic of a circuit board design. (e) Hadamard reconstruction of the region in (b) using vertical and (f) horizontal polarizations. Reproduced from [382] under the terms of the Creative Commons Attribution 4.0 License. With copyright permission.

modulation. They used an 800 nm, 100 fs optical pump onto a highly resistive 115 μm thick silicon wafer. The binary patterns were generated by reflecting the pump beam onto a digital micromirror device (DMD) [Fig. 2.36(a)]. Since the distance travelled by the THz beam in the silicon wafer was smaller than the wavelength, they were able to record an image before far-field Fraunhofer diffraction occurred. They demonstrated a resolution of 103 μm ($\sim \lambda/4$), significantly smaller than the 375 μm peak wavelength of the THz pulse [Figs. 2.36(b) and (c)]. Finally, by imaging a circuit board [Fig. 2.36(d)], they showed that the polarization of the THz pulse affected the resolution. They observed that the subwavelength conducting wires were more clearly observed when the THz radiation was parallel to the wires [Figs. 2.36(e) and (f)]. In Ref. [390], they used a similar THz near-field imaging system to map the photoconductivity of a graphene sheet.

In Ref. [389], the same group demonstrated that the thickness of the silicon plate plays a crucial role in determining the resolution of the reconstructed image. They experimentally demonstrated resolutions of 154, 100 and 9 μm ($\lambda/45$ at 0.75 THz) for thicknesses of 400, 110, and 6 μm, respectively [Figs. 2.37(a)–(c)]. Then, they used adaptive sampling to further

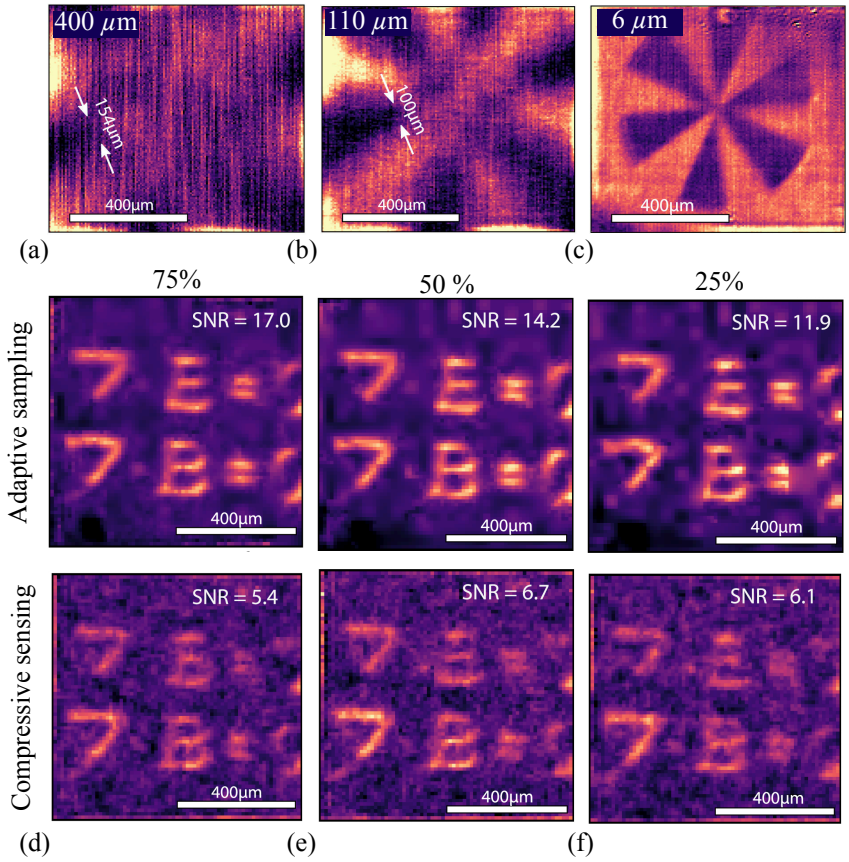

Figure 2.37 Improvement of the resolution by using thinner silicon wafer: (a) 400 μm, (b) 110 μm, and (c) 6 μm thick wafers. Comparison of reconstruction using adaptive sampling and compressive sensing, with (d) 75%, (e) 50%, and (f) 35% of the measurements required by the Nyquist theorem. Adapted with permission from [389].

reduce the number of required measurements. Using the Haar wavelet decomposition [391], they performed a coarse edge identification to determine where to sample with higher resolution. In Figs. 2.37(d)–(f), comparison of their adaptive sampling algorithm with standard compressive sensing revealed that, with the same number of measurements, adaptive sampling outperforms compressive sensing by increasing the SNR.

2.5.2.3 Metamaterial-Based SLM and Multiplexed Mask Encoding

Direct electronic SLM is desirable to reduce the complexity associated when adding a dedicated optical source to optically pump the semiconductor wafer [393]. In Ref. [392], instead of using an optically based SLM, Watts *et al.* introduced an active metamaterial SLM [Figs. 2.38(a) and (b)] originally reported in Refs. [394, 395]. The metamaterial SLM was electrically controlled to allow phase-sensitive mask encoding. By measuring the phase of

a detected signal with a lock-in amplifier, instead of simply measuring a binary mask, the authors were able to measure and symbolically represent negative and positive values with the in-phase and out-of-phase electrical signals. This allowed reducing the overall noise when using Hadamard masks. Furthermore, the metamaterial SLM allowed rapid changes of the binary masks. By displaying 45 masks for 22.4 ms each, they were able to demonstrate video recording at 1 fps [Figs. 2.38(c)–(f)].

The possibility of using phase information in mask encoding and signal led to the idea of multiplexed mask encoding. The concept is summarized by the constellation diagrams in Figs. 2.39(a) and (b). Thus, in Ref. [392], Watts *et al.* used in-phase and out-of-phase electrical signals to encode symbolically $\{+1\}$ and $\{-1\}$ values in the mask [2-phase-shift keying in Fig. 2.39(a)]. As in any communications system, the idea can be extended by using electrical signals with different phase values to symbolically represent more states. Consequently, multiple masks can be encoded simultaneously to further reduce the acquisition time. In Ref. [366], Nadell *et al.* demonstrated the encoding of two masks in parallel using quadrature amplitude modulation [Fig. 2.39(b)]. In practice, they used square waves with phases: $\{\pi/4; 3\pi/4; -3\pi/4; -\pi/4;\}$ to represent four possible combinations of symbols:

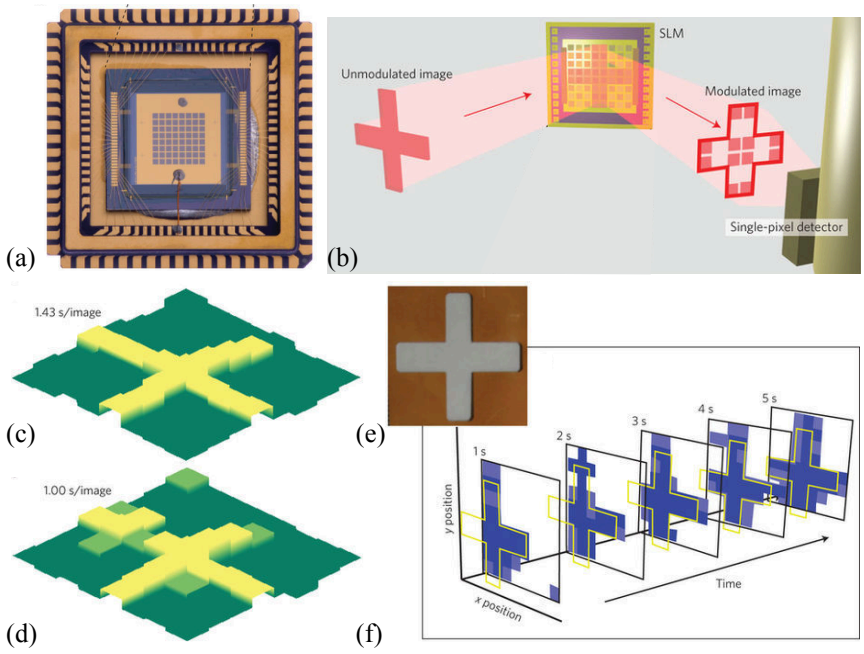

Figure 2.38 (a) Metamaterial SLM and (b) experimental setup. (c) Reconstructed object at 0.7 fps and (d) 1 fps of (e) a metallic cross. (f) Five frames of a 1 fps movie reconstructed with 45 masks displayed for 22.4 ms on the SLM. Reprinted by permission from Macmillan Publishers Ltd.: Watts *et al.*, Nat. Photonics **8**, 605–609 (2014) [392]. Copyright 2014.

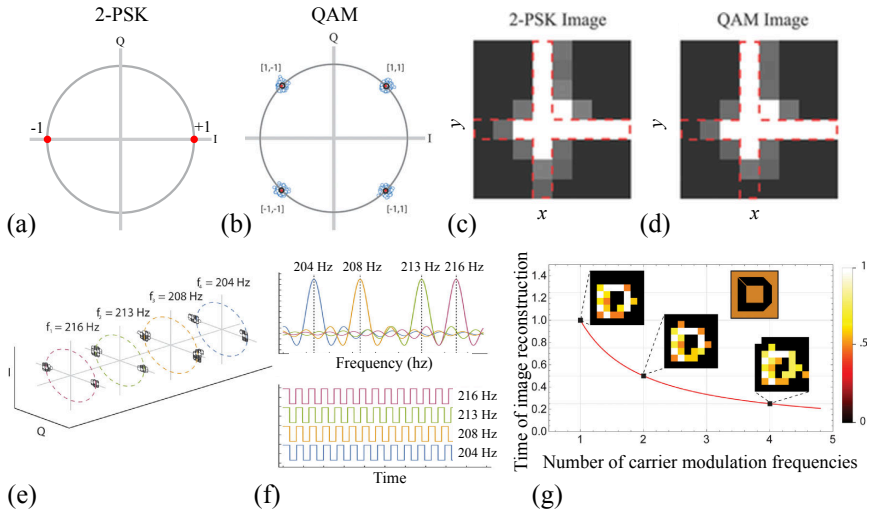

Figure 2.39 (a) Constellation diagram for the phase-shift key modulation with 2 states (2-PSK) and (b) 4 states (QAM). (c) Reconstruction of an inverted metallic cross using 2-PSK and (d) QAM. Adapted with permission from [392]. (e) Constellation diagram for frequency multiplexing. (f) The spectrum (top) and the square waveforms in the time domain (bottom) of the selected modulation frequencies. (g) Reduction of the time to reconstruct an image using an increasing number of carrier modulation frequencies and corresponding images. Adapted with permission from [365].

$\{1,1\}$, $\{-1,1\}$, $\{-1,-1\}$ and $\{1,-1\}$, where the first index corresponds to the value of the first mask and the second index the value of the second mask. Then, by coherently measuring the phase of the signal, the authors could acquire two elements of $\bar{y}$ in the time that only one element can be acquired using conventional mask change. By comparing the obtained image of their quadrature amplitude modulation [Fig. 2.39(c)] to a conventional 2-phase-shift keying [Fig. 2.39(d)], they measured less than 5% difference in the averaged l_2-norm.

In Ref. [365], the same group demonstrated frequency-division multiplexing with metamaterials. The idea was to encode simultaneously different masks using square waves of different frequencies [Fig. 2.39(e)]. To avoid crosstalk, the frequencies were selected such that they were all mutually orthogonal:

$$\int_0^\tau g_m(t)g_n(t)\mathrm{d}t = 0 \quad \text{for} \quad m \neq n \tag{2.37}$$

where τ is the integration time of a lock-in amplifier and $g(t)$ is the square waveform. In Ref. [365], up to four frequencies were selected for the image reconstruction [Fig. 2.39(f)]. As the number of frequencies n_f increased, the total acquisition time decreased as $1/n_f$ [Fig. 2.39(g)].

In principle, both frequency and phase multiplexing can be used at the same time to increase the number of channels and reduce the overall acquisition time. Eventually, when the number of channels equals the total number of pixels, the image can be acquired in a one-shot process. In practice, as in any communications system, the total number of channels is limited by the noise floor. Consequently, as the acquisition time decreases, so does the overall SNR.

2.5.3 Spectral/Temporal Encoding and Fourier Optics

In this section, we review spectral/temporal encoding techniques, in which the information about the image structure is encoded into the spectrum/temporal waveform. These methods rely on the Fourier transform relationships, linking the time/frequency domains to the space/k-space domains [Fig. 2.40].

2.5.3.1 Spectral and Temporal Encoding

A classic implementation of the space-to-time image transformation in the infrared/ visible range is the serial time-encoded amplified (STEAM) system [396,397]. In the STEAM system developed in Ref. [396], spatial dispersers were used to encode spatial information into a broadband spectrum. Then, using a dispersion compensating fiber and Raman amplification, the spectrum of an optical pulse was mapped in time domain. A single-pixel photodetector was then used to reconstruct the 2D image at a laser repetition rate of 6.1 MHz, allowing for the real-time video acquisition of fast dynamic phenomena.

Similar to the spatial disperser used in the STEAM system [399], blazed diffraction gratings have been introduced in the THz range to map the spectrum in 1D space. In Ref. [398], Schuman *et al.* fabricated an aluminum blazed diffraction grating with a groove depth and

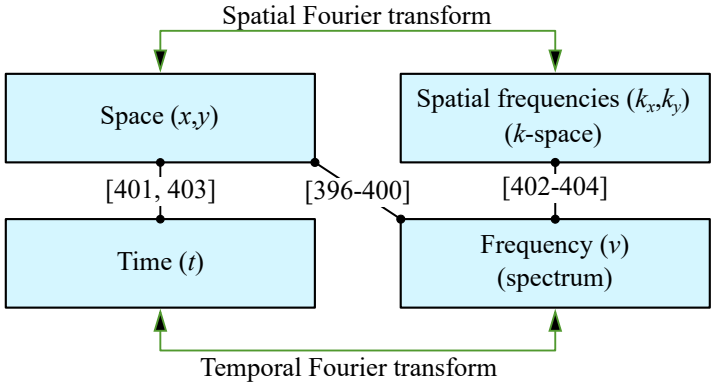

Figure 2.40 Schematic description of the spectral/temporal encoding. The references of Section 2.5.3 are indicated at the relative positions in the schematic.

period chosen to achieve an angular dispersion of 15 deg per 100 GHz. The authors selected the first diffractive order between 300 and 600 GHz since it achieved a high diffraction efficiency of 85%. The grating was then used in combination with an f-theta lens to ensure that the focal points of the individual frequencies were in the same plane, either in transmission [Fig. 2.41(a)] or in reflection geometry [Fig. 2.41(b)]. To calibrate the measurement, the THz detector was linearly scanned in the focal line, and a third-order polynomial was used to correlate the THz frequency with the spatial position [Fig. 2.41(c)]. Thus, by directly measuring the spectrum, a complete 1D line in the image can be acquired. In Fig. 2.41(d), metal letters attached to a sheet of paper were imaged in transmission and in reflection (inset) using blazed gratings. There, the horizontal axis has been acquired from the spectrum while the vertical axis was imaged by linearly scanning the object. It can be observed that the right side of the image exhibits better resolution than the left side, which can be directly attributed to the nonlinear frequency-to-space relationship measured in Fig. 2.41(c). A second grating perpendicular to the first one can be added to map the frequencies in 2D spatial coordinates [400,401]. In Ref. [402], the authors mapped a 60 cm $\times$ 60 cm area using 401 frequency points between 75 and 110 GHz.

In Ref. [403], Lee *et al.* demonstrated near-field imaging using spectral encoding with a metasurface. Gold cross-type mesh filters were fabricated via photolithography on a polyimide

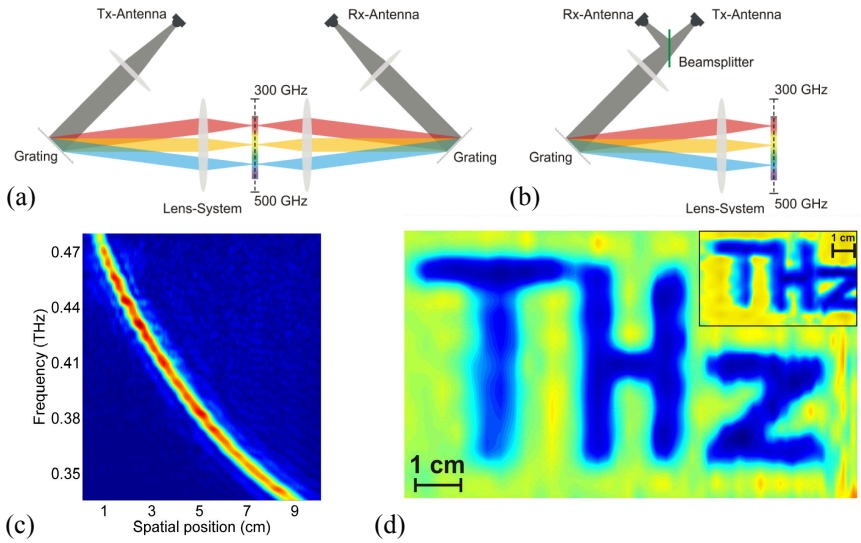

Figure 2.41 (a) Transmission and (b) reflection geometry with a blazed diffraction grating and an f-theta lens system. (c) Calibration measurement of the frequency as a function of the spatial position (d) Demonstration of THz imaging in transmission geometry. Inset: reflection geometry. Reprinted with permission from [398]. Copyright 2012 Optical Society of America.

substrate [Fig. 2.42(a)]. These filters act as transmission bandpass filters in the frequency domain. By spatially patterning the meshes with varying geometrical dimensions, the authors designed a metasurface able to map the spatial positions in the THz spectrum. Then, they demonstrated two reconstruction techniques using either an angular scan of the object [Figs. 42(c)–42(e)] or a translation scan of a metallic slit [Figs. 2.42(f)–(h)]. In the angular scan, the reconstruction was made with an inverse Radon transform, while in the translation scan, a collection of measurements represented the image directly in the spectrum. Using numerical simulations, they found that both reconstructions are sensitive to the Q factor of the mesh filter. For a uniform mesh distribution, the Q factor is defined as the ratio of the central wavelength to the bandwidth of the bandpass filter. Therefore, a larger Q factor characterizes a narrower bandpass filter. With the angular scan, due to the nature of the reconstruction, a lower Q factor caused a blur in the entire image. In the translation scan,

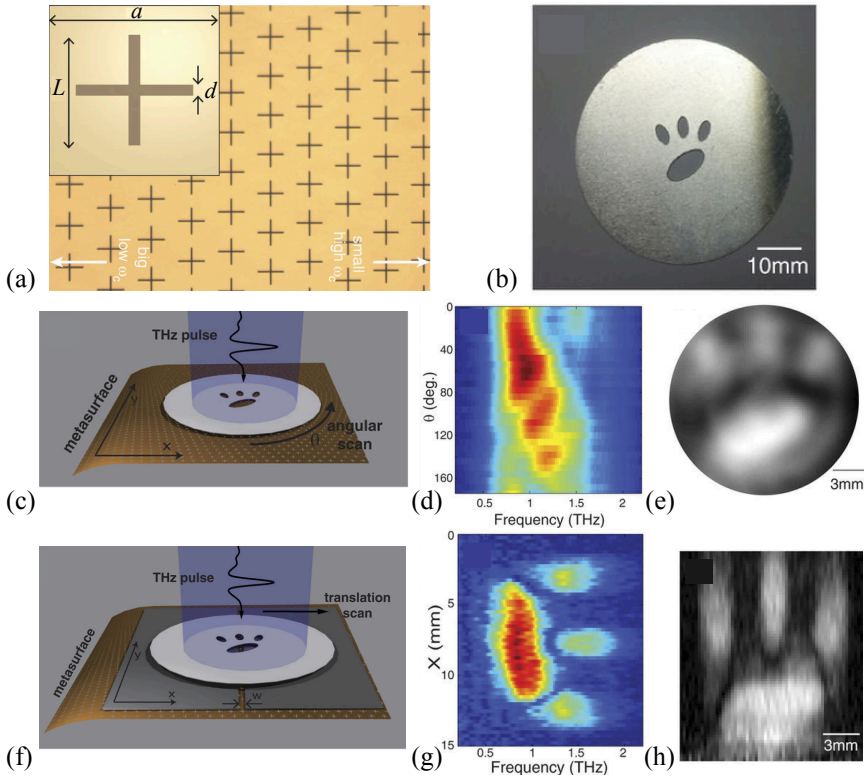

Figure 2.42 (a) Cross-type mesh-based metasurface with varying geometrical parameters. (b) Photograph of the sample. (c) Angular scan geometry, (d) THz spectrum as a function of the angle, and (e) reconstructed image with the radon transform. (f) Translational scan geometry, (g) THz spectrum as a function of the position of the slit, and (h) reconstructed image. Adapted from [403] under the terms of the Creative Commons Attribution 4.0 License. With copyright permission.

the Q factor affected the y axis resolution, while the x resolution was determined by the width of the slit.

An example of a space-to-time conversion imaging is demonstrated in Ref. [404]. With a THz-TDS system, Stübling *et al.* made a multipixel emitter unit by dividing a single THz pulse into multiple pulses using a set of polymer beam splitters [Fig. 2.43(a)]. On the detector side, specially designed mirrors were placed to redirect the individual pulses into a single-pixel THz photoconductive antenna. Then, a series of THz pulses appear in the time-domain measurement by scanning over a sufficiently large temporal window [Fig. 2.43(b)]. These pulses correspond to different spatial positions, as confirmed by the raster-scan above the emitter head [Fig. 2.43(c)]. Therefore, they can be used to reconstruct an image. As this configuration relies on scanning the optical delay line, the methods that we have described in Section 2.3.2 can be applied to reduce the acquisition time. Here, the authors used ASOPS in their system implementation.

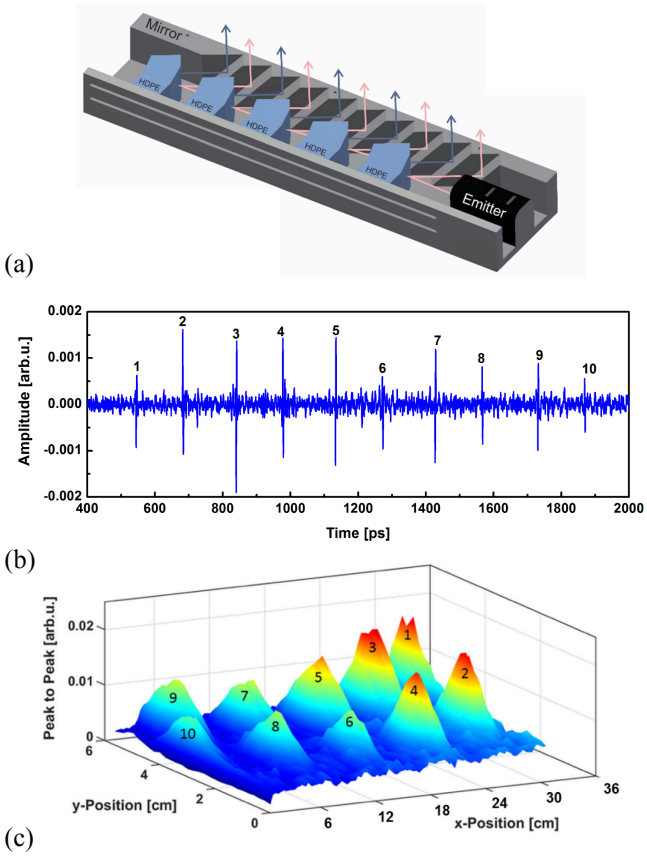

Figure 2.43 (a) The beam is divided into multiple spatial positions using beam splitters. (b) Time-domain measurement of the 10 pulses corresponding to the spatial positions in (d). Reprinted with permission from [404]. Copyright 2016 Optical Society of America.

2.5.3.2 Fourier Optics and k-space/frequency Duality

By using Fourier optics relationships, the spatial frequencies can be encoded into the spectrum [17, 405, 406]. The concept here is to use a diffractive element to retrieve a linear relationship between the k-vector and the frequency. The simplest implementation uses a lens to do the encoding [Fig. 2.44(a)]. The Fourier optics theory states that a given field profile $S(x, y, \nu)$ at the front focal plane (object plane) of a convex lens is Fourier transformed at the back focal plane (Fourier plane) according to [169]

$$U(\xi, \eta, \nu) = \frac{\nu}{jcF} \iint \mathrm{d}x\mathrm{d}y \cdot S(x, y, \nu) \cdot \exp\left[-\frac{j2\pi\nu}{cF}(x\xi + y\eta)\right] \tag{2.38}$$

where F is the lens focal length, c is the speed of light, and ν is the frequency. The coordinates (x, y) and (ξ, η) are the spatial positions in the object plane and the Fourier plane, respectively. The original field distribution $S(x, y, \nu)$ can then be reconstructed by using the inverse Fourier transform:

$$S(x, y, \nu) = \frac{j\nu}{cF} \iint \mathrm{d}\xi\mathrm{d}\eta \cdot U(\xi, \eta, \nu) \cdot \exp\left[+\frac{j2\pi\nu}{cF}(x\xi + y\eta)\right] \tag{2.39}$$

The spatial frequencies, also known as components of the k-space, are related to the (ξ, η) coordinates through

$$k_\xi = \frac{\xi\nu}{cF} \qquad\qquad k_\eta = \frac{\eta\nu}{cF} \tag{2.40}$$

Since the spatial frequencies are proportional to the frequency ν, one can use the THz spectrum to scan along a line in the k-space. In other words, by fixing the detector in the Fourier plane at (ξ_0, eta_0) and using a broadband source such as $\nu \in [\nu_{\min}, \nu_{\max}]$ Eq. 2.40 can be combined to give

$$k_\eta = \frac{\eta_0}{\xi_0} k_\xi \tag{2.41}$$

By changing the ratio η_0/ξ_0, the whole k-space can be sampled. The simplest way to change this ratio is to measure points along a circle of radius ρ_0 in the Fourier plane. Therefore, the 2D raster-scan [Fig. 2.44(b)] that provides a hyperspectral cube in the k-space [Fig. 2.44(c)] can be substituted by a 1D linear scan [Fig. 2.44(d)] along a circle, and the measured spectrum can be mapped into the radial dimension of the k-space [Fig. 2.44(e)].

This idea was demonstrated in the THz range by Lee *et al.* in Ref. [405]. In their implementation, they used a parabolic mirror as the diffractive element. An aperture of 5 mm diameter at 15 mm away from the optical axis was placed at the Fourier plane, while a second parabolic mirror focused the THz beam into a fixed single-pixel detector. Then, using a

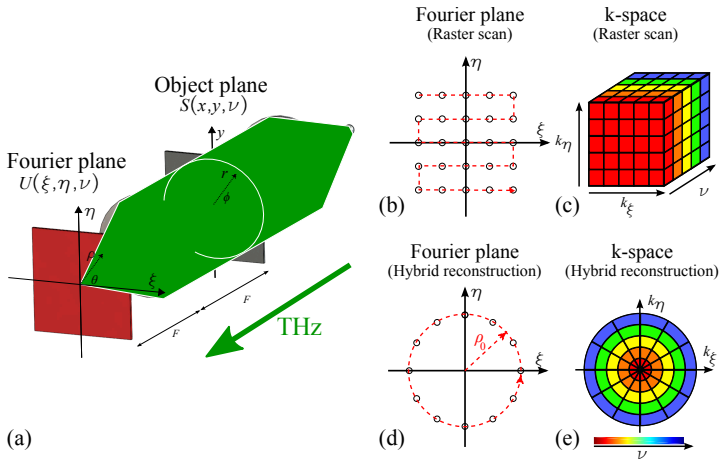

Figure 2.44 (a) General setup for k-space encoding using a lens. (b) Conventional raster-scan and (c) hyperspectral cube, and (d) circular scan and (e) k-space reconstruction using spectral encoding. Reprinted with permission from [17]. Copyright 2018 Optical Society of America.

THz-TDS setup, they measured several spectra for different angular positions of the mask. They demonstrated reconstruction of a metallic object using 10–30 THz-TDS traces.

In Ref. [406], the same group demonstrated similar spectral encoding using a slanted phase retarder made of Teflon at the position of the object. However, as in Ref. [405], mechanical rotation of the mask was necessary. Therefore, they also proposed to combine their approach with temporal encoding in k-space. For that purpose, they placed a mask in the Fourier plane that contained an angular pattern of holes, each containing additional phase retardation elements (Teflon disks of different thicknesses). The resultant long-time scan contained multiple THz pulses separated in time, each corresponding to a unique angular position in the k-space, which was then used to reconstruct the image.

In Ref. [17], Guerboukha *et al.* presented the rigorous mathematical theory behind the image reconstruction process reported in Refs. [405, 406], as well as several novel imaging modes, which included amplitude- and phase-based modalities. They started by expressing the Fourier integral 39 in polar coordinates:

$$S(\vec{r},\nu) = \frac{j\nu}{cF} \iint \mathrm{d}\theta\rho\mathrm{d}\rho \cdot U(\vec{\rho},\nu) \cdot \exp\left[+\frac{j2\pi\rho}{cF}\vec{r}\cdot\vec{\rho}\right] \tag{2.42}$$

In fact, the idea of spectral encoding implies that the integral over the radial coordinate $d\rho$ should somehow become an integral over the spectrum $d\nu$ in Eq. 2.42. Therefore, instead of the classic backward Fourier transform given Eq. 2.39, the authors chose a new form of the

reconstruction integral:

$$\tilde{S}(\vec{r}) = \iint \mathrm{d}\theta\nu\mathrm{d}\nu \cdot \frac{j\rho_0^2}{\nu cF} \cdot \frac{U(\rho_0,\nu,\theta)}{U_{\mathrm{ref}}(\nu)} \cdot \exp\left[+\frac{j2\pi\nu}{cF}\vec{r}\cdot\vec{\rho}_0\right] \tag{2.43}$$

Recognizing that the reconstruction $\tilde{S}(\vec{r})$ is different from the original object $S(\vec{r},\nu)$, the authors used in Eq. 2.43 a certain reference measurement $U_{\mathrm{ref}}(\nu)$ that allows attributing a physical meaning to the reconstruction $\tilde{S}(\vec{r})$ For example, in the case of amplitude imaging with binary metal masks (cut-outs in metal), the following reference was used:

$$U_{\mathrm{ref}}(\nu) = \frac{jcF}{\nu}U(0,\nu) \tag{2.44}$$

where $U(0,\nu)$ is a measurement in the middle of the Fourier plane with the metal mask in place. Then, they mathematically showed that the reconstructed image according to the definition given by Eq. 2.43 is simply the original object normalized by the total area:

$$\tilde{S}(r,\phi) = \frac{S(r,\phi)}{\iint S(r,\phi)\mathrm{d}\phi r\mathrm{d}r} \tag{2.45}$$

Figs. 2.45(a)–(f) present the experimental results when reconstructing a cut-out in the metal sheet in the form of a maple leaf (amplitude mask). The amplitude [Fig. 2.45(d)] and the phase [Fig. 2.45(e)] of the k-space reconstructed with the spectral encoding are comparable to those acquired with a raster scan [Figs. 2.45(a) and (b)]. However, the reconstructed object with the spectral encoding [Fig. 2.45(f)] required sampling of only 45 spatial positions, compared to the raster-scan with 4624 spatial positions [Fig. 2.45(c)].

Using the mathematical theory described above, the authors extended the idea to phase masks. As an example, they imaged a polymer plate (refractive index n_m) with a shallow 100 μm engraving. Interestingly, to enable imaging of phase masks, only the reference has to be modified in Eq. 2.43 as

$$U_{\mathrm{ref}}(\nu) = jcF \cdot U(0,\nu) \tag{2.46}$$

where $U(0,\nu)$ is a measurement in the center of the Fourier plane using a polymer plate without the engraving. Then, the authors showed that the imaginary part of the reconstructed object using Eq. 2.43 is proportional to the optical path $\Delta(\vec{r}) = (n_m - 1)h(\vec{r})$ due to the engraving:

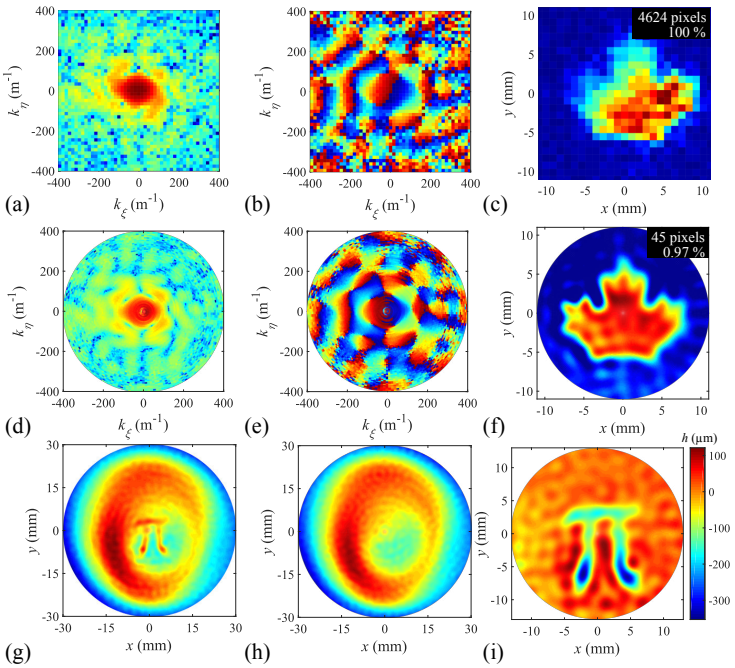

Figure 2.45 Reconstruction using the k-space/frequency duality. (a) Amplitude and (b) phase of the k-space, and (c) reconstruction at 0.57 THz. (d) Amplitude and (e) phase using the k-space/frequency duality, and (f) reconstruction. (g) Reconstruction using the k-space/frequency duality of an engraving into a polymer sample and (h) without the engraving. (i) Reconstruction of the depth of the engraving. Reprinted with permission from [17]. Copyright 2018 Optical Society of America.

$$\mathrm{Im}\{\tilde{S}(\vec{r})\} = -\frac{2\pi}{c}\frac{S(\vec{r})}{\iint S(\vec{r})\mathrm{d}\vec{r}}\Delta(\vec{r}) \tag{2.47}$$

Therefore, by measuring a plate with [Fig. 2.45(g)] and without the engraving [Fig. 2.45(h)], they were able to directly map the height of the engraving [Fig. 2.45(i)].

Contrary to the spectral encoding techniques described in Section 2.5.3.2, encoding an image into k-space requires no complex optical devices. Thus, a simple lens was used in Ref. [17] and the detector was simply positioned off-axis. In fact, instead of using a circular lens, one could use a cylindrical lens to perform 1D Fourier transform. Then, by simply scanning the object in the other dimension, every measured spectrum would provide a 1D line of the object. This type of configuration could be used in a conveyer belt system to obtain a 2D THz image.

The spatial resolution when using spectral encoding of the k-space can be directly derived from the Nyquist theorem that states that the minimal achievable resolution is $\delta x = 0.5/k_{\mathrm{max}}$, where k_{max} is the maximal spatial frequency sampled in k-space. Therefore, the resolution

of the image can be improved by measuring the larger k-space components located at the periphery of the limiting aperture (field of view) in the Fourier plane. When using spectral encoding of the k-space, Eq. 2.40 shows that $k_{\max} = \nu_{\max}\rho/cF$, with $\nu_{\max}$ being the maximal THz frequency, ρ the radial position of the detector (in the Fourier plane), and F the focal length. Therefore, the resolution becomes $\delta x = 0.5cF/\nu_{\max}\rho$ and can be increased by using a lens with a shorter focal length, by positioning the detector at a larger radial position and by using spectrally broader THz source.

Finally, we would like to discuss the impact of the THz spectral encoding and Fourier optics on the broadband spectral information. One must recognize that fast reconstruction algorithms as presented above [see Eq. 2.43] use spectral information to sample the k-space. Therefore, the reconstructed image is different from a hyperspectral image obtained, for example, using THz-TDS. Moreover, uneven power distribution in the pulse spectrum should be mitigated by acquisition of a reference spectrum of an empty system or a substrate (see, for example, the calibration step in Ref. [398] or the normalizations in Ref. [17]), which somewhat complicates the imaging procedure. Additionally, in the case of samples exhibiting significant frequency-dependent loss variations, image resolution might suffer due to effective loss of information at frequencies characterized by strong absorption. For example, for many dielectrics, one expects reduction of the maximal useful frequency value due to stronger sample absorption at higher frequencies. Inversely, if the sample has piecewise weakly dependent losses, then we expect excellent reconstruction results. For example, spectral encoding in Fourier space can be used together with a fast Fourier transform algorithm to efficiently reconstruct amplitude variations at the edges between distinct materials. This case is already important for defense and mail screening applications.

2.5.4 Section Summary and Future Directions

In this section, we have reviewed three main techniques to enable THz imaging with single-pixel detectors: (1) mechanical beam steering, (2) single-pixel imaging and compressive sensing, and (3) spectral/temporal encoding and Fourier optics. Historically, these techniques have been developed to mitigate the high cost and difficulty of manufacturing multipixel THz cameras. Today, these techniques are mature enough to be an integral part of the cost-effective imaging systems. Furthermore, the single-pixel detectors used in such systems are often phase sensitive and can measure both amplitude and phase of the electric field with very high SNR. This is a key advantage when compared to THz cameras that commonly detect only the signal intensity. Therefore, even with the advent of THz cameras, we believe that development of the single-pixel imaging techniques will remain highly pertinent.

The first single-pixel imaging technique that we have reviewed is mechanical beamsteering. Historically, to obtain a THz image, the sample was positioned at the focal point of focusing optics and physically moved pixel by pixel. In many situations, sample displacement is not desirable or even possible. Instead of moving the sample, one can mechanically steer the THz beam over the sample. A combination of oscillating mirrors and an f-theta lens can provide a simple and cost-effective solution for short-range applications, for example, in industrial environments using conveyer belts. In comparison, the Gregorian reflector system is seen as a desirable candidate for large stand-off distances, for example, in the security and defense sector. Eventually, the future development of non-mechanical beam-steering technology would allow stable and rapid dynamic scans. This has already been explored using electrically controlled liquid crystal devices [330], optically pumped semiconductor wafers [331–333], special THz generation techniques [334–336], or distributed arrays of emitters [326, 337]. In particular, in Ref. [326], Sengupta and Hajimiri fabricated a distributed array of active radiators in CMOS to generate a 0.28 THz beam. By tuning the relative phase of the 4×4 emitter array, the THz beam could be steered in two dimensions, over 80 deg in azimuth and elevation. Finally, we mention that the beam-steering technique is not strictly limited to single-pixel detectors. In fact, they could be used with THz cameras to increase the field of view.

In parallel, single-pixel imaging using compressive sensing has seen important development in the context of THz imaging. Within this method, the image is reconstructed by successive single-pixel measurements of a spatially modulated THz beam over the sample (aperture functions). Then, assuming that the object is naturally sparse, the compressive sensing theory can be used to reconstruct the image with a number of measurements smaller than the total number of pixels. As for real-time imaging, recent schemes involve the use of SLM. Spatial patterns can be optically encoded in a semiconductor wafer, which can also act as a substrate for near-field compressive sensing imaging. At the same time, electronic modulation allows for more complex pattern modulation. Notably, the simultaneous modulation of multiple masks can lead to major improvements in terms of acquisition rates. There, the different masks are encoded using sine waves of different phases and frequencies, to enable fast image acquisition through channel multiplexing and detection with a lock-in amplifier. Eventually, when the number of channels equals the total number of desired masks, the image can be acquired in a one-shot process. In practice, as in any communications system, the total number of channels is limited by the noise floor. Consequently, as the acquisition time decreases, so does the overall SNR. Finally, the developments in this field are intimately related to the development of efficient SLM devices with near-unity modulation factor and low transmission/reflection losses, to reduce the overall integration time of the detector and enable even faster acquisition

rates.

Finally, spectral encoding techniques take advantage of the relationships between time and space to encode the spatial information of a sample in the spectrum, the temporal waveform, or in the Fourier space. The idea here is to use a broadband pulse along with frequency-dependent diffraction devices to spread the frequencies over the sample. Then, the transmitted/reflected spectrum can be recorded using a single-pixel detector, for example, using a THz-TDS system. The diffraction device can be a diffraction grating, a specially designed metasurface, a series of polymer retarders, or just a common lens. If THz-TDS is used, one must be aware that the spatial dimensions are often traded for a 1D spectral dimension that is obtained by measuring the temporal waveform with an optical delay line. In this case, the spatial line acquisition rate is often determined by the speed of the optical delay line (see Section 2.3.2). In principle, as it is done in the visible range, one could also use THz cameras (Section 2.4) to directly measure the spectrum and therefore avoid the use of the optical delay line. In fact, in Section 2.3.4.3, we saw demonstration of such a device, using temporal encoding, a camera, and EOS.

2.6 Conclusion

In conclusion, THz imaging uses the properties of THz waves to interrogate matter in unique ways. In the past 20 years, important technological developments have taken place to enable real-time high-resolution imaging. Today, research in THz imaging is steadily shifting from laboratory-based instrumentation to commercial products. In this context, we have reviewed THz imaging with an emphasis on the imaging modalities and tools that could enable high-resolution real-time imaging and its fundamental and industrial applications.

We started this review by detailing recent advances in some of the most promising THz imaging modalities. Particularly, in THz transmission and reflection spectroscopy, the complex refractive index of a material can be obtained using Fresnel coefficients, which leads to the determination of the complex permittivity and conductivity. In THz pulsed imaging, the temporal delay between several reflected THz pulses is used to image through layered structures. THz-CT exploits the ability of THz waves to penetrate matter to reconstruct a volumetric image of an object. In THz near-field imaging, apertures and scattering tips are used to enable subwavelength resolution, thus beating the diffraction limit.

We then focused our attention on three major research directions to enable real-time THz imaging: THz-TDS real-time imaging, THz cameras, and THz single-pixel imaging.

Many of the developed imaging techniques rely on THz-TDS systems that allow coherent

measurement of the amplitude and phase of the pulsed THz electric field at the picosecond time scale. However, imaging with a THz-TDS system requires using relatively slow instrumentation that impedes real-time imaging. To speed up acquisition time of the THz signal, many modifications to the THz-TDS system subcomponents were proposed. Thus, to forgo the linear movement of the optical delay line, reflective or prism-based rotary delay lines have been developed. Alternatively, one can use asynchronous optical sampling, electronically controlled optical sampling, and optical sampling by cavity tuning, which are various techniques that can be used to avoid altogether the mechanical movement of a delay line. Additionally, we have mentioned that photoconductive antennas and EOS are currently the two key methods for coherent detection of THz pulses. While in their simplest form both techniques offer single-pixel coherent detection, recently there was significant progress in realizing arrays of THz photoconductive antennas, as well as using infrared/visible cameras with EOS, thus greatly speeding up image acquisition times.

In parallel, intensive research has been conducted to develop THz cameras similar to those available in the visible region of the spectrum. Among their technical requirements for mass deployment, they should operate at room temperature, be compatible with standard fabrication technologies (such as CMOS process), have little weight, small size, and low power consumption, and offer high sensitivities (for high frame rate THz imaging even without an active THz source). Two major technological trends are being pursued to realize THz cameras that would respond to those criteria: THz thermal cameras and THz FET-based cameras. On one hand, THz thermal cameras measure the heat generated by the absorption of the THz radiation. Pyroelectric cameras and microbolometers have been used for THz imaging. In particular, microbolometers have achieved remarkable sensitivities at room temperature thanks to the inclusion of a Fabry–Perot cavity, coupling antennas, and metamaterial absorbers to increase the absorbed THz radiation. On the other hand, the THz FET-based cameras measure a rectified voltage after interaction of the THz radiation with a plasma wave in the transistor channel. Theoretical works predicted both frequency-specific (resonant) and broadband (non-resonant) detection mechanisms, which have been used to describe the behavior of THz-FET detectors of a variety of materials, ranging from III–V semiconductors to graphene layers. The silicon FET is an attractive candidate for THz cameras, since it is compatible with CMOS process technology, therefore enabling scaling into high-resolution arrays at reduced costs.

At the same time, we have emphasized that single-pixel detectors can be efficiently used for fast acquisition of THz images within the framework of fast mechanical steering and computational imaging. Mechanical beam-steering with oscillating mirrors and f-theta lenses allow rapid image acquisition using a conveyor belt arrangement, while a Gregorian reflector

system can be used to construct an image at stand-off distances for security applications. Furthermore, in recent years, there were substantial developments in computational imaging, leading to a plethora of single-pixel imaging techniques that allow image reconstruction from a series of judicially designed singlepixel spectroscopic measurements. Thus, one can reconstruct an image by performing a series of single-pixel measurements with a series of aperture masks that partially conceal the image. By using the sparsity property of natural images, compressive sensing can reduce the number of measurements well below the limit imposed by the Nyquist theorem, resulting in reduced time acquisitions. By using SLM and advanced mask encoding methods, real-time THz single-pixel imaging is within reach, even in the near-field imaging context. Finally, taking advantage of the relationships between time and space, the spatial information about an object can be encoded in the spectrum or in the temporal waveform, using blazed diffraction gratings, specially designed metasurfaces of beam-splitting devices. Finally, by using the principles of Fourier optics with broadband pulses, the spatial frequency information about the imaged object can be efficiently reconstructed from the spectral data recorded in the k-space, thus leading to fast Fourier optics image modalities.

We would like to note that the three major research directions that we have reviewed in this work are not necessarily in direct competition with one another, nor are they mutually exclusive. In fact, they can profit from each other via the development of hybrid systems. For example, intensity-sensitive THz cameras are important for various applications where object differentiation via simple absorption is prevalent. At the same time, phase-sensitive THz-TDS imaging is of great importance for material characterization and finer measurements of local changes in material physical properties. At the same time, the hardware and computational techniques developed within the single-pixel imaging modality can be considerably enhanced or sped up by substituting single-pixel detectors with THz detector arrays.

To summarize, in this work, we presented a critical and comprehensive review of enabling hardware, instrumentation, algorithms, and potential applications in realtime high-resolution THz imaging. We believe that this review can serve a diverse community of fundamental and applied scientists as it covers extensively both practical aspects of imaging system designs, as well as fundamental physical and mathematical principles on which such designs are based. Finally, many practical applications of the imaging systems were presented, making this review of interest to a wider audience.

Funding. Canada Research Chairs I of Prof. Skorobogatiy in Ubiquitous THz photonics; Canada Foundation for Innovation (CFI); Natural Sciences and Engineering Research Council of Canada (NSERC); Fonds de Recherche du Québec—Nature et Technologies (FRQNT).

CHAPTER 3 GENERAL EXPERIMENTAL METHODOLOGY

In this chapter, we describe the general experimental methodology of our thesis and discuss how the following chapters are linked to it. We start by discussing the imaging system that we built, and we show how it unifies the imaging experiments performed during this thesis. We then discuss various fabrication technologies that we experimented throughout the thesis. Finally, we relate the following chapters to the experimental methodology described.

3.1 Fiber-coupled THz Time-domain Spectroscopy Imaging System

Our first major accomplishment was to design and build a fiber-coupled THz time-domain spectroscopy (THz-TDS) system. This system is used in the following chapters to obtain spectral amplitude and phase images. THz-TDS was explained in Section 2.3 of the literature review. In this section, we discuss specifically the one we designed [Fig. 3.1].

We use a Ti:Sapphire laser (Spectra-Physics Mai Tai, 100 fs, 800 nm, 100 MHz, up to 3 W) as an ultrafast laser source to optically pump emitter and detector antennas. To control the amount of power going in the emitter and detection lines, we use a combination of a half-wave plate and a polarizing beam splitter. As we discussed in Section 2.3.1.1, the polarization of the optical pump does not impact the emission/detection characteristics of the antennas.

Emission path: On the emitter side, a linear optical delay line is placed prior to a high-power interdigitated antenna (BATOP Gmbh, iPCA-21-05-1000-800h). This antenna is made of multiple pairs of parallel interdigitated electrodes, and can support high optical powers (up to 3 W), due to its large excitation area (1 mm^2). A lens array focuses the optical beam into multiple dipoles, each constructively interfering in the far field for high power THz emission. The emitter is supplied with a 5 kHz sine voltage of 15 V peak-to-peak. This electrical signal also acts as the reference in the lock-in amplifier as discussed below.

Detection path: On the detection side, to allow convenient mechanical scanning for imaging, we made our own fiber-coupled THz detector using a THz photoconductive antenna (Menlo-systems, Tera 8-1). In particular, the optical beam is first focused into a 2 m polarization-maintaining optical fiber with the input end rigidly fixed on the optical table, while the output is fixed in a fiber coupler mounted on a 300 mm-3D micropositioning stage (Thorlabs, LTS300). At the output end, the beam is collimated in air before exciting the detection antenna with 10 mW of optical power.

On the detection arm, the optical fiber adds positive group-velocity dispersion (GVD) to the

pulse, leading to a non-negligible pulse broadening that reduces the detector's THz bandwidth. Therefore, before focusing into the fiber, the optical pulse passes first through a dispersion pre-compensation system made of two diffraction gratings and a mirror. This system adds negative GVD to the pulse as detailed in [407]:

$$GVD[\mathrm{s}^2] = -\frac{\lambda^3 d}{\pi c^2 \Lambda^2}\left[1-\left(\frac{\lambda}{\Lambda}-\sin\theta\right)^2\right]^{3/2} \tag{3.1}$$

where λ is the central wavelength, c is the speed of light, Λ is the groove distance of the gratings, d is the distance between the gratings and θ is the incident angle defined in Fig. 3.1(b). By adjusting the geometrical parameters d and θ it is possible to balance the positive GVD of the fiber, and therefore minimize the pulse duration at the fiber output. In Fig. 3.1(c), we present several autocorrelation traces of the pulse for different values of d, measured at

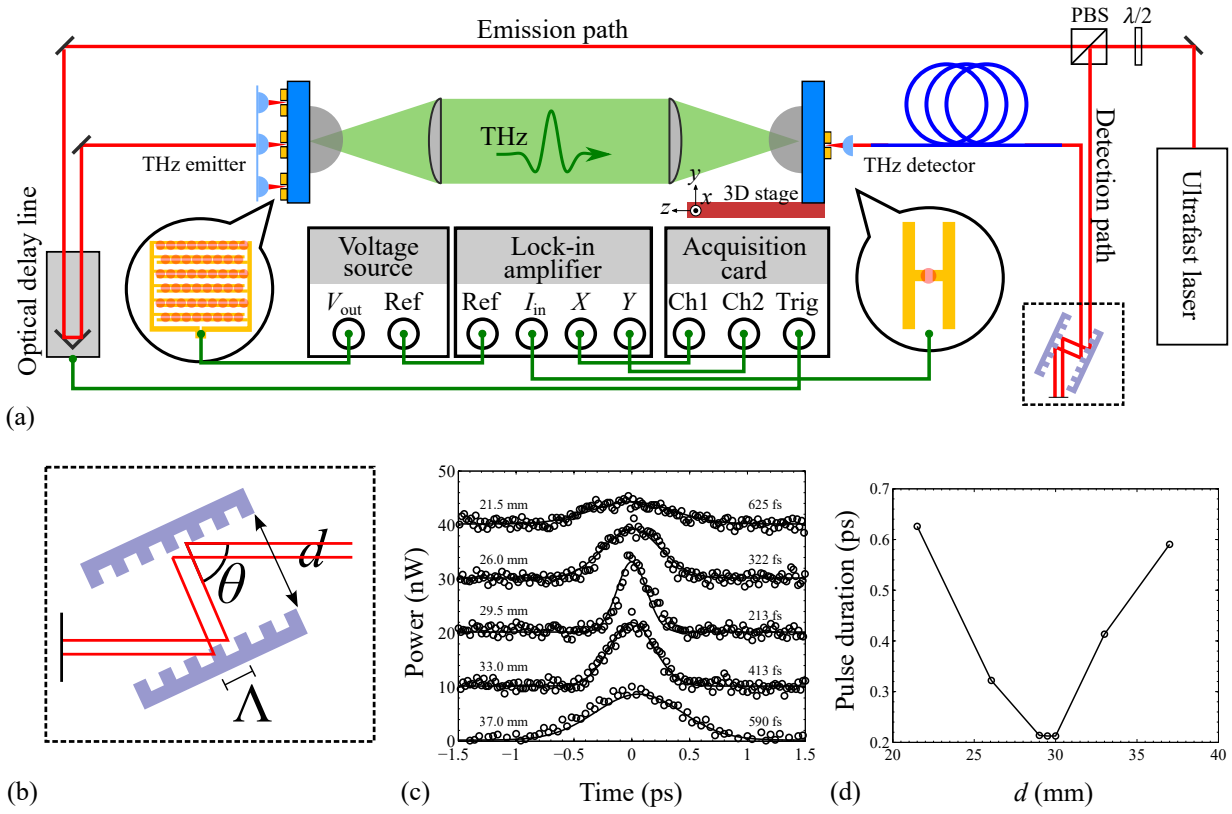

Figure 3.1 (a) Experimental setup depicting the fiber-coupled THz time-domain spectroscopy imaging system. The red line refers to the free-space beam, while the blue line is the optical fiber. (b) Dispersion compensation system with two diffraction gratings and a mirror. (c) Autocorrelation traces for different distances d between the mirrors. (c) Pulse duration (full width at half maximum) as a function of d.

the output of the optical fiber using an autocorrelation system (Newport, LSA-MT-KT). The pulse duration is minimized to 213 fs when the two gratings are separated by 29.5 mm [Fig 3.1(d)]. We note that the compensation system only corrects for positive GVD, while negative GVD (caused by the third order dispersion and/or non-linear effects) still occurs in the fiber. Therefore, we still have a pulse broadening from 100 fs to 213 fs. We mention that in principle one could use a dispersion compensation fiber at 1550 nm since THz emitters and detectors are commercially available at that wavelength. In our case, we wanted to use the high power 800 nm laser at at our disposal.

Measurement: The output photocurrent of the detection antenna is amplified with a lock-in amplifier (Stanford Research Systems, SRS830), with the reference being the sine voltage supplied on the THz emitter. Using an acquisition card (National Instruments, NI PCI-4472), we collect the two analog outputs of the lock-in amplifier corresponding to the quadrature components (X and Y) of the detected current referenced to the emitter signal.

As we mentioned earlier, the measured current is directly proportional to the electric field of the THz pulse [Eq. 2.22]. To obtain an electric field as a function of time, one needs to modify the time delay between the optical pulse and the THz pulse, both incident on opposite sides of the detector antenna. In this thesis, we used a 220 mm linear optical delay line (Thorlabs, DDS220) able to provide up to 1466 ps of time delay with ± 2 μm absolute on-axis accuracy. These values corresponds to a spectral resolution of 0.68 GHz and a maximum frequency of 37.5 THz, both appropriate for our THz spectra.

The acquisition of the THz pulse is triggered by the movement of the optical delay line. We set the digital output of the delay line controller (Thorlabs, BBD201) to deliver a 5 V signal when the delay line reaches a stable speed and 0 V in the acceleration and deceleration phases. We then use this signal to trigger the beginning of the measurement directly in the acquisition card. This way, instead of performing a lengthy step-by-step scan (that can take several minutes), we instruct the delay line to directly move at full speed to a given position. With this method, a THz pulse can be acquired in only 2-3 seconds.

The user specifies an acquisition rate f_{acq} and a stable speed on the delay line v. Assuming N measured data points, we deduce the total distance at stable speed:

$$\Delta z = \frac{N}{f_{\text{acq}}} v \tag{3.2}$$

The total optical delay is then calculated with

$$\Delta t = \frac{2\Delta z}{c} \tag{3.3}$$

with c the speed of light. The maximal THz frequency is then given by:

$$\nu_{\max} = \frac{f_{\text{acq}} c}{4v} \tag{3.4}$$

These formulas have been experimentally verified by noting that the water absorption peaks are correctly positioned in the resulting spectrum (for example at 0.55 THz, see Fig. 2.2).

A standard imaging goes as follows. First, the user sets the start and end positions of the x and y stages as well as the corresponding step sizes (for 3D imaging, z coordinates can also be specified). The user also indicates the start and end positions of the delay line. The software then instructs the 2 axis to move to the specified spatial positions. For each position, the delay line moves and reaches a stable speed, triggering the data acquisition. Each position is then saved in a text file consisting of two columns (quadrature components X and Y) of N data points. From N, we deduce the time and frequency vectors (following equations above). Using specific Matlab routines, we open, read the individual text files and allocate them in a specific 3D matrix related to the x, y and t (time) coordinates. Generally, a Fourier transform is calculated in the temporal dimension for spectral amplitude and phase imaging.

3.2 Advanced Manufacturing Techniques for the Terahertz Range

THz wavelengths being relatively large (few hundreds of micrometers to few millimeters), there is an interesting potential to use innovative prototyping techniques that are not even considered for optical applications. Indeed, using these techniques, one can easily get sub-wavelength surface roughness ($\sim \lambda/5$ to $\lambda/10$). In this section, we briefly describe the fabrication techniques that we have used throughout the thesis. Many of these techniques have already been vastly adopted in the literature (for example fused deposition modeling), while others, to the best of our knowledge, were rarely used.

Fused deposition modeling (FDM) is perhaps one of the most known additive manufacturing technology. Also simply referred to as 3D printing, in this technique, a polymer filament (for example polyactic acid, PLA) is brought to a temperature close to its melting point and passes through an extruder nozzle. Mounted on a 3-axis stage, this extruder moves and the filament is deposited layer by layer to construct the 3D object. The nominal resolution of FDM is mainly dictated by the extruder nozzle size (in our case 0.4 mm). We used this technique to fabricate optical components when working at low THz frequencies. For example, in Chapter 6, we made phase masks for 320 GHz ($\lambda \sim 0.97$ mm) [Fig. 3.2(a)]. We also extensively used this technique to fabricate optomechanical components (for example holders).

Stereolithography (SLA) is an additive manufacturing technique based on the ultraviolet curing of photopolymer resin. Initially liquid, this resin is poured in a receptacle capable of moving in the vertical direction. Beneath the resin, a UV laser projects an image corresponding to the axial slice of the 3D object, which in turn solidifies the photopolymer through a chemical reaction. The receptacle then moves vertically and the object is printed layer by layer. After the printing, the obtained 3D object must be washed with an isopropanol solution. This removes the unreacted resin. Optionally, an additional UV curing can be performed to further solidify the object. The resolution of SLA being high (~ 50 μm), it is commonly used in the dentistry and jewelery industries. We used this technique in Chapter 5 to fabricate phase image phantoms [Fig. 3.2(b)].

Computer numerical control (CNC) machining is a subtractive manufacturing technology in which a spindle mounted on motorized multi-axis stages removes material from a base substrate. Most CNC machines have at least 3 axis, with some having a fourth one which rotates the object. Depending on the CNC machine, the base material can be polymer, wood, metal, glass etc. The resolution of the fabricated object depends mainly on the drill size, but also on other parameters such as the thermal properties of the material, the vertical

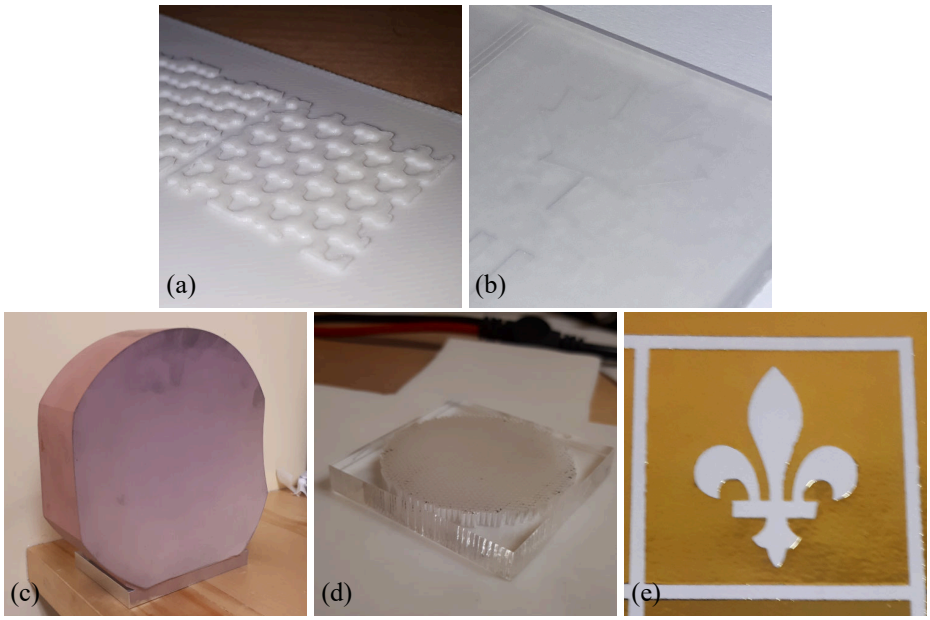

Figure 3.2 Various examples of samples fabricated using advanced fabrication technologies. (a) Fused deposition modeling of a phase mask used in Chapter 6. (b) Steoreolithography of a phase phantom used in Chapter 5. (c) CNC machining of a parabolic mirror metalized with silver aerosol paint. (d) Laser cutting of a planar porous lens used in Chapter 4. (e) Metal transfer using toner used to create a metal phantom used in Chapter 6.

and horizontal cutting speeds and so on. This technique can also produce smooth curved surfaces by using ball drill bits. For example, we fabricated curved THz parabolic mirrors that we metalized with silver-based aerosol paint [Fig. 3.2(c)].

Laser cutting is a subtractive manufacturing technique that uses a laser mounted on a 3-axis stage to cut and/or engrave materials. Depending on the laser, it can be used on a variety of materials from polymers to metals and glasses. Here, the resolution is mainly limited by the beam spot size, but it is also greatly affected by the thermal properties of the material, the laser power, wavelength and repetition rate, the cutting speed, etc. The porous components that we fabricated in Chapter 4 were made using this technique [Fig. 3.2(d)].

Metal transfer using toner is a very simple technique that we discovered around the end of our thesis. It allows to fabricate metallic features directly on a paper substrate using a special metal foil deposited on a thin layer of thermoplastic. The design is first printed on a paper with an office laser printer. The metallic foil is then placed on top of the print and both of them pass through a laminator. Due to heating, the toner and thermoplastic bond together, leading to a direct imprint of the metal layer on top of the printed design. Here, the resolution depends mainly on the resolution of the printer (measured in dots per inch, dpi). The quality of the paper is also important, as a smoother paper ensures a better transfer on the paper. At the end of our thesis, we fabricated THz polarizers by printing several parallel lines, and we confirmed that they worked as intended. We also used this technique to fabricate binary metal masks in Chapter 6 [Fig. 3.2(e)].

3.3 Organization of the Articles and Relations to the Methodology

The three following chapters are the core of this thesis as they present our original contributions to the problem of real-time THz imaging. Here, we briefly introduce them while presenting their relations to the experimental methodology discussed in this chapter.

In **Chapter 4**, we develop low-loss THz components using porous media (sub-objective 1). These components can be used to reduce the overall losses of imaging system, which in turn may reduce acquisition times. Using the Bruggeman model of effective media, we show that by using low-refractive index subwavelength inclusions (air holes) in a solid dielectric material, we can design optical components with smaller losses than their all-solid counterparts. In particular, we fabricate a porous planar lens and a porous orbital angular momentum (OAM) phase plate using laser cutting in a PMMA substrate. We study their effects on the THz beam and we demonstrate that they are functioning as intended. For that purpose, the porous components were positioned in the THz path and our fiber-coupled THz-TDS system

was used to obtain intensity images for the porous lens (by squaring the electric field), and amplitude and phase images for the porous OAM plate (at the designed frequency of 140 GHz) [Fig. 3.3(a)].

In **Chapter 5**, we use spectral encoding of the spatial frequency (k-space) to reconstruct an image using very few measurements (sub-objective 2). Since the spatial frequency is proportional to the THz frequency, we demonstrate that we can construct the k-space by measuring spectra at specific positions along a circular path in the Fourier plane. We study amplitude and phase objects and we show in both cases how to handle and interpret the measurements. These objects were fabricated using CNC machining followed by metalization (amplitude object) and stereolithography (phase object). They were positioned at the back-focal plane of a circular lens and the fiber-coupled detector scanned amplitude and phase spectra on a circle in the front-focal plane (Fourier plane) [Fig. 3.3(b)].

In **Chapter 6**, we implement super-resolution for subwavelength THz imaging (sub-objective 3). Super-resolution optical microscopy techniques are diverse computational techniques used in the visible range. Taking advantage of the statistical and localization properties of fluorophores, they are used to construct high resolution images from a collection of frames. We propose to use amplitude and phase modulation at a subwavelength scale to mimic the blinking behavior of the fluorophores. In our work, amplitude masks were made using the metal transfer with toner, while phase masks were 3D printed with fused deposition modeling. Our theory is based on the linear equation of imaging systems which simply states that the image is a convolution of the object with the point spread function. Therefore, many imaging experiments could have been applied to demonstrate our super-resolution technique. Here, we used a more conventional approach by fixing the detector and scanning the object at the focal plane of a pair of parabolic mirrors [Fig. 3.3(c)].

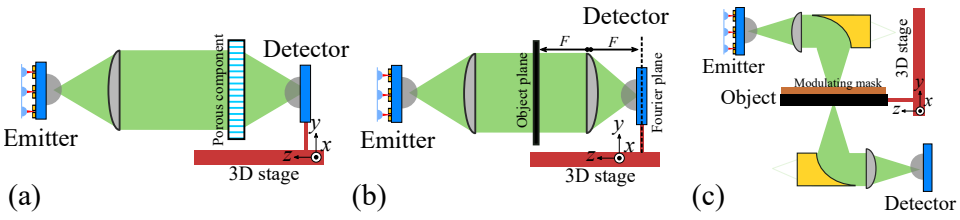

Figure 3.3 Specific experimental setups used in the following chapters. (a) Chapter 4: the porous components are positioned in the THz beam and their effects are studied by a fiber-coupled THz-TDS detector. (b) Chapter 5: the object is placed at the back-focal plane of a lens and the detector moved along a circular path in the front-focal plane (Fourier plane). (c) Chapter 6: both emitter and detector are fixed while the object and the modulating masks are scanned in the focal plane of a pair of parabolic mirrors.

CHAPTER 4 ARTICLE 2: PLANAR POROUS COMPONENTS FOR LOW-LOSS TERAHERTZ OPTICS

Hichem Guerboukha[1], Kathirvel Nallappan[1,2], Yang Cao[1], Mohamed Seghilani[3], José Azaña[3], and Maksim Skorobogatiy[1]
[1]Génie physique, Polytechnique Montréal
[2]Génie électrique, Polytechnique Montréal
[3]Centre ÉMT, Institut national de la recherche scientifique
Advanced Optical Materials, vol. 7, no. 5, p. 1900236 (2019)

Abstract: There is a strong interest in using the terahertz (THz) frequency band for applications in sensing, imaging, and wireless communications. To enable many of these applications, compact low-loss components for beamforming are required. Typically, such components are made using solid dielectric elements with spatially variable thickness, for example, planoconvex lenses or spiral phase plates. However, as losses in dielectrics typically greatly increase with THz frequency, so do the losses of the solid components. This work demonstrates that when introducing low-refractive index, low-loss subwavelength inclusions (air holes) into a solid material matrix, the loss of porous components can be greatly reduced compared to the loss of solid components with otherwise identical optical properties, thus opening a way to create efficient optical components even with nominally high-loss materials. Additionally, porous optical components can be created completely flat as spatially dependent optical path difference is achieved by varying the local porosity rather than the component thickness. This offers additional advantages for free-space alignment and integration of such components into optical systems. As an example, the design, fabrication, and experimental characterization of planar lenses and planar orbital angular momentum phase plates are carried out. It is then demonstrated how these porous components outperform their all-solid counterparts.

4.1 Introduction

Recently, there has been a strong interest in using the terahertz (THz) frequency band (from 100 GHz to 10 THz, wavelengths of 3 mm to 30 μm) for various applications in sensing [211] imaging [15] and wireless communications [408]. To enable many of these applications, low-loss beamforming components, such as lenses, polarizers, phase plates, beam steerers, etc., are needed [409]. Such devices generally operate by spatially modifying the phase of the incident plane wave. For example, for thin optical components located in the plane (x, y) made of an optically uniform material of refractive index (RI) n and with a spatially dependent thickness

$h(x, y)$, the local phase incurred by the wave due to the passage through the component is given by

$$\phi(x, y) = \frac{2\pi}{\lambda} n \cdot h(x, y) \tag{4.1}$$

where λ is the wavelength of light. Thus, by judiciously designing the component thickness $h(x, y)$, the wavefront of the planewave can be modified at will. For example, in simple convex dielectric lenses, the lens thickness is varied quadratically with the distance from the lens center which allows focusing of parallel beams. In the THz range, commercial lenses are available with materials such as TPX (polymethylpentene), PTFE (Teflon), and high-density polyethylene (HDPE). However, for dielectrics in general, the absorption losses increase quadratically with the frequency. For example, one of the lowest loss commercial materials—TP features a power absorption coefficient of ≈ 0.2 cm^{-1} at 0.5 THz, while it increases to ≈ 0.7 cm^{-1} at 2 THz. Alternatively, PTFE and HDPE are other popular materials with power absorption coefficient of ≈ 1.5cm^{-1} and ≈ 2.1cm^{-1} at 0.5 THz, respectively, and ≈ 2.5cm^{-1} at 2 THz [410,411]. Therefore, the conventional approach of designing beamforming components with variable thickness profile becomes challenging when increasing the THz operation frequency.

To overcome the loss challenge, one can use thinner optical components. Particularly, since the phase in Eq. 4.1 can be reduced (wrapped) into a $(0, 2\pi)$ interval, one can design thinner components with saw-like profiles that will have very similar performance to the components with a full (unwrapped) phase profile given by Eq. 4.1 [412, 413] However, these types of lenses— also known as Fresnel lenses—tend to show narrowband operation because of the chromatic dispersion of the underlying dielectric materials, and as a consequence, necessity of using different saw-like dielectric profiles at different frequencies.

Another method to design beamforming components is based on gradient index (GRIN) optics, which utilizes a nonuniform spatial distribution of the RI $n(x, y)$ with a fixed thickness h to modify the local phase incurred by the wave

$$\phi(x, y) = \frac{2\pi}{\lambda} n(x, y) \cdot h \tag{4.2}$$

Such components can be realized using metamaterials that consist of metals or dielectrics resonators engineered at a wavelength or subwavelength scale and patterned to produce an RI distribution at a larger scale [394]. Thanks to the micrometer scale of the THz wavelength, THz metamaterials are easier to manufacture in the THz band than in the visible range. Re-

cently, several designs of metamaterial beamforming devices have been proposed for the THz range, including lenses [414–419], deflectors [420–422], polarization controllers [423], orbital angular momentum phase plates [424] beam splitters [425] etc. Typically, these metamaterial devices function via a resonant mechanism that can lead to high ohmic losses in metallic metamaterials, as well as relatively narrowband operation.

Alternatively, one can use structured materials with spatially nonuniform distribution of deep subwavelength inclusions to design effective materials with spatially variable RI. In this case, effective medium theories can be used to predict structured material RI and losses. For example, this methodology was successfully employed in the THz frequency band to design lowloss porous waveguides [96, 97, 426–429] with elongated subwavelength air inclusions in a waveguide dielectric matrix. This type of structure was also used by Park *et al.* and Brincker *et al.* [430, 431] to design compact porous lens to replace the traditional hyperhemispherical lens of THz photoconductive antennas. In these works, silicon was chosen as the bulk medium due to its very low losses and dispersion in the THz range as well as its compatibility with GaAs growth process.

In this work, by extending this idea further, we show that using porous materials (with subwavelength porosity), it is possible to design low-loss THz bulk components even with nominally high-loss bulk materials. More importantly, we demonstrate that, for the same base material, porous optical components outperform their all-solid counterparts in terms of losses, while having otherwise identical optical characteristics. This is a nontrivial finding as porous materials tend to have lower refractive indices than their solid counterparts, therefore, to achieve identical optical characteristics, porous optical components tend to be thicker than the solid ones. Nevertheless, we find that with increased porosity, reduction in the porous material refractive index is less pronounced than reduction in the effective material loss, which is due to field enhancement inside of the low-RI, low-loss subwavelength inclusions. We believe that this work paves a way for building novel low-loss bulk and freeform optical components from otherwise high-loss functional materials (ultrahigh dielectric constant materials, highly dispersive materials, etc.), which is of great importance for many practical applications in THz imaging and communications.

As follows from the effective medium model within the Bruggeman approximation [428], when introducing zero-loss low-RI subwavelength air inclusions, the structured material losses reduce much faster with the porosity than the real part of the effective material RI. Thus, using the same dielectric base material, one can design porous materials that result in identical phase change [see Eq. 4.2] as that given by the solid materials [see Eq. 4.1], while having considerably lower absorption losses than their solid counterparts.

In this work, we first use the effective medium theory and finite element calculations to design several planar porous optical components that include a lens and an orbital angular momentum (OAM) phase plate and show that their losses are lower than those of their all-solid counterparts. We then fabricate these components using laser cutting technique (subtractive manufacturing). Finally, we characterize the fabricated component optical properties and compare them to the theoretical predictions. This paper is structured as follows. First, in Section 4.2, we present the numerical design of the low-loss THz components. Then, in Sections 4.3 and4.4, we fabricate and characterize the planar lens and the OAM phase plate, respectively. In particular, OAM is a well-established property of light that manifests itself as a helical wavefront with an azimuthal phase term. OAM states have been recently explored as additional spatial division multiplexing (SDM) technique for wireless communications [432–434] and are therefore of particular interest in the THz range.

4.2 Design of Low-loss Porous THz Components

The planar porous components considered in this work are designed by varying the local effective RI via introduction of low-RI subwavelength inclusions (n_a, for example air) into the higher RI host material (n_m). When the inclusion size is smaller than the wavelength of light, the THz wave will experience an effective material RI n_{eff} with a value bounded between n_a and n_m. Experimentally, air inclusions can be formed either by using additive manufacturing techniques such as 3D printing, or subtractive techniques such as CNC drilling or laser cutting. Within this work, we explore laser cutting technique for the fabrication of planar porous components with inclusions in the form of cylinders of subwavelength diameter [see Fig. 4.1(a)].

To model the complex effective RI of such materials, we first use Bruggeman model, which allows us to derive several simple analytical expressions for material RI and losses in the limit of high porosity. We then confirm the validity of the Bruggeman model by comparing its predictions to the effective RI and losses extracted from guided wave simulations in the infinitely periodic media with cylindrical inclusions performed using finite element COMSOL software.

In the following derivations, we assume that subwavelength inclusions are loss-less and made of air, with the correspondent dielectric permittivity

$$\varepsilon_a = n_a^2 = 1 \tag{4.3}$$

At the same time, we assume that the host material is lossy and characterized by the power

absorption coefficient α_m, meaning that the power decay with propagation distance is $\propto \exp(-\alpha_m z)$. This also means that the host material can be described by the following complex dielectric permittivity

$$\varepsilon_m = (n_m + ik_m)^2 = \left(n_m + i\alpha_m \frac{\lambda}{4\pi}\right)^2 \tag{4.4}$$

where n_m and k_m are the real and imaginary parts of the material RI. Using the Bruggeman model for cylindrical inclusions [428]

$$f\frac{\varepsilon_a - \varepsilon_{\text{eff}}}{\varepsilon_a + \varepsilon_{\text{eff}}} + (1-f)\frac{\varepsilon_m - \varepsilon_{\text{eff}}}{\varepsilon_m + \varepsilon_{\text{eff}}} = 0 \tag{4.5}$$

we can express the transverse component (with respect to the axis of the cylindrical inclusions) of the effective permittivity as

$$\varepsilon_{\text{eff}} = \sqrt{\left(\frac{1}{2} - f\right)^2 (\varepsilon_a - \varepsilon_m)^2 + \varepsilon_a \varepsilon_m} - \left(\frac{1}{2} - f\right)(\varepsilon_a - \varepsilon_m) \tag{4.6}$$

where f is the filling fraction of inclusions by area. From this expression, we can now define the real n_{eff} and imaginary k_{eff} parts of the porous component effective RI, as well as its effective absorption coefficient by power α_{eff} by noting that

$$\varepsilon_{\text{eff}} = (n_{\text{eff}} + ik_{\text{eff}})^2 = \left(n_{\text{eff}} + i\alpha_{\text{eff}} \frac{\lambda}{4\pi}\right)^2 \tag{4.7}$$

It is important to reiterate that the Bruggeman model [Eq. 4.5] gives an effective value of the transverse component of the material dielectric permittivity tensor. Therefore, when using only this value for the material effective permittivity, one assumes that the electromagnetic field vector in the medium is directed mostly perpendicular to the axis of the cylindrical inclusions. This is indeed correct within the paraxial approximation, which holds in our case when manipulating collimated beams (propagating along the inclusion axis) using flat optical components. If the direction of wave propagation in angled with respect to the cylinder axis of the holes, the porous component may exhibit birefringence. However, in the following theoretical analysis and experimental demonstration, the incident wave is perpendicular to the input plane of the optical component, and, therefore, the wave travels parallel to the cylinder axis inside the component. Therefore, in this arrangement, the optical components are not polarization sensitive. Moreover, if in place of arrays of cylindrical inclusions produced by laser cutting one would use arrays of cubic or circular inclusions produced by 3D

printing, the resultant porous materials will be nonbirefringent regardless of the direction of the propagating wave. In general, propagation through media with aligned cylindrical inclusions must be considered in the framework of anisotropic materials with distinct transverse and longitudinal values of the effective dielectric permittivity tensor.

In the limit of high porosity $f \to 1$ (high air filling fraction by area), from Eq. 4.6 we can derive the following asymptotic expressions for the complex effective RI of the medium (see Appendix A.1 for details)

$$n_{\text{eff}} = \text{Re}\{\sqrt{\varepsilon_{\text{eff}}}\} \approx n_a + (1-f)\frac{n_m^2 - n_a^2}{n_m^2 + n_a^2} n_a \tag{4.8}$$

$$\alpha_{\text{eff}} = \frac{4\pi}{\lambda}\text{Im}\{\sqrt{\varepsilon_{\text{eff}}}\} \approx \alpha_m \frac{4(1-f)n_a^3 n_m}{(n_m^2 + n_a^2)^2} \tag{4.9}$$

As we can see from Eq. 4.9, effective material losses can be reduced by using high fraction of the loss-less inclusions, as well as by choosing high RI contrast between the host material and that of the subwavelength inclusions. The latter is easy to understand by looking at the field distribution in the porous materials [see Fig. 4.1, inset in (b)]. There we observe a strong presence of the electric field in the low-loss material (hole). This is due to the continuity of the normal component of the displacement field across the interface, thus resulting in the electric field enhancement in the air hole compared to that in the host material $E_a \propto E_m \varepsilon_m / \varepsilon_a$ [435]. As we will see in what follows, it is this enhanced field presence in the low-loss subwavelength inclusions that allow designing porous optical components with lower losses compared to their solid counterparts with otherwise identical characteristics.

In Figs. 4.1(b) and (c), we compare the predictions of the Bruggeman model for the complex effective RI of the structured material with the numerical results obtained using the guided wave module of the finite element method (FEM) COMSOL Multiphysics software. In our simulation, we used a hexagonal periodic lattice (interhole spacing) of $\Lambda = 952\mu m$ with periodic boundary condition at the boundaries of the hexagonal cell [Fig. 4.1(a)], while varying the filling fraction and the frequency of the guided THz wave. Host material complex RI was taken as $\tilde{n}_m = n_m + ik_m = 1.61 + 0.0085i$ which corresponds to that of a PMMA (acrylic) at 150 GHz—a material that is typically used in laser cutting. This value, which is consistent with the literature [436], was experimentally found with a THz continuouswave (CW) spectroscopy system using a solid PMMA discussed later in the section. In Figs. 4.1(b) and (c) we present the dependence of the real and imaginary parts of the effective RI as a function of the filling fraction and THz frequency. As expected, we observe that the Bruggeman model (dotted line) becomes equivalent to the numerical calculations in the limit

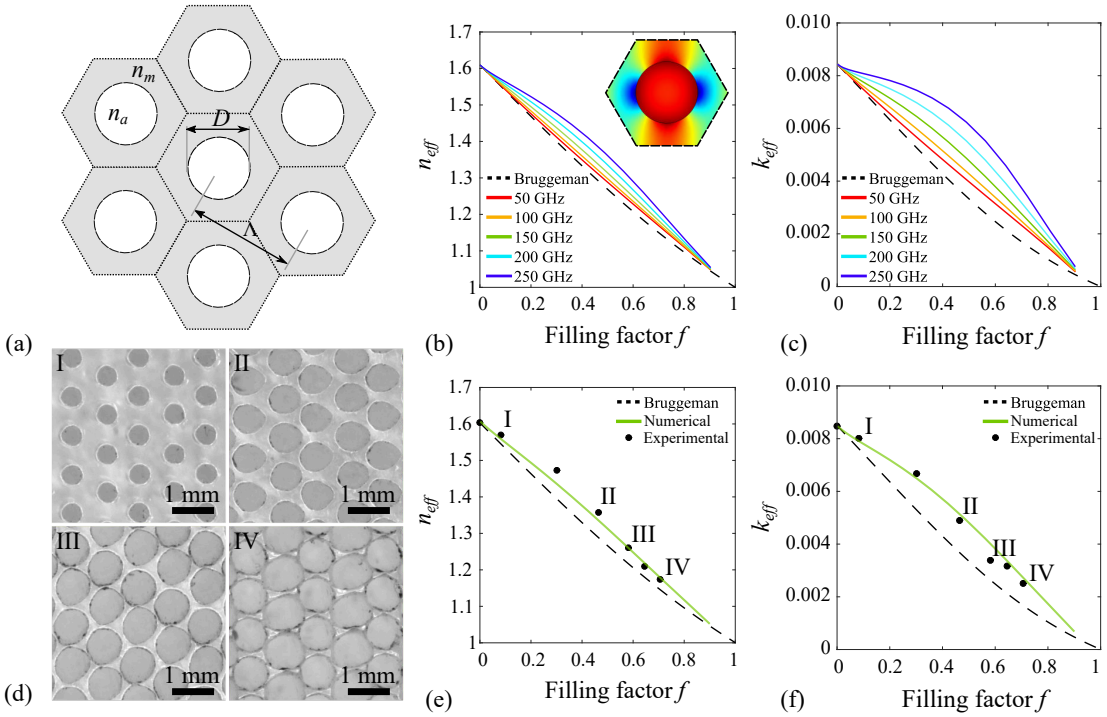

Figure 4.1 (a) Schematic of the cylinder inclusions (n_a) in a host material (n_m), with varying diameters D arranged in a hexagonal pattern of interhole distance Λ. (b) Real and (c) imaginary parts of the RI at different frequencies calculated theoretically using the Bruggeman model (dotted line) and numerically (color lines) as a function of the filling factor (by surface) of the loss-less air inclusions in the lossy host material. The inset in (b) shows the geometry of the unit cell used in the numerical simulations and the amplitude of the electric field of a typical guided wave. The periodic boundaries used in the simulation are identified by the dotted lines. (d) Microscopic images of the fabricated samples for different filling factors. (e) Real and (f) imaginary parts of the effective RI calculated theoretically using the Bruggeman model (dotted line) and numerically (green line) compared to the experimental results (black dots) at a frequency of 150 GHz.

of low and high filling fractions, and long wavelengths (low frequencies) at which the effective medium approximation is justified. In fact, at low frequencies, predictions of the Bruggeman model for the complex value of the material effective RI match well those of full simulations for any values of the filling fraction, which is mostly due to the relatively small RI contrast between PMMA and air. Interestingly, in Appendix A.2, we show that the numerical results can be fitted extremely well at all frequencies and filling fractions using a modified three component Bruggeman model.

The validity of the Bruggeman model was also verified experimentally by fabricating a series of porous plates with different air filling fractions (different hole diameters). We first experimented with additive manufacturing techniques, namely, fused deposition modeling (FDM)

and stereolithography (SLA) for the fabrication of porous components. While FDM is a single step fabrication method that requires no postprocessing, it has a limited resolution mainly dictated by the extruder nozzle size (in our case ≈0.4 mm). On the other hand, SLA can achieve much higher nominal resolutions (as low as 50 μm), however it requires a postprocessing step of removal of the unreacted photosensitive resin from the narrow cylindrical channels, which frequently results in clogging and structural deformations. Although these fabrication methods could work relatively well for millimeter-wave applications (for which the pores can be large), for application in THz, further perfecting of the FMD and SLA techniques is required to reduce the pore size and consistent feature definition. For completeness, we mention that much precise techniques such as photolithography can also be used for the fabrication of porous components via stacking of the individual plates, however such techniques are generally expensive and not easily scalable when thick 3D-structured optical components are needed.

In this work, we report using laser cutting to construct our porous components. This technology is becoming widely available thanks to its relatively low cost. It is highly precise (beam spot size ≈100 μm, positional accuracy ≈20 μm), can produce thick optical components, and even has rudimentary 3D capabilities such as cutting holes at variable angles to the normal of a surface. For laser cutters, the precision of the fabrication depends on many factors such as the power of the laser, the repetition rate, the beam spot size, the cutting speed, the number of passes, and so on. Furthermore, the mechanical and thermal properties of the material are also important parameters. In principle, the laser cutting technology can work on a variety of materials, such as polymers, woods, glasses, metals, etc.

To fabricate our porous components, we used a commercially available Trotec Speedy 300 laser engraver, which consists of a CO2 laser with a maximum power of 120 W. We chose a 5.75 mm thick PMMA plate (acrylic), which is a standard material for the laser cutting. The plates featured a hexagonal pattern of holes with the period of $\Lambda = 952$ μm (similar to the numerical simulations) and variable hole diameters [Fig. 4.1(d)]. As we will see in the following experimental demonstrations, the imperfections observed in the fabricated hole shapes and positions have little impact on the transmission properties, especially at lower frequencies. Moreover, when setting appropriate cutting laser parameters, the transmission characteristics are highly reproducible from sample to sample. The reproducibility and the robustness of the fabrication techniques are mainly due to the fact that the imperfections are deeply subwavelength, while even the imperfections themselves are reproducible from sample to sample due to high accuracy of the computer-controlled positioning system, as well as high quality of the laser used in the cutting process. To accurately determine the resulting filling fraction, we compared the weight of the porous plates with one without any hole.

The complex RI of the plates was then measured using a THz-CW spectroscopy system. A parallel THz beam was sent perpendicularly to the sample and then focused and detected using a fiber-coupled photomixer (more details about this system can be found in the work by Ma *et al.* [429]). We measured the transmitted THz amplitude and phase between 130 and 170 GHz, from which we obtained the real and imaginary parts of the RI using a measurement without any sample (reference) and the iterative algorithm described in the work by Guerboukha *et al.* [15]. We then averaged the RI in the spectral region to increase the accuracy of the measurement. In Figs. 4.1(e) and (f), we compare the experimental results with the Bruggeman model and the numerical simulation at 150 GHz. As expected, we observe that the effective complex RI of the plates follows the numerical simulations quite well.

In the following sections, we use the theoretical and experimental results presented so far for the complex RI of porous materials to design and fabricate a planar lens (Section 4.3) and an OAM phase plate (Section 4.4). These planar components were then characterized using THz imaging with a modified THz time-domain spectroscopy system, which allowed to map both the amplitude and the phase of the THz radiation at different frequencies.

4.3 Planar Porous Lenses

We now consider in more details the design of porous planar lenses and we compare their performance to their solid counterparts. We will discover that porous lenses can be designed to have much lower transmission losses than their all-solid analogues, while having otherwise identical optical properties.

For our comparison purposes, we start by designing a solid planoconvex lens with a radially symmetric thickness profile $h(r)$ as shown in Fig. 4.2(a). We assume that the lens is made of a material with real part of the RI n_m and power absorption coefficient α_m. The lens radius is taken as R and the lens front focal length as F. Assuming an incident planar wavefront, the lens thickness profile can be found by noting that the optical distance from any point on the lens input surface to the lens focal point should be the same (Fermat's principle). We therefore write for two rays, one entering at the lens periphery R and the other entering at a distance r from the lens center

$$h(r)n_m + n_a\sqrt{r^2 + (F + h(0) - h(r))^2} = h(R)n_m + n_a\sqrt{R^2 + (F + h(0) - h(R))^2} \quad (4.10)$$

Assuming that the lens radius and the lens thickness are much smaller than the lens focal

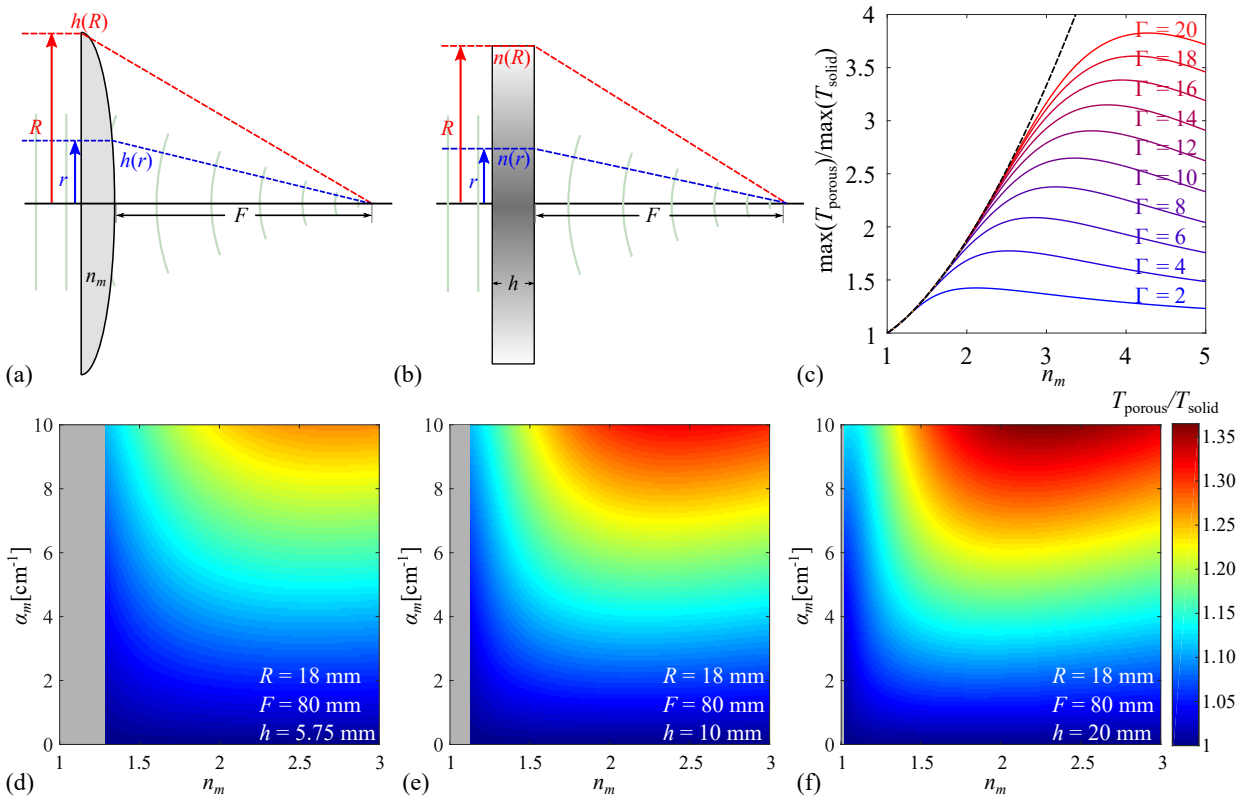

Figure 4.2 (a) Schematic of the planoconvex solid lens and (b) of the porous lens with two optical rays. (c) Analytical ratio of the transmission coefficients through the porous and solid lens as a function of the material refractive index for different $\Gamma = \alpha m R^2/2F$ as described by Eq. 4.22. When the material has very high losses ($\Gamma \gg 1$), the ratio tends to the asymptotic function defined in Eq. 4.23 (black dotted line). (d–f) Numerical ratio of the transmission coefficients through the porous and solid lens as a function of the n_m and α_m for a lens with a focal length of 80 mm and a radius of 18 mm for (d) 5.75 mm, (e) 10 mm, and (f) 20 mm. The gray areas correspond to regions where it is impossible to fabricate a porous lens with the given thickness, i.e., the condition at Eq. 4.16 is not respected.

distance $h(r)$, $F \ll R$, the equation above can be simplified to give the following lens thickness profile

$$h(r) \approx h(R) + \frac{n_a}{n_m + n_a} \frac{R^2 - r^2}{2F} \tag{4.11}$$

We can now estimate the total power transmission coefficient through the lens by integrating the transmission coefficients of the individual rays across the lens surface

$$T_{\text{solid}}^{\text{lens}} = \frac{1}{\pi R^2} \int_0^{2\pi} \mathrm{d}\theta \int_0^R r \mathrm{d}r \exp[-\alpha_m h(r)] = \frac{1 - \exp(-\xi_s^L)}{\xi_s^L} \exp[-\alpha_m h(R)] \tag{4.12}$$

where $\xi_s^L = \frac{n_a}{n_m - n_a} \frac{\alpha_m R^2}{2F}$, and $T_{\text{solid}}^{\text{lens}}$ is a monotonically decreasing function of ξ_s^L parameter.

We note that the maximal transmission through the solid lens is achieved when the lens thickness goes to zeros at the lens periphery $h(R) = 0$. In this case, we write

$$\max(T_{\text{solid}}^{\text{lens}}) = \frac{1 - \exp(-\xi_s^L)}{\xi_s^L} \tag{4.13}$$

We now design a planar porous lens and compare its losses to the solid one. In the porous lens, the thickness h of the plate is fixed, while the local RI varies according to the radial profile $n(r)$, where $n_a < n(r) < n_m$. The lens radius is taken as R and the lens front focal distance as F, which are the same as for the solid lens. As above, assuming a planar wavefront incident on the planar lens, the lens RI profile can be found by equating the optical paths for the two rays entering at the lens periphery R and at a distance r from the center [Fig. 4.2(b)]

$$h \cdot n(r) + n_a\sqrt{r^2 + F^2} = h \cdot n(R) + n_a\sqrt{R^2 + F^2} \tag{4.14}$$

Assuming that $h(r), F \ll R$, we can further simplify this equation to give the following lens RI profile

$$n(r) \approx n(R) + \frac{n_a}{h}\frac{R^2 - r^2}{2F} \tag{4.15}$$

Furthermore, since $n_a < n(r) < n_m$, there is a restriction on the minimal thickness of the porous plate for a given set of F and R. Indeed, this minimal lens thickness is given by

$$h = \frac{n_a}{n(0) - n(R)}\left(\sqrt{R^2 + F^2} - F\right) \rightarrow h_{\text{min}}^{\text{lens}} = \frac{n_a}{n_m - n_a}\frac{R^2}{2F} \tag{4.16}$$

We now turn to calculating the losses of the porous lens. Remembering that lens RI variation is enabled by controlling the local porosity of the material, then using Bruggeman approximation for the real part of the material RI [Eq. 4.8], we get the following expression for the porosity profile

$$n(r) \approx n_a + [1 - f(r)]\frac{n_m^2 - n_a^2}{n_m^2 + n_a^2}n_a = n(R) + \frac{n_a}{h}\frac{R^2 - r^2}{2F} \tag{4.17}$$

which allows us to find the corresponding air filling fraction profile

$$f(r) = 1 - \frac{1}{n_a}\frac{n_m^2 + n_a^2}{n_m^2 - n_a^2}\left[n(R) - n_a + \frac{n_a}{h}\frac{R^2 - r^2}{2F}\right] \tag{4.18}$$

Using now the Bruggeman approximation for the imaginary part [Eq. 4.9], we can now

establish the absorption profile of the porous lens

$$\alpha(r) \approx \alpha_m[1-f(r)]\frac{4n_a^3 n_m}{(n_m^2+n_a^2)^2} = \alpha_m \frac{4n_a^2 n_m}{n_m^4-n_a^4}\left[n(R)-n_a+\frac{n_a}{h}\frac{R^2-r^2}{2F}\right] \tag{4.19}$$

As previously, we can now estimate the total power transmission coefficient through the porous lens of profile $n(r)$ by the integral

$$T_{\text{porous}}^{\text{lens}} = \frac{1}{\pi R^2}\int_0^{2\pi} \mathrm{d}\theta \int_0^R r\mathrm{d}r \exp[-\alpha(r)h] = \frac{1-\exp(-\xi_p^L)}{\xi_p^L}\exp\left[-\alpha_m h \frac{4n_a^2 n_m}{n_m^4-n_a^4}(n(R)-n_a)\right] \tag{4.20}$$

where $\xi_p^L = \frac{4n_a^3 n_m}{n_m^4-n_a^4}\frac{\alpha_m R^2}{2F}$, and $T_{\text{porous}}^{\text{lens}}$ is a monotonically decreasing function of ξ_p^L parameter. The maximal transmision through the porous lens is achieved when the lens RI at the lens periphery equals that of air $n(R) = n_a$

$$\max(T_{\text{porous}}^{\text{lens}}) = \frac{1-\exp(-\xi_p^L)}{\xi_p^L} \tag{4.21}$$

By comparing Eq. 4.13 of the solid lens and Eq. 4.21 of the porous lens, we conclude that the transmission coefficient through the optimally designed porous lens is always higher than the transmission coefficient through the corresponding solid lens of identical radius and focal distance. This follows directly from the observation that $\xi_p - L < \xi_s^L$ for any value of the lens material refractive index n_m and that of the surrounding medium n_a as long as $n_m > n_a$. The effect is more pronounced for higher refractive index contrast between the two.

Interestingly, from Eqs. 4.13 and 4.21, we can now obtain an analytical expression for the ratio between the transmission coefficients through a porous lens and a solid lens

$$\frac{\max(T_{\text{porous}}^{\text{lens}})}{\max(T_{\text{solid}}^{\text{lens}})} = \frac{n_m^4-n_a^4}{4n_a^2 n_m(n_m-n_a)}\frac{\left[1-\exp\left(-\Gamma\frac{4n_m n_a^3}{n_m^4-1}\right)\right]}{\left[1-\exp\left(-\Gamma\frac{n_a}{n_m-n_a}\right)\right]} \tag{4.22}$$

with $\Gamma = \alpha_m R^2/2F$. In Fig. 4.2(c), we plot this ratio as a function of n_m for different values of Γ. As it can be observed, the ratio is greater than 1 for all values of n_m and Γ, indicating that the porous lens outperforms the solid one. In particular, in the limit of high absorption losses $\Gamma \gg 1$, one can calculate the following asymptotic result, which is represented by the dotted line in Fig. 4.2(c)

$$\lim_{\Gamma\to\infty}\left[\frac{\max(T_{\text{porous}}^{\text{lens}})}{\max(T_{\text{solid}}^{\text{lens}})}\right] = \frac{n_m^4-n_a^4}{4n_a^2 n_m(n_m-n_a)} \tag{4.23}$$

We note that the analytical ratio obtained in Eq. 4.22 is valid in the limit of high porosities

($f \to 1$). This is due to the use of the approximation of the Bruggeman model in Eqs. 4.8 and 4.9. In the following, we numerically compute the ratio of the average power transmission directly from the Bruggeman model, assuming $h(R) = 0$ and $n(R) = 1$

$$\frac{T^{\text{lens}}_{\text{porous}}}{T^{\text{lens}}_{\text{solid}}} = \frac{\int_0^R r\mathrm{d}r \exp[-\alpha(r)h]}{\int_0^R r\mathrm{d}r \exp[-\alpha_m h(r)]} \tag{4.24}$$

In this equation, $h(r)$ is obtained with Eq. 4.10. To obtain the loss profile $\alpha(r)$ for the porous lens, we first use Eq. 4.14 to obtain the real part of the planar lens refractive index profile $n(r)$. Then, using predictions of the Bruggeman model, we numerically solve the real part of Eq. 4.6 to find the corresponding distribution of the air-filling fraction $f(r)$. Finally, using the imaginary part of Eq. 4.6 with thus found $f(r)$, we find the complex value of the lens RI profile, and from Eq. 4.7, the loss profile $\alpha(r)$.

In Figs. 4.2(d)-(f), we map the ratio $T^{\text{lens}}_{\text{porous}}/T^{\text{lens}}_{\text{solid}}$ obtained numerically with Eq. 4.24 as a function of the material refractive index n_m and the absorption loss α_m, for a lens with a focal length of 80 mm, a radius of 18 mm, and thicknesses of 5.75, 10, and 20 mm. The numerical results show that this ratio is greater than 1 for all values of n_m and α_m indicating that the porous lens always outperforms (in terms of losses) the solid planoconvex lens with comparable optical properties. In particular, the overall ratio increases with the thickness of the plate, since thicker plates can be fabricated with plates with more porosity. In Figs. 4.2(d)-(f), the hatched areas indicate the regions where it is impossible to make a lens with such a value of the thickness, i.e. h is smaller than the minimal thickness stated in Eq. 4.16.

Using laser drilling in a PMMA plate of thickness $h = 5.75$ mm, we then designed and fabricated a planar lens with $F = 80$ mm and $R = 18$ mm [Figs. 4.3(a) and (b)]. The porous lens was realized by drilling holes of various diameters at the vertices of a hexagonal lattice with period $\Lambda = 952$ μm (identical to the FEM simulations). More precisely, for every vertex of a lattice, we would first find its distance r_i to the lens center. Then, using Eq. 4.15, we would calculate the desired refractive index at that position. Finally, using the FEM data for the porous material refractive index as a function of the material porosity at 150 GHz [Fig. 4.1(e)], we would find the target filling fraction and the corresponding hole diameter D_i to be placed at the vertex location.

When designing a porous lens, one can, in principle, select any value of the refractive index $n(R)$ at the lens edge in Eq. 4.15. However, to design a porous lens with minimal losses, the value of $n(R)$ has to be set as low as possible [see Eq. 4.19]. In practice, $n(R)$ cannot be equal to $n_a = 1$ simply because the filling fraction for circular holes in a hexagonal lattice is limited

to ≈ 0.91, while that in a square lattice is limited to ≈ 0.79. The maximal filling fraction is further reduced to ensure proper fabrication and mechanical stability. Experimentally, we found that a maximal value of the filling fraction for a hexagonal lattice is ≈ 0.7, which gives $n(R) \approx 1.2$ for a PMMA substrate. After fixing $n(R)$, the RI monotonically increases following Eq. 4.15 to reach its maximal value in the center of the lens $n(0) = n(R) + (n_a/h) \cdot R^2/2F$. Since this value cannot exceed the bulk refractive index of the PMMA material n_m, this sets an upper limit on the diameter and the focal length of the lens as expressed by Eq. 4.16. Typically, for shorter focal lengths, the diameter of the porous lens must be reduced. One can also increase the thickness of the planar lens to increase the overall porosity and reduce the losses.

To characterize the planar lens, we imaged the THz beam at various focal positions using a modified THz time-domain spectroscopy system with a movable detector [Fig. 4.3(c)]. This imaging system allowed us to obtain both amplitude and phase of the THz beam at different frequencies (for more details about this system, see the work by Guerboukha *et al.* [17]). We first imaged the reference beam incident on the planar lens. The intensity at 150 GHz is shown in Fig. 4.4(a). We measured a full width at half maximum (FWHM) of ≈ 45 mm,

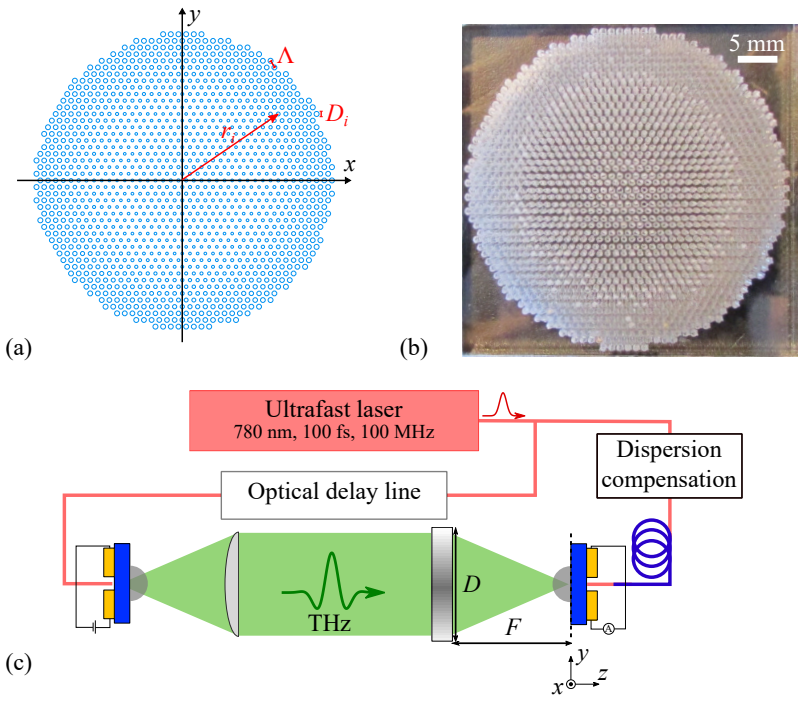

Figure 4.3 a) Design of the planar lens with the diameter of the holes varying as a function of the radius following Eq. 4.15. b) Photograph of the fabricated lens with $F = 80$ mm and $R = 18$ mm. c) Imaging system using a modified THz time-domain spectroscopy system with a movable detector.

which is larger than the porous lens diameter. This ensures that the incident beam has a uniform phase distribution. Then, we placed the planar lens and imaged the THz beam in the yz plane [Fig. 4.4(b)]. We observed that the beam was correctly focused at the focal distance F. In Fig. 4.4(c), we imaged the THz beam in the xy plane at various z positions, which allowed us to see the focusing behavior of the beam. In Fig. 4.4(d), we performed a detailed analysis of the focused beam at several wavelengths by fitting Gaussian curves in the spectral band from 75 to 300 GHz. By fitting the FWHM measured in the focal plane, we obtain

$$\text{FWHM} = 1.24\frac{\lambda F}{D} \tag{4.25}$$

which is represented by the red line in Fig. 4.4(e). The obtained fit is close to the Rayleigh criterion defining diffraction-limited focusing $\delta x = 1.22\lambda F/D$.

Even though the lens has been designed for the frequency of 150 GHz, we observe experimentally that its operational bandwidth extends from 100 to 300 GHz [see Figs. 4.4(d) and (e)]. This is in part due to the fact that the refractive index of PMMA is relatively constant in this spectral region. In the inset of Fig. 4.4(e), we plot the lens efficiency as a function of frequency obtained by dividing the detected power in the focal plane of a porous lens [Fig. 4.4(c)] by the power of the incident collimated THz beam [Fig. 4.4(a)]. The powers were calculated directly from the acquired images by summing the pixel values across the total area of the lens. For the design frequency of 150 GHz, we obtain a power transmission around $\approx 70\%$, which becomes even larger at lower frequencies.

When the frequency is increased well above the design frequency, the THz wavelength becomes comparable or smaller than the pore size, which leads to the breakdown of the effective medium theory and higher scattering losses. On the other hand, when decreasing the THz frequency, the effective medium theory (Bruggeman model) becomes even more valid [as can be clearly observed in Figs. 4.1(b) and (c)] and the designed lens operates as intended. In principle, the porous lens can be designed for any spectral region, by properly scaling the dimensions of the pores and the unit cell.

Furthermore, from Fig. 4.4(d), we observe geometrical aberrations in the focused beam at high frequencies. For example, at 250 GHz, we notice nonsymmetric side lobes of non-negligible amplitudes. Since these aberrations appear only at higher frequencies, we believe that they are due to the imperfections in the fabricated pore shapes and positions [see Fig. 4.1(d)]. However, a more detailed study is needed to evaluate quantitatively the frequency dependent aberrations of porous optical components and develop strategies to mitigate them.

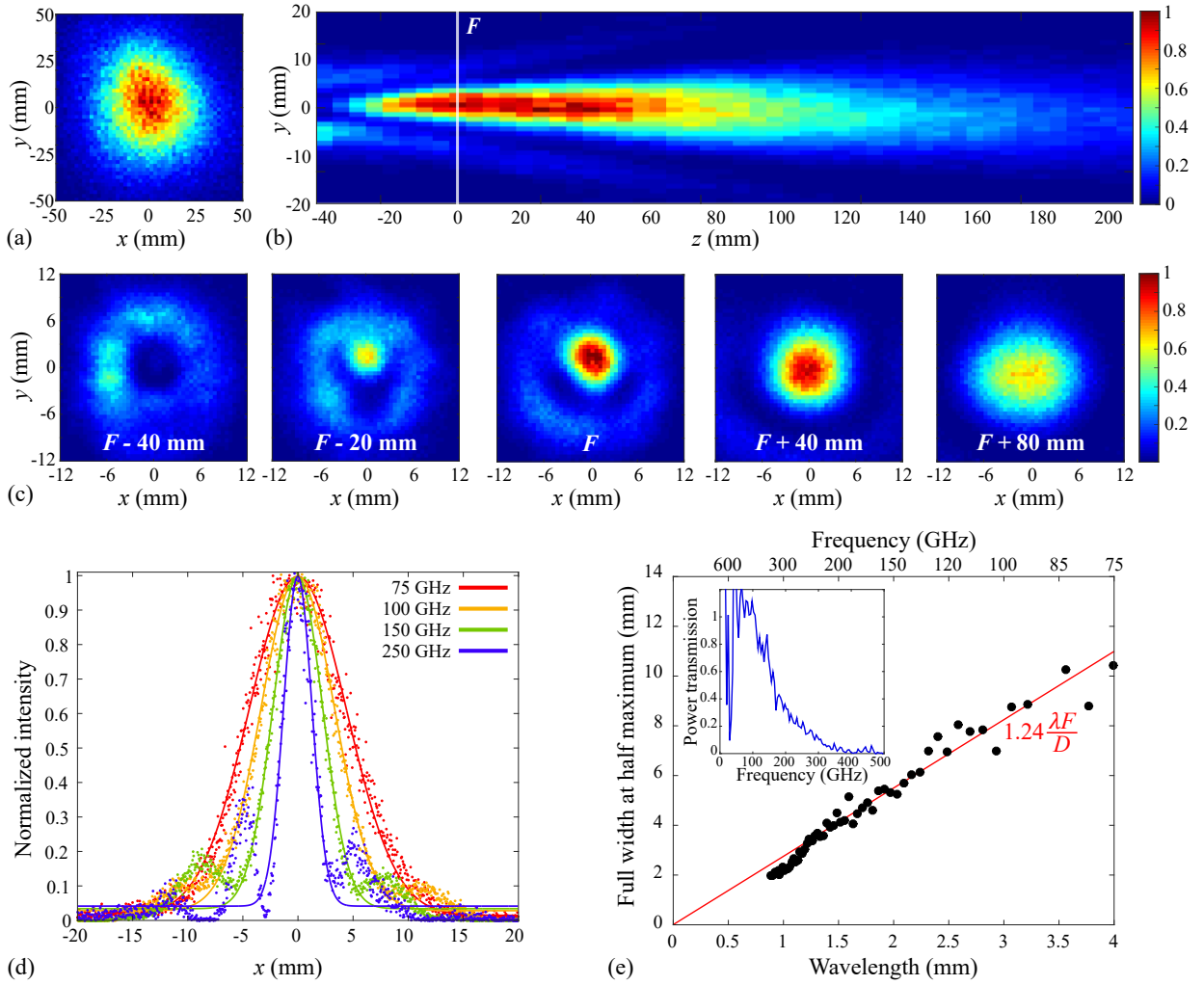

Figure 4.4 (a) Intensity of the THz beam incident on the lens at 150 GHz. b) Longitudinal intensity distribution at 150 GHz in the yz plane. (c) Images in the xy plane measured for various z positions at 150 GHz. (d) Intensity of the beam and Gaussian fit at the focal distance at different frequencies. (e) Full width at half maximum of the Gaussian fits (black dots) as a function of the wavelength. The red line corresponds to the linear fit $1.24\lambda F/D$. Inset shows the power transmission by summing the pixels value in the reference of (a) and the focal plane in (c) and taking the ratio.

4.4 Planar Porous Orbital Angular Momentum Phase Plates

In this section, using a methodology similar to previously, we present the design and fabrication of porous OAM phase plates. The OAM is a property of light which presents itself as an electric field with an azimuthal phase term $E \propto \exp(im\theta)$, characterized by the topological charge m that indicates the number of helices in a full rotation. The full expression can be obtained from the Laguerre–Gaussian decomposition with a helical phase and a donut-shaped

amplitude with a singularity in the center [437].

A simple method of generating OAM states from a planar wave is to use a spiral phase plate with a thickness that varies as a function of the angle

$$h(\theta) - h(0) = \frac{\lambda}{n_m - n_a}\frac{m\theta}{2\pi} \tag{4.26}$$

where λ is the wavelength and $h(0)$ is the thickness at the polar origin [Fig. 4.5(a)]. Our approach will be to fix the thickness h of the plate and vary the local RI as a function of the angle

$$n(\theta) - n(0) = \frac{\lambda}{h}\frac{m\theta}{2\pi} \tag{4.27}$$

where $n(0)$ is the RI at the polar origin [Fig. 4.5(b)]. Since $n_a < n(\theta) < n_m$, the minimal thickness of an OAM plate that can realize a topological charge m is

$$h_{\min}^{\mathrm{OAM}} = \frac{m\theta}{2\pi}\frac{\lambda}{n_m - n_a} \tag{4.28}$$

where we must require that $n(0) = n_a$ and $n(2\pi) = n_m$.

As it can be seen from Eqs. 4.26 and 4.27, an OAM phase profile for the topological charge m is designed for a specific wavelength. Moreover, in the absence of dispersion, the phase profile after the phase plate depends linearly on frequency [see Eq. 4.1]. Thus, at shorter wavelengths, the topological charge is no longer equal to the designed one and can even take noninteger values, meaning that the phase is making more than m turns around the origin. In particular, when the wavelength is half the designed wavelength, the topological charge of the OAM state at that wavelength becomes $2m$. Therefore, by judiciously designing the OAM phase plate, one could use the same OAM phase plate to obtain $m = 1$ at λ and $m = 2$ at $\lambda/2$, which may be useful in multiplexing multiple OAM states in a broadband spectrum.

In Appendix A.3, using a similar methodology as in the case of the porous lens, we demonstrate analytically that the porous OAM phase plate always outperforms the all-solid phase plate in terms of losses. Indeed, we arrive at the following equation for the power ratio between the transmission through a porous and a solid OAM phase plate

$$\frac{\max(T_{\mathrm{porous}}^{\mathrm{lens}})}{\max(T_{\mathrm{solid}}^{\mathrm{lens}})} = \frac{n_m^4 - n_a^4}{4n_a^2 n_m(n_m - n_a)}\frac{\left[1 - \exp\left(-\Gamma\frac{4n_m n_a^3}{n_m^4 - 1}\right)\right]}{\left[1 - \exp\left(-\Gamma\frac{n_a}{n_m - n_a}\right)\right]} \tag{4.29}$$

Remarkably, this expression is similar to the one calculated previously for the lens, where the only difference is that $\Gamma = \alpha_m m\lambda$. Therefore, the graph in Fig. 4.2(c) applies also for the

OAM phase plate, where we can observe that the ratio is always greater than 1 and increases with Γ.

As previously, to avoid the use of the Bruggeman approximations for high porosities ($f \to 1$), we numerically compute the ratio of the power transmission through the porous and the solid OAM phase plate, assuming $h(0) = 0$ and $n(0) = 1$

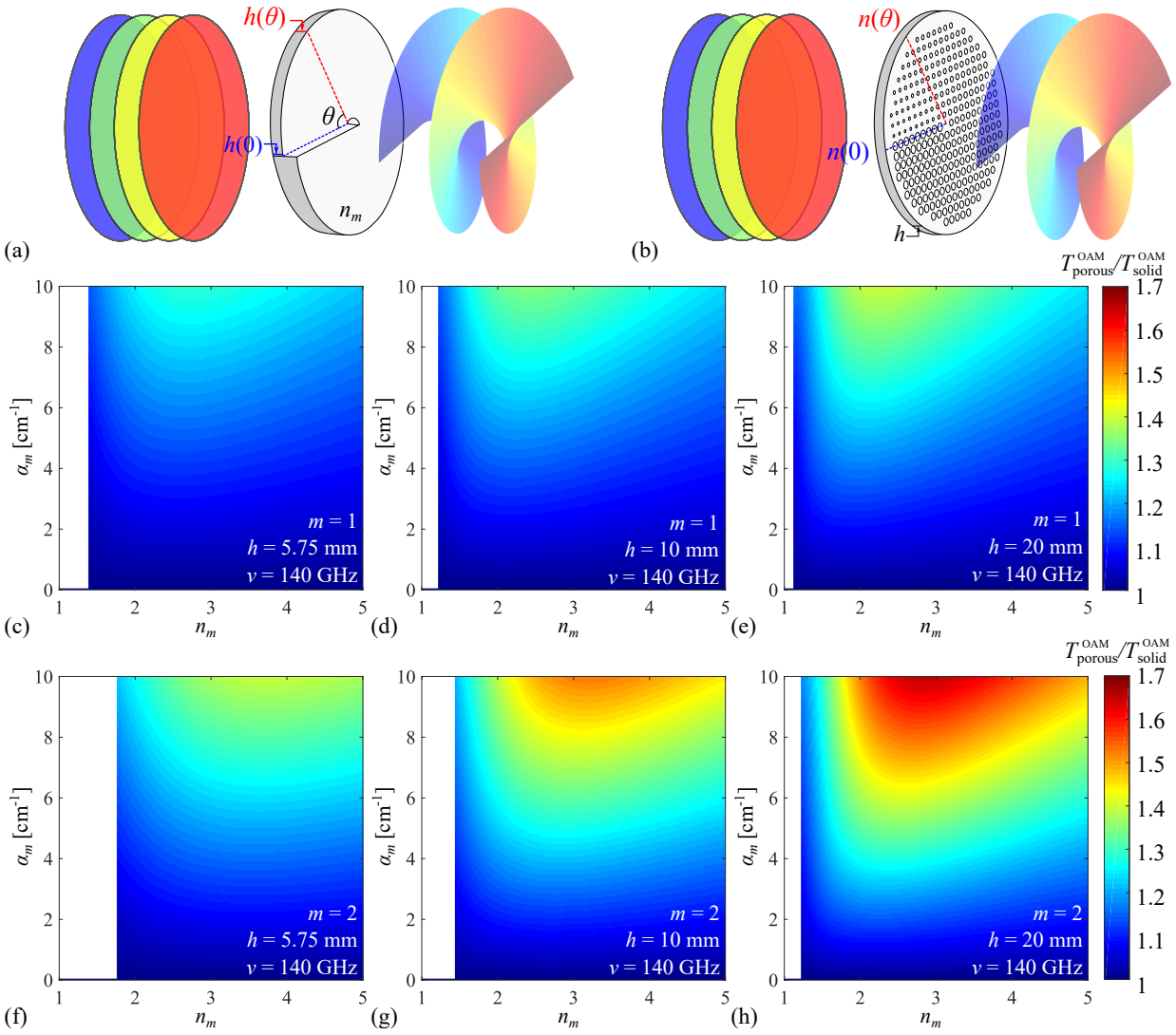

Figure 4.5 Schematic of (a) the solid OAM phase plate and (b) porous phase plate, where an incident planar wave is converted into a vortex beam. Transmission ratios of the OAM phase plate computed numerically with Eq. 4.27 as a function of n_m and α_m at a frequency of 140 GHz for $m = 1$ with (c) $h = 5.75$ mm, (d) $h = 10$ mm, (e) $h = 20$ mm, and for $m = 2$ with (f) $h = 5.75$ mm, (g) $h = 10$ mm, and (h) $h = 20$ mm. The gray areas correspond to regions where it is impossible to fabricate a porous OAM phase plate, i.e., the condition at Eq. 4.28 is not respected.

$$\frac{T^{\text{lens}}_{\text{porous}}}{T^{\text{lens}}_{\text{solid}}} = \frac{\int_0^{2\pi} \mathrm{d}\theta \exp[-\alpha(\theta)h]}{\int_0^{2\pi} \mathrm{d}\theta \exp[-\alpha_m h(\theta)]} \tag{4.30}$$

where $h(\theta)$ was obtained with Eq. 4.26 and we use the Bruggeman model [Eq. 4.6] to obtain $\alpha(\theta)$, in a manner similar to previously.

In Figs. 4.5(c)-(h), we map the ratio $T^{\text{OAM}}_{\text{porous}}/T^{\text{OAM}}_{\text{solid}}$ obtained numerically with Eq. 4.30 as a function of the material refractive index n_m and the absorption losses α_m. We select a frequency of 140 GHz, suited for our THz communications system,[37] and we compute the ratio for orders $m = 1, 2$ for different porous plate thicknesses 5.75, 10, and 20 mm. In all the cases, the porous plate outperforms the solid one, and we observe that the performance is increased with the order m and the thickness h.

Using laser drilling in a PMMA plate, we then designed and fabricated an OAM phase plate of 50 mm diameter with a topological charge of $m = 1$ for a frequency of 140 GHz [Figs. 4.6(a) and (b)]. We first placed a square lattice with an interhole distance of 1100 μm

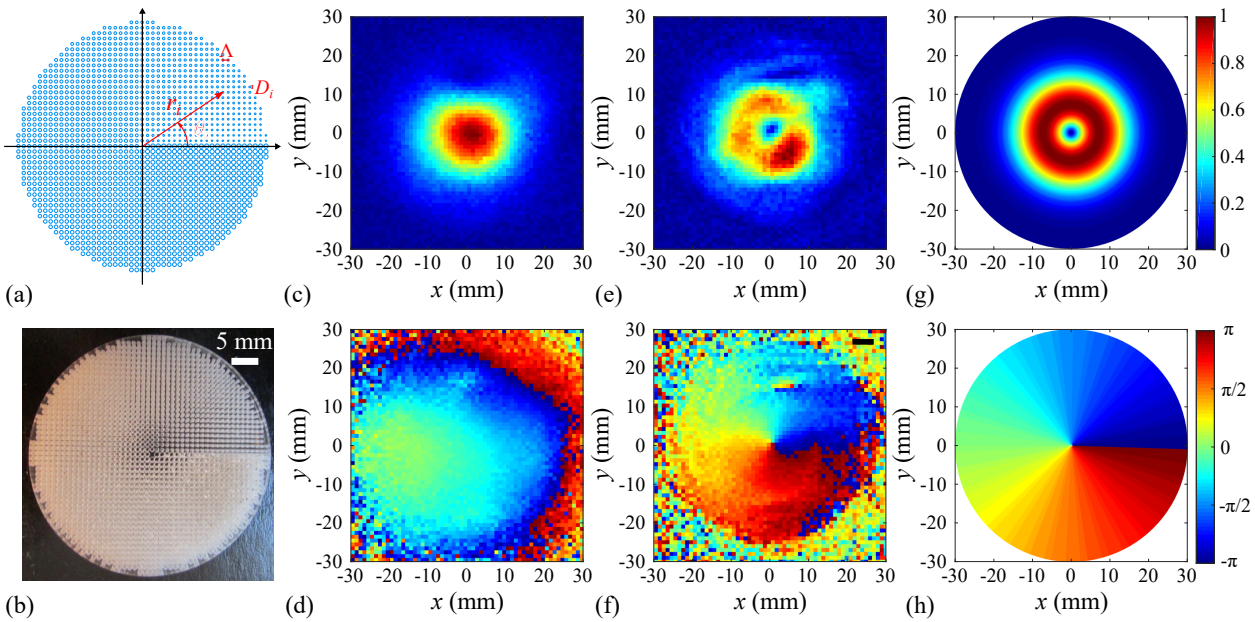

Figure 4.6 (a) Design of the OAM phase plate with the diameter of the holes varying as a function of the angle following Eq. 4.29. (b) Photograph of the fabricated sample for $m = 1$ and at a frequency of 140 GHz. (c) Amplitude and (d) phase of the 140 GHz beam without the phase plate (reference). (e) Amplitude and (f) phase of the 140 GHz beam with the OAM phase plate. (g) Amplitude and (h) phase of the Laguerre–Gaussian mode in Eq. 4.31 for $m = 1$, $p = 0$, and $w_0 = 10$ mm.

and we calculated the angle θ_i of every hole center. This allowed us to map the refractive index profile using Eq. 4.27. Using simulation results for 140 GHz, we then found the corresponding filling factor and diameter D_i . Using our THz time-domain spectroscopy system, we then imaged the THz beam at 140 GHz. The reference beam without the OAM phase plate shows a Gaussian-like amplitude distribution [Fig. 4.6(c)] and a planar phase front [Fig. 4.6(d)]. When placing the porous OAM phase plate, the amplitude is transformed into a donut [Fig. 4.6(e)] with a phase varying azimuthally from $-\pi$ to $+\pi$ [Fig. 4.6(f)].

We compare our experimental results with the analytical expression of the Laguerre–Gaussian orthogonal mode set for the electric field, which is a standard definition used to describe OAM states [438]

$$LG_{pm}(r,\theta) = \frac{1}{w_0}\sqrt{\frac{2p!}{\pi(p+|m|)!}}\left(\frac{r\sqrt{2}}{w_0}\right)^{|m|}\exp\left(-\frac{r^2}{w_0^2}\right)L_p^{|m|}\left(\frac{2r^2}{w_0^2}\right)\exp(im\theta) \tag{4.31}$$

where $L_p^|m|$ is the generalized Laguerre polynomial obtained from the Laguerre polynomial L_p with

$$L_p^{|m|}(x) = (-1)^{|m|}\frac{\mathrm{d}^{|m|}}{\mathrm{d}x^{|m|}}L_{p+|l|}(x) \tag{4.32}$$

In Eq. 4.31, w_0 is the beam waist FWHM$/\sqrt{2\ln 2}$, m is the OAM topological charge, and p is the number of radial nodes in the intensity profile. In Figs. 4.6(g) and (h), we present respectively the amplitude and phase of Eq. 4.31 using $w_0 = 10$ mm, $m = 1$, and $p = 0$. Compared to the Laguerre–Gaussian mode, we observe angular variations in the amplitude in our experimental results. This is directly caused by the nonuniform loss distribution of the porous material [see Eq. A.17] in Appendix A.3). As for the experimental phase, it agrees well with the theoretical expression, with a phase varying azimuthally from $-\pi$ to $+\pi$.

4.5 Conclusion

In conclusion, we have designed, fabricated, and characterized low-loss planar porous components for THz beamforming. Our approach uses low-RI subwavelength inclusions in a solid material to design optical components with smaller losses than their all-solid counterparts with otherwise identical optical properties. This is possible due to the fact that the electric field is enhanced in the subwavelength air holes compared to that in the host material, which results in a faster decrease of the losses of the effective material compared to its refractive index when increasing porosity. Using the Bruggeman effective medium theory, we demonstrated the validity of this approach analytically and confirmed it with numerical simulations and experimental measurements. We then fabricated and characterized a planar porous lens

and a planar porous OAM phase plate. We observed a diffraction-limited focusing using the planar lens, as well as a THz beam with a topological charge of 1 using the OAM phase plate. In principle, one could even combine both the lens and the OAM phase plate into a single porous component, since the first requires radial dependence of the RI profile while the second rather uses angular dependence. We believe that this work opens a new research direction aimed at using nominally high-loss materials with other interesting functionalities (for example high RI, high group velocity dispersion, etc.) to build novel low-loss THz components

Acknowledgements. This work was supported by the Canada Research Chair 1 of Prof. Skorobogatiy in Ubiquitous THz photonics and Canada Foundation for Innovation (CFI). H. Guerboukha acknowledges the support of the Natural Sciences and Engineering Research Council of Canada (NSERC) and the Fonds de Recherche du Québec-Nature et Technologies (FRQNT).

CHAPTER 5 ARTICLE 3: EXPLOITING k-SPACE/FREQUENCY DUALITY TOWARD REAL-TIME TERAHERTZ IMAGING

Hichem Guerboukha[1], Kathirvel Nallappan[1,2], and Maksim Skorobogatiy[1]
[1]Génie physique, Polytechnique Montréal
[2]Génie électrique, Polytechnique Montréal
Optica, vol. 5, no. 2, pp. 109-116 (2018)

Abstract: Imaging at terahertz frequencies has recently received considerable attention because many materials are semitransparent to THz waves. The principal challenge that impedes a widespread use of THz imaging is the slow acquisition time of a conventional point-by-point raster scan. In this work, we present a theoretical formulation and an experimental demonstration of a novel technique for fast compressionless terahertz imaging based on broadband Fourier optics. The technique exploits k-vector/frequency duality in Fourier optics that allows the use of a single-pixel detector to perform angular scans along a circular path, while the broadband spectrum is used to scan along the radial dimension in Fourier domain. The proposed compressionless image reconstruction technique (hybrid inverse transform) requires only a small number of measurements that scales linearly with an image's linear size, thus promising real-time acquisition of high-resolution THz images. Additionally, our imaging technique handles equally well and on an equal theoretical footing amplitude contrast and phase contrast images, which makes this technique useful for many practical applications. A detailed analysis of the technique's advantages and limitations is presented, and its place among other existing THz imaging techniques is clearly identified.

5.1 Introduction

The terahertz frequency range (0.1–10 THz, wavelengths of 3 mm–30 μm) has received considerable attention over the years, thanks to the prospect of numerous advanced imaging applications benefiting from the fact that many materials are semitransparent to THz waves (for example, polymers, plastic packaging, paper, etc.) [77, 211]. Moreover, unlike X-rays, THz radiation is non-ionizing, thus posing no risks to living beings. Many applications have been demonstrated in various applied fields such as security [439], biomedical [440], pharmaceutical [128], food industry [441], and art conservation [442]. Despite all the interest and potential, many challenges remain that impede the widespread use of THz imaging.

One of the main limiting factors is the acquisition time of a THz image. Currently, spectral

imaging is done using THz time-domain spectroscopy (THz-TDS) systems. The emitted THz pulse contains multiple frequencies and the detection is based on a time-domain sampling of the electric field, which provides direct access, through frequency Fourier transform, to the amplitude and the phase of the picosecond pulse.

There are two main types of broadband THz detectors: 1) THz photoconductive antennas (THz-PCA) [206] and 2) THz detection based on electro-optic sampling (EOS) in nonlinear crystals [73]. Both techniques are highly sensitive, but the THz-PCA generally performs better at frequencies below 3 THz with a higher signal-to-noise (SNR) ratio thanks to the use of lock-in amplifiers and single pixel detectors. On the other hand, EOS has a better sensitivity at higher frequencies [73,443,444], but lacks the ability to use lock-in amplification when used together with CCD arrays. For spectral imaging, both methods share many similar challenges.

The first challenge is the slow time-domain pulse sampling typically based on a mechanical optical delay line. A potential solution to this problem is an asynchronous optical sampling that allows to forgo mechanical delay line and features repetition rates of several kHz [242]. However, this method is expensive because it uses two synchronized femtosecond lasers. A cheaper solution can be the use of fast rotary optical delay lines. These generally come either in a prism [23, 236, 237, 445] or a mirror [229, 232–234, 446] configuration.

The second challenge is the single-pixel nature of the THZ-PCA detectors. Some attempts were made recently to integrate several antennas on the same semiconductor chip [214, 252, 253,447]. For example, in [214], the authors demonstrated a one-dimensional (1D) linear array of 15 pixels that was able to reduce the acquisition time from 9 h to 36 min. However, low THz signals were reported and were mainly attributed to focusing optics that are complicated to manufacture. Additionally, dense integration of multiple antennas on a chip is problematic due to crosstalk and interference between them. In the EOS technology, on the other hand, it is possible to replace the single-pixel photodiode by a charge-coupled device (CCD) [448]. However, due to the impossibility of integrating lock-in amplifiers into the imaging setup, the loss in signal is severe, thus requiring additional data post-processing such as the dynamic subtraction technique [255] or the averaging over multiple frames.

Together, the two above-mentioned challenges are currently the major limiting factors that prevent the proliferation of THz spectral imaging to real-time imaging applications. With a single pixel detector, spectral imaging experiments are generally performed by physically moving the sample in the focal plane of focusing optics. When performing time-domain sampling using an optical delay line (based on a linear micropositioning stage), a single pixel with a spectral resolution of ∼1-3 GHz is typically acquired in 1-5 s. Therefore, even a low

spatial resolution 32 × 32 spectral image of 1024 pixels takes ∼1 h to acquire.

Due to the complexity in building high sensitivity THz multipixel arrays, the general trend in the THz community is use advanced signal processing techniques such as compressive sensing (CS) to reduce the number of pixels required to reconstruct an image [354]. When applied to imaging, the CS theory is based on the assumption that most objects have a sparse representation in a given basis. This concept allows the efficient reconstruction of a $N \times N$ image with less than N^2 measurements. Primarily in CS systems, a single THz frequency is employed because spectral information is typically not required. For example, using Fourier optics and a moving single-pixel detector, a THz image of 4096 pixels was reconstructed with only 500 measurements (12%) at a fixed frequency of 0.2 THz [368]. However, this approach required mechanical movement of the detector. In [369], the same authors fixed the single-pixel detector and used a set of binary metal masks in the object plane. These masks formed a basis from which a 1024-pixel image was reconstructed using 300 (29%) to 600 (59%) measurements at a fixed frequency of 0.1 THz.

The possibility of reducing the number of measurements with the use of a single-pixel detector resulted in a spurt of activity in CS applied to THz imaging [372,373,384,389,392]. Recently, researchers have used an optically controlled silicon mask in the THz path [392] to create patterns similar to binary metal masks. A THz image of 1024 pixels was obtained with only 63 measurements in 2 s. In [384], the same group used an electronically controlled spatial light modulator in the THz beam to demonstrate image acquisition at 1 Hz by using 45 masks/s. In [389], THz near-field imaging using CS is demonstrated. Despite these advances, most of the prior research in CS was done on reconstructing amplitude modulated images predominantly in the form of binary metal masks with cutouts. However, in addition to amplitude information, practical applications frequently require phase sensing. For example, in quality control, a scratch on the surface of a plastic sheet will result in a weak amplitude contrast, but a strong phase contrast.

An alternative to CS that samples spatial information at a single THz frequency is to use broadband signals to encode spatial information in their spectra. In fact, using time or spectral data to encode the information of an image is the basis of many imaging techniques at other frequencies. For example, in optical coherence tomography, the depth information is encoded in the spectrum [449]. Additionally, originating from radar technology, synthetic aperture imaging (SAI) allows the reconstruction of an image using the echoes of a scattered field measured in time domain. SAI was implemented in the THz range, providing sub-millimeter resolution. With THz-TDS, the scattered wave can be directly mapped in time domain and direct phase measurement of the electric waveform avoids the use of interference

with a reference wave [450]. The measurement can also be done with a CW source, where the axial dimension is obtained by sweeping the frequency [451].

Furthermore, dimensionality reduction of an image can be done using spectral information. The serial time-encoded amplified (STEAM) imaging system described in [396,397] is a powerful implementation of the space-to-time image transformation. In the STEAM system, 2D spatial information of the image is encoded into a broadband spectrum using spatial dispersers. Then, using dispersion-compensating fiber and Raman amplification, the spectrum of an optical pulse is mapped into the time domain. By using a single-pixel fast photodetector, one can then reconstruct a 2D image at the laser repetition rate. Similar to the spatial dispersers used in the STEAM system [399], in the THz and millimeter wave range, the echelon diffractive gratings have been used to encode the image in 1D [398] or 2D [402] spatial coordinates. The position in space is then obtained by scanning the frequency in the spectrum.

In this work, we present a compressionless imaging technique based on the k-space/frequency duality in Fourier optics that is capable of reconstructing amplitude and phase contrast THz images using only a small number of measurements proportional to the linear size of the object rather than its area. As noted in [405], in Fourier space a spectral frequency can be equated with a spatial frequency, which opens the possibility to substitute the sampling over a 2D k-space by sampling over a 1D k-space and frequency. Therefore, we first use a single pixel THz-PCA detector and a lock-in amplifier to record the broadband time pulses at some strategically chosen points in the Fourier space. Then, we use a hybrid inverse transform developed in our group to reconstruct both amplitude and phase images from the time traces collected in Fourier space. A detailed analysis of the amplitude and phase image resolution is then presented using experimental measurements and numerical data. Unlike the techniques based on compressive sensing theory, our method is lossless (in term of information), as both spatial and spectral data is used for image reconstruction. Based on solid mathematical formulation, our hybrid inverse transform can be equally well applied both to amplitude and phase imaging.

5.2 Results

5.2.1 Hybrid Image Reconstruction Algorithm using a Generalized Fourier Optics Approach

In what follows, we first introduce a hybrid image reconstruction algorithm based on a generalization of a Fourier optics approach to broadband pulses. The Fourier optics theory

states that, for a fixed frequency ν, a field profile $S(x, y, \nu)$ generated by an object that is placed in the front focal plane (object plane) of a convex lens is Fourier-transformed according to [169]

$$U(\xi, \eta, \nu) = \frac{\nu}{jcF} \iint \mathrm{d}x\mathrm{d}y \cdot S(x, y, \nu) \cdot \exp\left[-\frac{j2\pi\nu}{cF}(x\xi + y\eta)\right] \tag{5.1}$$

where F is the lens focal distance and c is the speed of light. The Fourier transform $U(\xi, \eta, \nu)$ of the original field can be measured directly in the back focal plane of the lens (also known as the Fourier plane), where (ξ, η) are the Cartesian coordinates of the observation point [see the schematics in Fig. 5.1(a)]. Moreover, the original field distribution $S(x, y, \nu)$ generated by the object can be reconstructed using the inverse Fourier transform,

$$S(x, y, \nu) = \frac{j\nu}{cF} \iint \mathrm{d}\xi\mathrm{d}\eta \cdot U(\xi, \eta, \nu) \cdot \exp\left[+\frac{j2\pi\nu}{cF}(x\xi + y\eta)\right] \tag{5.2}$$

The spatial frequencies, also known as components of the k-space, are related to the (ξ, η) coordinates as

$$k_\xi = \frac{\xi\nu}{cF} \qquad\qquad k_\eta = \frac{\eta\nu}{cF} \tag{5.3}$$

When using broadband pulses, a raster scanning in the Fourier plane [Fig. 5.1(b)] results in the acquisition of a hyperspectral cube where, for each frequency, there is an image in the k-space [Fig. 5.1(c)]. However, as the k-components 5.3 are proportional to the frequency ν, one quickly arrives at the intriguing idea of sampling the k-space using the broadband nature of the THz-TDS pulse, rather than by a mechanical scanning of the k-space by displacing the detector. Indeed, by fixing a detector at a fixed position with coordinates (ξ_0, η_0) and using a broadband light $\nu \in [\nu_{\min}, \nu_{\max}]$ one can sample a linear segment of the k-space described by

$$k_\eta = \frac{\eta_0}{\xi_0} k_\xi \quad \text{with} \quad k_\eta \in \frac{\xi_0}{cF}[\nu_{\min}, \nu_{\max}] \tag{5.4}$$

By changing the ratio η_0/ξ_0, the whole k-space can be sampled. The simplest way to change this ratio is to measure several points along a circle of fixed radius ρ_0 in the (ξ, η) plane [Fig. 5.1(d) and (e)]. Mathematically, for further consideration, it is more convenient to write the Fourier transform 5.1 in polar coordinates as

$$U(\vec{\rho}, \nu) = \frac{\nu}{jcF} \iint \mathrm{d}\phi\mathrm{d}r \cdot S(\vec{r}, \nu) \cdot \exp\left[-\frac{j2\pi\rho}{cF}\vec{r} \cdot \vec{\rho}\right] \tag{5.5}$$

where $\vec{\rho}$ is the position vector in the observation point in the Fourier plane, while $\vec{r}$ is the

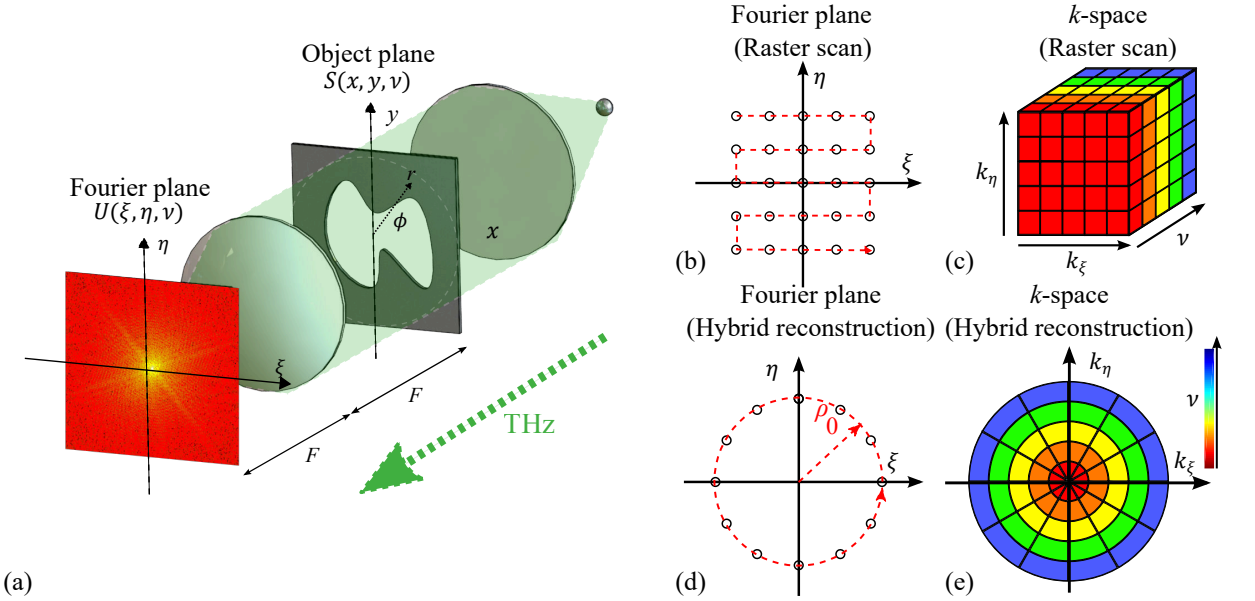

Figure 5.1 Hybrid image reconstruction algorithm: (a) schematic of the object plane and the Fourier plane; (b) raster scanning on a 2D Cartesian grid in the Fourier plane; and (c) corresponding hyperspectral k-space cube. (d) Hybrid reconstruction algorithm with a 1D circular scan in the Fourier plane and (e) corresponding k-space inferred using spectral information.

position vector in the object plane. The inverse Fourier transform 5.2 is then written as

$$\begin{aligned} S(\vec{r},\nu) &= \frac{j\nu}{cF}\iint \mathrm{d}\theta\rho\mathrm{d}\rho\cdot U(\vec{\rho},\nu)\cdot\exp\left[+\frac{j2\pi\rho}{cF}\vec{r}\cdot\vec{\rho}\right] \\ &= \iint \mathrm{d}\theta\left(\frac{j\nu\rho}{cF}\right)\mathrm{d}\left(\frac{j\nu\rho}{cF}\right)\cdot\frac{U(\vec{\rho},\nu)}{j\nu/cF}\cdot\exp\left[+2\pi\frac{j\vec{\rho}}{cF}\cdot\vec{r}\right] \end{aligned} \tag{5.6}$$

As can be seen from the integral in Eq. 5.6, the frequency ν of the probing wave and the distance of the detector from the origin ρ in the Fourier plane are entering the formulation in a symmetrical fashion. Therefore, in principle, the integral over the spatial coordinate in the Fourier plane $\vec{\rho}$ at a fixed frequency ν_0 can be replaced by an integral over the frequency ν at a fixed radius ρ_0. In other words, instead of fixing the frequency of the probing wave and recording the Fourier image by 2D scanning of the point detector, we can instead only scan along a single 1D circular path of radius ρ_0, while using the broadband spectrum of the probing pulse to sample the k-space along the radial direction. In this way, the full 2D raster scan at a fixed frequency over the Fourier plane is avoided and is substituted by a time-domain scan along a single circle.

Mathematically, we therefore define a new hybrid inverse transform by substituting the inte-

gration over the 2D Fourier space in 5.6 by a hybrid integration over a 1D spatial coordinate and frequency,

$$\tilde{S}(\vec{r}) = \iint \mathrm{d}\theta\nu\mathrm{d}\nu \cdot \frac{j\rho_0^2}{\nu cF} \cdot U(\rho_0, \nu, \theta) \cdot \exp\left[+\frac{j2\pi\nu}{cF}\vec{r}\cdot\vec{\rho}_0\right] \tag{5.7}$$

It is important to note that the image $\tilde{S}(\vec{r})$ reconstructed using Eq. 5.7 is different from the original image $S(\vec{r}, \nu)$, as given by the standard inverse Fourier transform Eq. 5.6. Indeed, $S(\vec{r}, \nu)$ is a hyperspectral image that can be different for different frequencies ν. In contrast, $\tilde{S}\vec{r}$ is a compounded image that incorporates information from all the frequencies sampled by the pulse. Therefore, one must recognize that although the definition of the hybrid inverse transform 5.7 is derived using physical arguments, its final form should be considered as a mathematical abstraction, and therefore can be generalized even further as

$$\tilde{S}(\vec{r}) = \iint \mathrm{d}\theta\nu\mathrm{d}\nu \cdot \frac{j\rho_0^2}{\nu cF} \cdot \frac{U(\rho_0, \nu, \theta)}{U_{\mathrm{ref}}(\nu)} \cdot \exp\left[+\frac{j2\pi\nu}{cF}\vec{r}\cdot\vec{\rho}_0\right] \tag{5.8}$$

where $U_{\mathrm{ref}}(\nu)$ is a certain frequency-dependent reference function responsible for the normalization of the integral at Eq. 5.8. As we will see later, this normalization step is crucial for correct phase and amplitude retrieval, as well as for correct interpretation of the image given by Eq. 5.8. In what follows, we demonstrate that, in several important cases of amplitude and phase masks, the properly normalized hybrid transform 5.8 recovers the original amplitude and phase information.

5.2.2 Amplitude Masks

First, we consider the case of an object in the form of an amplitude mask. The resultant image $S(\vec{r}, \nu)$ is assumed to be space–frequency separable and, in the object plane, is defined as

$$S(\vec{r}, \nu) = S(\vec{r})E(\nu) \tag{5.9}$$

A typical example of this imaging modality would be a binary mask represented by an opaque screen with a cutout pattern (image) that is illuminated with a pulsed light. In this case, $S(\vec{r})$ is a function that has only two values (1 or 0) depending whether it corresponds to the cutout or the opaque part of the screen. Here, $E(\nu)$ is the frequency dependent field of the probing pulse. Furthermore, as a reference function $U_{\mathrm{ref}}(\nu)$ in the hybrid inverse transform 5.7, we take the normalized THz-TDS trace as measured by a point detector in the center of

the Fourier plane ($\rho_0 = 0$) with the amplitude mask still present in the object plane,

$$U_{\text{ref}}(\nu) = (jcF/\nu) \cdot U(0, \nu) \tag{5.10}$$

In practice, we first perform a time-domain measurement in the origin of the Fourier plane, then $U(0, \nu)$ is found using a frequency Fourier transform of the measured time-domain pulse. Using Eq. 5.5, one can also write 5.10 as

$$U_{\text{ref}}(\nu) = (jcF/\nu) \cdot U(0, \nu) = E(\nu) \iint \mathrm{d}\vec{r} \cdot S(\vec{r}) \tag{5.11}$$

In this case, the hybrid inverse transform becomes

$$\tilde{S}(r, \phi) = \iint \mathrm{d}\theta \mathrm{d}\nu \cdot \left[\nu \left(\frac{\rho_0}{cF} \right)^2 \frac{U(\vec{\rho}_0, \nu)}{U_0(0, \nu)} \right] \cdot \exp \left[+\frac{j2\pi\nu}{cF} \vec{r} \cdot \vec{\rho}_0 \right] \tag{5.12}$$

Note that the reference $U_{\text{ref}}(\nu)$ is chosen to contain an additional multiplicative factor jcF/ν that is necessary to ensure that the reconstructed image $\tilde{S}(r, \phi)$ is proportional to the original one $S(\vec{r}, \nu)$. In fact, from the detailed mathematical analysis presented in Appendix B.2.2, it follows that, in the case of amplitude masks, the hybrid inverse transform results in the original image normalized by a constant factor proportional to the area of the image,

$$\tilde{S}(r, \phi) = \frac{S(r, \phi)}{\iint \mathrm{d}\phi r \mathrm{d}r S(r, \phi)} \tag{5.13}$$

As an example, in Fig. 5.2, we experimentally demonstrate the imaging of a metallic mask with a cutout in the form of a Canadian maple leaf [Fig. 5.2(a)]. Our intent here is to demonstrate the reconstruction of a complex image using the broadband spectrum and very few pixels in the Fourier plane. For comparison, we first perform regular imaging by recording the field distribution in the Fourier plane by raster scanning with a point detector on a 102×102 mm grid with 1.5 mm resolution (4624 pixels). At each pixel, a full-frequency spectrum is recorded, thus a complete hyperspectral image is acquired. As an example, in Figs. 5.2(b) and (c) we present image amplitude and phase distributions in the Fourier plane at the particular frequency of 0.57 THz. The reconstruction of the original image is then performed using the standard inverse Fourier transform in Cartesian coordinates [Eq. 5.2]. The result contains both amplitude and phase information for every frequency. In Fig. 5.2(d), we present the amplitude distribution of the reconstructed image at 0.57 THz that corresponds to the amplitude and phase distributions in the Fourier plane presented in Figs. 5.2(b) and (c).

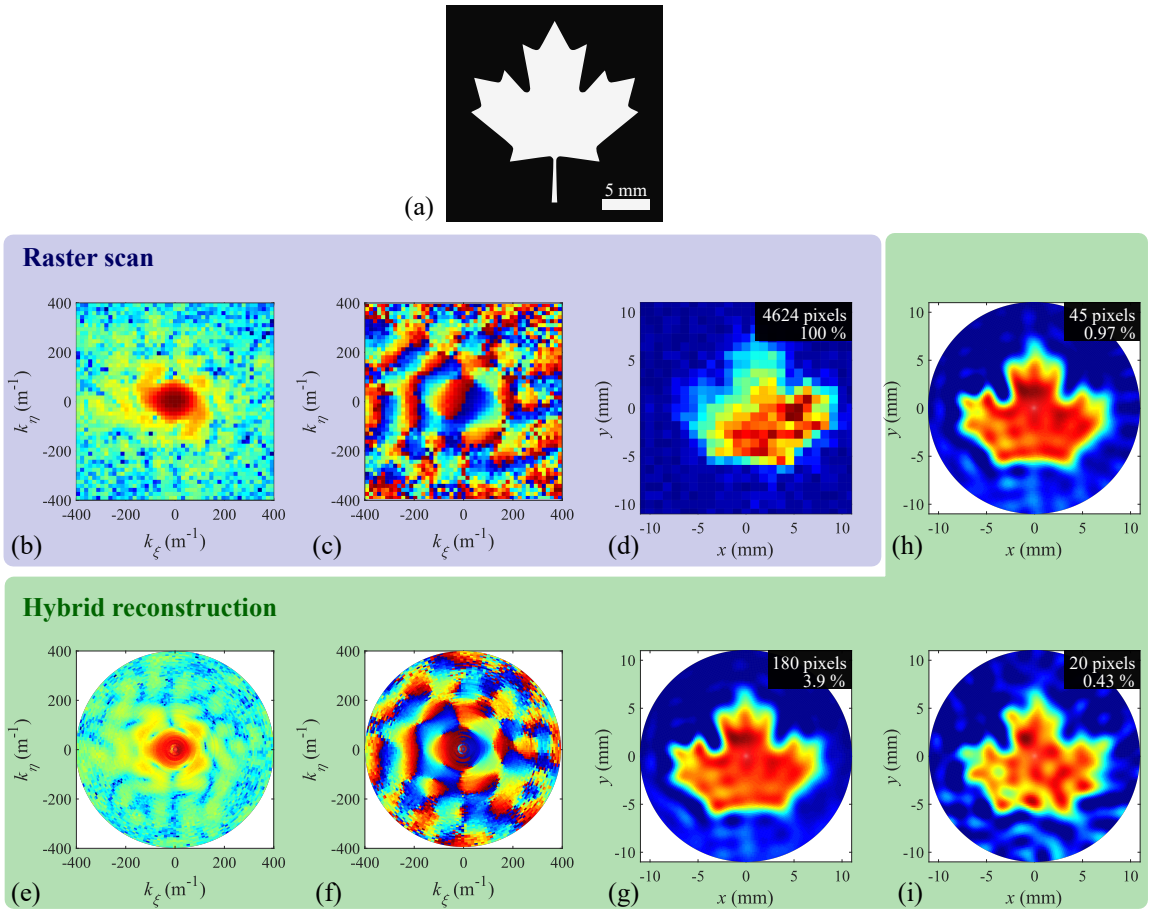

Figure 5.2 Reconstruction of a binary amplitude image in the form of a maple leaf cutout in the metallic plate. (a) Schematic of the maple leaf cutout. Standard raster scanning: (b) amplitude and (c) phase of the k-space at a single frequency of 0.57 THz (4624 pixels). (d) Image reconstruction using the standard inverse Fourier transform 5.2. Image reconstruction using the hybrid inverse transform 5.12: (e) inferred k-space amplitude and (f) phase distribution using spectra of the THz time traces acquired at 180 pixels positioned along a circle of radius $\rho_0 = 25$mm around the origin of the Fourier plane. (g) Image reconstructed using hybrid inverse transform 5.12 with 180 pixels, (h) 45 pixels, and (i) 20 pixels.

We now show that the hybrid inverse transform presented in this section [Eq. 5.12] can reconstruct a simple binary image with considerably fewer pixels. Thus, in Figs. 5.2(a) and (f), we present the recorded amplitude and phase distributions of the image in the k-space using only 180 pixels in the Fourier plane. These points are sampled on a circle of radius $\rho_0 = 25$mm with the center at the origin. The traces are acquired at equal angular intervals. The data is then normalized by the complex spectrum recorded at the origin of the k-space [expression 5.11]. The k-space at Figs. 5.2(e) and (f) is constructed by interpreting the spectral data as components of the k-space with Eq. 5.3. As expected, this k-space compares

remarkably with the k-space obtained through raster-scanning [Fig2. 5.2(b) and (c)]. Finally, the image is reconstructed numerically using the integration in polar coordinates of Eq. 5.12 [Fig. 5.2(g)]. Additionally, in Figs. 5.2(h) and (i), we study the quality of the reconstructed image when using a different number of pixels on the circle (between 45 and 20). We note that even when using as little as 20 pixels, the maple leaf can still be clearly recognized.

5.2.3 Phase Masks

Second, we study the case of an object in the form of a dispersionless phase mask with no absorption. As an example, we can consider imaging scratches on the surface of a transparent material plate/film surrounded by air [see Fig. 5.3(a)]. In this case, the optical path of the probing light in the object plane is given by

$$\Delta(\vec{r}) = \Delta_0 - \mu(\vec{r}) = [L_a n_a + L_m n_m] - [(n_m - n_a)h(\vec{r})] \tag{5.14}$$

where n_a and n_m are the frequency-independent refractive indices of the air and the material, L_a and L_m are the distances travelled in the air and in the material, while $h(\vec{r})$ is the spatially dependent depth of the scratch. In this case, the field distribution in the object plane can be written as

$$S(\vec{r}, \nu) = S(\vec{r})E(\nu) \cdot \exp[j2\pi\nu(\Delta_0 - \mu(\vec{r}))/c] \tag{5.15}$$

where $S(\vec{r})$ defines the slow amplitude variation of the aperture-limited beam in the object plane, $E(\nu)$ is the frequency dependent field of the probing pulse, and $\mu(\vec{r}) = (n_m - n_a)h(\vec{r})$ is the optical path differential (a scratch, for example) across the object plane that we want to image.

In the case of phase masks, we define the reference U_{ref} in the hybrid inverse transform 5.8 using a THz pulse recorded at the origin of the k-space ($\rho_0 = 0$) and measured using a reference sample without the scratch ($h(\vec{r}) = 0$),

$$U_{\text{ref}}(\nu) = (jcF) \cdot U(0, \nu) = \nu E(\nu) \exp(j2\pi\nu\Delta_0/c) \iint \mathrm{d}\vec{r} \cdot S(\vec{r}) \tag{5.16}$$

Note that unlike in the case of 5.11 used for amplitude masks, there is no division by the frequency in 5.16. This is an important difference with the case of amplitude masks that is detailed in the Appendix B.2.3. The hybrid inverse transform 5.8 then becomes

$$\tilde{S}(r, \phi) = \iint \mathrm{d}\theta \mathrm{d}\nu \cdot \left[\left(\frac{\rho_0}{cF} \right)^2 \frac{U(\vec{\rho}_0, \nu)}{U_0(0, \nu)} \right] \cdot \exp\left[+ \frac{j2\pi\nu}{cF} \vec{r} \cdot \vec{\rho}_0 \right] \tag{5.17}$$

In Appendix B.2.3, we demonstrate that the imaginary part of the reconstructed image 5.17 is directly proportional to the optical path differential in the object plane,

$$\mathrm{Im}\{\tilde{S}(\vec{r})\} = -\frac{2\pi}{c}\frac{S(\vec{r})}{\iint \mathrm{d}\vec{r} S(\vec{r})}(n_m - n_a)h(\vec{r}) \tag{5.18}$$

where the term $S(\vec{r}/\iint \mathrm{d}\vec{r} S(\vec{r}))$ represents the slow-varying amplitude of the incident aperture-limited beam that can be measured independently (if desired) using the binary mask method described earlier. Moreover, we find experimentally, that our imaging approach given by the hybrid inverse transform 5.17 is so sensitive that it can readily detect nonuniformities in the phase distribution across the imaging plate. Such nonuniformities can be due to defects in the substrate geometry and composition, substrate misalignment, or even due to phase variation in the wavefront of the probing beam. Mathematically, this means that instead of a constant phase Δ_0 used in 5.15, we have to assume a somewhat nonuniform phase distribution $\Delta_0(\vec{r})$ across the surface of a reference substrate. Therefore, to improve the quality of phase imaging, we find it beneficial to substract the phase image of a pure substrate from the phase image of a phase mask written on a similar substrate. The phase image of a substrate $\mathrm{Im}\{\tilde{S}_0(\vec{r})\}$ is reconstructed in exactly the same fashion as the phase image $\mathrm{Im}\{\tilde{S}(\vec{r})\}$ of a phase mask written on a similar substrate, by performing exactly the same steps and using the same reference (in both cases) as described above.

As an example, we demonstrate the imaging of the Greek letter π inscribed as a 100 μm deep engraving in a $L_m = 1$ mm thick slab of photosensitive resin (PlasCLEAR) printed using a stereolithography 3D printer (Asiga Freeform PRO2) [Figs. 5.3(a) and (b)]. This polymer is transparent in the THz region and has an almost constant refractive index of $n_m = 1.654$ [99]. The amplitude and the phase distributions of the image in the k-space are presented in Figs. 5.3(c) and (d). As in the case of the amplitude masks, these were inferred using the k-space/frequency duality in Fourier optics. In what follows, our goal is to map the height $h(\vec{r})$ of the engraving. First, we compute the imaginary part of the hybrid inverse transform $\mathrm{Im}\{\tilde{S}(\vec{r})\}$ 5.18, which is shown in Fig. 5.3(e). There, the π engraving is clearly visible, but it is surrounded by a halo due to the somewhat nonuniform substrate used in the experiment. Two additional steps are required to extract the absolute value of the scratch depth $h(\vec{r})$. First, as described above, we retrieve the phase image of the somewhat nonuniform substrate without the scratch $\mathrm{Im}\{\tilde{S}_0(\vec{r})\}$, which is shown in Fig. 5.3(f). Then, the phase variation across the reference substrate is removed from the image with the scratch by subtracting the two phase images $\mathrm{Im}\{\tilde{S}(\vec{r})\} - \mathrm{Im}\{\tilde{S}_0(\vec{r})\}$, and the result is shown in Fig. 5.3(g). There, we can see that the phase image has been considerably improved and only the letter π is visible. To extract the absolute value of the scratch depth, we need to further divide the

phase image $\mathrm{Im}\{\tilde{S}(\vec{r})\} - \mathrm{Im}\{\tilde{S}_0(\vec{r})\}$ by the slow varying amplitude of the aperture-limited beam $S(\vec{r})/\iint \mathrm{d}\vec{r} S(\vec{r})$. As mentioned earlier, this value can be found by performing a hybrid inverse transform [Eq. 5.12] while treating the substrate without a scratch as an amplitude mask. Finally, the height distribution can be extracted using Eq. 5.18 and, as seen from the Fig. 5.3(h), the π symbol is an engraving of depth around 100 μm.

5.3 Discussion

5.3.1 Image Resolution

First, we quote the resolution of a standard Fourier optics technique when using raster scanning in the Fourier plane. In this case, the minimal achievable resolution in the object plane follows the Fourier transform properties. Particularly, using the Nyquist theorem, the minimal resolution achievable is $\delta r = 0.5/k_{\max}$, where $k_{\max}$ is the maximal spatial frequency sampled in the k-space. When using raster scanning, the resolution is therefore limited by

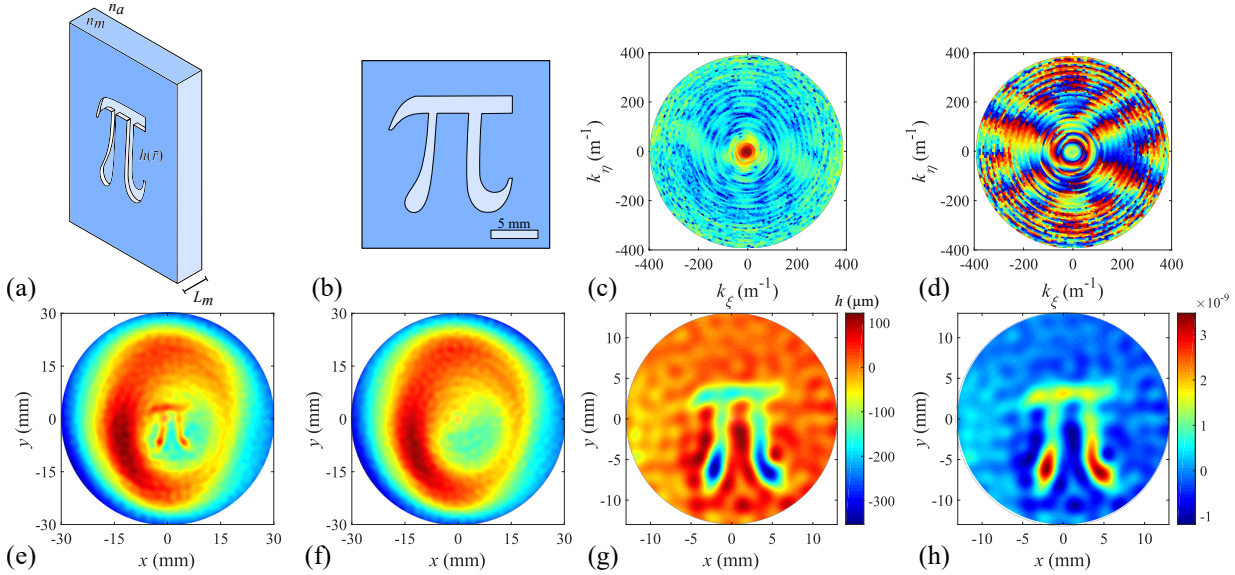

Figure 5.3 Reconstruction of a phase contrast image in the form of the shallow engraving of the Greek letter π onto a slab of transparent plastic. (a)–(b) Schematic of the sample $n_a = 1$, $n_m = 1.654$, and $L_m = 1$ mm. Image reconstruction using the hybrid inverse transform of Eq. 5.17: (c) inferred k-space amplitude and (d) phase distribution using spectra of the THz time traces acquired at 180 pixels positioned along a circle of radius $\rho_0 = 25$ mm around the origin of the Fourier plane. (e) Reconstructed phase image of a substrate with engraving $\mathrm{Im}\{\tilde{S}(\vec{r})\}$ and (f) without the engraving $\mathrm{Im}\{\tilde{S}_0(\vec{r})\}$. (g) Improved phase image of the engraving $\mathrm{Im}\{\tilde{S}(\vec{r})\} - \mathrm{Im}\{\tilde{S}_0(\vec{r})\}$. (h) Reconstructed depth of the engraving from Eq. 5.18 and a supplementary beam amplitude measurement.

the grid size $\Delta\xi$ in the Fourier plane. For example, in the x direction, with the definitions in Figs. 5.4(a) and (b), the resolution is $dx = 0.25/\Delta k_\xi = 0.25\lambda F/\Delta\xi$, where $\Delta\xi$ is the grid size in the Fourier plane. Therefore, the resolution improves when using smaller wavelengths and a larger grid size. In the meantime, the grid spacing in the k-space dk_x limits the field of view (maximal image size) such as $\Delta x = 1/dk_x = \lambda F/d\xi$, where $d\xi$ is the grid spacing in the Fourier plane.

In the hybrid inverse transform, $k_{\max}$ is a function of the maximal radial position of the detector $\rho_{\max}$ and the maximal THz frequency $\nu_{\max}$ of the pulse, so that $k_{\max} = \nu_{\max}$. Therefore, the minimal achievable resolution is set by the Nyquist theorem to $\delta r = 0.5cF/\nu_{\max}\rho_{\max} = 0.5\lambda_{\min}F/\rho_{\max}$, where $\lambda_{\min} = c/\nu_{\max}$.

In the case of amplitude masks, as shown in Appendix B.3.1, the resolution of the hybrid inverse transform algorithm [Eq. 5.12] closely follows the Nyquist theorem limit $\delta r = 0.5\lambda_{\min}F/\rho_0$, where ρ_0 is the radius of the circle along which the time-domain data is sampled. Particularly, we find that the hybrid inverse transform acts as a linear smoothing filter that simply averages the image inside a circle of radius $\approx \delta r$ defined above.

In the case of phase masks, as shown in Appendix B.3.2, the resolution of the hybrid inverse transform algorithm [Eq. 5.17] is somewhat more complex. First, the resolution in the object plane is limited by the Nyquist theorem. Second, a spatially dependent correction term proportional to the local optical path variation due to surface inhomogeneity (presence of the engraving) must be added to the resolution, $\delta r(\vec{r}) = [0.5\lambda_{\min} + h(\vec{r})(n_m - n_a)] \cdot F/\rho_0$, where $h(\vec{r})$ is the local height of the scratch, while n_m and n_a are the refractive indices of the substrate material and surrounding air. To experimentally demonstrate the effect of both the radial position of the detector and the THz bandwidth on the image resolution, we present in Fig. 5.4 imaging of the paper cutout in the form of a snowflake fabricated using a commercial paper puncher [Fig. 5.4(c)]. The paper cutout can be considered as a phase mask due to the subwavelength thickness of the paper and its low absorption, therefore the hybrid inverse transform in the form of Eq. 5.17 is used. In Figs. 5.4(d)-(i), we summarize our measurements by presenting the reconstructed phase images as a function of increasing THz frequencies ($\nu_{\max}$) and radial positions (ρ_0). From these images, we conclude that the resolution of the system can be enhanced either by using spectrally broader THz pulses or by positioning the detector as far from the origin of the Fourier plane as possible. Indeed, by increasing the THz bandwidth, the resolution of the image clearly improves, as it can be seen qualitatively by comparing Figs. 5.4(d)-(f) and Figs. 5.4(g)-(i). Moreover, by positioning the point detector at a larger radial position ρ_0, the image resolution again is enhanced, as seen by comparing Figs. 5.4(d)-(g), (e)–(h), and (f)–(i). There, the small dendrites in

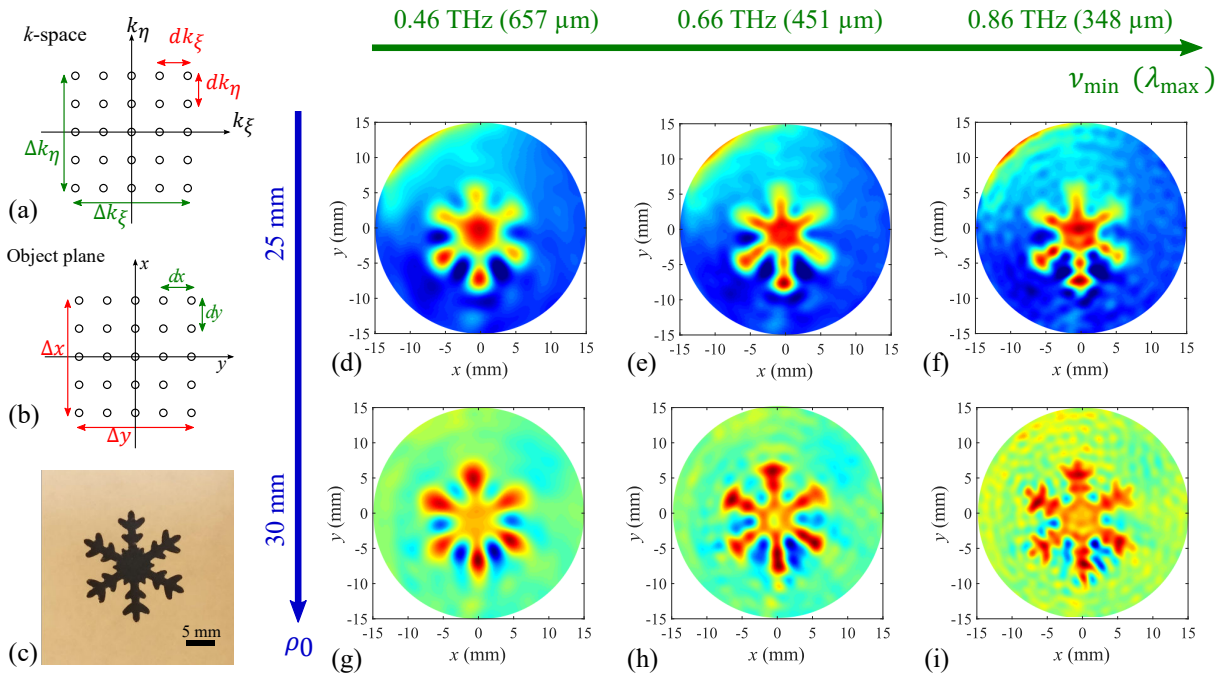

Figure 5.4 Impact of the THz bandwidth and the radial position of the detector on phase image resolution. Schematics of (a) the k-space and (b) the object plane showing relations between resolutions and image sizes. (c) Photograph of the phase mask in the form of a snowflake cutout in very thin (100 μm) paper. Reconstructed phase images using Eq. 5.17 with $\rho_0 = 25$ mm and (d) $\nu_{\max} = 0.46$ THz, (e) $\nu_{\max} = 0.66$ THz, and (f) $\nu_{\max} = 0.86$ THz. Reconstruction with $\rho_0 = 30$ mm and (g) $\nu_{\max} = 0.46$ THz, (h) $\nu_{\max} = 0.66$ THz, and (i) $\nu_{\max} = 0.86$ THz.

the snowflake become resolvable when the radial position ρ_0 is increased. We note that the improvement in the image resolution stops when the radial position of the detector (ρ_0) is increased beyond the size of the limiting aperture of the optical system (lens size).

5.3.2 Advantages and Limitations of the Hybrid Image Algorithm

Now, we would like to comment on the concept of applying the presented imaging method in the context of industrial-strength, real-time THz imaging systems. The main advantage of our method is its ability to reduce significantly the image acquisition time, while retaining the high SNR offered by the TDS-THz setups based on photoconductive antennas, albeit with the loss of spectral data. In fact, the acquisition time of our method scales proportionally to the object linear size rather than its area, which is the case in standard 2D raster scanning setups.

Moreover, as our system is based on the THz-TDS setup, the same imaging system can

perform both hybrid imaging of the whole object (with the loss of the spectral data), followed by a more precise hyperspectral imaging using a slow raster scan of a smaller target area of an object. Both amplitude imaging modality and phase imaging modality are supported by the hybrid imaging setup, thus allowing efficient imaging of the objects with high intensity contrast (amplitude modality) encountered for example in objects with deep carvings or cutouts, as well as the low intensity contrast (phase modality) encountered for example in objects with small scratches or imperfections on their surface.

Additionally, we note that hybrid imaging based on the k-space/frequency duality opens a realistic approach to completely forgo mechanical scanning in high-speed 2D THz imaging systems. Indeed, we note that the main reason why the standard 2D raster scanning is slow is the mechanical scanning of the sample. Thus, with the current state of the art in micropositioning stages, a reliable line sampling (back and forth along a single line of a ≈ 5 cm long image) can be done with ≈ 1 Hz rates. Therefore, even a modestly large image containing 100 lines would take several minutes to acquire. At this point, we are not even talking about the hyperspectral imaging, but rather about imaging with a monochromatic THz source. Within our approach, we require the acquisition of full THz time traces along a single circle in the Fourier space. Currently, this acquisition is accomplished using a 1D scan with a point detector. Alternatively, mechanical scanning of a point detector along a circle in the k-space can be forgone by adopting a $4f$ system layout (instead of the $2f$ system used in our work), while using absorbing photomasks in the Fourier plane for sampling [405]. In this arrangement, a single pixel detector would be placed at a focal distance of the second lens, while dynamic absorbing masks in the Fourier plane [372, 392] can be used to sample along the circle path. The fastest method, however, would be to use a circular array of THz photoconductive antennas, which have been already demonstrated by several research groups [214, 252, 253, 447], thus resulting in a simultaneous interrogation of all the spatial points along a circular path in the k-space.

Finally, according to our methodology, the sampling in the second dimension is performed via interpretation of the frequency spectrum of a registered broadband THz pulse. Currently, a slow linear delay line is used for the THz pulse acquisition, thus limiting per pixel pulse acquisition rates to 1 Hz. Slow linear delay lines can be substituted by the much faster rotary delay lines that were recently demonstrated by several research groups [23, 229, 232–234, 236, 237, 445, 446] and that can enhance the acquisition rate to $\sim 10 - 100$ Hz. In fact, mechanical optical delay lines can be replaced altogether by opto-electronic delay lines integrated into the fs lasers used in the THz-TDS systems, thus resulting in full THz spectral scanning rates of ~ 100 Hz per pixel [242]. In any case, even if the optical delay line can be made infinitely fast, the spectrum acquisition time in the THz-TDS systems is limited by the

lock-in averaging time constant of ~ 10 ms, which is a minimal time required per frequency to get a reliable intensity reading with a SNR of 20–40 dB in amplitude. Using a modest spectral resolution of ~ 30 GHz, a full THz spectrum of up to 3 THz can then be acquired in ~ 1 s. Alternatively, tunable THz systems based on frequency difference generation in photomixers can also be used to detect spectral information [39]. While using technology similar to the photoconductive antennas, and featuring spectral acquisition rates of ~ 1 Hz, such signals offer considerably higher SNRs and signal intensities. Therefore, the use of linear THz antenna arrays together with fast delay lines (specifically, opto-electronic delay lines) negates the need for any moving parts in the THz imaging systems based on photoconductive antennas. This would result in $\sim$Hz acquisition rates of medium resolution ($\sim 100 \times 100$), THz images with very high SNRs, either in amplitude contrast or phase contrast modalities. These acquisition rates can be further improved either by sacrificing SNR while using faster optical delay lines, or not sacrificing SNR by using more powerful (albeit considerably more expensive) broadband THz sources such as those based on the two-color fs laser mixing and plasma filamentation (see [452], for example).

5.4 Conclusion

In conclusion, we have demonstrated a hybrid Fourier imaging-based reconstruction method that uses both spatial and spectral information to map the spatial frequencies in the Fourier plane. Then, using solid mathematical foundations, we develop theoretically and demonstrate numerically and experimentally the application of several algorithms for compressionless reconstruction of high-contrast amplitude images and low-contrast phase images. This work is motivated by the need for a real-time, high SNR THz imaging system capable of medium-to-high spatial resolution. We believe that the proposed hybrid spatial/spectral image acquisition modality in the Fourier plane can enable such systems with already existing technologies.

Funding. Canada Research Chairs; Canada Foundation for Innovation (CFI) (Project 34633) in Ubiquitous THz Photonics.

CHAPTER 6 TERAHERTZ SUBWAVELENGTH IMAGING USING SUPER-RESOLUTION DETERMINISTIC FLUCTUATIONS

6.1 Introduction

Terahertz science and technology (0.1-10 THz, wavelengths of 3 mm-30 μm) are now mature research fields with many fundamental and practical applications in sensing and imaging [1, 15]. THz subwavelength imaging aims at developing THz microscopes able to resolve deeply subwavelength features [172]. To improve the spatial resolution beyond the diffraction limit, a current trend in the THz research is to measure the wave in the near-field region using focusing optical components such as apertures [192], metallic tips [204], solid immersion lenses [182], dielectric cuboids [178], etc. While these techniques offer significant gains in spatial resolution, they inherently lack the ability to rapidly obtain a THz image, due to the necessity of a slow pixel-by-pixel raster scan.

To overcome this challenge, several designs of subwavelength imaging systems have been proposed where the sample is in direct contact with a multipixel detector for parallel pixel acquisition. In one of these approaches, the sample is brought in contact with a nonlinear crystal which is then used for two-dimensional electro-optic sampling with sensitive visible CCD cameras [261, 453]. Recently, a fully integrated THz near-field camera was developed where both the emitter and detector were fabricated on the same chip using SiGe hetero-junction bipolar transistor technology [185].

Computational imaging techniques have also been developed for applications in the terahertz range, including single-pixel imaging and compressive sensing [369, 384]. There, the sample is placed on a semiconductor substrate that also acts as a spatial light modulator when optically pumped. Specially designed patterns obtained using a digital micromirror device are then used as illumination masks for imaging with single-pixel detector [382, 454]. Moreover, subwavelength imaging is achieved by placing the sample in direct contact with the mask, allowing to encode near-field features in the reconstructed image.

In the meantime, in the visible range of the spectrum, super-resolution imaging techniques have been developed in the past years to significantly beat the diffraction limit [455, 456]. These techniques involve a computational treatment of a collection of images (frames), along with the statistical and localization properties of fluorophores. One of these techniques is known as super-resolution optical fluctuation imaging (SOFI) [457, 458]. By assuming that the fluorescent labels switch rapidly and stochastically between binary on/off states, a higher

resolution image is reconstructed from a collection of frames, using the statistics of cumulants. We are interested in applying a similar methodology for the THz range. However, there are no natural fluorophores in the THz range [459]. Nonetheless, since the wavelengths in THz are large enough, we propose in this work to conceive "artificial blinking fluorophores" by using a collection of blinking masks brought close to the object. This methodology can already be technically realized using spatial light modulation as in THz single-pixel imaging for example [382]. In addition, since we directly control the form of the blinking masks, rather than relying on statistics of a large number of frames, we can design efficient super-resolution masks using very few frames. This is important, because the video frame rate is one of the challenges in modern super-resolution imaging, even in the visible range.

This paper is organized as follows. First, in Section 6.2, we develop the theoretical background for the design of the illumination masks. We then construct phase masks and demonstrate experimental super-resolution imaging at the second order. Next, in Section 6.3, we show how to modify the super-resolution algorithm to be able to use binary on/off amplitude masks, again at the second order. Finally, in Section 6.4, we demonstrate how to improve the resolution further, by providing solutions to the higher order problem.

6.2 Super-resolution Reconstruction using Deterministic Fluctuations

Considering a linear imaging system, the measured image $E(\vec{r})$ is the spatial convolution of the object $O(\vec{r})$ with the system's impulse response $S(\vec{r})$, also known as the point spread function (PSF):

$$E(\vec{r}) = \iint \mathrm{d}\vec{r}_1 S(\vec{r} - \vec{r}_1) O(\vec{r}_1) M(\vec{r}_1, t) \tag{6.1}$$

In Eq. 6.1 $M(\vec{r}_1, t)$ corresponds to the complex mask set where the different frames are encoded in the "temporal" variable t. We start by considering the square of the image. By denoting $\langle ... \rangle$ the temporal average over the frames, we obtain

$$\langle E^2(\vec{r}, t) \rangle = \iint \mathrm{d}\vec{r}_1 \mathrm{d}\vec{r}_2 S(\vec{r} - \vec{r}_1) S(\vec{r} - \vec{r}_2) O(\vec{r}_1) O(\vec{r}_2) \cdot \langle M(\vec{r}_1, t) M(\vec{r}_2, t) \rangle \tag{6.2}$$

It is straightforward to see that taking the square of the image does not directly contribute to a higher resolution image. However, by judiciously designing the set of masks, we can obtain a high-resolution reconstruction. In the following, we detail three conditions that dictate the form of the mask set $M(\vec{r}, t)$.

First, we assume that

$$S(\vec{r} - \vec{r}_1) S(\vec{r} - \vec{r}_2) = 0 \text{ if } |\vec{r}_1 - \vec{r}_2| > D \tag{6.3}$$

where D is the characteristic width of the PSF. This essentially means that two features are resolved if they are already well separated in space, which is easily verified for Gaussian-like PSFs [Fig. 6.1(a)]. In other words, two features that are very far from one another can be turned ON at the same time without affecting the resolution of the resulting image. This condition contributes to a significant reduction of the number of required frames. Using that condition, the mask set can be constructed using a group of subpixels periodically patterned to cover the whole object. Due to Eq. 6.3, this group of pixels must have a dimension somewhat related to the PSF size. Furthermore, we are not limited to using square tiling, as the triangular tiling and the hexagonal tiling can also span the two-dimensional plane [Fig. 6.1(b)].

In the second condition, we assume that the mask set is derived from an orthogonal basis

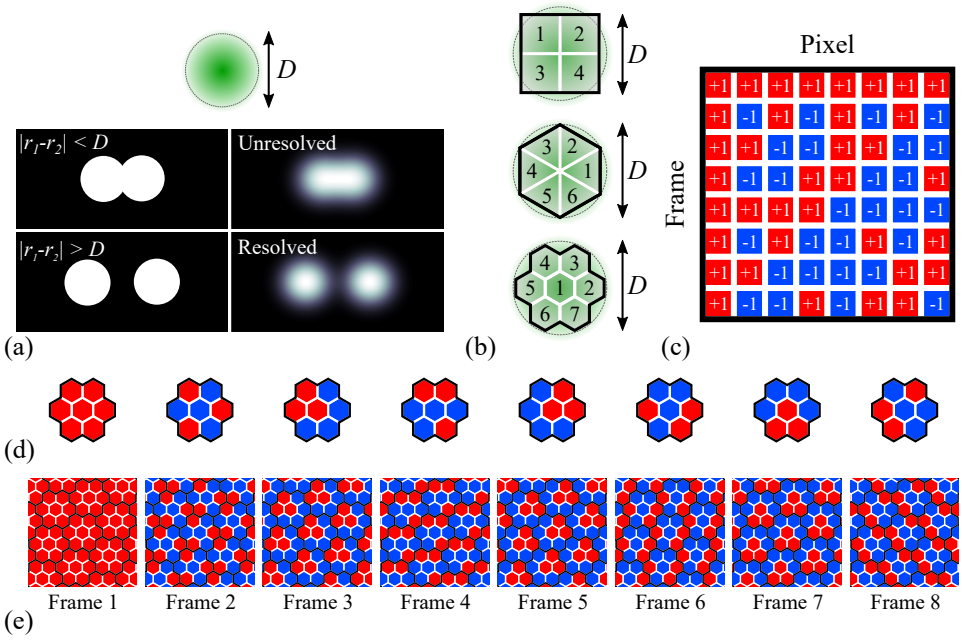

Figure 6.1 Super-resolution reconstruction with deterministic fluctuations. (a) Two features are said to be resolved if they are separated in space beyond the characteristic size D of the PSF. (b) Square (4 pixels), triangular (6 pixels) and hexagonal (7 pixels) arrangement of pixels to cover the 2D space. (c) Hadamard matrix used in the second-order reconstruction where the pixels are encoded in the columns, and the frames in the rows. (d) 8 elementary group of 7 pixels arranged in a hexagonal tiling based on the Hadamard basis, and (e) corresponding 8 frames where the 8 group of pixels are repeated to cover the whole field-of-view.

such that

$$\langle M(\vec{r}_1,t)M(\vec{r}_2,t)\rangle = \frac{1}{N_t}\sum_{i=1}^{N_t} M(\vec{r_1},t_i)M(\vec{r_1},t_i) = \begin{cases}\alpha_1 & \text{if } \vec{r_1}=\vec{r_2}\\ 0 & \text{else}\end{cases} \tag{6.4}$$

where N_t is the total number of frames and α_1 is a constant than can be ignored following an appropriate normalization. The mask set can be better visualized using a matrix notation, where the rows are the temporal frames, while the columns are the pixels. For example, such a mask set can be constructed from the Hadamard matrix where the columns are all mutually orthogonal vectors [Fig. 6.1(c)]. In the context of our theory, the matrix is not necessarily square, as there may be more frames than the number of pixels. Due to the first condition, the orthogonality condition [Eq. 6.4] needs to be applied only to the subpixels forming the patterned tiling. Indeed, using such condition, we ensure that every pixel of the mask is orthogonal to every other pixel, guaranteeing that every frame leads to a reconstruction of higher resolution.

Finally, the third condition requires that for every pixel:

$$\sum_{i=1}^{N_t} M(\vec{r},t_i) = \alpha_2 \quad \forall\vec{r} \tag{6.5}$$

where α_2 is a given constant that is the same for all pixels. This condition ensures that every subpixel contributes equally to the reconstruction. In other words, this ensures that the object is uniformly illuminated by the mask set when changing the frames.

Using the Hadamard matrix, one can construct a mask set that respects the three above-mentioned conditions. In Fig. 6.1(c)-(e), we construct such a set using the Hadamard basis of dimension 8 and 7 hexagonal pixels. The Hadamard basis of dimension 8 is shown in Fig. 6.1(c), where we consider the rows as the temporal frames and the columns as the pixels. After neglecting the first column (which would violate the uniform illumination condition of Eq. 6.3), we can arrange the 7 remaining pixels on a hexagonal lattice [Fig. 6.1(d)] to create 8 consecutive frames [Fig. 6.1(e)].

With the above-mentioned conditions and an appropriate set of masks, the reconstructed image then becomes:

$$\langle E^2(\vec{r},t)\rangle = \iint \mathrm{d}\vec{r}_1 S^2(\vec{r}-\vec{r_1})O^2(\vec{r_1}) \tag{6.6}$$

Eq. 6.6 shows that the reconstructed image is now a convolution of the object with the square

of the PSF. In general, the PSF can be expressed as a Gaussian of width σ:

$$S(\vec{r}) = \exp\left(-\frac{|\vec{r}|^2}{\sigma^2}\right) \tag{6.7}$$

Therefore, taking the square of that Gaussian yields another Gaussian of a reduced width $\tilde{\sigma} = \sigma/\sqrt{2}$, thereby leading to an improved resolution.

We present in Fig. 6.2 an experimental result of our super-resolution reconstruction technique. As a sample we use a metal mask in the form of the fleur-de-lys. As explained above, the 8 frames are formed using 7 pixels derived from the Hadamard basis arranged in a hexagonal lattice with an inter-hole distance of 2 mm [Fig. 6.2(a)]. To realize the +1 and -1 elements of the Hadamard basis, we use phase masks obtained by varying the thickness of a 3D printed mask in PLA (refractive index 1.6). Indeed, the incurred phase vary following $\phi = 2\pi(n-1)d/\lambda$, with n and d the refractive index and thickness. Thus, by varying the thickness from 0 to 800 μm, we modify the local phase from 0 to π at 0.32 THz, to create +1 and -1 elements respectively. We fabricate 8 masks that correspond to the 8 frames of the Hadamard basis.

We then use THz time-domain spectroscopy for amplitude [Fig. 6.2(b)] and phase [Fig. 6.2(c)] imaging [17]. The object with the superimposed phase mask were placed in the focal plane of a pair of parabolic mirrors and raster-scanned to obtain an image. This imaging technique can be used as it respects the equation of linear imaging [Eq. 6.1]. As can be seen, interference patterns caused by the phase masks are obtained in the measured frames. Next, following Eq. 6.6, we compute our super-resolution image by taking the average of the square of each frame $\langle E(\vec{t},t)\rangle$. The original image amplitude and phase are shown in Fig. 6.2(d), while our super-resolution image is shown in Fig. 6.2(e). Since we consider that the collection of frames $\langle E(\vec{r},t)\rangle$ is complex, so is $\langle E^2(\vec{r},t)\rangle$. Therefore, we obtain an amplitude and phase super-resolution image as shown in Fig. 6.2(e). It is worth noticing that our algorithm squares the object [Eq. 6.6]. This has the effect of distorting the relative values of the amplitude and phase. In Fig. 6.2(f), we plot $\sqrt{\langle E(\vec{r},t)\rangle}$, which allows to maintain the same values while also increasing the resolution. Finally, to better see the effect of our algorithm on the resolution, we plot the amplitude and phase cross-sections at the position where the leaves meet. In the original image, the three middle leaves can hardly be distinguished, while our super-resolution reconstruction is clearly able to resolve them. By taking the square-root, we restore correct amplitude and phase values while also resolving the three leaves.

6.3 Binary Amplitude Masks

In the previous section, we showed the reconstruction of second order using a spatial phase modulation. Here, we show an alternate reconstruction that can use amplitude modulation. This case is important, because modern spatial light modulators developed in the terahertz range modify the local amplitude of the THz radiation [382, 454].

Starting from the Hadamard basis shown previously [Fig. 6.1(c)], we can derive a set of masks with >40% transmission that contains only 0 and 1 elements. These elements can be interpreted as opaque and transparent regions of a binary amplitude mask, for example a metal mask. Simply by replacing the -1 elements by 0 and after omitting the first column once again, the new constituted mask set is now a solution to the following modified super-

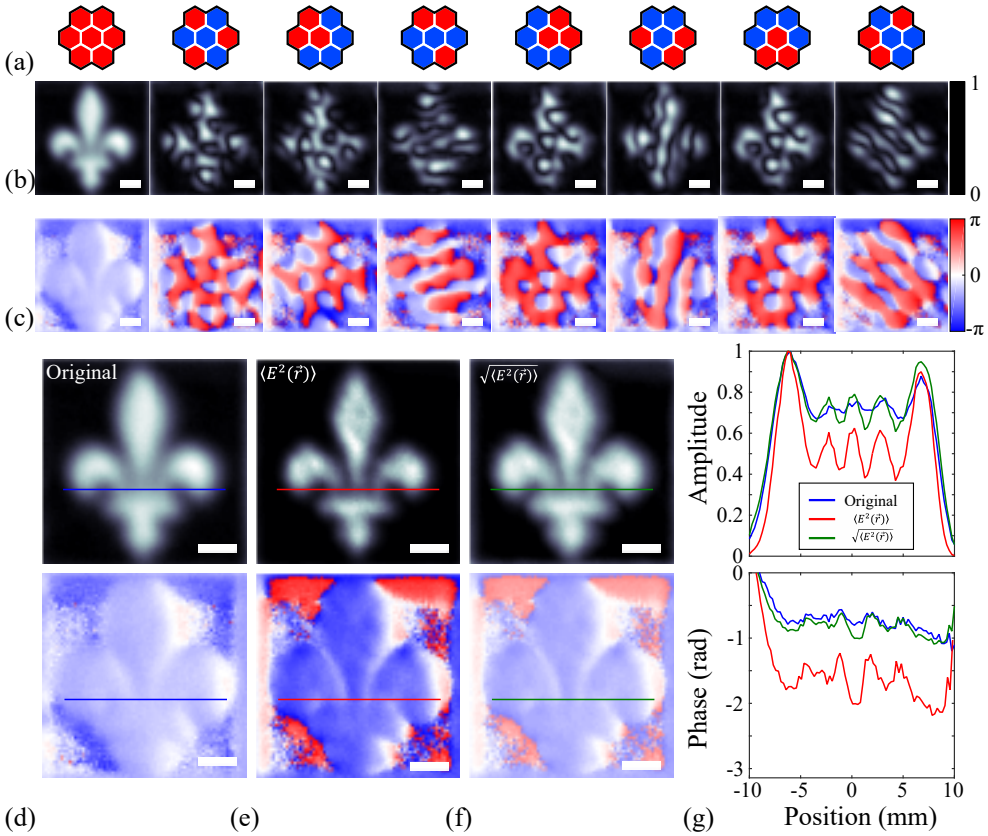

Figure 6.2 Second order reconstruction using phase masks and Hadamard basis. (a) Elementary phase pixels, and (b) amplitude and (c) phase of the corresponding measured frames. (d) Amplitude (top) and phase (bottom) of the original image, (e) the super-resolution reconstruction using $\langle E^2 \rangle$ and (f) the super-resolution reconstruction using $\sqrt{\langle E^2 \rangle}$). (g) Cross-section of the amplitude (top) and phase (bottom) at the position where the three leaves meet. Bar is 5 mm.

resolution algorithm:

$$\begin{aligned}\langle E^2(\vec{r},t)\rangle - \langle E(\vec{r},t)\rangle^2 = \iint \mathrm{d}\vec{r}_1\mathrm{d}\vec{r}_2 S(\vec{r}-\vec{r}_1)S(\vec{r}-\vec{r}_2)O(\vec{r}_1)O(\vec{r}_2) \\ \cdot \left(\langle M(\vec{r}_1,t)M(\vec{r}_2,t)\rangle - \langle M(\vec{r}_1,t)\rangle \langle M(\vec{r}_2,t)\rangle\right)\end{aligned} \tag{6.8}$$

Indeed, one can easily verify that the new mask set with 7 pixels respects the following orthogonality condition:

$$\begin{aligned}&\langle M(\vec{r}_1,t)M(\vec{r}_2,t)\rangle - \langle M(\vec{r}_1,t)\rangle \langle M(\vec{r}_2,t)\rangle \\ &\qquad = \frac{1}{N_t}\sum_{i=1}^{N_t} M(\vec{r_1},t_i)M(\vec{r_1},t_i) - \frac{1}{N_t}\sum_{i=1}^{N_t} M(\vec{r_1},t_i)\frac{1}{N_t}\sum_{i=1}^{N_t} M(\vec{r_2},t_i) \\ &\qquad = \begin{cases}\alpha_1 & \text{if } \vec{r_1}=\vec{r_2} \\ 0 & \text{else}\end{cases}\end{aligned} \tag{6.9}$$

Again, using a set of masks that respects this new definition of the orthogonality, the super-resolution algorithm reconstructs a higher resolution image since the PSF is now squared:

$$\langle E^2(\vec{r},t)\rangle - \langle E(\vec{r},t)\rangle^2 = \iint \mathrm{d}\vec{r}_1 S^2(\vec{r}-\vec{r}_1)O^2(\vec{r}_1) \tag{6.10}$$

The super-resolution in Eq. 6.10 has the form of the variance of the measured frames. In addition to be compatible with binary amplitude masks, the case described here indicates that there is no restriction in the definition of the super-resolution algorithm. In principle, one can use any function of the measured frames to reconstruct a higher resolution image as long as the corresponding orthogonality condition is respected with the appropriate mask set.

We experimentally demonstrate in Fig. 6.3 the reconstruction of a super-resolution image using the binary amplitude mask derived from the Hadamard basis [Fig. 6.3(a)]. As expected, the measured frames [in amplitude Fig. 6.3(b) and phase Fig. 6.3(c)] show no significant spatial variation of the phase as compared to the previous case. The original image and the reconstruction are shown in Fig. 6.3(d). Compared to the phase masks which are designed for a specific THz frequency (since the phase evolves with the wavelength), here the reconstruction can be performed on a larger bandwidth. When using our super-resolution algorithm, we reconstruct a higher resolution image. However, when increasing the THz frequency, we start observing artifacts in the reconstruction image in the form of multiple dots. These start to appear because the size of the PSF at higher frequencies becomes comparable or smaller than the individual elements of the patterned mask (therefore violating the condition

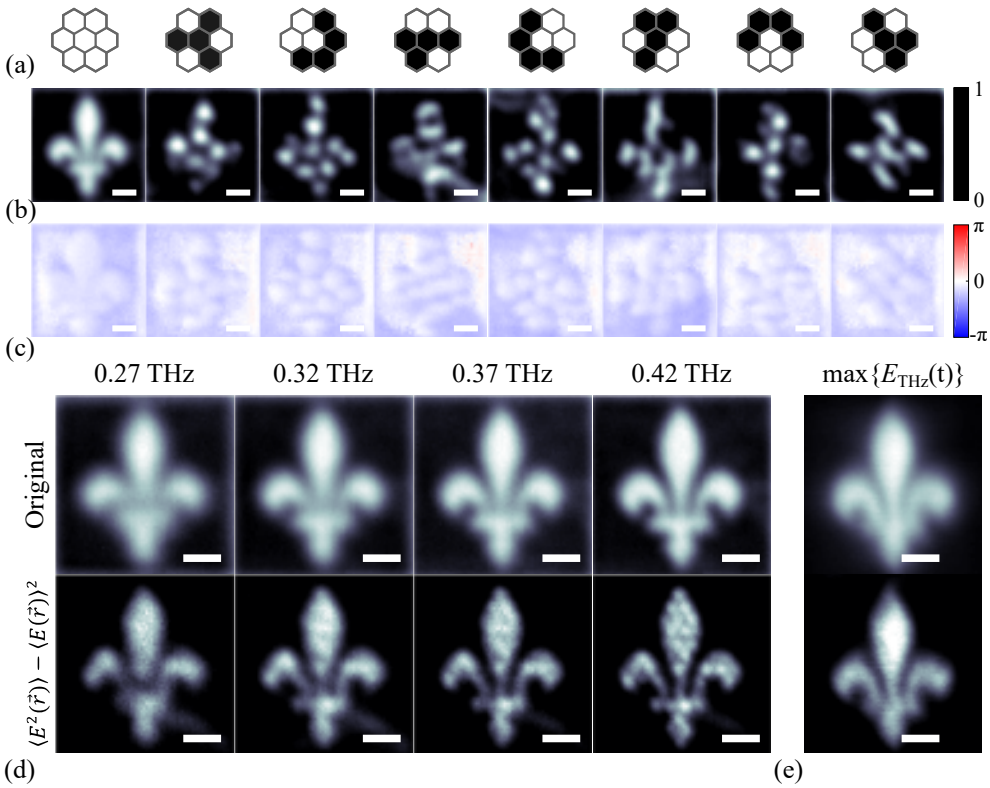

Figure 6.3 Second order reconstruction using binary masks and a modified Hadamard basis. (a) Elementary binary pixels and (b) amplitude and (c) phase of the corresponding measured frames. (d) Comparison of the original image (top) and the super-resolution reconstruction using $\langle E^2\rangle - \langle E\rangle^2$ (bottom) for different frequencies and (e) when considering the maximum amplitude peak in time domain. Bar is 5 mm.

of Eq. 6.3).

Finally, although we used in our experiments a THz-TDS imaging system able to provide amplitude and phase imaging at several frequencies, the super-resolution algorithms shown here are not restricted to coherent measurements. Indeed, our super-resolution algorithm does not specify the nature of the frames $E(\vec{r},t)$. As long as the image can be represented as the convolution of some measurand with a given PSF [Eq. 6.1], we can apply our super-resolution algorithm. In Fig. 6.3(e), we show the reconstruction using the maximum value of the peak THz electric field in time-domain. This measurand is often used to reconstruct THz images as it provides rapid images without the need to move the delay line of the THz-TDS system [454]. Again, we observe the resolution improvement.

6.4 Super-resolution Reconstruction of Higher Orders

In the previous sections, we restricted the algorithm to second-order improvement of the resolution. Naturally, one can construct higher order super-resolution by using more multipliers in the initial definition of the super-resolution algorithm. In general, for a n-order super-resolution, the reconstruction becomes

$$\begin{aligned}\langle E^n(\vec{r},t)\rangle = \iint \mathrm{d}\vec{r}_1 \cdots \mathrm{d}\vec{r}_n S(\vec{r}-\vec{r}_1)S(\vec{r}-\vec{r}_2)\cdots S(\vec{r}-\vec{r}_n)O(\vec{r}_1)O(\vec{r}_2)\cdots O(\vec{r}_n) \\ \langle M(\vec{r}_1,t)M(\vec{r}_2,t)\cdots M(\vec{r}_n,t)\rangle\end{aligned} \tag{6.11}$$

where if the "orthogonality" condition is defined as

$$\begin{aligned}\langle M(\vec{r}_1,t)M(\vec{r}_2,t)\cdots M(\vec{r}_n,t)\rangle &= \frac{1}{N_t}\sum_{i=1}^{N_t} M(\vec{r_1},t_i)M(\vec{r_2},t_i)\cdots M(\vec{r_n},t_i) \\ &= \begin{cases}\alpha_1 & \text{if } \vec{r_1}=\vec{r_2}=\cdots=\vec{r_n} \\ 0 & \text{else}\end{cases}\end{aligned} \tag{6.12}$$

then the reconstructed image is now the convolution with the n power of the PSF:

$$\langle E^n(\vec{r},t)\rangle \iint \mathrm{d}\vec{r}_1 S^n(\vec{r}-\vec{r}_1)O^n(\vec{r}_1) \tag{6.13}$$

As previously, considering a Gaussian PSF of width σ [Eq. 6.7], taking the n power of that Gaussian provides another Gaussian with a reduced width $\tilde{\sigma} = \sigma/\sqrt{n}$, leading to an improved resolution.

Finding a basis that strictly respects the orthogonality condition at Eq. 6.13 for a given order n is not trivial. Obviously, the identity matrix would work as a basis for any order. It would correspond to a successive illumination of every pixel by an opaque aperture. However, following Bethe's study of diffraction by a circular hole [195,196], the transmitted electric field decreases with the third power of the aperture size, decreasing at the same time the overall signal-to-noise ratio. In contrast, a pure phase mask allows for a complete transmission of the light. As we showed in Section 6.2, the pure Hadamard basis is a solution with 100% transmission for second order. The modified Hadamard basis with binary elements presented in Section 6.3 allows for >40% transmission of the light at each frame.

When increasing the order, similarly, one is interested in using mask sets with maximal transmission, preferably pure phase masks. It is important to mention that the condition defined in Eq. 6.12 is not the traditional orthogonality definition when increasing the order

above 2. Indeed, orthogonality is strictly defined for pairs of vectors, while here we can have triplets, quadruplets, etc. To the best of our knowledge, this problem of finding orthogonal basis for higher orders is still an open problem and has not been treated in the scientific literature. Besides, one is not restricted to using a higher order super-resolution reconstruction as defined in Eq. 6.11. Indeed, as we discussed in the previous section, any function of the measured frames can be used to reconstruct a super-resolution image as long as the corresponding orthogonality condition is respected by the considered mask set.

Nonetheless, there are solutions to the problem of finding high order orthogonal basis that respect Eq. 6.12. Remarkably, we found a general solution to the third order super-resolution problem, for any number of pixels N_p. In the following, we present this solution while also providing some hints on how to address the problem. As shown previously, we adopt a matrix notation where M is a rectangular matrix of dimensions $N_t \times N_p$, where the rows correspond to different frames, while the columns correspond to the pixels. Denoting the columns of this matrix as $p_1, p_2, \ldots, p_{N_p}$, Eq. 6.12 can be written as the following matrix operation:

$$\begin{aligned} \langle p_1 p_2 \cdots p_n \rangle &= \frac{1}{N_t} \mathrm{tr}\left[\mathrm{diag}(p_1)\mathrm{diag}(p_2)\cdots\mathrm{diag}(p_n)\right] \\ &= \begin{cases} \alpha_1 & \text{if } p_1 = p_2 = \cdots = p_n \\ 0 & \text{else} \end{cases} \end{aligned} \tag{6.14}$$

where $\mathrm{tr}(A)$ is the trace of the matrix A and $\mathrm{diag}(a)$ is the diagonal matrix of the vector a:

$$\mathrm{diag}(a) = \mathrm{diag}\left(\begin{bmatrix} a_1 \\ a_2 \\ \vdots \\ a_m \end{bmatrix}\right) = \begin{bmatrix} a_1 & 0 & \cdots & 0 \\ 0 & a_2 & \cdots & 0 \\ \vdots & \vdots & \ddots & \vdots \\ 0 & 0 & 0 & a_m \end{bmatrix} \tag{6.15}$$

This matrix notation is important because it offers tractable computational programming to find the solutions. For the third order, Eq. 6.14 reduces to

$$\langle p_i p_j p_k \rangle = \frac{1}{N_t} \mathrm{tr}\left[\mathrm{diag}(p_i)\mathrm{diag}(p_j)\mathrm{diag}(p_k)\right] = \begin{cases} \alpha_1 & \text{if } i = j = k \\ 0 & \text{else} \end{cases} \tag{6.16}$$

To verify the orthogonality condition for a given matrix, one could compute the $(N_p)^n$ possible combinations of vector multiplications to ensure that they are always equal to 0, except when the indices are equal. However, we can easily verify that the product defined in Eq. 6.14 is

commutative by permutation of the vectors. Therefore, in reality, there are only

$$\binom{N_p + n - 1}{n} = \frac{(n + N_p - 1)!}{n!(N_p - 1)!} \tag{6.17}$$

possible combinations. Again, this is important for computational reasons, as it reduces considerably the number of required calculations.

We found a general pure phase solution to the third order super-resolution problem, for any number of pixels N_p. The matrix representing the mask set is constructed by concatenating the three following matrices. By denoting I_N the identity matrix of size N and by denoting $J_{N\times M}$ the matrix of ones of size $N \times M$, the three matrices can be written as:

$$\begin{aligned} A_1 &= J_{N_p\times N_p} - I_{N_p} + iI_{N_p} \\ A_2 &= J_{N_p\times N_p} - I_{N_p} - iI_{N_p} \\ A_3 &= -J_{2(N_p-3)\times N_p} \end{aligned} \tag{6.18}$$

The matrix resulting by concatenating these three matrices in the temporal dimension is a solution to the third order super-resolution reconstruction [Eq. 6.16]. Compared to the Hadamard basis, this solution contains four phase elements: $+1, -1, +i, -i$. The number of required frames is a function of the number of pixels: $N_t = 4N_p - 6$. However, one can see that all the pixels in the last $2(N_p - 3)$ frames are constituted of -1 elements. Therefore, one can in principle measure it only once and consider it $2(N_p - 3)$ times when taking the average. The total number of required frames would then be $N_t = 2N_p + 1$.

We show in Fig. 6.4(a) an example of such a matrix with $N_p = 4$ pixels and $N_t = 10$ frames. To demonstrate that the matrix respects the orthogonality condition, we compute the 20 possible combinations (neglecting the commutative operations) of vectors entering the third order orthogonality definition [Eq. 6.16]. As we can see in Fig. 6.4(b), the 20 possible multiplications always yield 0, except in the 4 cases where all the three vectors are identical. We arrange the 4 pixels on a 2×2 square grid and we present the corresponding 10 frames in Fig. 6.4(c).

In Fig. 6.4(e), we numerically compare different orders of reconstruction of a 40×40 mm object representing a snowflake [Fig. 6.4(d)]. The convolution of the object with a Gaussian PSF of width 1.5 mm is shown in Fig. 6.4(e). To apply our super-resolution algorithm, we consider 16 subpixels arranged in a 4×4 square grid lattice of size $D = 3.44$ mm, comparable to the full width at half maximum of the considered Gaussian PSF. The 16 pixels are periodically patterned to cover the whole object. We then attribute a value to every subpixel (according

to the selected basis) before multiplying it to the object and computing the N_t convolutions with the PSF [Eq. 6.1]. Finally, to obtain higher resolution images, we compute the n-order reconstruction [Eq. 6.13] from the set of resulting frames. The result for Order 2 is obtained with a Hadamard basis of 16 frames [Fig. 6.4(f)], while the result for Order 3 is constructed using the matrix described in Eq. 6.18 with 33 frames [Fig. 6.4(g)]. To clearly demonstrate that the third order basis is truly an orthogonal solution to the problem defined in Eq. 6.16, we also compute in Fig. 6.4(h) the third order reconstruction using purely random phases

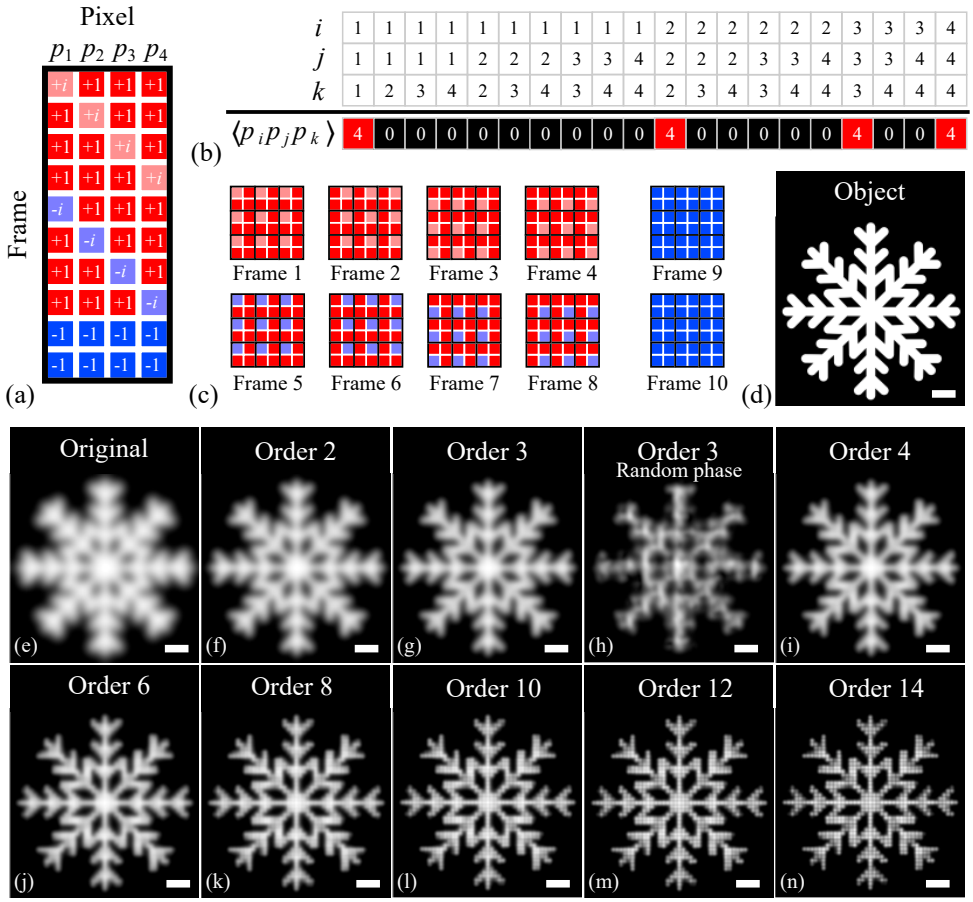

Figure 6.4 Super-resolution reconstruction of higher orders. (a) Rectangular matrix of third order constructed from Eq. 6.18 with $N_p = 4$ pixels. (b) The third order orthogonality operation $\langle p_i p_j p_k \rangle$ is always equal to 0, except when $i = j = k$. (c) Arrangement of the 10 frames made of patterned elementary 2×2 square tiles. (d) Object representing a snowflake and (e) original image obtained with convolution with a Gaussian. (f-n) Super-resolution reconstruction of different orders: (f) Order 2 with Hadamard basis (16 frames). (g) Order 3 following Eq. 6.18 (33 frames). (h) Order 3 with random phase mask to show that the solution we found leads to exact reconstruction (33 frames). (i) Order 4 with the pure phase basis shown in Appendix C (256 frames). (j) Order 6, (k) Order 8, (l) Order 10, (m) Order 12 (n) Order 14 with an identity matrix (16 frames). Bar is 5 mm.

in the matrix. As it is possible to see, the random phase solution incorrectly reconstructs the object. For Order 4 in Fig. 6.4(i), we use the pure phases basis shown in Appendix C (256 frames). Finally, the results for Order 6 to 14 are obtained using an identity matrix corresponding to successive illuminations of the subpixels (16 frames).

As one can see, the reconstruction of the snowflake generally improves when increasing the order n. However, there is a limit in the improvement as shown in Fig. 6.4(l)-(n) (bottom row). Artifacts in the reconstruction in the form of multiple dots start to appear because the individual subpixels of the patterned mask become larger than the width of the n-power PSF. To solve this issue, one could reduce the size of individual subpixels by using more pixels in the matrix. Indeed, in the limit of very small subpixels, the blinkers can be considered as point sources, leading to an exact reconstruction of the original object (in absence of noise). Of course, this would be accompanied with an increase of the total required frames.

6.5 Conclusion

To conclude, we presented a super-resolution reconstruction technique for the THz range. This method is based on super-resolution optical microscopy techniques developed in the visible range, particularly super-resolution optical fluctuation imaging (SOFI). Since there are no natural fluorophores in the THz range, we proposed to fabricate artificial blinkers using spatial light modulation. Starting from the equation of linear imaging systems, we found that it is possible to construct super-resolution images using appropriate mask sets. We experimentally demonstrated pure phase masks and binary amplitude masks with a second order super-resolution reconstruction, using only 8 frames. We also showed how to extend the super-resolution algorithm to higher orders, and we demonstrated a general solution for the third order reconstruction.

This works opens new possibilites in terahertz subwavelength imaging. Simply based on the equation of linear imaging systems [Eq. 6.1] along with spatial modulation of the phase or amplitude of the THz wave, our methodology can already be applied in different imaging scenarios. For example, it can be directly translated to single-pixel imaging by modifying the photomodulated illumination masks [382, 454]. Moreover, as we showed, this technique can be used with incoherent measurements, which opens new possibilities for subwavelength imaging using commercially available THz thermal cameras and THz field-effect transistor-based cameras. Finally, this work can be of interest to the large optical community at other wavelengths, as it provides a clear theoretical framework to manipulate light at a subwavelength scale in order to improve the resolution beyond the diffraction limit.

CHAPTER 7 GENERAL DISCUSSION

In this chapter, we provide a general discussion about how the previous chapters can help reach our main objective of achieving real-time THz imaging. We first discuss the use of various polymers for the fabrication of porous lenses. We then study spectral encoding of the k-space with cylindrical lenses. Finally, we investigate the use of incoherent measurements when using our super-resolution algorithm.

7.1 Porous Lenses in Imaging Systems

In Chapter 4, we demonstrated how porous optical components can achieve lower losses than their all-solid counterparts of identical properties. As we discussed previously, the internal losses of a THz imaging system is an important parameter since ultrasensitive THz detectors are still lacking. In turn, this impacts the acquisition time because more signal averaging may be necessary to obtain an image. In this section, based on the results of Chapter 4, we are interested to know whether commonly used polymers can be used to design low-loss lenses.

We start with Eq. 4.22 which states the power transmission ratio for a lens:

$$\frac{T_{\text{porous}}^{\text{lens}}}{T_{\text{solid}}^{\text{lens}}} = \frac{n_m^4 - n_a^4}{4n_a^2 n_m (n_m - n_a)} \frac{\left[1 - \exp\left(-\Gamma \frac{4n_m n_a^3}{n_m^4 - 1}\right)\right]}{\left[1 - \exp\left(-\Gamma \frac{n_a}{n_m - n_a}\right)\right]} \tag{7.1}$$

with $\Gamma = \alpha_m R^2/2F$. As a reminder, n_m and α_m are the refractive index and power absorption losses of the solid material, while R and F are the radius and focal length of the designed lens. Also, as we discussed in the chapter, Eq. 7.1 is valid in the limit of the Bruggeman model (wavelength larger than the hole size) and for high porosities (when the filling factor $f \to 1$).

For our comparison of different polymers, we consider the experimental results reported by Jin *et al.* [410]. There, refractive indices and power absorption losses in the range from 0.2 to 3 THz were obtained using a THz-TDS in transmission geometry using a similar methodology as that shown in Section 2.2.2. Table 7.1 shows the polymers used in that article along with the measured refractive index at 1 THz. For the following calculations, we assume constant refractive index, which is in agreement for the reported polymers in the spectral region under study. The power absorption losses are shown in Fig. 7.1(a) and (b), where the data points were extracted from Fig. 3b of Ref. [410].

Table 7.1 Polymer samples and corresponding refractive index reported by Jin *et al.* [410]

Abbreviation	Full name	Refractive index (at 1 THz)
Polyaramid	Polymetaphenylene isophthallamide	1.801
PA6	Polyamide nylon 6	1.736
PET	Polyethylene terephthalate	1.712
ABS	Polyacrylonitrile-butadiens-styrene	1.650
PMMA	Polymethlmethacrylate	1.596
PC	Polycarbonate	1.651
HDPE	High density polyethylene	1.534
PTFE	Polytetrafluoroethylene	1.445
PP	Polypropylene	1.510

With Eq. 7.1, we calculate in Fig. 7.1(c,d) the transmission ratios between a porous and a solid lens for each polymer. For our calculations, we consider a lens with a focal length of 80 mm and a radius of 18 mm (similar to the experiments in Chapter 4). For the high losses materials [Fig. 7.1(c)], we reach large transmission ratios, with above 40% in general and as high as 65% for Polyaramid. As we previously discussed, these results were expected for very lossy materials. More interestingly, even with low-loss polymers that are more seriously considered for lens fabrication, we observe a 5% to 10% increase in the transmitted power [Fig. 7.1(b)]. This result is indeed very promising, especially since imaging systems generally contains multiple lenses.

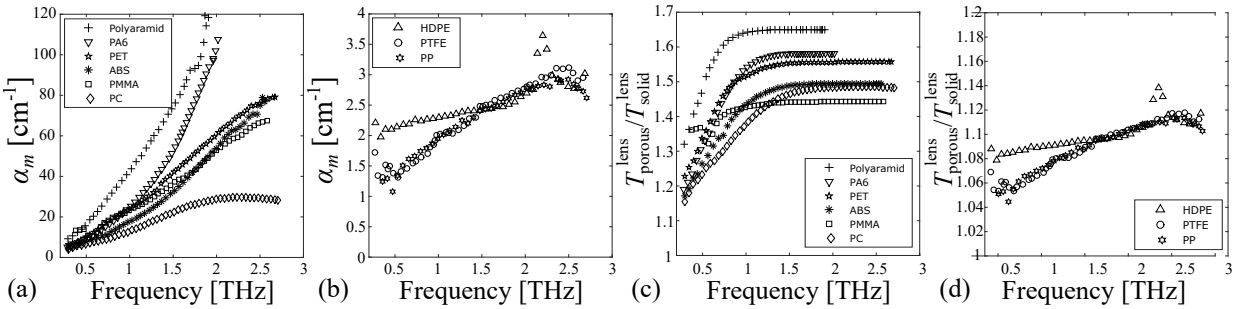

Figure 7.1 Power absorption losses as reported by Jin *et al.* [410] for common (a) high and (b) low losses polymers. Transmission ratio of the porous over all-solid lens with $F = 80$ mm and $R = 18$ mm for common (c) high and (d) low losses polymers.

7.2 Spectral Encoding of the k-space with Cylindrical Lenses

In Chapter 5, we showed that by spectrally encoding the k-space we can reconstruct an image using very few spectral measurements measured along a circular path in the Fourier plane. In the following, we would like to mention few additional points that may be useful to enable real-time THz imaging using k-space encoding.

First, one could use the symmetry of the Fourier plane to further reduce the number of measurements. Indeed, if the object is purely real (or can be considered real assuming a weak imaginary part), then its 2D Fourier transform is Hermitian, i.e. $F(k_x, k_y) = F^*(-k_x, -k_y)$, with (k_x, k_y) a point in the Fourier plane and * indicating the complex conjugate. Therefore, in principle, one can measure only half of the circular path and deduce the opposite values using this centrosymmetric property.

Second, the main problem of our experimental setup is undoubtedly the slow circular movement of the detector in the Fourier plane. Ideally, multiple fixed detectors would be positioned along this circular path for parallel spectra acquisition. This requires however a complex antenna design. Another possibility would be to fix the detector to a stable Fourier position and rotate the object itself.

Third, an interesting alternative to our experimental setup would be to use a cylindrical lens. Indeed, while the spherical lens essentially acts a 2D Fourier transformer, the cylindrical lens would perform 1D Fourier transform along the lens axis. This type of geometry could then be used in conjunction with a translating stage, for example a conveyor belt, to enable real-time imaging in industrial environments. However, as we will in the following numerical calculations, the Fourier transform is affected differently by the cylindrical lens and the detector size becomes an important parameter.

In the following, we use the Fresnel diffraction integral (see Appendix D for more details) to calculate the propagation of the THz wave from the input object plane to the Fourier plane [Fig. 7.2(a)]. We consider a planar phase THz wave incident on the object at a frequency of 300 GHz. We select a lens with a radius of $R = 50$ mm and a focal length of $F = 150$ mm, similar to the experiments of Chapter 5. As an object, we consider the maple leaf shown in Fig. 7.2(b) positioned at a focal length from the lens. We are interested in calculating the electric field in the Fourier plane (at a focal length distance from the lens).

The calculations involves the three following steps:

1. Propagation from the object to the lens over a distance $z = 150$ mm

2. Multiplication by the following lens function

$$\varphi(x,y) = \begin{cases} \exp\left[-i\frac{k}{2F}(x^2+y^2)\right] & \text{if } x^2+y^2 < R \quad \text{(spherical lens)} \\ \exp\left[-i\frac{k}{2F}x^2\right] & \text{if } x^2+y^2 < R \quad \text{(cylindrical lens)} \\ 0 & \text{else} \end{cases} \tag{7.2}$$

3. Propagation from the lens to the Fourier plane over a distance $z = 150$ mm

We show in Fig. 7.2(c) the calculation result of the propagation from the object to the lens. Then, we multiply by the spherical lens function in Fig. 7.2(d), and by the cylindrical lens

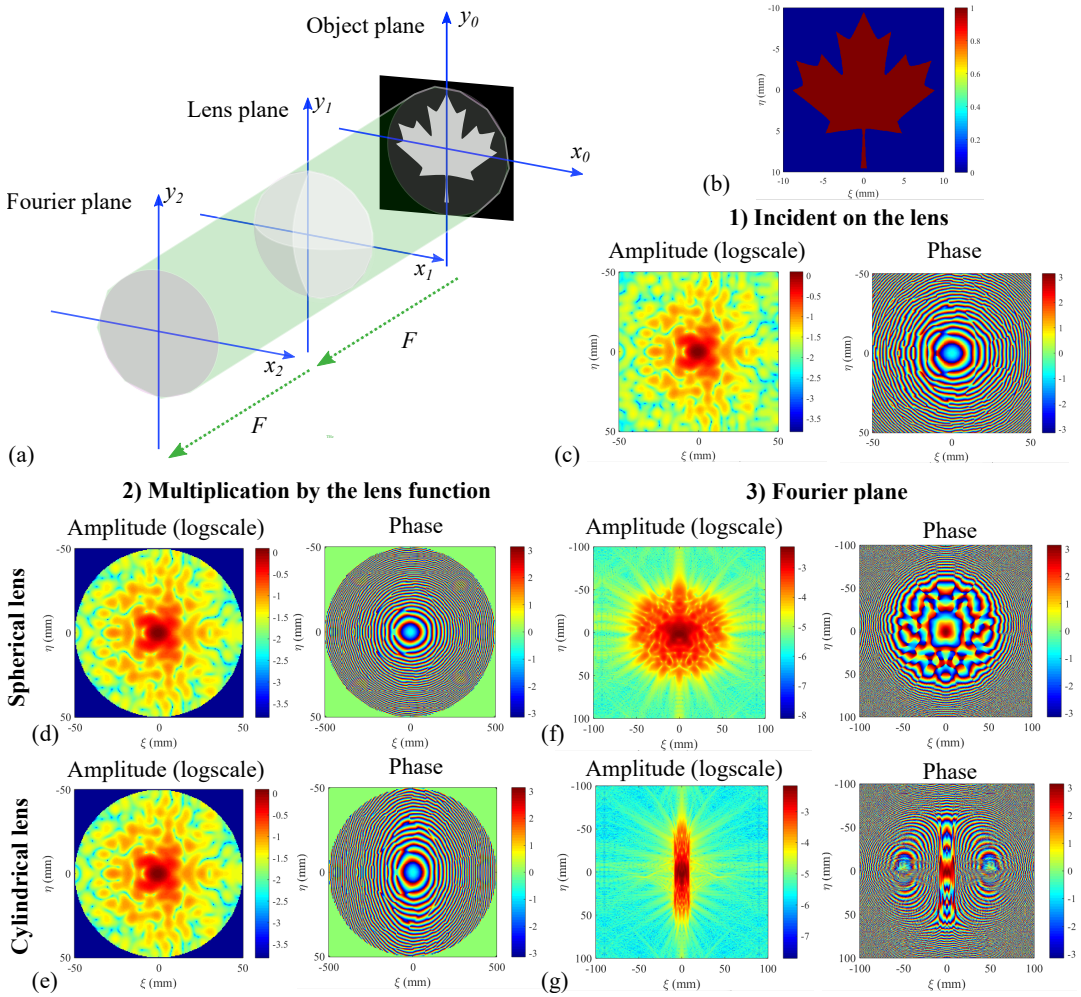

Figure 7.2 (a) Geometry used in the calculations of the Fourier transform. (b) Binary amplitude sample representing a maple leaf. (c) Amplitude and phase incident on the lens. (d) Multiplication by a spherical and (e) cylindrical lens. (f) Result in the Fourier plane for a spherical and (g) cylindrical lens.

in Fig. 7.2(e). The propagation to the Fourier plane is calculated and shown in Fig. 7.2(f) and (g) for the spherical and cylindrical lens respectively.

In Fig. 7.3, we compute the inverse Fourier transforms of the results obtained in the Fourier plane. As expected, for the spherical lens a 2D inverse Fourier transform is able to reconstruct the original maple leaf as shown in Fig. 7.3(a). As for the cylindrical lens, the maple leaf is correctly reconstructed only when considering 1D Fourier transform on each individual y lines [7.3(b)].

However, it is important to mention that these results do not take into account the finite size of the detector in the Fourier plane. Indeed, in the experiments, we used a photoconductive antenna attached to a silicon lens with a diameter of 10 mm. The large detector size impacts the actual reconstruction as we show in the following. To simulate the effect of the detector

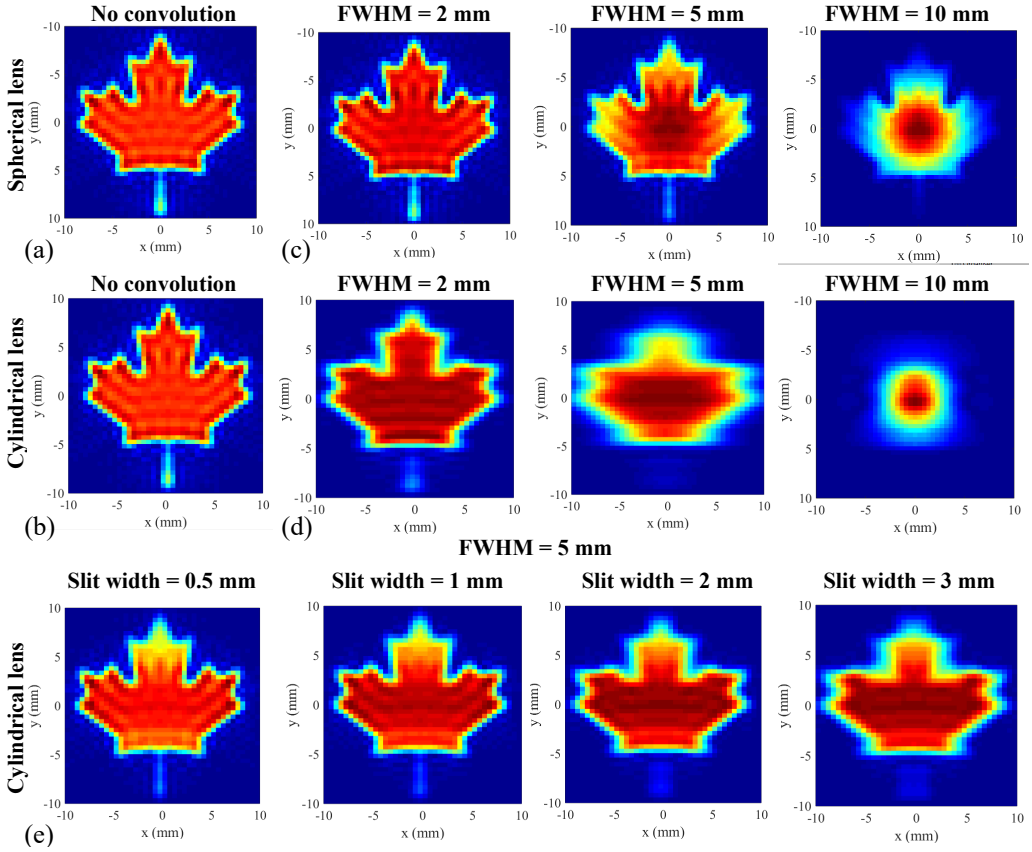

Figure 7.3 Reconstruction of the maple leaf. (a) 2D inverse Fourier transform with spherical lens. (b) 1D inverse Fourier transform on individual y lines with cylindrical lens. (c) Reconstruction results when considering a convolution with a Gaussian of different FWHMs for a spherical and (d) cylindrical lens. (e) Addition of a slit of different widths for the cylindrical lens considering a convolution with a Gaussian of 5 mm FWHM.

size, before computing the inverse Fourier transform, we convolve the Fourier plane result $U_F(x_0, y_0)$ with a 2D Gaussian function:

$$U_1(x_1, y_1) = \iint U_F(x_0, y_0) \exp\left[-\frac{(x_0 - x_1)^2 + (y_0 - y_1)^2}{2\sigma^2}\right] \mathrm{d}x_0 \mathrm{d}y_0 \tag{7.3}$$

where the full width at half maximum (FWHM) is related to the σ parameter: FWHM $= 2\sqrt{2\ln 2}\sigma$.

We show in Fig. 7.3(c) and (d) the results of the inverse Fourier transforms when considering a convolution with Gaussians of different FWHMs. To understand the effect of the detector size, one has to note that the step size in the Fourier plane dk_x is inversely proportional to the field-of-view $\Delta x = 1/dk_x$ of the reconstructed image. This is particularly evident in the case of the spherical lens [Fig. 7.3(c)]. There, as the FWHM increases, the field-of-view decreases as it can be observed by the concentration of the amplitude in image center.

For the cylindrical lens, it is slightly more complex. As we can see in Fig. 7.3(d), the reconstruction is more sensitive to the size of the detector. Indeed, while the field-of-view argument still holds in the direction of the Fourier transform, it becomes invalid in the perpendicular direction. This is because the cylindrical lens only acts on one axis, while the detector is considered spherical and acts on both axis. In fact, in the perpendicular direction, the resolution of the reconstructed image is limited by the detector size itself, as the detector performs an "averaging" along this axis.

To reduce the "averaging" effect along the perpendicular direction, one could use a slit aperture positioned in front of the detector, aligned parallel to the Fourier transform axis of the cylindrical lens. To simulate this effect numerically, we modify the convolution by multiplying the Gaussian (FWHM of 5 mm) by a step function corresponding to the width of the slit. The resulting reconstructions are shown in Fig. 7.3(e). As expected, the reconstruction improves with smaller slit widths.

7.3 Real-time Super-resolution Imaging with Incoherent Measurements and a THz Camera

In Chapter 6, we showed how deterministic fluctuations at the subwavelength scale could be used to obtain super-resolution images beyond the diffraction limit. Here, we want to further discuss how this technique could help reach real-time operation in THz microscopy imaging.

As we discussed in Section 2.4, there is an on-going research to develop THz microscopes able to resolve deeply subwavelength features. In the meantime, THz cameras are becoming more

sensitive (Section 2.4). Therefore, we can expect in a near future the development of THz microscopic systems using similar configuration as those developed in the visible range. The super-resolution technique we demonstrated could then be directly applied in those systems.

We show in Fig. 7.4(a), a concept idea for such a microscope using binary amplitude masks. The sample could be deposited on a thin semiconductor substrate. Using optical pumping and a digital micromirror device, the different binary masks could then be successively projected on the semiconductor. To avoid the use of a pumping optical source, one could also use metal masks mechanically positioned in front of the sample. A similar idea could be used for phase modulation [Fig. 7.4(b)], where 3D printed masks could be successively aligned in front of the sample.

However, in our experiments, we used a THz-TDS system able to resolve the amplitude and phase electric field, while THz cameras are generally sensitive to the square of the electric field (intensity). In the following, using the experimental results obtained in Chapter 6, we demonstrate that our algorithm is valid even with incoherent measurements.

Indeed, our algorithm starts with the equation of linear imaging systems:

$$\langle E^2(\vec{r},t)\rangle = \iint \mathrm{d}\vec{r}_1\mathrm{d}\vec{r}_2 S(\vec{r}-\vec{r}_1)S(\vec{r}-\vec{r}_2)O(\vec{r}_1)O(\vec{r}_2)\cdot\langle M(\vec{r}_1,t)M(\vec{r}_2,t)\rangle \tag{7.4}$$

where $O(\vec{r})$ is the object, $S(\vec{r})$ is the point spread function (PSF) and $M(\vec{r},t)$ is the complex mask function. Here, we do not specify the nature of the measured image $E(\vec{r})$. In the experiments of Chapter 6, we used THz-TDS imaging, thus we considered complex $E(\vec{r})$. In the following, we use the same experimental results of Sections 6.3 (amplitude masks) and 6.2 (phase masks). To simulate incoherent amplitude-only measurement, we take the absolute value of the measured frames $E(\vec{r}) = |E_{\mathrm{meas}}(\vec{r})|$. As we show in Fig. 7.4(c) and (d), the resulting super-resolution reconstructions are identical to what was obtained when considering the phase as well [Fig. 6.3 and 6.2 respectively]. In this demonstration, we used the amplitude while THz cameras might be sensitive to the intensity (square of the amplitude). If one wanted to use intensities, we note that the size of the patterned mask need to be modified, since the width of the PSF is reduced (due to the squaring).

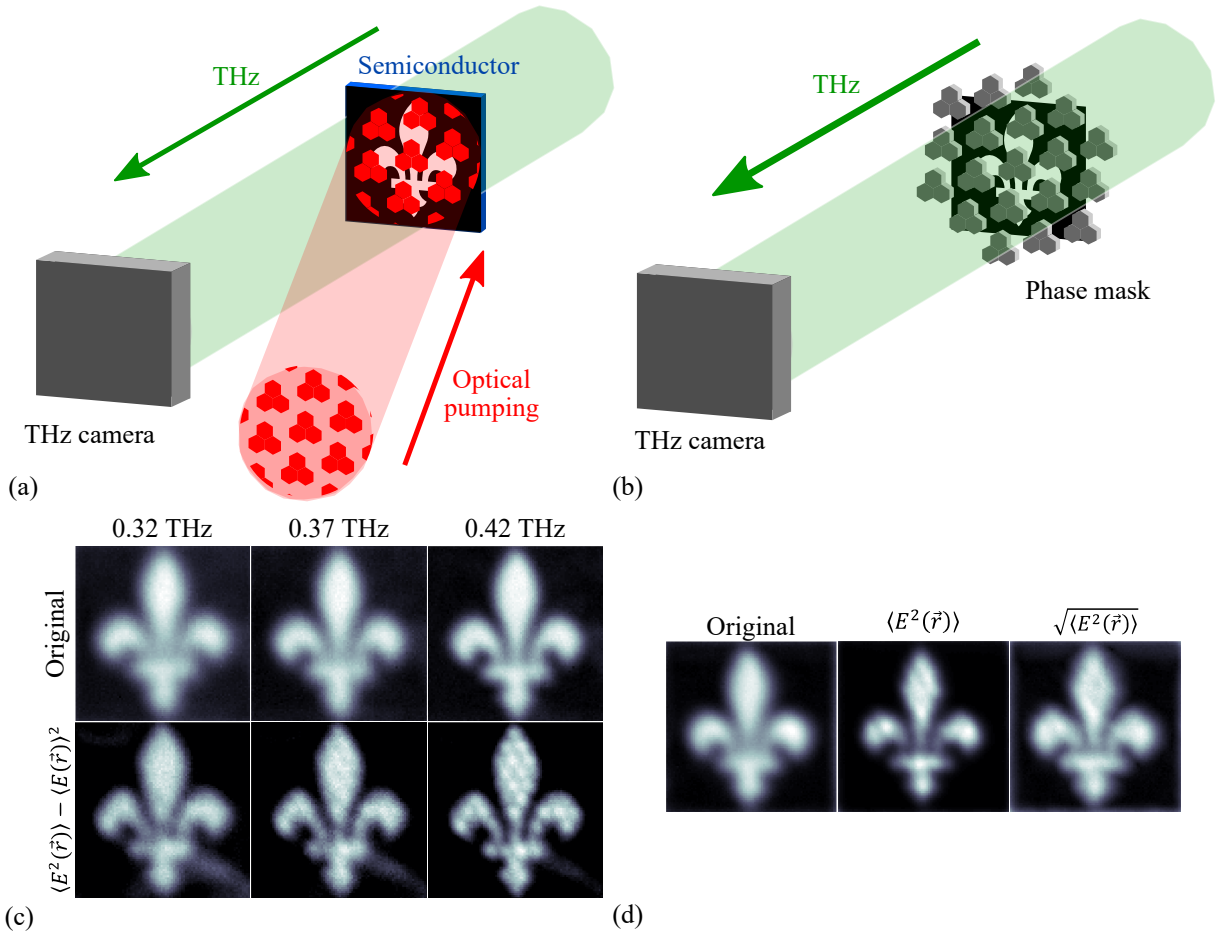

Figure 7.4 Concept idea for using the super-resolution technique with THz camera and (a) binary amplitude masks obtained with optical pumping of a semiconductor and (b) phase masks aligned in front of the object. (c) Results obtained when considering amplitude-only measurements and amplitude and (d) phase modulation.

CHAPTER 8 CONCLUSION AND RECOMMENDATIONS

In this thesis, we have developed techniques to achieve real-time THz imaging. The THz band is a part of the electromagnetic spectrum that has yet to be largely unfolded. In the past two decades, many applications of THz imaging have been explored in various fields. However, despite all the interest, the image acquisition time is still a major hurdle to a wider use of THz imaging.

We started this thesis by reviewing the state-of-the-art in THz imaging, with an emphasis on the technologies enabling real-time operation. After listing key imaging modalities developed in the past years, we focused on practical realizations of real-time THz imaging. We saw that the research can be divided in three main directions, each having its own advantages and drawbacks. 1) Real-time THz-TDS imaging promises hyperspectral coherent amplitude and phase imaging, 2) THz cameras are being developed in a similar fashion than those that exist in the visible range, and 3) Real-time image acquisition using single-pixel detectors is an interesting direction mixing computational techniques to advanced opto-mechanical instrumentation. By covering both theoretical and practical aspects of THz imaging systems, this review can serve a diverse community of fundamental scientists, applied engineers and industrial experts.

We then presented our experimental setup which consisted mainly on a THz-TDS imaging system with a fiber-coupled photoconductive antenna detector for convenient THz scanning. We also discussed various advanced prototyping technologies that we have used throughout the experiments.

Three objectives aimed at achieving real-time THz imaging were at the core of this thesis. These may pave the way to future research.

First, we designed low-loss THz components using porous media to address the problem of low detector sensitivity in imaging systems. We showed that low-refractive index subwavelength inclusions (air holes) in a solid dielectric material can lead to the design of planar optical components with smaller losses than their all-solid counterparts of identical properties. In particular, we fabricated and characterized a planar porous lens and a planar porous orbital angular momentum phase plate. As we then showed, using low-loss polymers can lead to significant increase in the transmitted power. For example, using PTFE (a commonly used polymer for THz lenses) can bring 10% increase at 1.5 THz. This has yet to demonstrated experimentally, the main question being how to easily fabricate 20 μm porous ($\lambda/10$) features in thick polymer slabs. Moreover, following our methodology, other beamforming components

can be designed, such as beamsteerers, cylindrical lenses, Bessel beam generators and so on. More importantly, incorporating porous lenses in imaging systems can increase the image signal-to-noise ratio. Again, this can be shown experimentally.

Second, using spectral encoding of the spatial frequencies, we reduced the number of required measurements to construct a THz image. This is turn reduces the overall image acquisition time. Using Fourier optics, a simple lens and the linear relationship between the spatial frequency and the THz frequency, we demonstrated imaging of amplitude and phase objects using as little as 20 spectral measurements. Future research may study objects with other spectral features, for example absorption peaks. Another interesting subject would be to reconstruct 3D objects using spectral encoding. This could be done using the more general wavelength-dependent diffraction formula. Finally, with cylindrical lens and minor modifications on the size of the detector, real-time THz imaging with a translating stage (conveyor belt) is within reach.

Third, we developed a super-resolution technique aimed at achieving real-time THz microscopy. Using phase and amplitude modulation on a subwavelength scale, we showed how to reconstruct images beyond the diffraction limit from a small set of modulating frames. We showed experimental solutions to the second order reconstruction, and we demonstrated a general solution to the third order. Future research may be directed at finding general solutions to the fourth order and beyond. This may be accompanied by experimental demonstrations. Furthermore, this technique is simply based on the equation of linear imaging systems, therefore it can be applied to various imaging setups, including single-pixel imaging and THz cameras. To rapidly shuffle the modulating frames, one could borrow the optically-pumped semiconductor spatial light modulator developed for single-pixel imaging. With the advent of sensitive THz cameras, we could see the development of microscopy systems similar to those of the visible range. Lastly, using amplitude and phase masks to mimic the fluorophore blinking may also be useful in adapting other super-resolution techniques developed in the visible range.

REFERENCES

[1] S. S. Dhillon *et al.*, "The 2017 terahertz science and technology roadmap," *Journal of Physics D: Applied Physics*, vol. 50, no. 4, p. 043001, Jan. 2017.

[2] D. M. Mittleman, "Perspective: Terahertz science and technology," *Journal of Applied Physics*, vol. 122, no. 23, p. 230901, Dec. 2017.

[3] ——, "Twenty years of terahertz imaging [invited]," *Optics Express*, vol. 26, no. 8, p. 9417, Apr. 2018.

[4] A. Redo-Sanchez *et al.*, "Review of terahertz technology readiness assessment and applications," *Journal of Infrared, Millimeter, and Terahertz Waves*, vol. 34, no. 9, pp. 500–518, Jul. 2013.

[5] M. Yin, S. Tang, and M. Tong, "The application of terahertz spectroscopy to liquid petrochemicals detection: A review," *Applied Spectroscopy Reviews*, vol. 51, no. 5, pp. 379–396, Jan. 2016.

[6] M. Haaser *et al.*, "Application of terahertz pulsed imaging to analyse film coating characteristics of sustained-release coated pellets," *International Journal of Pharmaceutics*, vol. 457, no. 2, pp. 521–526, Dec. 2013.

[7] J. Sibik and J. A. Zeitler, "Direct measurement of molecular mobility and crystallisation of amorphous pharmaceuticals using terahertz spectroscopy," *Advanced Drug Delivery Reviews*, vol. 100, pp. 147–157, May 2016.

[8] M. Kawase, "Application of terahertz waves to food science," *Food Science and Technology Research*, vol. 18, no. 5, pp. 601–609, 2012.

[9] J. Qin, Y. Ying, and L. Xie, "The detection of agricultural products and food using terahertz spectroscopy: A review," *Applied Spectroscopy Reviews*, vol. 48, no. 6, pp. 439–457, Aug. 2013.

[10] K. Wang, D.-W. Sun, and H. Pu, "Emerging non-destructive terahertz spectroscopic imaging technique: Principle and applications in the agri-food industry," *Trends in Food Science & Technology*, vol. 67, pp. 93–105, Sep. 2017.

[11] H.-B. Liu *et al.*, "Terahertz spectroscopy and imaging for defense and security applications," *Proceedings of the IEEE*, vol. 95, no. 8, pp. 1514–1527, Aug. 2007.

[12] S. R. Murrill *et al.*, "Terahertz imaging system performance model for concealed-weapon identification," *Applied Optics*, vol. 47, no. 9, p. 1286, Mar. 2008.

[13] J. B. Jackson *et al.*, "A survey of terahertz applications in cultural heritage conservation science," *IEEE Transactions on Terahertz Science and Technology*, vol. 1, no. 1, pp. 220–231, Sep. 2011.

[14] A. Cosentino, "Terahertz and cultural heritage science: Examination of art and archaeology," *Technologies*, vol. 4, no. 1, p. 6, Feb. 2016.

[15] H. Guerboukha, K. Nallappan, and M. Skorobogatiy, "Toward real-time terahertz imaging," *Advances in Optics and Photonics*, vol. 10, no. 4, pp. 843–938, 2018.

[16] H. Guerboukha *et al.*, "Planar porous components for low-loss terahertz optics," *Advanced Optical Materials*, vol. 7, no. 15, p. 1900236, May 2019.

[17] H. Guerboukha, K. Nallappan, and M. Skorobogatiy, "Exploiting k-space/frequency duality toward real-time terahertz imaging," *Optica*, vol. 5, no. 2, p. 109, Jan. 2018.

[18] J. Federici and L. Moeller, "Review of terahertz and subterahertz wireless communications," *Journal of Applied Physics*, vol. 107, no. 11, p. 111101, Jun. 2010.

[19] T. Kleine-Ostmann and T. Nagatsuma, "A review on terahertz communications research," *Journal of Infrared, Millimeter, and Terahertz Waves*, vol. 32, no. 2, pp. 143–171, Jan. 2011.

[20] H.-J. Song and T. Nagatsuma, "Present and future of terahertz communications," *IEEE Transactions on Terahertz Science and Technology*, vol. 1, no. 1, pp. 256–263, Sep. 2011.

[21] I. F. Akyildiz, J. M. Jornet, and C. Han, "Terahertz band: Next frontier for wireless communications," *Physical Communication*, vol. 12, pp. 16–32, Sep. 2014.

[22] T. Nagatsuma, G. Ducournau, and C. C. Renaud, "Advances in terahertz communications accelerated by photonics," *Nature Photonics*, vol. 10, no. 6, pp. 371–379, May 2016.

[23] R. J. Falconer and A. G. Markelz, "Terahertz spectroscopic analysis of peptides and proteins," *Journal of Infrared, Millimeter, and Terahertz Waves*, vol. 33, no. 10, pp. 973–988, Jun. 2012.

[24] S. Fan *et al.*, "The growth of biomedical terahertz research," *Journal of Physics D: Applied Physics*, vol. 47, no. 37, p. 374009, Aug. 2014.

[25] L. Xie, Y. Yao, and Y. Ying, "The application of terahertz spectroscopy to protein detection: A review," *Applied Spectroscopy Reviews*, vol. 49, no. 6, pp. 448–461, Dec. 2013.

[26] T. C. Bowman, M. El-Shenawee, and L. K. Campbell, "Terahertz imaging of excised breast tumor tissue on paraffin sections," *IEEE Transactions on Antennas and Propagation*, vol. 63, no. 5, pp. 2088–2097, May 2015.

[27] F. Sizov and A. Rogalski, "THz detectors," *Progress in Quantum Electronics*, vol. 34, no. 5, pp. 278–347, Sep. 2010.

[28] M. Hangyo, "Development and future prospects of terahertz technology," *Japanese Journal of Applied Physics*, vol. 54, no. 12, p. 120101, Nov. 2015.

[29] T. Otsuji, "Trends in the research of modern terahertz detectors: plasmon detectors," *IEEE Transactions on Terahertz Science and Technology*, vol. 5, no. 6, pp. 1110–1120, Nov. 2015.

[30] A. Maestrini *et al.*, "Schottky diode-based terahertz frequency multipliers and mixers," *Comptes Rendus Physique*, vol. 11, no. 7-8, pp. 480–495, Aug. 2010.

[31] A. Dobroiu *et al.*, "Terahertz imaging system based on a backward-wave oscillator," *Applied Optics*, vol. 43, no. 30, p. 5637, Oct. 2004.

[32] M. Mineo and C. Paoloni, "Corrugated rectangular waveguide tunable backward wave oscillator for terahertz applications," *IEEE Transactions on Electron Devices*, vol. 57, no. 6, pp. 1481–1484, Jun. 2010.

[33] W. He *et al.*, "Generation of broadband terahertz radiation using a backward wave oscillator and pseudospark-sourced electron beam," *Applied Physics Letters*, vol. 107, no. 13, p. 133501, Sep. 2015.

[34] S. Kumar, "Recent progress in terahertz quantum cascade lasers," *IEEE Journal of Selected Topics in Quantum Electronics*, vol. 17, no. 1, pp. 38–47, Jan. 2011.

[35] L. Li *et al.*, "Terahertz quantum cascade lasers with 1 w output powers," *Electronics Letters*, vol. 50, no. 4, pp. 309–311, Feb. 2014.

[36] M. A. Belkin and F. Capasso, "New frontiers in quantum cascade lasers: high performance room temperature terahertz sources," *Physica Scripta*, vol. 90, no. 11, p. 118002, Oct. 2015.

[37] X. Wang *et al.*, "High-power terahertz quantum cascade lasers with ∼0.23 w in continuous wave mode," *AIP Advances*, vol. 6, no. 7, p. 075210, Jul. 2016.

[38] K. A. McIntosh *et al.*, "Terahertz photomixing with diode lasers in low-temperature-grown GaAs," *Applied Physics Letters*, vol. 67, no. 26, pp. 3844–3846, Dec. 1995.

[39] S. Preu *et al.*, "Tunable, continuous-wave terahertz photomixer sources and applications," *Journal of Applied Physics*, vol. 109, no. 6, p. 061301, Mar. 2011.

[40] T. Ishibashi *et al.*, "Unitraveling-carrier photodiodes for terahertz applications," *IEEE Journal of Selected Topics in Quantum Electronics*, vol. 20, no. 6, pp. 79–88, Nov. 2014.

[41] Y. J. Ding, "Progress in terahertz sources based on difference-frequency generation [invited]," *Journal of the Optical Society of America B*, vol. 31, no. 11, p. 2696, Oct. 2014.

[42] K. Kawase *et al.*, "Coherent tunable THz-wave generation from LiNbO3 with monolithic grating coupler," *Applied Physics Letters*, vol. 68, no. 18, pp. 2483–2485, Apr. 1996.

[43] ——, "Injection-seeded terahertz-wave parametric generator with wide tunability," *Applied Physics Letters*, vol. 80, no. 2, pp. 195–197, Jan. 2002.

[44] S. Hayashi and K. Kawase, "Terahertz-wave parametric sources," in *Recent Optical and Photonic Technologies*. InTech, Jan. 2010.

[45] H. Minamide *et al.*, "Kilowatt-peak terahertz-wave generation and sub-femtojoule terahertz-wave pulse detection based on nonlinear optical wavelength-conversion at room temperature," *Journal of Infrared, Millimeter, and Terahertz Waves*, vol. 35, no. 1, pp. 25–37, Dec. 2013.

[46] D. H. Auston, K. P. Cheung, and P. R. Smith, "Picosecond photoconducting hertzian dipoles," *Applied Physics Letters*, vol. 45, no. 3, pp. 284–286, Aug. 1984.

[47] P. Smith, D. Auston, and M. Nuss, "Subpicosecond photoconducting dipole antennas," *IEEE Journal of Quantum Electronics*, vol. 24, no. 2, pp. 255–260, Feb. 1988.

[48] C. Fattinger and D. Grischkowsky, "Terahertz beams," *Applied Physics Letters*, vol. 54, no. 6, pp. 490–492, Feb. 1989.

[49] X.-C. Zhang and D. H. Auston, "Optoelectronic measurement of semiconductor surfaces and interfaces with femtosecond optics," *Journal of Applied Physics*, vol. 71, no. 1, pp. 326–338, Jan. 1992.

[50] X.-C. Zhang and D. Auston, "Optically induced THz electromagnetic radiation from planar photoconducting structures," *Journal of Electromagnetic Waves and Applications*, vol. 6, no. 1-4, pp. 85–106, Jan. 1992.

[51] P. U. Jepsen, R. H. Jacobsen, and S. R. Keiding, "Generation and detection of terahertz pulses from biased semiconductor antennas," *Journal of the Optical Society of America B*, vol. 13, no. 11, p. 2424, Nov. 1996.

[52] Y. C. Shen *et al.*, "Ultrabroadband terahertz radiation from low-temperature-grown GaAs photoconductive emitters," *Applied Physics Letters*, vol. 83, no. 15, pp. 3117–3119, Oct. 2003.

[53] A. Rice *et al.*, "Terahertz optical rectification from 110 zinc-blende crystals," *Applied Physics Letters*, vol. 64, no. 11, pp. 1324–1326, Mar. 1994.

[54] A. Schneider *et al.*, "Generation of terahertz pulses through optical rectification in organic DAST crystals: theory and experiment," *Journal of the Optical Society of America B*, vol. 23, no. 9, p. 1822, Sep. 2006.

[55] K.-L. Yeh *et al.*, "Generation of 10μj ultrashort terahertz pulses by optical rectification," *Applied Physics Letters*, vol. 90, no. 17, p. 171121, Apr. 2007.

[56] C. P. Hauri *et al.*, "Strong-field single-cycle THz pulses generated in an organic crystal," *Applied Physics Letters*, vol. 99, no. 16, p. 161116, Oct. 2011.

[57] C. Vicario *et al.*, "High efficiency THz generation in DSTMS, DAST and OH1 pumped by cr:forsterite laser," *Optics Express*, vol. 23, no. 4, p. 4573, Feb. 2015.

[58] N. Oda, "Uncooled bolometer-type terahertz focal plane array and camera for real-time imaging," *Comptes Rendus Physique*, vol. 11, no. 7-8, pp. 496–509, Aug. 2010.

[59] D. Dufour *et al.*, "Review of terahertz technology development at INO," *Journal of Infrared, Millimeter, and Terahertz Waves*, vol. 36, no. 10, pp. 922–946, Jul. 2015.

[60] F. Simoens, J. Meilhan, and J.-A. Nicolas, "Terahertz real-time imaging uncooled arrays based on antenna-coupled bolometers or FET developed at CEA-leti," *Journal of Infrared, Millimeter, and Terahertz Waves*, vol. 36, no. 10, pp. 961–985, Aug. 2015.

[61] Q. Li *et al.*, "Real-time terahertz scanning imaging by use of a pyroelectric array camera and image denoising," *Journal of the Optical Society of America A*, vol. 27, no. 11, p. 2381, Oct. 2010.

[62] S.-H. Ding *et al.*, "Continuous-wave terahertz digital holography by use of a pyroelectric array camera," *Optics Letters*, vol. 36, no. 11, p. 1993, May 2011.

[63] E. Hack *et al.*, "Comparison of thermal detector arrays for off-axis THz holography and real-time THz imaging," *Sensors*, vol. 16, no. 2, p. 221, Feb. 2016.

[64] M. J. E. Golay, "The theoretical and practical sensitivity of the pneumatic infra-red detector," *Review of Scientific Instruments*, vol. 20, no. 11, pp. 816–820, Nov. 1949.

[65] R. Han *et al.*, "Active terahertz imaging using schottky diodes in CMOS: Array and 860-GHz pixel," *IEEE Journal of Solid-State Circuits*, vol. 48, no. 10, pp. 2296–2308, Oct. 2013.

[66] S.-P. Han *et al.*, "Real-time continuous-wave terahertz line scanner based on a compact 1 by 240 ingaas schottky barrier diode array detector," *Optics Express*, vol. 22, no. 23, p. 28977, Nov. 2014.

[67] R. Tauk *et al.*, "Plasma wave detection of terahertz radiation by silicon field effects transistors: Responsivity and noise equivalent power," *Applied Physics Letters*, vol. 89, no. 25, p. 253511, Dec. 2006.

[68] W. Knap *et al.*, "Field effect transistors for terahertz detection: Physics and first imaging applications," *Journal of Infrared, Millimeter, and Terahertz Waves*, Aug. 2009.

[69] R. A. Hadi *et al.*, "A 1 k-pixel video camera for 0.7-1.1 terahertz imaging applications in 65-nm cmos," *IEEE Journal of Solid-State Circuits*, vol. 47, no. 12, pp. 2999–3012, Dec. 2012.

[70] Q. Wu and X.-C. Zhang, "Free-space electro-optic sampling of terahertz beams," *Applied Physics Letters*, vol. 67, no. 24, pp. 3523–3525, Dec. 1995.

[71] P. U. Jepsen *et al.*, "Detection of THz pulses by phase retardation in lithium tantalate," *Physical Review E*, vol. 53, no. 4, pp. R3052–R3054, Apr. 1996.

[72] A. Nahata *et al.*, "Coherent detection of freely propagating terahertz radiation by electro-optic sampling," *Applied Physics Letters*, vol. 68, no. 2, pp. 150–152, Jan. 1996.

[73] Q. Wu, T. D. Hewitt, and X.-C. Zhang, "Two-dimensional electro-optic imaging of THz beams," *Applied Physics Letters*, vol. 69, no. 8, pp. 1026–1028, Aug. 1996.

[74] Z. G. Lu, P. Campbell, and X.-C. Zhang, "Free-space electro-optic sampling with a high-repetition-rate regenerative amplified laser," *Applied Physics Letters*, vol. 71, no. 5, pp. 593–595, Aug. 1997.

[75] J. Dai, X. Xie, and X.-C. Zhang, "Detection of broadband terahertz waves with a laser-induced plasma in gases," *Physical Review Letters*, vol. 97, no. 10, Sep. 2006.

[76] J. Dai, J. Liu, and X.-C. Zhang, "Terahertz wave air photonics: Terahertz wave generation and detection with laser-induced gas plasma," *IEEE Journal of Selected Topics in Quantum Electronics*, vol. 17, no. 1, pp. 183–190, Jan. 2011.

[77] B. B. Hu and M. C. Nuss, "Imaging with terahertz waves," *Optics Letters*, vol. 20, no. 16, p. 1716, Aug. 1995.

[78] T. L. ffler *et al.*, "Visualization and classification in biomedical terahertz pulsed imaging," *Physics in Medicine and Biology*, vol. 47, no. 21, pp. 3847–3852, Oct. 2002.

[79] A. J. Fitzgerald, "Classification of terahertz-pulsed imaging data from excised breast tissue," *Journal of Biomedical Optics*, vol. 17, no. 1, p. 016005, Feb. 2012.

[80] J. P. Guillet *et al.*, "Review of terahertz tomography techniques," *Journal of Infrared, Millimeter, and Terahertz Waves*, vol. 35, no. 4, pp. 382–411, Feb. 2014.

[81] A. Ushakov *et al.*, "Broadband in-line terahertz 2D imaging: comparative study with time-of-flight, cross-correlation, and fourier transform data processing," *Journal of the Optical Society of America B*, vol. 35, no. 5, p. 1159, Apr. 2018.

[82] L. Zhang *et al.*, "Terahertz multiwavelength phase imaging without 2π ambiguity," *Optics Letters*, vol. 31, no. 24, p. 3668, Nov. 2006.

[83] P. A. Chizhov *et al.*, "Measurement of spatio-temporal field distribution of THz pulses in electro-optic crystal by interferometry method," *Quantum Electronics*, vol. 45, no. 5, pp. 434–436, May 2015.

[84] R. W. McGowan, R. A. Cheville, and D. Grischkowsky, "Direct observation of the gouy phase shift in THz impulse ranging," *Applied Physics Letters*, vol. 76, no. 6, pp. 670–672, Feb. 2000.

[85] P. Kužel *et al.*, "Gouy shift correction for highly accurate refractive index retrieval in time-domain terahertz spectroscopy," *Optics Express*, vol. 18, no. 15, p. 15338, Jul. 2010.

[86] L. Duvillaret, F. Garet, and J.-L. Coutaz, "A reliable method for extraction of material parameters in terahertz time-domain spectroscopy," *IEEE Journal of Selected Topics in Quantum Electronics*, vol. 2, no. 3, pp. 739–746, 1996.

[87] J. F. O'Hara, W. Withayachumnankul, and I. Al-Naib, "A review on thin-film sensing with terahertz waves," *Journal of Infrared, Millimeter, and Terahertz Waves*, vol. 33, no. 3, pp. 245–291, Mar. 2012.

[88] T. D. Dorney, R. G. Baraniuk, and D. M. Mittleman, "Material parameter estimation with terahertz time-domain spectroscopy," *Journal of the Optical Society of America A*, vol. 18, no. 7, p. 1562, Jul. 2001.

[89] M. Hangyo, T. Nagashima, and S. Nashima, "Spectroscopy by pulsed terahertz radiation," *Measurement Science and Technology*, vol. 13, no. 11, pp. 1727–1738, Oct. 2002.

[90] P. Bolivar *et al.*, "Measurement of the dielectric constant and loss tangent of high dielectric-constant materials at terahertz frequencies," *IEEE Transactions on Microwave Theory and Techniques*, vol. 51, no. 4, pp. 1062–1066, Apr. 2003.

[91] W. Withayachumnankul *et al.*, "Simple material parameter estimation via terahertz time-domain spectroscopy," *Electronics Letters*, vol. 41, no. 14, p. 800, 2005.

[92] I. Pupeza, R. Wilk, and M. Koch, "Highly accurate optical material parameter determination with THz time-domain spectroscopy," *Optics Express*, vol. 15, no. 7, p. 4335, 2007.

[93] M. Naftaly and R. E. Miles, "Terahertz time-domain spectroscopy for material characterization," *Proceedings of the IEEE*, vol. 95, no. 8, pp. 1658–1665, Aug. 2007.

[94] S. P. Mickan and X.-C. Zhang, "T-ray sensing and imaging," *International Journal of High Speed Electronics and Systems*, vol. 13, no. 02, pp. 601–676, Jun. 2003.

[95] S. Atakaramians *et al.*, "Terahertz dielectric waveguides," *Advances in Optics and Photonics*, vol. 5, no. 2, p. 169, Jun. 2013.

[96] A. Markov, H. Guerboukha, and M. Skorobogatiy, "Hybrid metal wire–dielectric terahertz waveguides: challenges and opportunities [invited]," *Journal of the Optical Society of America B*, vol. 31, no. 11, p. 2587, Oct. 2014.

[97] H. Guerboukha *et al.*, "Silk foam terahertz waveguides," *Advanced Optical Materials*, vol. 2, no. 12, pp. 1181–1192, Sep. 2014.

[98] T. Ma *et al.*, "Graded index porous optical fibers – dispersion management in terahertz range," *Optics Express*, vol. 23, no. 6, p. 7856, Mar. 2015.

[99] J. Li *et al.*, "3D printed hollow core terahertz bragg waveguides with defect layers for surface sensing applications," *Optics Express*, vol. 25, no. 4, p. 4126, Feb. 2017.

[100] P. U. Jepsen, U. Møller, and H. Merbold, "Investigation of aqueous alcohol and sugar solutions with reflection terahertz time-domain spectroscopy," *Optics Express*, vol. 15, no. 22, p. 14717, 2007.

[101] L. Thrane *et al.*, "THz reflection spectroscopy of liquid water," *Chemical Physics Letters*, vol. 240, no. 4, pp. 330–333, Jun. 1995.

[102] U. Møller *et al.*, "Terahertz reflection spectroscopy of debye relaxation in polar liquids [invited]," *Journal of the Optical Society of America B*, vol. 26, no. 9, p. A113, Aug. 2009.

[103] P. U. Jepsen and B. M. Fischer, "Dynamic range in terahertz time-domain transmission and reflection spectroscopy," *Optics Letters*, vol. 30, no. 1, p. 29, Jan. 2005.

[104] P. U. Jepsen, J. K. Jensen, and U. Møller, "Characterization of aqueous alcohol solutions in bottles with THz reflection spectroscopy," *Optics Express*, vol. 16, no. 13, p. 9318, Jun. 2008.

[105] M. Naftaly and R. Dudley, "Methodologies for determining the dynamic ranges and signal-to-noise ratios of terahertz time-domain spectrometers," *Optics Letters*, vol. 34, no. 8, p. 1213, Apr. 2009.

[106] R. M. Woodward *et al.*, "Terahertz pulse imaging in reflection geometry of human skin cancer and skin tissue," *Physics in Medicine and Biology*, vol. 47, no. 21, pp. 3853–3863, Oct. 2002.

[107] F. A. Hegmann, O. Ostroverkhova, and D. G. Cooke, "Probing organic semiconductors with terahertz pulses," in *Photophysics of Molecular Materials*. Wiley-VCH Verlag GmbH & Co. KGaA, Apr. 2006, pp. 367–428.

[108] J. Lloyd-Hughes and T.-I. Jeon, "A review of the terahertz conductivity of bulk and nano-materials," *Journal of Infrared, Millimeter, and Terahertz Waves*, vol. 33, no. 9, pp. 871–925, May 2012.

[109] M. C. Nuss, D. H. Auston, and F. Capasso, "Direct subpicosecond measurement of carrier mobility of photoexcited electrons in gallium arsenide," *Physical Review Letters*, vol. 58, no. 22, pp. 2355–2358, Jun. 1987.

[110] M. C. Beard, G. M. Turner, and C. A. Schmuttenmaer, "Transient photoconductivity in GaAs as measured by time-resolved terahertz spectroscopy," *Physical Review B*, vol. 62, no. 23, pp. 15 764–15 777, Dec. 2000.

[111] R. Ulbricht *et al.*, "Carrier dynamics in semiconductors studied with time-resolved terahertz spectroscopy," *Reviews of Modern Physics*, vol. 83, no. 2, pp. 543–586, Jun. 2011.

[112] J. D. Buron *et al.*, "Graphene conductance uniformity mapping," *Nano Letters*, vol. 12, no. 10, pp. 5074–5081, Sep. 2012.

[113] K. S. Novoselov, "Electric field effect in atomically thin carbon films," *Science*, vol. 306, no. 5696, pp. 666–669, Oct. 2004.

[114] A. K. Geim and K. S. Novoselov, "The rise of graphene," *Nature Materials*, vol. 6, no. 3, pp. 183–191, Mar. 2007.

[115] A. C. Ferrari *et al.*, "Science and technology roadmap for graphene, related two-dimensional crystals, and hybrid systems," *Nanoscale*, vol. 7, no. 11, pp. 4598–4810, 2015.

[116] P. Bøggild *et al.*, "Mapping the electrical properties of large-area graphene," *2D Materials*, vol. 4, no. 4, p. 042003, Sep. 2017.

[117] P. A. George *et al.*, "Ultrafast optical-pump terahertz-probe spectroscopy of the carrier relaxation and recombination dynamics in epitaxial graphene," *Nano Letters*, vol. 8, no. 12, pp. 4248–4251, Dec. 2008.

[118] J. L. Tomaino *et al.*, "Terahertz imaging and spectroscopy of large-area single-layer graphene," *Optics Express*, vol. 19, no. 1, p. 141, Dec. 2010.

[119] ——, "High-contrast imaging of graphene via time-domain terahertz spectroscopy," *Journal of Infrared, Millimeter, and Terahertz Waves*, vol. 33, no. 8, pp. 839–845, Mar. 2012.

[120] M. J. Paul *et al.*, "Terahertz imaging of inhomogeneous electrodynamics in single-layer graphene embedded in dielectrics," *Applied Physics Letters*, vol. 101, no. 9, p. 091109, Aug. 2012.

[121] J. D. Buron *et al.*, "Graphene mobility mapping," *Scientific Reports*, vol. 5, no. 1, Jul. 2015.

[122] ——, "Terahertz wafer-scale mobility mapping of graphene on insulating substrates without a gate," *Optics Express*, vol. 23, no. 24, p. 30721, Nov. 2015.

[123] R. K. May *et al.*, "Terahertz in-line sensor for direct coating thickness measurement of individual tablets during film coating in real-time," *Journal of Pharmaceutical Sciences*, vol. 100, no. 4, pp. 1535–1544, Apr. 2011.

[124] D. M. Mittleman *et al.*, "T-ray tomography," *Optics Letters*, vol. 22, no. 12, p. 904, Jun. 1997.

[125] J. A. Zeitler *et al.*, "Terahertz pulsed spectroscopy and imaging in the pharmaceutical setting - a review," *Journal of Pharmacy and Pharmacology*, vol. 59, no. 2, pp. 209–223, Feb. 2007.

[126] Y.-C. Shen, "Terahertz pulsed spectroscopy and imaging for pharmaceutical applications: A review," *International Journal of Pharmaceutics*, vol. 417, no. 1-2, pp. 48–60, Sep. 2011.

[127] M. Haaser *et al.*, "Terahertz pulsed imaging as an advanced characterisation tool for film coatings—a review," *International Journal of Pharmaceutics*, vol. 457, no. 2, pp. 510–520, Dec. 2013.

[128] A. J. Fitzgerald, B. E. Cole, and P. F. Taday, "Nondestructive analysis of tablet coating thicknesses using terahertz pulsed imaging," *Journal of Pharmaceutical Sciences*, vol. 94, no. 1, pp. 177–183, Jan. 2005.

[129] L. Ho *et al.*, "Analysis of sustained-release tablet film coats using terahertz pulsed imaging," *Journal of Controlled Release*, vol. 119, no. 3, pp. 253–261, Jun. 2007.

[130] R. K. May *et al.*, "Hardness and density distributions of pharmaceutical tablets measured by terahertz pulsed imaging," *Journal of Pharmaceutical Sciences*, vol. 102, no. 7, pp. 2179–2186, Jul. 2013.

[131] P. Bawuah *et al.*, "Detection of porosity of pharmaceutical compacts by terahertz radiation transmission and light reflection measurement techniques," *International Journal of Pharmaceutics*, vol. 465, no. 1-2, pp. 70–76, Apr. 2014.

[132] K. Su, Y.-C. Shen, and J. A. Zeitler, "Terahertz sensor for non-contact thickness and quality measurement of automobile paints of varying complexity," *IEEE Transactions on Terahertz Science and Technology*, vol. 4, no. 4, pp. 432–439, Jul. 2014.

[133] C. L. Koch-Dandolo *et al.*, "Reflection terahertz time-domain imaging for analysis of an 18th century neoclassical easel painting," *Applied Optics*, vol. 54, no. 16, p. 5123, May 2015.

[134] A. J. L. Adam *et al.*, "TeraHertz imaging of hidden paint layers on canvas," *Optics Express*, vol. 17, no. 5, p. 3407, Feb. 2009.

[135] K. Fukunaga and M. Picollo, "Terahertz spectroscopy applied to the analysis of artists' materials," *Applied Physics A*, vol. 100, no. 3, pp. 591–597, Mar. 2010.

[136] C. Seco-Martorell *et al.*, "Goya's artwork imaging with terahertz waves," *Optics Express*, vol. 21, no. 15, p. 17800, Jul. 2013.

[137] E. Abraham and K. Fukunaga, "Terahertz imaging applied to the examination of artistic objects," *Studies in Conservation*, vol. 60, no. 6, pp. 343–352, Nov. 2014.

[138] A. Redo-Sanchez *et al.*, "Terahertz time-gated spectral imaging for content extraction through layered structures," *Nature Communications*, vol. 7, no. 1, Sep. 2016.

[139] A. Aghasi and J. Romberg, "Convex cardinal shape composition," *SIAM Journal on Imaging Sciences*, vol. 8, no. 4, pp. 2887–2950, Jan. 2015.

[140] S.-H. Cho *et al.*, "Fast terahertz reflection tomography using block-based compressed sensing," *Optics Express*, vol. 19, no. 17, p. 16401, Aug. 2011.

[141] A. Brahm *et al.*, "Volumetric spectral analysis of materials using terahertz-tomography techniques," *Applied Physics B*, vol. 100, no. 1, pp. 151–158, Mar. 2010.

[142] S. Wang and X.-C. Zhang, "Pulsed terahertz tomography," *Journal of Physics D: Applied Physics*, vol. 37, no. 4, pp. R1–R36, Jan. 2004.

[143] V. P. Wallace *et al.*, "Three-dimensional imaging of optically opaque materials using nonionizing terahertz radiation," *Journal of the Optical Society of America A*, vol. 25, no. 12, p. 3120, Nov. 2008.

[144] B. Ferguson *et al.*, "T-ray computed tomography," *Optics Letters*, vol. 27, no. 15, p. 1312, Aug. 2002.

[145] ——, "Towards functional 3D t-ray imaging," *Physics in Medicine and Biology*, vol. 47, no. 21, pp. 3735–3742, Oct. 2002.

[146] A. C. Kak and M. Stanley, "7. algebraic reconstruction algorithms," in *Principles of Computerized Tomographic Imaging*. Society for Industrial and Applied Mathematics, Jan. 2001, pp. 275–296.

[147] B. Recur *et al.*, "Investigation on reconstruction methods applied to 3D terahertz computed tomography," *Optics Express*, vol. 19, no. 6, p. 5105, Mar. 2011.

[148] A. Brahm *et al.*, "Wavelet based identification of substances in terahertz tomography measurements," *Journal of Infrared, Millimeter, and Terahertz Waves*, vol. 35, no. 11, pp. 974–986, Sep. 2014.

[149] M. Bessou *et al.*, "Three-dimensional terahertz computed tomography of human bones," *Applied Optics*, vol. 51, no. 28, p. 6738, Sep. 2012.

[150] B. Recur *et al.*, "Propagation beam consideration for 3D THz computed tomography," *Optics Express*, vol. 20, no. 6, p. 5817, Feb. 2012.

[151] ——, "Ordered subsets convex algorithm for 3D terahertz transmission tomography," *Optics Express*, vol. 22, no. 19, p. 23299, Sep. 2014.

[152] A. Bitman *et al.*, "Computed tomography using broadband bessel THz beams and phase contrast," *Optics Letters*, vol. 39, no. 7, p. 1925, Mar. 2014.

[153] E. Abraham *et al.*, "Refraction losses in terahertz computed tomography," *Optics Communications*, vol. 283, no. 10, pp. 2050–2055, May 2010.

[154] S. Mukherjee *et al.*, "Elimination of fresnel reflection boundary effects and beam steering in pulsed terahertz computed tomography," *Journal of Infrared, Millimeter, and Terahertz Waves*, vol. 34, no. 9, pp. 539–555, Jun. 2013.

[155] A. Brahm *et al.*, "Optical effects at projection measurements for terahertz tomography," *Optics & Laser Technology*, vol. 62, pp. 49–57, Oct. 2014.

[156] J.-P. Caumes *et al.*, "Terahertz tomographic imaging of XVIIIth dynasty egyptian sealed pottery," *Applied Optics*, vol. 50, no. 20, p. 3604, Jul. 2011.

[157] M. Bessou *et al.*, "Advantage of terahertz radiation versus x-ray to detect hidden organic materials in sealed vessels," *Optics Communications*, vol. 285, no. 21-22, pp. 4175–4179, Oct. 2012.

[158] E. Abraham *et al.*, "Terahertz, x-ray and neutron computed tomography of an eighteenth dynasty egyptian sealed pottery," *Applied Physics A*, vol. 117, no. 3, pp. 963–972, Sep. 2014.

[159] J. B. Perraud *et al.*, "Terahertz imaging and tomography as efficient instruments for testing polymer additive manufacturing objects," *Applied Optics*, vol. 55, no. 13, p. 3462, Apr. 2016.

[160] P. Hillger *et al.*, "Low-cost 0.5 THz computed tomography based on silicon components," in *2017 42nd International Conference on Infrared, Millimeter, and Terahertz Waves (IRMMW-THz)*. IEEE, Aug. 2017.

[161] D. Coquillat *et al.*, "High-speed InP-based double heterojunction bipolar transistors and varactors for three-dimensional terahertz computed tomography," in *2017 42nd International Conference on Infrared, Millimeter, and Terahertz Waves (IRMMW-THz)*. IEEE, Aug. 2017.

[162] Q. Li *et al.*, "Terahertz computed tomography using a continuous-wave gas laser," *Journal of Infrared, Millimeter, and Terahertz Waves*, vol. 33, no. 5, pp. 548–558, Apr. 2012.

[163] T. Kashiwagi *et al.*, "Computed tomography image using sub-terahertz waves generated from a high-tc superconducting intrinsic josephson junction oscillator," *Applied Physics Letters*, vol. 104, no. 8, p. 082603, Feb. 2014.

[164] S. R. Tripathi *et al.*, "Terahertz wave three-dimensional computed tomography based on injection-seeded terahertz wave parametric emitter and detector," *Optics Express*, vol. 24, no. 6, p. 6433, Mar. 2016.

[165] B. Li *et al.*, "Terahertz computed tomography in three-dimensional using a pyroelectric array detector," in *Holography: Advances and Modern Trends V*, M. Hrabovský, J. T. Sheridan, and A. Fimia, Eds. SPIE, May 2017.

[166] M. Jewariya *et al.*, "Fast three-dimensional terahertz computed tomography using real-time line projection of intense terahertz pulse," *Optics Express*, vol. 21, no. 2, p. 2423, Jan. 2013.

[167] N. Rothbart *et al.*, "Fast 2-d and 3-d terahertz imaging with a quantum-cascade laser and a scanning mirror," *IEEE Transactions on Terahertz Science and Technology*, vol. 3, no. 5, pp. 617–624, Sep. 2013.

[168] T. Mohr, A. Herdt, and W. Elsässer, "2D tomographic terahertz imaging using a single pixel detector," *Optics Express*, vol. 26, no. 3, p. 3353, Jan. 2018.

[169] J. W. Goodman, *Introduction to Fourier Optics*. McGraw-Hill, 1996.

[170] T. Yuan, J. Xu, and X.-C. Zhang, "Development of terahertz wave microscopes," *Infrared Physics & Technology*, vol. 45, no. 5-6, pp. 417–425, Oct. 2004.

[171] W. Withayachumnankul *et al.*, "T-ray sensing and imaging," *Proceedings of the IEEE*, vol. 95, no. 8, pp. 1528–1558, Aug. 2007.

[172] A. J. L. Adam, "Review of near-field terahertz measurement methods and their applications," *Journal of Infrared, Millimeter, and Terahertz Waves*, vol. 32, no. 8-9, pp. 976–1019, Jul. 2011.

[173] F. Blanchard *et al.*, "Real-time, subwavelength terahertz imaging," *Annual Review of Materials Research*, vol. 43, no. 1, pp. 237–259, Jul. 2013.

[174] N. N. Zinov'ev and A. V. Andrianov, "Confocal terahertz imaging," *Applied Physics Letters*, vol. 95, no. 1, p. 011114, Jul. 2009.

[175] M. A. Salhi, I. Pupeza, and M. Koch, "Confocal THz laser microscope," *Journal of Infrared, Millimeter, and Terahertz Waves*, Nov. 2009.

[176] U. S. de Cumis *et al.*, "Terahertz confocal microscopy with a quantum cascade laser source," *Optics Express*, vol. 20, no. 20, p. 21924, Sep. 2012.

[177] M. Flammini *et al.*, "Confocal terahertz imaging of ancient manuscripts," *Journal of Infrared, Millimeter, and Terahertz Waves*, vol. 38, no. 4, pp. 435–442, Nov. 2016.

[178] H. H. N. Pham *et al.*, "Enhancement of spatial resolution of terahertz imaging systems based on terajet generation by dielectric cube," *APL Photonics*, vol. 2, no. 5, p. 056106, May 2017.

[179] L. Yue *et al.*, "A millimetre-wave cuboid solid immersion lens with intensity-enhanced amplitude mask apodization," *Journal of Infrared, Millimeter, and Terahertz Waves*, vol. 39, no. 6, pp. 546–552, Mar. 2018.

[180] Y. Yang *et al.*, "Dielectric sphere-coupled THz super-resolution imaging," *Applied Physics Letters*, vol. 113, no. 3, p. 031105, Jul. 2018.

[181] N. V. Chernomyrdin *et al.*, "Solid immersion terahertz imaging with sub-wavelength resolution," *Applied Physics Letters*, vol. 110, no. 22, p. 221109, May 2017.

[182] ——, "Reflection-mode continuous-wave 0.15λ-resolution terahertz solid immersion microscopy of soft biological tissues," *Applied Physics Letters*, vol. 113, no. 11, p. 111102, Sep. 2018.

[183] A. J. Adam *et al.*, "THz near-field measurements of metal structures," *Comptes Rendus Physique*, vol. 9, no. 2, pp. 161–168, Mar. 2008.

[184] M. A. Seo *et al.*, "Fourier-transform terahertz near-field imaging of one-dimensional slit arrays: mapping of electric-field-, magnetic-field-, and poynting vectors," *Optics Express*, vol. 15, no. 19, p. 11781, Aug. 2007.

[185] J. Grzyb, B. Heinemann, and U. R. Pfeiffer, "Solid-state terahertz superresolution imaging device in 130-nm SiGe BiCMOS technology," *IEEE Transactions on Microwave Theory and Techniques*, vol. 65, no. 11, pp. 4357–4372, Nov. 2017.

[186] K. Ahi and M. Anwar, "Developing terahertz imaging equation and enhancement of the resolution of terahertz images using deconvolution," in *Terahertz Physics, Devices, and Systems X: Advanced Applications in Industry and Defense*, M. F. Anwar, T. W. Crowe, and T. Manzur, Eds. SPIE, May 2016.

[187] K. Ahi, "Mathematical modeling of THz point spread function and simulation of THz imaging systems," *IEEE Transactions on Terahertz Science and Technology*, vol. 7, no. 6, pp. 747–754, Nov. 2017.

[188] O. Mitrofanov *et al.*, "Collection-mode near-field imaging with 0.5-THz pulses," *IEEE Journal of Selected Topics in Quantum Electronics*, vol. 7, no. 4, pp. 600–607, 2001.

[189] S. Hunsche *et al.*, "THz near-field imaging," *Optics Communications*, vol. 150, no. 1-6, pp. 22–26, May 1998.

[190] Q. Chen *et al.*, "Near-field terahertz imaging with a dynamic aperture," *Optics Letters*, vol. 25, no. 15, p. 1122, Aug. 2000.

[191] A. J. Macfaden *et al.*, "3 μm aperture probes for near-field terahertz transmission microscopy," *Applied Physics Letters*, vol. 104, no. 1, p. 011110, Jan. 2014.

[192] O. Mitrofanov *et al.*, "Photoconductive terahertz near-field detector with a hybrid nanoantenna array cavity," *ACS Photonics*, vol. 2, no. 12, pp. 1763–1768, Dec. 2015.

[193] ——, "Terahertz pulse propagation through small apertures," *Applied Physics Letters*, vol. 79, no. 7, pp. 907–909, Aug. 2001.

[194] J. F. Federici *et al.*, "Terahertz near-field imaging," *Physics in Medicine and Biology*, vol. 47, no. 21, pp. 3727–3734, Oct. 2002.

[195] H. A. Bethe, "Theory of diffraction by small holes," *Physical Review*, vol. 66, no. 7-8, pp. 163–182, Oct. 1944.

[196] C. Bouwkamp, "On the diffraction of electromagnetic waves by small circular disks and holes," *Philips Research Reports*, vol. 5, pp. 401–422, 1950.

[197] K. Ishihara *et al.*, "Terahertz near-field imaging using enhanced transmission through a single subwavelength aperture," *Japanese Journal of Applied Physics*, vol. 44, no. No. 29, pp. L929–L931, Jul. 2005.

[198] ——, "Terahertz-wave near-field imaging with subwavelength resolution using surface-wave-assisted bow-tie aperture," *Applied Physics Letters*, vol. 89, no. 20, p. 201120, Nov. 2006.

[199] N. C. J. van der Valk and P. C. M. Planken, "Electro-optic detection of subwavelength terahertz spot sizes in the near field of a metal tip," *Applied Physics Letters*, vol. 81, no. 9, pp. 1558–1560, Aug. 2002.

[200] H.-T. Chen, R. Kersting, and G. C. Cho, "Terahertz imaging with nanometer resolution," *Applied Physics Letters*, vol. 83, no. 15, pp. 3009–3011, Oct. 2003.

[201] A. J. Huber *et al.*, "Terahertz near-field nanoscopy of mobile carriers in single semiconductor nanodevices," *Nano Letters*, vol. 8, no. 11, pp. 3766–3770, Nov. 2008.

[202] M. Yamashita *et al.*, "Imaging of large-scale integrated circuits using laser-terahertz emission microscopy," *Optics Express*, vol. 13, no. 1, p. 115, 2005.

[203] P. Klarskov *et al.*, "Nanoscale laser terahertz emission microscopy," *ACS Photonics*, vol. 4, no. 11, pp. 2676–2680, Oct. 2017.

[204] T. L. Cocker *et al.*, "An ultrafast terahertz scanning tunnelling microscope," *Nature Photonics*, vol. 7, no. 8, pp. 620–625, Jul. 2013.

[205] ——, "Tracking the ultrafast motion of a single molecule by femtosecond orbital imaging," *Nature*, vol. 539, no. 7628, pp. 263–267, Nov. 2016.

[206] Y.-S. Lee, "Generation and detection of broadband terahertz pulses," in *Principles of Terahertz Science and Technology*. Springer US, 2009, pp. 1–66.

[207] Y. C. Shen *et al.*, "Generation and detection of ultrabroadband terahertz radiation using photoconductive emitters and receivers," *Applied Physics Letters*, vol. 85, no. 2, pp. 164–166, Jul. 2004.

[208] N. T. Yardimci *et al.*, "High-power terahertz generation using large-area plasmonic photoconductive emitters," *IEEE Transactions on Terahertz Science and Technology*, vol. 5, no. 2, pp. 223–229, Mar. 2015.

[209] M. Jarrahi, "Advanced photoconductive terahertz optoelectronics based on nano-antennas and nano-plasmonic light concentrators," *IEEE Transactions on Terahertz Science and Technology*, vol. 5, no. 3, pp. 391–397, May 2015.

[210] M. Ashida, "Ultra-broadband terahertz wave detection using photoconductive antenna," *Japanese Journal of Applied Physics*, vol. 47, no. 10, pp. 8221–8225, Oct. 2008.

[211] Jan. 2011.

[212] C. Berry *et al.*, "Significant performance enhancement in photoconductive terahertz optoelectronics by incorporating plasmonic contact electrodes," *Nature Communications*, vol. 4, no. 1, Mar. 2013.

[213] N. T. Yardimci and M. Jarrahi, "High sensitivity terahertz detection through large-area plasmonic nano-antenna arrays," *Scientific Reports*, vol. 7, no. 1, Feb. 2017.

[214] A. Brahm *et al.*, "Multichannel terahertz time-domain spectroscopy system at 1030 nm excitation wavelength," *Optics Express*, vol. 22, no. 11, p. 12982, May 2014.

[215] J. R. Freeman, H. E. Beere, and D. A. Ritchie, "Generation and detection of terahertz radiation," in *Terahertz Spectroscopy and Imaging*. Springer Berlin Heidelberg, 2012, pp. 1–28.

[216] A. Nahata, A. S. Weling, and T. F. Heinz, "A wideband coherent terahertz spectroscopy system using optical rectification and electro-optic sampling," *Applied Physics Letters*, vol. 69, no. 16, pp. 2321–2323, Oct. 1996.

[217] J. Hebling *et al.*, "Velocity matching by pulse front tilting for large area THz-pulse generation," *Optics Express*, vol. 10, no. 21, p. 1161, Oct. 2002.

[218] A. G. Stepanov, J. Hebling, and J. Kuhl, "Efficient generation of subpicosecond terahertz radiation by phase-matched optical rectification using ultrashort laser pulses with tilted pulse fronts," *Applied Physics Letters*, vol. 83, no. 15, pp. 3000–3002, Oct. 2003.

[219] J. Hebling *et al.*, "Generation of high-power terahertz pulses by tilted-pulse-front excitation and their application possibilities," *Journal of the Optical Society of America B*, vol. 25, no. 7, p. B6, Apr. 2008.

[220] H. Hirori *et al.*, "Single-cycle terahertz pulses with amplitudes exceeding 1 MV/cm generated by optical rectification in LiNbO3," *Applied Physics Letters*, vol. 98, no. 9, p. 091106, Feb. 2011.

[221] M. J. Khan, J. C. Chen, and S. Kaushik, "Optical detection of terahertz radiation by using nonlinear parametric upconversion," *Optics Letters*, vol. 32, no. 22, p. 3248, Nov. 2007.

[222] R. Guo *et al.*, "Highly sensitive coherent detection of terahertz waves at room temperature using a parametric process," *Applied Physics Letters*, vol. 93, no. 2, p. 021106, Jul. 2008.

[223] K. Murate *et al.*, "A high dynamic range and spectrally flat terahertz spectrometer based on optical parametric processes in LiNbO3," *IEEE Transactions on Terahertz Science and Technology*, vol. 4, no. 4, pp. 523–526, Jul. 2014.

[224] M. Mohara *et al.*, "Pharmaceutical tablet inspection with injection-seeded terahertz parametric generation technique," in *2016 41st International Conference on Infrared, Millimeter, and Terahertz waves (IRMMW-THz)*. IEEE, Sep. 2016.

[225] L. Liu and N. G. Chen, "Double-pass rotary mirror array for fast scanning optical delay line," *Applied Optics*, vol. 45, no. 21, p. 5426, Jul. 2006.

[226] P.-L. Hsiung *et al.*, "High-speed path-length scanning with a multiple-pass cavity delay line," *Applied Optics*, vol. 42, no. 4, p. 640, Feb. 2003.

[227] X. Liu, M. J. Cobb, and X. Li, "Rapid scanning all-reflective optical delay line for real-time optical coherence tomography," *Optics Letters*, vol. 29, no. 1, p. 80, Jan. 2004.

[228] K. Locharoenrat, "Optical delay line for rapid scanning low-CoherenceReflectometer," *International Journal of Information and Electronics Engineering*, 2012.

[229] D. C. Edelstein, R. B. Romney, and M. Scheuermann, "Rapid programmable 300 ps optical delay scanner and signal-averaging system for ultrafast measurements," *Review of Scientific Instruments*, vol. 62, no. 3, pp. 579–583, Mar. 1991.

[230] J. Xu and X.-C. Zhang, "Circular involute stage," *Optics Letters*, vol. 29, no. 17, p. 2082, Sep. 2004.

[231] G.-J. Kim *et al.*, "Terahertz pulse detection using rotary optical delay line," *Japanese Journal of Applied Physics*, vol. 46, no. 11, pp. 7332–7335, Nov. 2007.

[232] ——, "High speed scanning of terahertz pulse by a rotary optical delay line," *Review of Scientific Instruments*, vol. 79, no. 10, p. 106102, Oct. 2008.

[233] M. Skorobogatiy, "Linear rotary optical delay lines," *Optics Express*, vol. 22, no. 10, p. 11812, May 2014.

[234] H. Guerboukha *et al.*, "Time resolved dynamic measurements at THz frequencies using a rotary optical delay line," *IEEE Transactions on Terahertz Science and Technology*, vol. 5, no. 4, pp. 564–572, Jul. 2015.

[235] J. Ballif *et al.*, "Rapid and scalable scans at 21 m/s in optical low-coherence reflectometry," *Optics Letters*, vol. 22, no. 11, p. 757, Jun. 1997.

[236] J. Szydlo *et al.*, "Air-turbine driven optical low-coherence reflectometry at 28.6-kHz scan repetition rate," *Optics Communications*, vol. 154, no. 1-3, pp. 1–4, Aug. 1998.

[237] T. Probst *et al.*, "Cost-efficient delay generator for fast terahertz imaging," *Optics Letters*, vol. 39, no. 16, p. 4863, Aug. 2014.

[238] G. J. Fiechtner *et al.*, "Asynchronous optical sampling:a new combustion diagnostic for potential use in turbulent, high-pressure flames," *Optics Letters*, vol. 14, no. 5, p. 260, Jan. 1989.

[239] ——, "Measurements of atomic sodium in flames by asynchronous optical sampling: theory and experiment," *Applied Optics*, vol. 31, no. 15, p. 2849, May 1992.

[240] T. Yasui, E. Saneyoshi, and T. Araki, "Asynchronous optical sampling terahertz time-domain spectroscopy for ultrahigh spectral resolution and rapid data acquisition," *Applied Physics Letters*, vol. 87, no. 6, p. 061101, Aug. 2005.

[241] C. Janke *et al.*, "Asynchronous optical sampling for high-speed characterization of integrated resonant terahertz sensors," *Optics Letters*, vol. 30, no. 11, p. 1405, Jun. 2005.

[242] A. Bartels *et al.*, "Ultrafast time-domain spectroscopy based on high-speed asynchronous optical sampling," *Review of Scientific Instruments*, vol. 78, no. 3, p. 035107, Mar. 2007.

[243] O. Kliebisch, D. C. Heinecke, and T. Dekorsy, "Ultrafast time-domain spectroscopy system using 10 GHz asynchronous optical sampling with 100 kHz scan rate," *Optics Express*, vol. 24, no. 26, p. 29930, Dec. 2016.

[244] S. Kray *et al.*, "Electronically controlled coherent linear optical sampling for optical coherence tomography," *Optics Express*, vol. 18, no. 10, p. 9976, Apr. 2010.

[245] Y. Kim and D.-S. Yee, "High-speed terahertz time-domain spectroscopy based on electronically controlled optical sampling," *Optics Letters*, vol. 35, no. 22, p. 3715, Nov. 2010.

[246] R. J. B. Dietz *et al.*, "All fiber-coupled THz-TDS system with kHz measurement rate based on electronically controlled optical sampling," *Optics Letters*, vol. 39, no. 22, p. 6482, Nov. 2014.

[247] D. Stehr *et al.*, "High-performance fiber-laser-based terahertz spectrometer," *Optics Letters*, vol. 35, no. 22, p. 3799, Nov. 2010.

[248] T. Hochrein *et al.*, "Optical sampling by laser cavity tuning," *Optics Express*, vol. 18, no. 2, p. 1613, Jan.

[249] R. Wilk *et al.*, "OSCAT: Novel technique for time-resolved experiments without moveable optical delay lines," *Journal of Infrared, Millimeter, and Terahertz Waves*, vol. 32, no. 5, pp. 596–602, Jun. 2010.

[250] ——, "Terahertz spectrometer operation by laser repetition frequency tuning," *Journal of the Optical Society of America B*, vol. 28, no. 4, p. 592, Mar. 2011.

[251] A. Brahm *et al.*, "Development of a multichannel lock-in amplifier for terahertz time-domain systems," in *2012 37th International Conference on Infrared, Millimeter, and Terahertz Waves*. IEEE, Sep. 2012.

[252] B. Pradarutti *et al.*, "Terahertz line detection by a microlens array coupled photoconductive antenna array," *Optics Express*, vol. 16, no. 22, p. 18443, Oct. 2008.

[253] K. Nallappan *et al.*, "A dynamically reconfigurable terahertz array antenna for 2D-imaging applications," in *2017 Photonics North (PN)*. IEEE, Jun. 2017.

[254] Z. Jiang and X.-C. Zhang, "2D measurement and spatio-temporal coupling of few-cycle THz pulses," *Optics Express*, vol. 5, no. 11, p. 243, Nov. 1999.

[255] Z. Jiang, X. G. Xu, and X.-C. Zhang, "Improvement of terahertz imaging with a dynamic subtraction technique," *Applied Optics*, vol. 39, no. 17, p. 2982, Jun. 2000.

[256] F. Miyamaru *et al.*, "Terahertz two-dimensional electrooptic sampling using high speed complementary metal-oxide semiconductor camera," *Japanese Journal of Applied Physics*, vol. 43, no. No. 4A, pp. L489–L491, Mar. 2004.

[257] X. Wang *et al.*, "Terahertz real-time imaging with balanced electro-optic detection," *Optics Communications*, vol. 283, no. 23, pp. 4626–4632, Dec. 2010.

[258] B. Pradarutti *et al.*, "Multichannel balanced electro-optic detection for terahertz imaging," *Optics Express*, vol. 15, no. 26, p. 17652, 2007.

[259] N. C. J. van der Valk, T. Wenckebach, and P. C. M. Planken, "Full mathematical description of electro-optic detection in optically isotropic crystals," *Journal of the Optical Society of America B*, vol. 21, no. 3, p. 622, Mar. 2004.

[260] X. Wang *et al.*, "Terahertz polarization real-time imaging based on balanced electro-optic detection," *Journal of the Optical Society of America A*, vol. 27, no. 11, p. 2387, Oct. 2010.

[261] F. Blanchard *et al.*, "Real-time terahertz near-field microscope," *Optics Express*, vol. 19, no. 9, p. 8277, Apr. 2011.

[262] F. Blanchard and K. Tanaka, "Improving time and space resolution in electro-optic sampling for near-field terahertz imaging," *Optics Letters*, vol. 41, no. 20, p. 4645, Oct. 2016.

[263] A. Doi *et al.*, "Near-field THz imaging of free induction decay from a tyrosine crystal," *Optics Express*, vol. 18, no. 17, p. 18419, Aug. 2010.

[264] F. Blanchard *et al.*, "Terahertz spectroscopy of the reactive and radiative near-field zones of split ring resonator," *Optics Express*, vol. 20, no. 17, p. 19395, Aug. 2012.

[265] A. Doi *et al.*, "Improving spatial resolution of real-time terahertz near-field microscope," *Journal of Infrared, Millimeter, and Terahertz Waves*, vol. 32, no. 8-9, pp. 1043–1051, Aug. 2011.

[266] Z. Jiang and X.-C. Zhang, "Electro-optic measurement of THz field pulses with a chirped optical beam," *Applied Physics Letters*, vol. 72, no. 16, pp. 1945–1947, Apr. 1998.

[267] ——, "Single-shot spatiotemporal terahertz field imaging," *Optics Letters*, vol. 23, no. 14, p. 1114, Jul. 1998.

[268] ——, "Measurement of spatio-temporal terahertz field distribution by using chirped pulse technology," *IEEE Journal of Quantum Electronics*, vol. 36, no. 10, pp. 1214–1222, Oct. 2000.

[269] J. Shan *et al.*, "Single-shot measurement of terahertz electromagnetic pulses by use of electro-optic sampling," *Optics Letters*, vol. 25, no. 6, p. 426, Mar. 2000.

[270] T. Yasuda *et al.*, "Real-time two-dimensional terahertz tomography of moving objects," *Optics Communications*, vol. 267, no. 1, pp. 128–136, Nov. 2006.

[271] T. Yasui *et al.*, "Real-time terahertz color scanner for moving objects," *Optics Express*, vol. 16, no. 2, p. 1208, Jan. 2008.

[272] M. Schirmer *et al.*, "Biomedical applications of a real-time terahertz color scanner," *Biomedical Optics Express*, vol. 1, no. 2, p. 354, Aug. 2010.

[273] O. Morikawa, M. Tonouchi, and M. Hangyo, "Sub-THz spectroscopic system using a multimode laser diode and photoconductive antenna," *Applied Physics Letters*, vol. 75, no. 24, pp. 3772–3774, Dec. 1999.

[274] I. S. Gregory *et al.*, "Multi-channel homodyne detection of continuous-wave terahertz radiation," *Applied Physics Letters*, vol. 87, no. 3, p. 034106, Jul. 2005.

[275] K. Shibuya, M. Tani, and M. Hangyo, "Compact and inexpensive continuous-wave sub-THz imaging system using a fiber-coupled multimode laser diode," in *2006 Joint 31st International Conference on Infrared Millimeter Waves and 14th International Conference on Teraherz Electronics*. IEEE, Sep. 2006.

[276] M. Scheller and M. Koch, "Terahertz quasi time domain spectroscopy," *Optics Express*, vol. 17, no. 20, p. 17723, Sep. 2009.

[277] M. Scheller *et al.*, "Terahertz quasi-time-domain spectroscopy imaging," *Applied Optics*, vol. 50, no. 13, p. 1884, Apr. 2011.

[278] T. Probst, A. Rehn, and M. Koch, "Compact and low-cost THz QTDS system," *Optics Express*, vol. 23, no. 17, p. 21972, Aug. 2015.

[279] R. B. Kohlhaas *et al.*, "Terahertz quasi time-domain spectroscopy based on telecom technology for 1550 nm," *Optics Express*, vol. 25, no. 11, p. 12851, May 2017.

[280] X. Wu and K. Sengupta, "Dynamic waveform shaping with picosecond time widths," *IEEE Journal of Solid-State Circuits*, vol. 52, no. 2, pp. 389–405, Feb. 2017.

[281] M. M. Assefzadeh and A. Babakhani, "Broadband oscillator-free THz pulse generation and radiation based on direct digital-to-impulse architecture," *IEEE Journal of Solid-State Circuits*, vol. 52, no. 11, pp. 2905–2919, Nov. 2017.

[282] X. Wu and K. Sengupta, "On-chip THz spectroscope exploiting electromagnetic scattering with multi-port antenna," *IEEE Journal of Solid-State Circuits*, vol. 51, no. 12, pp. 3049–3062, Dec. 2016.

[283] N. Karpowicz *et al.*, "Comparison between pulsed terahertz time-domain imaging and continuous wave terahertz imaging," *Semiconductor Science and Technology*, vol. 20, no. 7, pp. S293–S299, Jun. 2005.

[284] Y.-S. Lee, "Continuous-wave terahertz sources and detectors," in *Principles of Terahertz Science and Technology*. Springer US, 2009, pp. 1–41.

[285] J. Yang, S. Ruan, and M. Zhang, "Real-time, continuous-wave terahertz imaging by a pyroelectric camera," *Chinese Optics Letters*, vol. 6, no. 1, pp. 29–31, Jun. 2008.

[286] P. L. Richards, "Bolometers for infrared and millimeter waves," *Journal of Applied Physics*, vol. 76, no. 1, pp. 1–24, Jul. 1994.

[287] N. Nemoto *et al.*, "High-sensitivity and broadband, real-time terahertz camera incorporating a micro-bolometer array_newline with resonant cavity structure," *IEEE Transactions on Terahertz Science and Technology*, vol. 6, no. 2, pp. 175–182, Mar. 2016.

[288] A. W. Lee and Q. Hu, "Real-time, continuous-wave terahertz imaging by use of a microbolometer focal-plane array," *Optics Letters*, vol. 30, no. 19, p. 2563, Oct. 2005.

[289] A. Lee *et al.*, "Real-time imaging using a 4.3-THz quantum cascade laser and a 320 /spl times/ 240 microbolometer focal-plane array," *IEEE Photonics Technology Letters*, vol. 18, no. 13, pp. 1415–1417, Jul. 2006.

[290] B. N. Behnken *et al.*, "Real-time imaging using a 28 THz quantum cascade laser and uncooled infrared microbolometer camera," *Optics Letters*, vol. 33, no. 5, p. 440, Feb. 2008.

[291] M. A. Demyanenko *et al.*, "Imaging with a 90 frames per second microbolometer focal plane array and high-power terahertz free electron laser," *Applied Physics Letters*, vol. 92, no. 13, p. 131116, Mar. 2008.

[292] A. W. M. Lee *et al.*, "Real-time terahertz imaging over a standoff distance (>25meters)," *Applied Physics Letters*, vol. 89, no. 14, p. 141125, Oct. 2006.

[293] N. Oda *et al.*, "Microbolometer terahertz focal plane array and camera with improved sensitivity in the sub-terahertz region," *Journal of Infrared, Millimeter, and Terahertz Waves*, vol. 36, no. 10, pp. 947–960, Jul. 2015.

[294] M. Nishita *et al.*, "Ror2 signaling regulates golgi structure and transport through IFT20 for tumor invasiveness," *Scientific Reports*, vol. 7, no. 1, Jan. 2017.

[295] D.-T. Nguyen *et al.*, "Broadband THz uncooled antenna-coupled microbolometer array—electromagnetic design, simulations and measurements," *IEEE Transactions on Terahertz Science and Technology*, vol. 2, no. 3, pp. 299–305, May 2012.

[296] F. Simoens and J. Meilhan, "Terahertz real-time imaging uncooled array based on antenna- and cavity-coupled bolometers," *Philosophical Transactions of the Royal Society A: Mathematical, Physical and Engineering Sciences*, vol. 372, no. 2012, p. 20130111, Mar. 2014.

[297] F. Alves *et al.*, "Strong terahertz absorption using SiO2/al based metamaterial structures," *Applied Physics Letters*, vol. 100, no. 11, p. 111104, Mar. 2012.

[298] B. Kearney *et al.*, "Al/SiOx/al single and multiband metamaterial absorbers for terahertz sensor applications," *Optical Engineering*, vol. 52, no. 1, p. 013801, Jan. 2013.

[299] W. Withayachumnankul *et al.*, "Plasmonic resonance toward terahertz perfect absorbers," *ACS Photonics*, vol. 1, no. 7, pp. 625–630, Jun. 2014.

[300] K. Fan *et al.*, "All-dielectric metasurface absorbers for uncooled terahertz imaging," *Optica*, vol. 4, no. 6, p. 601, May 2017.

[301] I. E. Carranza *et al.*, "Terahertz metamaterial absorbers implemented in CMOS technology for imaging applications: Scaling to large format focal plane arrays," *IEEE Journal of Selected Topics in Quantum Electronics*, vol. 23, no. 4, pp. 1–8, Jul. 2017.

[302] W. Knap *et al.*, "Nanometer size field effect transistors for terahertz detectors," *Nanotechnology*, vol. 24, no. 21, p. 214002, Apr. 2013.

[303] W. Knap and M. Dyakonov, "Field effect transistors for terahertz applications," in *Handbook of Terahertz Technology for Imaging, Sensing and Communications*. Elsevier, 2013, pp. 121–155.

[304] A. Lisauskas *et al.*, "Exploration of terahertz imaging with silicon MOSFETs," *Journal of Infrared, Millimeter, and Terahertz Waves*, vol. 35, no. 1, pp. 63–80, Jan. 2014.

[305] M. Dyakonov and M. Shur, "Plasma wave electronics: novel terahertz devices using two dimensional electron fluid," *IEEE Transactions on Electron Devices*, vol. 43, no. 10, pp. 1640–1645, 1996.

[306] J.-Q. Lü and M. S. Shur, "Terahertz detection by high-electron-mobility transistor: Enhancement by drain bias," *Applied Physics Letters*, vol. 78, no. 17, pp. 2587–2588, Apr. 2001.

[307] F. Schuster *et al.*, "Broadband terahertz imaging with highly sensitive silicon CMOS detectors," *Optics Express*, vol. 19, no. 8, p. 7827, Apr. 2011.

[308] E. Ojefors *et al.*, "A 0.65 THz focal-plane array in a quarter-micron CMOS process technology," *IEEE Journal of Solid-State Circuits*, vol. 44, no. 7, pp. 1968–1976, Jul. 2009.

[309] D. Glaab *et al.*, "Terahertz heterodyne detection with silicon field-effect transistors," *Applied Physics Letters*, vol. 96, no. 4, p. 042106, Jan. 2010.

[310] W. Knap *et al.*, "Resonant detection of subterahertz radiation by plasma waves in a submicron field-effect transistor," *Applied Physics Letters*, vol. 80, no. 18, pp. 3433–3435, May 2002.

[311] T. Otsuji, M. Hanabe, and O. Ogawara, "Terahertz plasma wave resonance of two-dimensional electrons in InGaP/InGaAs/GaAs high-electron-mobility transistors," *Applied Physics Letters*, vol. 85, no. 11, pp. 2119–2121, Sep. 2004.

[312] M. Lee, M. C. Wanke, and J. L. Reno, "Millimeter wave mixing using plasmon and bolometric response in a double-quantum-well field-effect transistor," *Applied Physics Letters*, vol. 86, no. 3, p. 033501, Jan. 2005.

[313] A. E. Fatimy *et al.*, "Resonant and voltage-tunable terahertz detection in InGaAs/InP nanometer transistors," *Applied Physics Letters*, vol. 89, no. 13, p. 131926, Sep. 2006.

[314] V. I. Gavrilenko *et al.*, "Electron transport and detection of terahertz radiation in a GaN/AlGaN submicrometer field-effect transistor," *Semiconductors*, vol. 41, no. 2, pp. 232–234, Feb. 2007.

[315] M. S. Vitiello *et al.*, "Room-temperature terahertz detectors based on semiconductor nanowire field-effect transistors," *Nano Letters*, vol. 12, no. 1, pp. 96–101, Dec. 2011.

[316] L. Vicarelli *et al.*, "Graphene field-effect transistors as room-temperature terahertz detectors," *Nature Materials*, vol. 11, no. 10, pp. 865–871, Sep. 2012.

[317] L. Viti *et al.*, "Black phosphorus terahertz photodetectors," *Advanced Materials*, vol. 27, no. 37, pp. 5567–5572, Aug. 2015.

[318] W. Knap *et al.*, "Plasma wave detection of sub-terahertz and terahertz radiation by silicon field-effect transistors," *Applied Physics Letters*, vol. 85, no. 4, pp. 675–677, Jul. 2004.

[319] N. Pala *et al.*, "Nonresonant detection of terahertz radiation by silicon-on-insulator MOSFETs," *Electronics Letters*, vol. 41, no. 7, p. 447, 2005.

[320] A. Lisauskas *et al.*, "Rational design of high-responsivity detectors of terahertz radiation based on distributed self-mixing in silicon field-effect transistors," *Journal of Applied Physics*, vol. 105, no. 11, p. 114511, Jun. 2009.

[321] S. Boppel *et al.*, "CMOS detector arrays in a virtual 10-kilopixel camera for coherent terahertz real-time imaging," *Optics Letters*, vol. 37, no. 4, p. 536, Feb. 2012.

[322] ——, "Performance and performance variations of sub-1 THz detectors fabricated with 0.15 [micro sign]m CMOS foundry process," *Electronics Letters*, vol. 47, no. 11, p. 661, 2011.

[323] M. Bauer *et al.*, "Antenna-coupled field-effect transistors for multi-spectral terahertz imaging up to 425 THz," *Optics Express*, vol. 22, no. 16, p. 19235, Jul. 2014.

[324] H. Sherry *et al.*, "A 1kpixel CMOS camera chip for 25fps real-time terahertz imaging applications," in *2012 IEEE International Solid-State Circuits Conference*. IEEE, Feb. 2012.

[325] J. Zdanevičius *et al.*, "Camera for high-speed THz imaging," *Journal of Infrared, Millimeter, and Terahertz Waves*, vol. 36, no. 10, pp. 986–997, Jun. 2015.

[326] K. Sengupta and A. Hajimiri, "A 0.28 THz power-generation and beam-steering array in CMOS based on distributed active radiators," *IEEE Journal of Solid-State Circuits*, vol. 47, no. 12, pp. 3013–3031, Dec. 2012.

[327] Y. Tousi and E. Afshari, "A high-power and scalable 2-d phased array for terahertz CMOS integrated systems," *IEEE Journal of Solid-State Circuits*, vol. 50, no. 2, pp. 597–609, Feb. 2015.

[328] U. R. Pfeiffer *et al.*, "A 0.53 THz reconfigurable source module with up to 1 mW radiated power for diffuse illumination in terahertz imaging applications," *IEEE Journal of Solid-State Circuits*, vol. 49, no. 12, pp. 2938–2950, Dec. 2014.

[329] C. Jiang *et al.*, "A fully integrated 320 GHz coherent imaging transceiver in 130 nm SiGe BiCMOS," *IEEE Journal of Solid-State Circuits*, vol. 51, no. 11, pp. 2596–2609, Nov. 2016.

[330] B. Scherger *et al.*, "Discrete terahertz beam steering with an electrically controlled liquid crystal device," *Journal of Infrared, Millimeter, and Terahertz Waves*, vol. 33, no. 11, pp. 1117–1122, Jul. 2012.

[331] S. Busch *et al.*, "Optically controlled terahertz beam steering and imaging," *Optics Letters*, vol. 37, no. 8, p. 1391, Apr. 2012.

[332] J. Neu, R. Beigang, and M. Rahm, "Metamaterial-based gradient index beam steerers for terahertz radiation," *Applied Physics Letters*, vol. 103, no. 4, p. 041109, Jul. 2013.

[333] M. I. B. Shams *et al.*, "A 740-GHz dynamic two-dimensional beam-steering and forming antenna based on photo-induced reconfigurable fresnel zone plates," *IEEE Transactions on Terahertz Science and Technology*, vol. 7, no. 3, pp. 310–319, May 2017.

[334] K. ichiro Maki and C. Otani, "Terahertz beam steering and frequency tuning by using the spatial dispersion of ultrafast laser pulses," *Optics Express*, vol. 16, no. 14, p. 10158, Jun. 2008.

[335] H. Füser and M. Bieler, "Terahertz beam steering by optical coherent control," *Applied Physics Letters*, vol. 102, no. 25, p. 251109, Jun. 2013.

[336] B. C. Smith, J. F. Whitaker, and S. C. Rand, "Steerable THz pulses from thin emitters via optical pulse-front tilt," *Optics Express*, vol. 24, no. 18, p. 20755, Aug. 2016.

[337] K. Sengupta and A. Hajimiri, "Mutual synchronization for power generation and beam-steering in CMOS with on-chip sense antennas near 200 GHz," *IEEE Transactions on Microwave Theory and Techniques*, vol. 63, no. 9, pp. 2867–2876, Sep. 2015.

[338] G. Ok *et al.*, "High-speed terahertz imaging toward food quality inspection," *Applied Optics*, vol. 53, no. 7, p. 1406, Feb. 2014.

[339] ——, "High-performance sub-terahertz transmission imaging system for food inspection," *Biomedical Optics Express*, vol. 6, no. 5, p. 1929, Apr. 2015.

[340] S. Katletz *et al.*, "Efficient terahertz en-face imaging," *Optics Express*, vol. 19, no. 23, p. 23042, Oct. 2011.

[341] D.-S. Yee *et al.*, "High-speed terahertz reflection three-dimensional imaging using beam steering," *Optics Express*, vol. 23, no. 4, p. 5027, Feb. 2015.

[342] M. Wienold *et al.*, "Real-time terahertz imaging through self-mixing in a quantum-cascade laser," *Applied Physics Letters*, vol. 109, no. 1, p. 011102, Jul. 2016.

[343] K. B. Cooper *et al.*, "THz imaging radar for standoff personnel screening," *IEEE Transactions on Terahertz Science and Technology*, vol. 1, no. 1, pp. 169–182, Sep. 2011.

[344] N. Llombart, R. J. Dengler, and K. B. Cooper, "Terahertz antenna system for a near-video-rate radar imager [antenna applications]," *IEEE Antennas and Propagation Magazine*, vol. 52, no. 5, pp. 251–259, Oct. 2010.

[345] N. Llombart *et al.*, "Confocal ellipsoidal reflector system for a mechanically scanned active terahertz imager," *IEEE Transactions on Antennas and Propagation*, vol. 58, no. 6, pp. 1834–1841, Jun. 2010.

[346] K. B. Cooper *et al.*, "A high-resolution imaging radar at 580 GHz," *IEEE Microwave and Wireless Components Letters*, vol. 18, no. 1, pp. 64–66, Jan. 2008.

[347] K. Cooper *et al.*, "Penetrating 3-d imaging at 4- and 25-m range using a submillimeter-wave radar," *IEEE Transactions on Microwave Theory and Techniques*, vol. 56, no. 12, pp. 2771–2778, Dec. 2008.

[348] A. Garcia-Pino *et al.*, "A bifocal ellipsoidal gregorian reflector system for THz imaging applications," *IEEE Transactions on Antennas and Propagation*, vol. 60, no. 9, pp. 4119–4129, Sep. 2012.

[349] E. Heinz *et al.*, "Progress in passive submillimeter-wave video imaging," in *Passive and Active Millimeter-Wave Imaging XVII*, D. A. Wikner and A. R. Luukanen, Eds. SPIE, Jun. 2014.

[350] ——, "Passive 350 GHz video imaging systems for security applications," *Journal of Infrared, Millimeter, and Terahertz Waves*, vol. 36, no. 10, pp. 879–895, Jun. 2015.

[351] M. F. Duarte *et al.*, "Single-pixel imaging via compressive sampling," *IEEE Signal Processing Magazine*, vol. 25, no. 2, pp. 83–91, Mar. 2008.

[352] M. Harwit and N. J. A. Sloane, *Hadamard Transform Optics*. Elsevier, 1979.

[353] Study Group VIII, *Terminal equipment and protocols for telematic services*, International Telecommunication Union Std. ITU-T T.83 (11/1994), 1998.

[354] D. Donoho, "Compressed sensing," *IEEE Transactions on Information Theory*, vol. 52, no. 4, pp. 1289–1306, Apr. 2006.

[355] E. Candes, J. Romberg, and T. Tao, "Robust uncertainty principles: exact signal reconstruction from highly incomplete frequency information," *IEEE Transactions on Information Theory*, vol. 52, no. 2, pp. 489–509, Feb. 2006.

[356] M. Lustig, D. Donoho, and J. M. Pauly, "Sparse MRI: The application of compressed sensing for rapid MR imaging," *Magnetic Resonance in Medicine*, vol. 58, no. 6, pp. 1182–1195, 2007.

[357] Y. Zhang, "Theory of compressive sensing via ℓ 1-minimization: a non-RIP analysis and extensions," *Journal of the Operations Research Society of China*, vol. 1, no. 1, pp. 79–105, Mar. 2013.

[358] E. Candes and M. Wakin, "An introduction to compressive sampling," *IEEE Signal Processing Magazine*, vol. 25, no. 2, pp. 21–30, Mar. 2008.

[359] M. Fornasier and H. Rauhut, "Compressive sensing," in *Handbook of Mathematical Methods in Imaging*. Springer New York, 2015, pp. 205–256.

[360] E. van den Berg and M. P. Friedlander, "Probing the pareto frontier for basis pursuit solutions," *SIAM Journal on Scientific Computing*, vol. 31, no. 2, pp. 890–912, Jan. 2009.

[361] M. F. Duarte and Y. C. Eldar, "Structured compressed sensing: From theory to applications," *IEEE Transactions on Signal Processing*, vol. 59, no. 9, pp. 4053–4085, Sep. 2011.

[362] Y. Pati, R. Rezaiifar, and P. Krishnaprasad, "Orthogonal matching pursuit: recursive function approximation with applications to wavelet decomposition," in *Proceedings of 27th Asilomar Conference on Signals, Systems and Computers*. IEEE Comput. Soc. Press, 1993.

[363] D. Needell and J. Tropp, "CoSaMP: Iterative signal recovery from incomplete and inaccurate samples," *Applied and Computational Harmonic Analysis*, vol. 26, no. 3, pp. 301–321, May 2009.

[364] F. Marvasti *et al.*, "A unified approach to sparse signal processing," *EURASIP Journal on Advances in Signal Processing*, vol. 2012, no. 1, Feb. 2012.

[365] C. M. Watts *et al.*, "Frequency-division-multiplexed single-pixel imaging with metamaterials," *Optica*, vol. 3, no. 2, p. 133, Feb. 2016.

[366] C. C. Nadell *et al.*, "Single pixel quadrature imaging with metamaterials," *Advanced Optical Materials*, vol. 4, no. 1, pp. 66–69, Oct. 2015.

[367] S. A. N. Saqueb and K. Sertel, "Phase-sensitive single-pixel THz imaging using intensity-only measurements," *IEEE Transactions on Terahertz Science and Technology*, vol. 6, no. 6, pp. 810–816, Nov. 2016.

[368] W. L. Chan *et al.*, "Terahertz imaging with compressed sensing and phase retrieval," *Optics Letters*, vol. 33, no. 9, p. 974, Apr. 2008.

[369] ——, "A single-pixel terahertz imaging system based on compressed sensing," *Applied Physics Letters*, vol. 93, no. 12, p. 121105, Sep. 2008.

[370] ——, "Terahertz imaging with compressed sensing and phase retrieval," in *2007 Conference on Lasers and Electro-Optics (CLEO)*. IEEE, May 2007.

[371] S. Yu, A. S. Khwaja, and J. Ma, "Compressed sensing of complex-valued data," *Signal Processing*, vol. 92, no. 2, pp. 357–362, Feb. 2012.

[372] H. Shen *et al.*, "Spinning disk for compressive imaging," *Optics Letters*, vol. 37, no. 1, p. 46, Dec. 2011.

[373] Y. C. Shen *et al.*, "Terahertz pulsed spectroscopic imaging using optimized binary masks," *Applied Physics Letters*, vol. 95, no. 23, p. 231112, Dec. 2009.

[374] N. P. Pitsianis, D. J. Brady, and X. Sun, "Sensor-layer image compression based on the quantized cosine transform," in *Visual Information Processing XIV*, Z. ur Rahman, R. A. Schowengerdt, and S. E. Reichenbach, Eds. SPIE, May 2005.

[375] Z. Xu and E. Y. Lam, "Image reconstruction using spectroscopic and hyperspectral information for compressive terahertz imaging," *Journal of the Optical Society of America A*, vol. 27, no. 7, p. 1638, Jun. 2010.

[376] K. H. Jin *et al.*, "Compressed sensing pulse-echo mode terahertz reflectance tomography," *Optics Letters*, vol. 34, no. 24, p. 3863, Dec. 2009.

[377] L. Gan, "Block compressed sensing of natural images," in *2007 15th International Conference on Digital Signal Processing*. IEEE, Jul. 2007.

[378] M. Rahm, J.-S. Li, and W. J. Padilla, "THz wave modulators: A brief review on different modulation techniques," *Journal of Infrared, Millimeter, and Terahertz Waves*, vol. 34, no. 1, pp. 1–27, Nov. 2012.

[379] Y. Bai *et al.*, "Review about the optical-controlled terahertz waves modulator," *Applied Spectroscopy Reviews*, vol. 50, no. 9, pp. 707–727, Jul. 2015.

[380] M. R. Hashemi, S. Cakmakyapan, and M. Jarrahi, "Reconfigurable metamaterials for terahertz wave manipulation," *Reports on Progress in Physics*, vol. 80, no. 9, p. 094501, Jul.

[381] R. Degl'Innocenti *et al.*, "All-integrated terahertz modulators," *Nanophotonics*, vol. 7, no. 1, pp. 127–144, Jan. 2018.

[382] R. I. Stantchev *et al.*, "Noninvasive, near-field terahertz imaging of hidden objects using a single-pixel detector," *Science Advances*, vol. 2, no. 6, p. e1600190, Jun. 2016.

[383] H. Alius and G. Dodel, "Amplitude-, phase-, and frequency modulation of far-infrared radiation by optical excitation of silicon," *Infrared Physics*, vol. 32, pp. 1–11, Jan. 1991.

[384] D. Shrekenhamer, C. M. Watts, and W. J. Padilla, "Terahertz single pixel imaging with an optically controlled dynamic spatial light modulator," *Optics Express*, vol. 21, no. 10, p. 12507, May 2013.

[385] M. Shams *et al.*, "Approaching real-time terahertz imaging with photo-induced coded apertures and compressed sensing," *Electronics Letters*, vol. 50, no. 11, pp. 801–803, May 2014.

[386] A. Kannegulla *et al.*, "Coded-aperture imaging using photo-induced reconfigurable aperture arrays for mapping terahertz beams," *IEEE Transactions on Terahertz Science and Technology*, vol. 4, no. 3, pp. 321–327, May 2014.

[387] S. Augustin *et al.*, "Compressed sensing in a fully non-mechanical 350 GHz imaging setting," *Journal of Infrared, Millimeter, and Terahertz Waves*, vol. 36, no. 5, pp. 496–512, Jan. 2015.

[388] E. J. Candès, T. Strohmer, and V. Voroninski, "PhaseLift: Exact and stable signal recovery from magnitude measurements via convex programming," *Communications on Pure and Applied Mathematics*, vol. 66, no. 8, pp. 1241–1274, Nov. 2012.

[389] R. I. Stantchev *et al.*, "Compressed sensing with near-field THz radiation," *Optica*, vol. 4, no. 8, p. 989, Aug. 2017.

[390] S. M. Hornett *et al.*, "Subwavelength terahertz imaging of graphene photoconductivity," *Nano Letters*, vol. 16, no. 11, pp. 7019–7024, Oct. 2016.

[391] D. B. Phillips *et al.*, "Adaptive foveated single-pixel imaging with dynamic supersampling," *Science Advances*, vol. 3, no. 4, p. e1601782, Apr. 2017.

[392] C. M. Watts *et al.*, "Terahertz compressive imaging with metamaterial spatial light modulators," *Nature Photonics*, vol. 8, no. 8, pp. 605–609, Jun. 2014.

[393] W. L. Chan *et al.*, "A spatial light modulator for terahertz beams," *Applied Physics Letters*, vol. 94, no. 21, p. 213511, May 2009.

[394] H.-T. Chen *et al.*, "Active terahertz metamaterial devices," *Nature*, vol. 444, no. 7119, pp. 597–600, Nov. 2006.

[395] N. I. Landy *et al.*, "Perfect metamaterial absorber," *Physical Review Letters*, vol. 100, no. 20, May 2008.

[396] K. Goda, K. K. Tsia, and B. Jalali, "Serial time-encoded amplified imaging for real-time observation of fast dynamic phenomena," *Nature*, vol. 458, no. 7242, pp. 1145–1149, Apr. 2009.

[397] A. Mahjoubfar *et al.*, "Time stretch and its applications," *Nature Photonics*, vol. 11, no. 6, pp. 341–351, Jun. 2017.

[398] S. Schumann *et al.*, "Spectrum to space transformed fast terahertz imaging," *Optics Express*, vol. 20, no. 17, p. 19200, Aug. 2012.

[399] S. A. Diddams, L. Hollberg, and V. Mbele, "Molecular fingerprinting with the resolved modes of a femtosecond laser frequency comb," *Nature*, vol. 445, no. 7128, pp. 627–630, Feb. 2007.

[400] M. E. Gehm *et al.*, "Single-shot compressive spectral imaging with a dual-disperser architecture," *Optics Express*, vol. 15, no. 21, p. 14013, Oct. 2007.

[401] A. Wagadarikar *et al.*, "Single disperser design for coded aperture snapshot spectral imaging," *Applied Optics*, vol. 47, no. 10, p. B44, Feb. 2008.

[402] O. Furxhi, D. L. Marks, and D. J. Brady, "Echelle crossed grating millimeter wave beam scanner," *Optics Express*, vol. 22, no. 13, p. 16393, Jun.

[403] K. Lee *et al.*, "THz near-field spectral encoding imaging using a rainbow metasurface," *Scientific Reports*, vol. 5, no. 1, Sep. 2015.

[404] E.-M. Stübling *et al.*, "Development of a multi-channel time-to-space terahertz spectrometer," *Optics Express*, vol. 24, no. 20, p. 23146, Sep. 2016.

[405] K. Lee *et al.*, "Coherent optical computing for t-ray imaging," *Optics Letters*, vol. 35, no. 4, p. 508, Feb. 2010.

[406] K. Lee and J. Ahn, "Single-pixel coherent diffraction imaging," *Applied Physics Letters*, vol. 97, no. 24, p. 241101, Dec. 2010.

[407] F. Ellrich *et al.*, "Compact fiber-coupled terahertz spectroscopy system pumped at 800 nm wavelength," *Review of Scientific Instruments*, vol. 82, no. 5, p. 053102, May 2011.

[408] K. Sengupta, T. Nagatsuma, and D. M. Mittleman, "Terahertz integrated electronic and hybrid electronic–photonic systems," *Nature Electronics*, vol. 1, no. 12, p. 622, 2018.

[409] D. Headland *et al.*, "Tutorial: Terahertz beamforming, from concepts to realizations," *APL Photonics*, vol. 3, no. 5, p. 051101, 2018.

[410] Y.-S. Jin, G.-J. Kim, and S.-G. Jeon, "Terahertz dielectric properties of polymers," *Journal of the Korean Physical Society*, vol. 49, no. 2, pp. 513–517, 2006.

[411] A. Podzorov and G. Gallot, "Low-loss polymers for terahertz applications," *Applied optics*, vol. 47, no. 18, pp. 3254–3257, 2008.

[412] E. Walsby *et al.*, "Multilevel silicon diffractive optics for terahertz waves," *Journal of Vacuum Science & Technology B: Microelectronics and Nanometer Structures Processing, Measurement, and Phenomena*, vol. 20, no. 6, pp. 2780–2783, 2002.

[413] M. Sypek *et al.*, "Highly efficient broadband double-sided fresnel lens for THz range," *Optics letters*, vol. 37, no. 12, pp. 2214–2216, 2012.

[414] X.-Y. Jiang *et al.*, "An ultrathin terahertz lens with axial long focal depth based on metasurfaces," *Optics Express*, vol. 21, no. 24, pp. 30 030–30 038, 2013.

[415] C.-C. Chang *et al.*, "Demonstration of a highly efficient terahertz flat lens employing tri-layer metasurfaces," *Optics letters*, vol. 42, no. 9, pp. 1867–1870, 2017.

[416] D. Jia *et al.*, "Transmissive terahertz metalens with full phase control based on a dielectric metasurface," *Optics letters*, vol. 42, no. 21, pp. 4494–4497, 2017.

[417] D. Headland *et al.*, "Dielectric resonator reflectarray as high-efficiency nonuniform terahertz metasurface," *Acs Photonics*, vol. 3, no. 6, pp. 1019–1026, 2016.

[418] M. Brincker *et al.*, "Microstructured gradient-index lenses for THz photoconductive antennas," *Aip Advances*, vol. 6, no. 2, p. 025015, 2016.

[419] H. Chen *et al.*, "Sub-wavelength tight-focusing of terahertz waves by polarization-independent high-numerical-aperture dielectric metalens," *Optics express*, vol. 26, no. 23, pp. 29 817–29 825, 2018.

[420] X. Su *et al.*, "Active metasurface terahertz deflector with phase discontinuities," *Optics express*, vol. 23, no. 21, pp. 27 152–27 158, 2015.

[421] X. Zhang *et al.*, "Broadband terahertz wave deflection based on c-shape complex metamaterials with phase discontinuities," *Advanced Materials*, vol. 25, no. 33, pp. 4567–4572, 2013.

[422] J. Neu, R. Beigang, and M. Rahm, "Metamaterial-based gradient index beam steerers for terahertz radiation," *Applied Physics Letters*, vol. 103, no. 4, p. 041109, 2013.

[423] N. K. Grady *et al.*, "Terahertz metamaterials for linear polarization conversion and anomalous refraction," *Science*, vol. 340, no. 6138, pp. 1304–1307, 2013.

[424] H. Zhou *et al.*, "Generation of terahertz vortices using metasurface with circular slits," *IEEE Photonics Journal*, vol. 6, no. 6, pp. 1–7, 2014.

[425] T. Niu *et al.*, "Terahertz reflectarray as a polarizing beam splitter," *Optics express*, vol. 22, no. 13, pp. 16 148–16 160, 2014.

[426] A. Hassani, A. Dupuis, and M. Skorobogatiy, "Low loss porous terahertz fibers containing multiple subwavelength holes," *Applied Physics Letters*, vol. 92, no. 7, p. 071101, 2008.

[427] ——, "Porous polymer fibers for low-loss terahertz guiding," *Optics express*, vol. 16, no. 9, pp. 6340–6351, 2008.

[428] M. Skorobogatiy, *Nanostructured and Subwavelength Waveguides: fundamentals and applications*. John Wiley & Sons, 2012.

[429] T. Ma *et al.*, "Analog signal processing in the terahertz communication links using waveguide bragg gratings: example of dispersion compensation," *Optics express*, vol. 25, no. 10, pp. 11 009–11 026, 2017.

[430] S.-G. Park *et al.*, "Subwavelength silicon through-hole arrays as an all-dielectric broadband terahertz gradient index metamaterial," *Applied Physics Letters*, vol. 105, no. 9, p. 091101, 2014.

[431] M. Brincker *et al.*, "Microstructured gradient-index lenses for THz photoconductive antennas," *AIP Advances*, vol. 6, no. 2, p. 025015, Feb. 2016.

[432] J. Wang *et al.*, "Terabit free-space data transmission employing orbital angular momentum multiplexing," *Nature photonics*, vol. 6, no. 7, p. 488, 2012.

[433] Y. Yan *et al.*, "High-capacity millimetre-wave communications with orbital angular momentum multiplexing," *Nature communications*, vol. 5, p. 4876, 2014.

[434] H. Zhao *et al.*, "Demonstration of orbital angular momentum multiplexing and demultiplexing based on a metasurface in the terahertz band," *ACS Photonics*, vol. 5, no. 5, pp. 1726–1732, 2017.

[435] S. Atakaramians *et al.*, "Porous fibers: a novel approach to low loss THz waveguides," *Optics Express*, vol. 16, no. 12, pp. 8845–8854, 2008.

[436] R. Piesiewicz *et al.*, "Properties of building and plastic materials in the THz range," *International Journal of Infrared and Millimeter Waves*, vol. 28, no. 5, pp. 363–371, Mar. 2007.

[437] M. Seghilani and J. Azaña, "All-fiber OAM generation/conversion using helically patterned photonic crystal fiber," *IEEE Photonics Technology Letters*, vol. 30, no. 4, pp. 347–350, 2018.

[438] A. M. Yao and M. J. Padgett, "Orbital angular momentum: origins, behavior and applications," *Advances in Optics and Photonics*, vol. 3, no. 2, pp. 161–204, 2011.

[439] J. F. Federici *et al.*, "THz imaging and sensing for security applications—explosives, weapons and drugs," *Semiconductor Science and Technology*, vol. 20, no. 7, pp. S266–S280, Jun. 2005.

[440] E. Pickwell and V. P. Wallace, "Biomedical applications of terahertz technology," *Journal of Physics D: Applied Physics*, vol. 39, no. 17, pp. R301–R310, Aug. 2006.

[441] A. Gowen, C. O'Sullivan, and C. O'Donnell, "Terahertz time domain spectroscopy and imaging: Emerging techniques for food process monitoring and quality control," *Trends in Food Science & Technology*, vol. 25, no. 1, pp. 40–46, May 2012.

[442] E. Abraham *et al.*, "Non-invasive investigation of art paintings by terahertz imaging," *Applied Physics A*, vol. 100, no. 3, pp. 585–590, Mar. 2010.

[443] S.-G. Park, M. Melloch, and A. Weiner, "Analysis of terahertz waveforms measured by photoconductive and electrooptic sampling," *IEEE Journal of Quantum Electronics*, vol. 35, no. 5, pp. 810–819, May 1999.

[444] Z. Jiang and X.-C. Zhang, "Free-space electro-optic techniques," in *Springer Series in Optical Sciences*. Springer Berlin Heidelberg, 2003, pp. 155–192.

[445] G. Lamouche *et al.*, "Optical delay line using rotating rhombic prisms," in *Coherence Domain Optical Methods and Optical Coherence Tomography in Biomedicine XI*, J. G. Fujimoto, J. A. Izatt, and V. V. Tuchin, Eds. SPIE, Feb. 2007.

[446] C.-L. Wang and C.-L. Pan, "Scanning optical delay device having a helicoid reflecting mirror," USA U.S. Patent US5 907 423A, May 25, 1999. [Online]. Available: https://patents.google.com/patent/US5907423

[447] K. Nallappan *et al.*, "A dynamically reconfigurable terahertz array antenna for near-field imaging applications," 2017.

[448] Z. Jiang and X.-C. Zhang, "Terahertz imaging via electrooptic effect," *IEEE Transactions on Microwave Theory and Techniques*, vol. 47, no. 12, pp. 2644–2650, 1999.

[449] D. Huang *et al.*, "Optical coherence tomography," *Science*, vol. 254, no. 5035, pp. 1178–1181, Nov. 1991.

[450] K. McClatchey, M. T. Reiten, and R. A. Cheville, "Time resolved synthetic aperture terahertz impulse imaging," *Applied Physics Letters*, vol. 79, no. 27, pp. 4485–4487, Dec. 2001.

[451] M. S. Heimbeck *et al.*, "Terahertz interferometric synthetic aperture tomography for confocal imaging systems," *Optics Letters*, vol. 37, no. 8, p. 1316, Apr. 2012.

[452] F. Blanchard *et al.*, "Improved terahertz two-color plasma sources pumped by high intensity laser beam," *Optics Express*, vol. 17, no. 8, p. 6044, Mar. 2009.

[453] F. Amirkhan *et al.*, "Characterization of thin-film optical properties by THz near-field imaging method," *Journal of the Optical Society of America B*, vol. 36, no. 9, p. 2593, Aug. 2019. [Online]. Available: https://doi.org/10.1364/josab.36.002593

[454] J. Zhao *et al.*, "Spatial sampling of terahertz fields with sub-wavelength accuracy via probe-beam encoding," *Light: Science & Applications*, vol. 8, no. 1, Jun. 2019. [Online]. Available: https://doi.org/10.1038/s41377-019-0166-6

[455] A. G. Godin, B. Lounis, and L. Cognet, "Super-resolution microscopy approaches for live cell imaging," *Biophysical Journal*, vol. 107, no. 8, pp. 1777–1784, Oct. 2014. [Online]. Available: https://doi.org/10.1016/j.bpj.2014.08.028

[456] D. Wöll and C. Flors, "Super-resolution fluorescence imaging for materials science," *Small Methods*, vol. 1, no. 10, p. 1700191, Aug. 2017. [Online]. Available: https://doi.org/10.1002/smtd.201700191

[457] T. Dertinger *et al.*, "Fast, background-free, 3d super-resolution optical fluctuation imaging (SOFI)," *Proceedings of the National Academy of Sciences*, vol. 106, no. 52, pp. 22 287–22 292, Dec. 2009. [Online]. Available: https://doi.org/10.1073/pnas.0907866106

[458] ——, "Achieving increased resolution and more pixels with superresolution optical fluctuation imaging (SOFI)," *Optics Express*, vol. 18, no. 18, p. 18875, Aug. 2010. [Online]. Available: https://doi.org/10.1364/oe.18.018875

[459] C. G. Wade *et al.*, "Real-time near-field terahertz imaging with atomic optical fluorescence," *Nature Photonics*, vol. 11, no. 1, pp. 40–43, Nov. 2016. [Online]. Available: https://doi.org/10.1038/nphoton.2016.214

APPENDIX A SUPPLEMENTARY MATERIAL FOR: PLANAR POROUS COMPONENTS FOR LOW-LOSS TERAHERTZ OPTICS

A.1 Approximation of the Bruggeman Model for High Filling Factors

In this section, we use the Bruggeman model to express the effective RI n_{eff} and absorption losses α_{eff} when $f \to 1$. The results shown here are used in the main text to obtain theoretical expressions of the transmission ratio of the porous components versus their non-porous counterparts. We start with Eq. 4.6 for the effective permittivity:

$$\varepsilon_{\text{eff}} = \sqrt{\left(\frac{1}{2} - f\right)^2 (\varepsilon_a - \varepsilon_m) + \varepsilon_a \varepsilon_m} - \left(\frac{1}{2} - f\right)(\varepsilon_a - \varepsilon_m) \tag{A.1}$$

Let $\Delta\varepsilon = \varepsilon_a - \varepsilon_m$. We can expand Eq. A.1 to

$$\begin{aligned}
\varepsilon_{\text{eff}} &= \sqrt{\left(\frac{1}{2} - f\right)^2 \Delta\varepsilon^2 + \varepsilon_a \varepsilon_m} - \left(\frac{1}{2} - f\right)\Delta\varepsilon \\
&= \sqrt{\left(1 - f - \frac{1}{2}\right)^2 \Delta\varepsilon^2 + \varepsilon_a \varepsilon_m} - \left(1 - f - \frac{1}{2}\right)\Delta\varepsilon \\
&= \sqrt{(1-f)^2\Delta\varepsilon^2 - (1-f)\Delta\varepsilon^2 + \frac{1}{4}\Delta\varepsilon^2 + \varepsilon_a\varepsilon_m} - (1-f)\Delta\varepsilon + \frac{\Delta\varepsilon}{2}
\end{aligned} \tag{A.2}$$

For the following, we suppose $f \to 1$. Therefore, $(1-f) \to 0$ and $(1-f)^2\Delta\varepsilon^2 \ll (1-f)\Delta\varepsilon^2$, and we can approximate:

$$\begin{aligned}
\varepsilon_{\text{eff}} &\approx \sqrt{\frac{1}{4}\Delta\varepsilon^2 + \varepsilon_a\varepsilon_m - (1-f)\Delta\varepsilon^2} - (1-f)\Delta\varepsilon + \frac{\Delta\varepsilon}{2} \\
&= \sqrt{\frac{1}{4}(\varepsilon_a + \varepsilon_m)^2 - (1-f)\Delta\varepsilon^2} - (1-f)\Delta\varepsilon + \frac{\Delta\varepsilon}{2} \\
&= \frac{\varepsilon_a + \varepsilon_m}{2}\sqrt{1 - (1-f)\Delta\varepsilon^2\frac{4}{(\varepsilon_a + \varepsilon_m)^2}} - (1-f)\Delta\varepsilon + \frac{\Delta\varepsilon}{2}
\end{aligned} \tag{A.3}$$

Since $f \to 1$, we can further approximate $\sqrt{1-(1-f)\Delta\varepsilon^2\frac{4}{(\varepsilon_a+\varepsilon_m)^2}} \approx 1-(1-f)\Delta\varepsilon^2\frac{2}{(\varepsilon_a+\varepsilon_m)^2}$. Then,

$$\begin{aligned}
\varepsilon_{\text{eff}} &\approx \frac{\varepsilon_a+\varepsilon_m}{2}\left[1-\frac{2\Delta\varepsilon^2(1-f)}{(\varepsilon_a+\varepsilon_m)^2}\right]-(1-f)\Delta\varepsilon+\frac{\Delta\varepsilon}{2} \\
&= \frac{\varepsilon_a+\varepsilon_m}{2}+\frac{\varepsilon_a-\varepsilon_m}{2}-(1-f)(\varepsilon_a-\varepsilon_m)-(1-f)\frac{\Delta\varepsilon^2}{\varepsilon_a+\varepsilon_m} \\
&= \varepsilon_a+(1-f)(\varepsilon_m-\varepsilon_a)\left[1-\frac{\varepsilon_m-\varepsilon_a}{\varepsilon_m+\varepsilon_a}\right] \\
&= \varepsilon_a+2\varepsilon_a(1-f)\frac{\varepsilon_m-\varepsilon_a}{\varepsilon_m+\varepsilon_a} \\
&= \varepsilon\left[1+2(1-f)\frac{\varepsilon_m-\varepsilon_a}{\varepsilon_m+\varepsilon_a}\right]
\end{aligned} \tag{A.4}$$

We can then deduce the effective RI with $n_{\text{eff}} = \Re\{\sqrt{\varepsilon_{\text{eff}}}\}$. Since $f \to 1$, we have:

$$n_{\text{eff}} = \Re\{\sqrt{\varepsilon_{\text{eff}}}\} \approx n_a + (1-f)\frac{\varepsilon_m-\varepsilon_a}{\varepsilon_m+\varepsilon_a}n_a \tag{A.5}$$

and the effective power losses:

$$\alpha_{\text{eff}} = \frac{4\pi}{\lambda}\Im\{\sqrt{\varepsilon_{\text{eff}}}\} \approx \alpha_m\frac{4(1-f)\varepsilon_a^{3/2}n_m}{(\varepsilon_a+\varepsilon_m)^2} \tag{A.6}$$

A.2 Fitting of the Simulation Results with a Modified Three Component Bruggeman Model

According to the Bruggeman model with two terms, the transverse component of the effective permittivity of a porous material comprised of subwavelength inclusion (with permittivity $\varepsilon_a = n_a^2$) in a host material (with permittivity $\varepsilon_m = (n_m + ik_m)^2$) can be found by solving [428]:

$$f\frac{\varepsilon_a-\varepsilon_{\text{eff}}}{\varepsilon_a+\varepsilon_{\text{eff}}}+(1-f)\frac{\varepsilon_m-\varepsilon_{\text{eff}}}{\varepsilon_m+\varepsilon_{\text{eff}}} = 0 \tag{A.7}$$

where f is the fraction of inclusions and $\varepsilon_{\text{eff}} = (n_{\text{eff}} + ik_{\text{eff}})^2 = (n_{\text{eff}} + i\alpha_{\text{eff}}\lambda/4\pi)$ is the effective permittivity, with n_{eff} and α_{eff} the effective RI and effective power absorption losses respectively.

In Fig. 4.1(b)-(c) of the main paper, we observed that the numerical results obtained with finite-element method COMSOL Multiphysics commercial software approach the theoretical Bruggeman model at low THz frequencies. In this section, we show that by slightly modifying the Bruggeman model, we can accurately fit the numerical curves at higher frequencies. We

add a third term to the classical Bruggeman model:

$$f\frac{\varepsilon_a - \varepsilon_{\text{eff}}}{\varepsilon_a + \varepsilon_{\text{eff}}} + (1-f)\frac{\varepsilon_m - \varepsilon_{\text{eff}}}{\varepsilon_m + \varepsilon_{\text{eff}}} + \tilde{f}_x\frac{\tilde{\varepsilon}_x - \varepsilon_{\text{eff}}}{\tilde{\varepsilon}_m + \varepsilon_{\text{eff}}} = 0 \tag{A.8}$$

where $\tilde{\varepsilon}_x$ is the complex permittivity associated with the third component (first fitting parameter) and $\tilde{f}_x$ the strength of this contribution. Furthermore, we require that $\tilde{f}_x \to 0$ when $f \to 0$ and $f \to 1$, which leads to:

$$\tilde{f}_x = f(1-f)\tilde{\delta} \tag{A.9}$$

where $\tilde{\delta}$ is a second complex fitting parameter. We show in Fig. A.1 the results of the fitting to the numerical simulations of Fig. 4.1(b)-(c). While the classical Bruggeman with two terms (dotted line) cannot accurately fit the numerical results, the introduced parameters $\tilde{\varepsilon}_x$ and $\tilde{\delta}$ allows to correctly fit (red lines) the model of Eq. A.8 even at high frequencies.

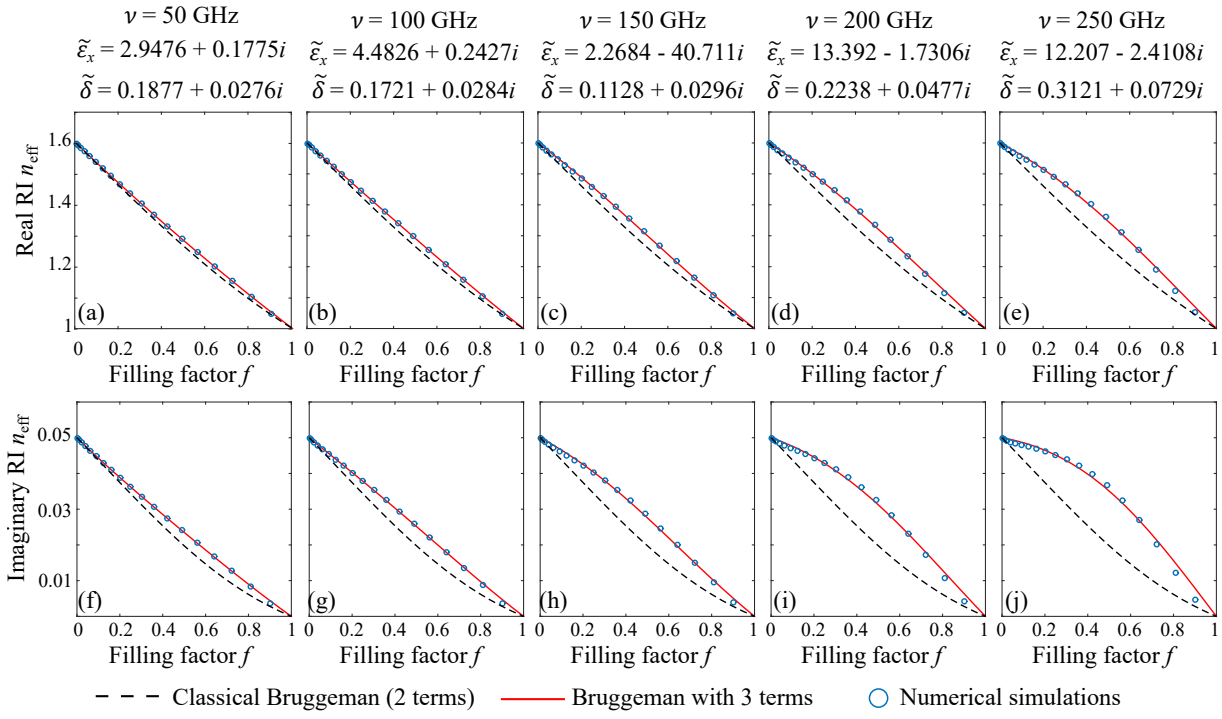

Figure A.1 Numerical reconstruction of a phase mask of 100 μm minimal line width. (a) Target image featuring pairs of "ones" and "zeros" lines of increasing widths. The smallest line is 100 μm, the increment in the line width is also 100 μm. The lines of "ones" are the scratches of depth h, while the lines of "zeros" correspond to unperturbed substrate. Reconstructed optical path variation across the substrate for a fixed bandwidth $\lambda_{\text{min}} = 150$ μm ($\nu_{\text{max}} = 2$ THz) and variable scratch depths (b) $h = 75$ μm, (c) $h = 100$ μm, (d) $h = 125$ μm, (e) $h = 150$ μm and (f) $h = 250$ μm

A.3 Analytical Derivations of the Power Transmissions Through the Porous and All-solid OAM Phase Plate

In this section, we use the Bruggeman model to derive analytical expressions of the transmission power through the porous and all-solid OAM phase plates. We then calculate the ratio of both transmissions to demonstrate that the porous OAM phase plate always outperforms its all-solid counterpart in terms of losses. A simple method of generating OAM states from a planar wave is to use spiral phase plate with a thickness that varies as a function of the angle:

$$h(\theta) - h(0) = \frac{\lambda}{n_m - n_a}\frac{m\theta}{2\pi} \tag{A.10}$$

where λ is the wavelength and $h(0)$ is the thickness at the polar origin [Fig. 4.5(a)]. The total power transmission through the spiral plate can be calculated with:

$$\begin{aligned} T_{\text{solid}}^{\text{OAM}} &= \frac{1}{\pi R^2}\int_0^R \mathrm{d}r \int_0^{2\pi} \mathrm{d}\theta \exp[-\alpha_m h(\theta)] \\ &= \frac{1-\exp(-\xi_s^O)}{\xi_s^O}\exp[-\alpha_m h(0)] \end{aligned} \tag{A.11}$$

where $\xi_s^O = m\lambda\frac{\alpha_m}{n_m - n_a}$. The transmission through the spiral plate is maximized for $h(0) = 0$ to give:

$$\max(T_{\text{solid}}^{\text{OAM}}) = \frac{1-\exp(-\xi_s^O)}{\xi_s^O} \tag{A.12}$$

We now design a porous OAM phase plate by fixing the thickness h, while varying the local RI as a function of the angle:

$$n(\theta) - n(0) = \frac{\lambda}{h}\frac{m\theta}{2\pi} \tag{A.13}$$

where $n(0)$ is the RI at the polar origin [Fig. 4.5(b)]. Since $n_a < n(\theta) < n_m$, the minimal thickness of an OAM plate that can realize a topological charge m is:

$$h_{\text{min}}^{\text{OAM}} = \frac{m\theta}{2\pi}\frac{\lambda}{n_m - n_a} \tag{A.14}$$

where we must require that $n(0) = n_a$ and $n(2\pi) = n_m$. Using the Bruggeman approximation for the real part of the RI [Eq. 4.8], we can write:

$$n(\theta) \approx n_a + [1 - f(\theta)]\frac{n_m^2 - n_a^2}{n_m^2 + n_a^2}n_a = n(0) + \frac{\lambda}{h}\frac{m\theta}{2\pi} \tag{A.15}$$

which allows us to find the air filling factor distribution:

$$f(\theta) = 1 - \frac{1}{n_a}\frac{n_m^2 + n_a^2}{n_m^2 - n_a^2}\left[n(0) - n_a + \frac{\lambda}{h}\frac{m\theta}{2\pi}\right] \tag{A.16}$$

Using the Bruggeman approximation for the losses [Eq. 4.9], we write the absorption profile of the porous OAM phase plate:

$$\begin{aligned}\alpha(\theta) &\approx \alpha_m[1 - f(\theta)]\frac{4n_a^3 n_m}{(n_m^2 + n_a^2)^2} \\ &= \alpha_m \frac{4n_a^2 n_m}{n_m^4 - n_a^4}\left[n(0) - n_a + \frac{\lambda}{h}\frac{m\theta}{2\pi}\right]\end{aligned} \tag{A.17}$$

As previously, we can now calculate the total power transmission coefficient through the porous lens with the integral:

$$\begin{aligned}T_{\text{porous}}^{OAM} &= \frac{1}{\pi R^2}\int_0^R \mathrm{d}r \int_0^{2\pi} \mathrm{d}\theta \exp[-\alpha(\theta)h] \\ &= \exp\left[-\alpha_m \frac{4n_a^2 n_m}{n_m^4 - n_a^4}(n(0) - n_a)h\right]\left[\frac{1 - \exp(-\xi_p^O)}{\xi_p^O}\right]\end{aligned} \tag{A.18}$$

where $\xi_p^O = \alpha_m \frac{4n_a^2 n_m}{n_m^4 - n_a^4} m\lambda$, and $T_{\text{porous}}^{\text{OAM}}$ is a monotonically decreasing function of ξ_p^O parameter. The transmission through the porous lens is maximized for $n(0) = n_a$:

$$\max(T_{\text{porous}}^{\text{OAM}}) = \frac{1 - \exp(-\xi_p^O)}{\xi_p^O} \tag{A.19}$$

By comparing Eq. 4.12 and Eq. 4.19, we conclude that the transmission through the porous phase plate is always higher than the transmission through the solid spiral plate, which follows directly from the fact that $\xi_p^O < \xi_s^O$ for any values of n_m and n_a, as long as $n_m > n_a$. As before, we can derive an analytical expression for the ratio between the transmission coefficients through the porous and solid OAM phase plates:

$$\frac{\max(T_{\text{porous}}^{\text{OAM}})}{\max(T_{\text{solid}}^{\text{OAM}})} = \frac{n_m^4 - n_a^4}{4n_a^2 n_m(n_m - n_a)}\frac{1 - \exp\left(-\Gamma\frac{4n_m n_a^3}{n_m^4 - 1}\right)}{1 - \exp\left(-\Gamma\frac{n_a}{n_m - n_a}\right)} \tag{A.20}$$

This expression is similar to the one calculated previously for the lens, where the only difference is that $\Gamma = \alpha_m m\lambda$. Therefore, the graph in Fig. 4.2(c) applies also for the OAM phase plate, where we can observe that the ratio is always greater than 1 and increases with Γ.

APPENDIX B SUPPLEMENTARY MATERIAL FOR: EXPLOITING K-SPACE/FREQUENCY DUALITY TOWARD REAL-TIME TERAHERTZ IMAGING

This document provides supplementary information to "Exploiting k-space/frequency duality toward real-time terahertz imaging," https://doi.org/10.1364/OPTICA.5.000109. In this document, we first present the experimental setup used to obtain the experimental results in the main paper. Second, we develop the mathematical theory behind the spectral resolution for the cases of the binary mask and the phase mask. Finally, we study the resolution of the image reconstruction method in the two above-mentioned cases.

B.1 Experimental Setup

The experimental setup is based on a THz-time domain spectroscopy system and depicted in Fig. B.1(a). A Ti:Sapphire laser (100 fs, 800 nm, 100 MHz) delivers 300 mW and 10 mW to the THz photoconductive emitter and detector antennae (PCA) respectively. On the emitter side, a linear delay line is placed prior to a highpower interdigitated antenna supplied with 15 V at 5 kHz. In our setup, we use a fiber coupled detector in order to allow convenient scanning of the Fourier plane. In particular, the optical beam is focused into a polarization maintaining optical fiber with the input end rigidly fixed in the fiber coupler on the optical table, while the output end is fixed in a fiber coupler mounted on a 3D micropositioning stage. At the output end of the fiber, the beam is collimated in air before exciting the detection antenna.

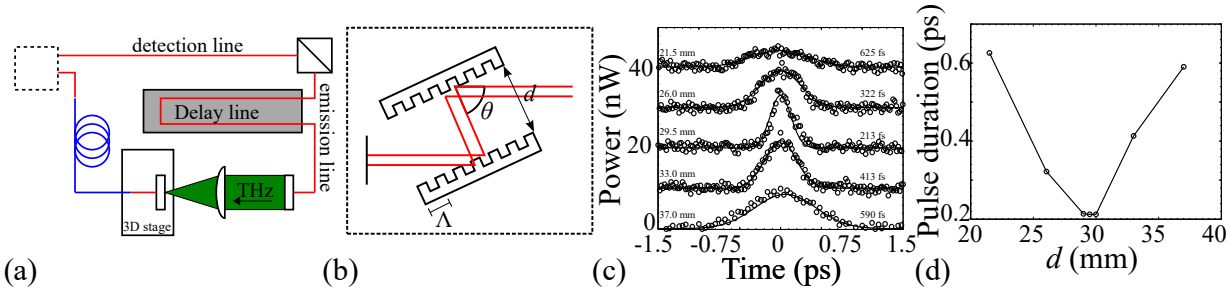

Figure B.1 Experimental setup. (a) Fiber-coupled THz-TDS. The red lines refer to the free-space beam, while the blue line is the optical fiber. (b) Dispersion compensation system with two diffraction gratings. (c) Autocorrelation traces for different distances between the gratings. The curves are fitted with a Gaussian function. (d) Pulse duration (full width at half maximum) as the function of the distance between the gratings.

The optical fiber adds positive group-velocity dispersion (GVD) to the pulse, leading in a non-negligible pulse broadening that reduces the THz bandwidth of the detector. Therefore, before focusing into the fiber, the optical pulse passes through a dispersion pre-compensation system made of two diffraction gratings and a mirror that adds negative GVD to the pulse. The output current of the antenna is amplified with a lock-in amplifier before being recorded by a data acquisition card connected to a computer. Thus, the acquired data is a current proportional to the electric field as a function of time. A temporal Fourier transform is then performed on the pulse to get the amplitude and phase as a function of the THz frequency. Finally, the hybrid inverse transform described in the paper is applied in order to retrieve the field distribution in the object plane.

The optical fiber adds positive group-velocity dispersion (GVD) to the pulse, leading to a non-negligible pulse broadening that reduces the THz bandwidth of the detector. Therefore, before focusing into the fiber, the optical pulse is passed through a dispersion precompensation system made of two diffraction gratings and a mirror [Fig. B.1(b)]. To counterbalance the fiber's positive GVD, this system adds negative GVD as detailed in [407]:

$$GVD[\mathrm{s}^2] = -\frac{\lambda^3 d}{\pi c^2 \Lambda^2}\left[1-\left(\frac{\lambda}{\Lambda}-\sin\theta\right)^2\right]^{3/2} \tag{B.1}$$

where λ is the central wavelength, c is the speed of light, Λ is the groove distance of the gratings, d is the distance between the gratings and θ is the incident angle defined in Fig. B.1(b). By adjusting the geometrical parameters d and θ, it is possible to counterbalance the positive GVD of the fiber, and therefore minimize the pulse duration at the output of the fiber. In Fig. B.1(c), we present several autocorrelation traces of the pulse for different values of d, recorded using an autocorrelator kit from Newport. As it can be seen in Fig. B.1(d), the pulse duration is minimized to 213 fs when using $d = 29.5$ mm between the gratings. We note that the compensation system only corrects for positive GVD. In the meantime, negative GVD due to the third order dispersion or non-linear effects still occur in the fiber and are not compensated by our system. Therefore, in our system, we still have a pulse broadening. Also, in principle, one could use a dispersion compensation fiber at 1550 nm since THz emitters and detectors are commercially available at that wavelength.

B.2 Mathematical Theory

B.2.1 A Closer Look at the Image Reconstruction Algorithm

The objective of this section is to determine what image is retrieved when using the hybrid inverse transform presented by Eq. 5.8. As the integral of Eq. 5.7 used in the reconstruction integrates information about the object over all frequencies, the reconstructed image $\tilde{S}(\vec{r})$ is different from the original image $S(\vec{r},\nu)$. In order to understand how $\tilde{S}(\vec{r})$ is related to the original image $S(\vec{r},\nu)$, we substitute the optical Fourier transform of the image $U(\vec{\rho},\nu)$ as measured in the Fourier plane of our setup [Eq. 5.5] into the hybrid inverse transform developed in this paper [Eq. 5.7] and get

$$\tilde{S}(\vec{r}) = \iint \mathrm{d}\theta\nu\mathrm{d}\nu \iint \mathrm{d}\phi' r'\mathrm{d}r' \left(\frac{\rho_0}{cF}\right)^2 \frac{S(\vec{r'},\nu)}{U_{\mathrm{ref}}(\nu)} \exp\left[-\frac{j2\pi\nu}{cF}\vec{\rho}_0(\vec{r'}-\vec{r})\right] \tag{B.2}$$

where r' and ϕ' are the integration variables that are defined in Fig. B.2. We can simplify the expressions above by defining $\vec{\varepsilon} = \vec{r'} - \vec{r}$ and ϕ_ε as shown in Fig. B.2. Then, Eq. B.2 can be written as:

$$\begin{aligned}\tilde{S}(\vec{r}) &= \iint \mathrm{d}\theta\nu\mathrm{d}\nu \iint \mathrm{d}\phi_\varepsilon\vec{\varepsilon}\mathrm{d}\vec{\varepsilon}\left(\frac{\rho_0}{cF}\right)^2 \frac{S(\vec{r}+\vec{\varepsilon},\nu)}{U_{\mathrm{ref}}(\nu)} \exp\left[-\frac{j2\pi\nu}{cF}\vec{\rho}_0\cdot\vec{\varepsilon}\right] \\ &= \iint \mathrm{d}\theta\nu\mathrm{d}\nu \iint \mathrm{d}\phi_\varepsilon\vec{\varepsilon}\mathrm{d}\vec{\varepsilon}\left(\frac{\rho_0}{cF}\right)^2 \frac{S(\vec{r}+\vec{\varepsilon},\nu)}{U_{\mathrm{ref}}(\nu)} \exp\left[-\frac{j2\pi\nu}{cF}\rho_0\varepsilon\cos(\theta-\phi_\varepsilon)\right]\end{aligned} \tag{B.3}$$

The integral above can be further simplified by integrating over θ, thus arriving to the

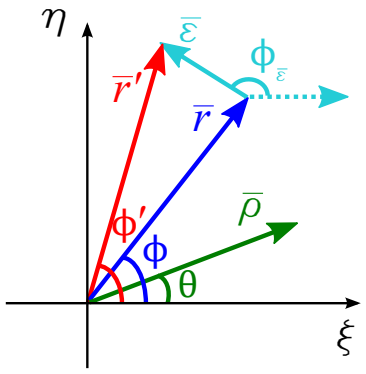

Figure B.2 Definition of various integration variables used throughout the paper.

following final expression for the hybrid inverse transform:

$$\tilde{S}(\vec{r}) = 2\pi \int_0^\infty \nu \mathrm{d}\nu \int_0^{2\pi} \mathrm{d}\phi_\varepsilon \int_0^\infty \varepsilon \mathrm{d}\varepsilon \left[\left(\frac{\rho_0}{cF} \right)^2 \frac{S(\vec{r}+\vec{\varepsilon},\nu)}{U_{\mathrm{ref}}(\nu)} \right] J_0 \left(\frac{2\pi\rho_0}{cF} \nu\varepsilon \right) \tag{B.4}$$

where we have used the integral representation of the Bessel function from Section B [Eq. B.19]. In order to continue further, we now need to specify the structure of the original object $S(\vec{r},\nu)$. In the following sections, we consider two particular types of objects - those based on amplitude and phase masks.

B.2.2 Amplitude Masks

First, we consider the case of space-frequency separable amplitude masks that result in the image of the general form $S(\vec{r},\nu) = S(\vec{r})E(\nu)$. We find that when using the reference function $U_{\mathrm{ref}}(\nu)$ as defined by Eq. 5.11, the hybrid inverse transform [Eq. B.4] gives the following:

$$\tilde{S}(\vec{r}) = \frac{2\pi}{\iint \mathrm{d}\vec{r} S(\vec{r})} \left(\frac{\rho_0}{cF} \right)^2 \int_0^{2\pi} \mathrm{d}\phi_\varepsilon \int_0^\infty \varepsilon \mathrm{d}\varepsilon S(\vec{r}+\vec{\varepsilon}) \int_0^\infty \nu \mathrm{d}\nu J_0 \left(\frac{2\pi\rho_0\varepsilon}{cF} \nu \right) \tag{B.5}$$

The last integral can be readily evaluated analytically using integral representations of the delta function [Eq. B.21] in terms of the Bessel functions:

$$\int_0^\infty \nu \mathrm{d}\nu J_0 \left(\frac{2\pi\rho_0}{cF} \nu \right) = \frac{cF}{2\pi\rho_0\varepsilon} \delta \left(\frac{2\pi\rho_0\varepsilon}{cF} \right) \tag{B.6}$$

where $\delta(2\pi\rho_0\varepsilon/cF)$ is the Dirac delta function. Then,

$$\tilde{S}(\vec{r}) = \frac{1}{\iint \mathrm{d}\vec{r} S(\vec{r})} \left(\frac{\rho_0}{cF} \right) \int_0^{2\pi} \mathrm{d}\phi_\varepsilon \int_0^\infty \varepsilon \mathrm{d}\varepsilon S(\vec{r}+\vec{\varepsilon}) \delta \left(\frac{2\pi\rho_0\varepsilon}{cF} \right) \tag{B.7}$$

These integrals can then be evaluated analytically by using the properties of the Dirac delta function (equation S22):

$$\tilde{S}(\vec{r}) = \frac{S(\vec{r})}{\iint \mathrm{d}\vec{r} S(\vec{r})} \tag{B.8}$$

where the denominator is simply a constant proportional to the area of the image. Therefore, we conclude that in the case of a space-frequency separable amplitude mask, the hybrid inverse transform of the Fourier image results in the original image normalized by the area of the image. If the maximum frequency used in the reconstruction is finite, we can also use Eq. B.5 in order to estimate the resultant image resolution as demonstrated in the Section B below.

B.2.3 Phase Masks

We now consider the case of phase masks that result in the image of the general form $S(\vec{r},\nu) = S(\vec{r})E(\nu)\exp[j2\pi\nu(\Delta_0 - \mu(\vec{r}))/c]$. As for the choice of the reference function $U_{\text{ref}}(\nu)$ in the inversion algorithm [Eq. B.4], one would be tempted to use the same normalization as in the case of amplitude masks. However, as we will see in what follows, in order to ensure convergence of all the integrals, we need to modify the reference function. Particularly, in the case of phase masks we define the reference $U_{\text{ref}}(\nu)$ as the Fourier transform of a pulse at the origin of the k-space ($\rho_0 = 0$), measured using a flat reference sample $\mu(\vec{r} = 0)$:

$$U_{\text{ref}}(\nu) = \nu^m \frac{jcF}{\nu} U(0,\nu) = \nu^m E(\nu) \exp\left(\frac{j2\pi\nu\Delta_0}{c}\right) \iint \mathrm{d}\vec{r} S(\vec{r}) \tag{B.9}$$

where ν^m is an additional frequency multiplier with an exponent m that must be chosen to ensure the convergence of the inversion algorithm. Using Eq. B.4 for the hybrid inverse transform together with the reference function defined in Eq. B.9, we find:

$$\tilde{S}(\vec{r}) = \frac{2\pi}{\iint \mathrm{d}\vec{r} S(\vec{r})} \left(\frac{\rho_0}{cF}\right)^2 \int_0^{2\pi} \mathrm{d}\phi_\varepsilon \int_0^\infty \varepsilon \mathrm{d}\varepsilon S(\vec{r}+\vec{\varepsilon}) K_m(\vec{r},\vec{\varepsilon}) \tag{B.10}$$

where we define:

$$K_m = \int_0^\infty \nu^{1-m} \mathrm{d}\nu \exp\left[-\frac{j2\pi\nu}{c}\mu(\vec{r}+\vec{\varepsilon})\right] J_0\left(\frac{2\pi\rho_0\varepsilon}{cF}\nu\right) \tag{B.11}$$

In the case of amplitude masks considered earlier, we used $m = 0$, however, in the case of phase masks this choice generally results in the divergence of the integral of Eq. B.10. Indeed, using basic properties of the Bessel function [Eq. B.26] we find that:

$$K_0(\vec{r},\vec{\varepsilon}) = \left(\frac{c}{2\pi}\right)^2 \left(\frac{F}{\rho_0}\right)^2 \mu_0(\vec{r}) \cdot \begin{cases} \frac{-1}{\left[\mu_0(\vec{r}+\vec{\varepsilon})^2 - \varepsilon^2\right]^{3/2}} & \text{if } 0 < \varepsilon < \mu_0(\vec{r}+\vec{\varepsilon}) \\ \frac{j}{\left[\varepsilon^2 - \mu_0(\vec{r}+\vec{\varepsilon})^2\right]^{3/2}} & \text{if } \varepsilon > \mu_0(\vec{r}+\vec{\varepsilon}) \end{cases} \tag{B.12}$$

where the normalized optical path is defined as $\mu_0(\vec{r}+\vec{\varepsilon}) = F/\rho_0 \mu(\vec{r}+\vec{\varepsilon})$. Therefore, the integration over ε in Eq. B.10 can be divided into the sum of two integrals over different regions of ε values. From the form of Eq. B.12 it follows that generally both of these integrals are divergent, thus rendering $\tilde{S}(\vec{r})$ ill defined. Therefore, $m = 0$ is not an acceptable choice for the reference function.

On the other hand, if we select $m = 1$, then using Eq. B.27

$$K_1(\vec{r},\vec{\varepsilon}) = \frac{cF}{2\pi\rho_0} \cdot \begin{cases} \frac{-j}{\sqrt{\mu_0(\vec{r}+\vec{\varepsilon})^2-\varepsilon^2}} & \text{if } 0 < \varepsilon < \mu_0(\vec{r}+\vec{\varepsilon}) \\ \frac{1}{\sqrt{\varepsilon^2-\mu_0(\vec{r}+\vec{\varepsilon})^2}} & \text{if } \varepsilon > \mu_0(\vec{r}+\vec{\varepsilon}) \end{cases} \tag{B.13}$$

where again $\mu_0(\vec{r}+\vec{\varepsilon}) = F/\rho_0\mu(\vec{r}+\vec{\varepsilon})$. Now, we can write Eq. B.10 as the sum of the two integrals:

$$\tilde{S}(\vec{r}) = \frac{2\pi}{\iint \mathrm{d}S(\vec{r})}\left(\frac{\rho_0}{cF}\right)^2 \int_0^{2\pi} \mathrm{d}\phi_\varepsilon \left[S_{\varepsilon<\mu_0(\vec{r}+\vec{\varepsilon})} + S_{\varepsilon>\mu_0(\vec{r}+\vec{\varepsilon})}\right] \tag{B.14}$$

where

$$S_{\varepsilon<\mu_0(\vec{r}+\vec{\varepsilon})} = -\frac{jcF}{2\pi\rho_0}\int_0^{\mu_0(\vec{r}+\vec{\varepsilon})} \mathrm{d}\varepsilon \frac{\varepsilon \cdot S(\vec{r}+\vec{\varepsilon})}{\sqrt{\mu_0(\vec{r}+\vec{\varepsilon})^2-\varepsilon^2}} \tag{B.15}$$

and

$$S_{\varepsilon>\mu_0(\vec{r}+\vec{\varepsilon})} = -\frac{cF}{2\pi\rho_0}\int_{\mu_0(\vec{r}+\vec{\varepsilon})}^{\infty} \mathrm{d}\varepsilon \frac{\varepsilon \cdot S(\vec{r}+\vec{\varepsilon})}{\sqrt{\varepsilon^2-\mu_0(\vec{r}+\vec{\varepsilon})^2}} \tag{B.16}$$

We note that the contribution $S_{\varepsilon>\mu_0(\vec{r}+\vec{\varepsilon})}$ is purely real, and it is generally divergent if the function $S(\vec{r}+\vec{\varepsilon})$ (amplitude mask) is not zero at infinity. In the meantime, the contribution $S_{\varepsilon<\mu_0(\vec{r}+\vec{\varepsilon})}$ is purely imaginary and is always finite. Moreover, if the spatial region of the optical path variation $\mu(\vec{r})$ is large enough so its value can be considered constant $\mu_0(\vec{r}+\vec{\varepsilon}) = \mu_0(\vec{r})$ inside a circle of radius $\varepsilon \sim \mu_0(\vec{r})$, and if a similar condition is respected by the amplitude mask $S(\vec{r})$, then we can evaluate Eq. B.15 exactly

$$\begin{aligned} S_{\varepsilon<\mu_0(\vec{r}+\vec{\varepsilon})} &= -\frac{jcF}{2\pi\rho_0}\int_0^{\mu_0(\vec{r}+\vec{\varepsilon})} \mathrm{d}\varepsilon \frac{\varepsilon \cdot S(\vec{r}+\vec{\varepsilon})}{\sqrt{\mu_0(\vec{r}+\vec{\varepsilon})^2-\varepsilon^2}} \\ &= -\frac{jcF}{2\pi\rho_0}S(\vec{r})\int_0^{\mu_0(\vec{r}+\vec{\varepsilon})} \mathrm{d}\varepsilon \frac{\varepsilon \cdot S(\vec{r}+\vec{\varepsilon})}{\sqrt{\mu_0(\vec{r}+\vec{\varepsilon})^2-\varepsilon^2}} \\ &= -\frac{jcF}{2\pi\rho_0}S(\vec{r})\mu_0(\vec{r}) \end{aligned} \tag{B.17}$$

Therefore, from Eq. B.14, we find that the imaginary part of the hybrid inverse transform $\tilde{S}(\vec{r})$ computed with $m = 1$ is proportional to the spatial variation of the optical path in the image plane:

$$\Im\{\tilde{S}(\vec{r})\} = -\frac{2\pi}{c}\frac{S(\vec{r})}{\iint \mathrm{d}\vec{r}S(\vec{r})}\mu(\vec{r}) \tag{B.18}$$

If the maximum frequency used in the reconstruction is finite, we can also use Eq. B.10 to estimate the resultant image resolution as demonstrated below.

B.2.4 Mathematical Identities

In this section, we list various mathematical identities used throughout the paper.

- Integral representation of the Bessel function of a real argument and some of its basic properties

$$J_0(x) = \frac{1}{2\pi}\int_0^{2\pi} \mathrm{d}\theta \exp(\pm jx\cos\theta) \tag{B.19}$$

$$J_1(ax) = -\frac{1}{a}J_0'(ax) \tag{B.20}$$

- Dirac delta functions, properties and integral representations

$$\delta(x) = \int_{-\infty}^{\infty} \mathrm{d}\theta \exp(j2\pi x\xi) \tag{B.21}$$

$$\delta(ax) = \frac{1}{|a|}\delta(x) \tag{B.22}$$

$$\int_0^{\infty} xJ_0(ax)\mathrm{d}x = \frac{1}{a}\delta(a) \tag{B.23}$$

$$\int_{-\infty}^{\infty} f(x)\delta(x)\mathrm{d}x = f(0) \tag{B.24}$$

- Some integrals involving the Bessel functions

$$\int_0^{\infty} uJ_0(au)\mathrm{d}x = \frac{x}{a}J_1(ax) \tag{B.25}$$

$$\int_0^{\infty} x\exp(-jax)J_0(bx)\mathrm{d}x = \begin{cases} \frac{ja}{(b^2-a^2)^{3/2}} & \text{if } |b| > |a| \\ \frac{-a}{(a^2-b^2)^{3/2}} & \text{if } |a| > |b| \end{cases} \tag{B.26}$$

$$\int_0^{\infty} \exp(-jax)J_0(bx)\mathrm{d}x = \begin{cases} \frac{1}{\sqrt{b^2-a^2}} & \text{if } |b| > |a| \\ \frac{-j\mathrm{sgn}(a)}{\sqrt{a^2-b^2}} & \text{if } |a| > |b| \end{cases} \tag{B.27}$$

B.3 Resolution of the Reconstructed Images

B.3.1 Resolution of the Amplitude Masks

The image resolution in the case of amplitude masks can be readily deduced from the hybrid inverse transform Eq. B.5:

$$\tilde{S}(\vec{r}) = \frac{2\pi}{\iint \mathrm{d}\vec{r}S(\vec{r})}\left(\frac{\rho_0}{cF}\right)^2 \int_0^{2\pi}\mathrm{d}\phi_\varepsilon \int_0^{\infty} \varepsilon\mathrm{d}\varepsilon S(\vec{r}+\vec{\varepsilon}) \int_0^{\infty} \nu\mathrm{d}\nu J_0\left(\frac{2\pi\rho_0\varepsilon}{cF}\nu\right) \tag{B.28}$$

We note that, as the probing pulse has a finite duration (bandwidth limited pulse), the maximal frequency in the integral above is limited to $\nu_{\max}$. This also sets the minimal resolution achievable by the hybrid inverse transform, which, as we show below, is proportional to the smallest probed wavelength ($\lambda_{\min} = c/\nu_{\max}$). To demonstrate this point mathematically, we consider the last integral in Eq. B.28. However, instead of integrating to infinity, we now integrate up to $\nu_{\max}$. In this case, using the Bessel identity [Eq. B.25], the last integral of Eq. B.28 becomes:

$$\int_0^{\nu_{\max}} \nu \mathrm{d}\nu J_0\left(\frac{2\pi\rho_0\varepsilon}{cF}\nu\right) = \frac{cF\nu_{\max}}{2\pi\rho_0\varepsilon} J_1\left(\frac{2\pi\rho_0\varepsilon}{cF}\nu_{\max}\right) \tag{B.29}$$

Then, by using the Eq. B.24, Eq. B.28 transforms into:

$$\begin{aligned}
\tilde{S}(\vec{r}) &= \frac{\nu_{\max}}{\iint \mathrm{d}\vec{r} S(\vec{r})} \frac{\rho_0}{cF} \int_0^{2\pi} \mathrm{d}\phi_{\vec{\varepsilon}} \int_0^{\infty} \mathrm{d}\varepsilon S(\vec{r}+\vec{\varepsilon}) J_1\left(\frac{2\pi\rho_0\varepsilon}{cF}\nu_{\max}\right) \\
&= -\frac{1}{2\pi \iint \mathrm{d}\vec{r} S(\vec{r})} \int_0^{2\pi} \mathrm{d}\phi_{\vec{\varepsilon}} \int_0^{\infty} \mathrm{d}\varepsilon S(\vec{r}+\vec{\varepsilon}) J_0'\left(\frac{2\pi\rho_0\varepsilon}{cF}\nu_{\max}\right) \\
&= -\frac{1}{2\pi \iint \mathrm{d}\vec{r} S(\vec{r})} \int_0^{2\pi} \mathrm{d}\phi_{\vec{\varepsilon}} \left[S(\vec{r}) + \int_0^{\infty} \mathrm{d}\varepsilon \frac{\partial S(\vec{r}+\vec{\varepsilon})}{\partial\varepsilon} J_0\left(\frac{2\pi\rho_0\varepsilon}{cF}\nu_{\max}\right)\right] \\
&= \frac{S(\vec{r})}{\iint \mathrm{d}\vec{r} S(\vec{r})} + \frac{1}{2\pi \iint \mathrm{d}\vec{r} S(\vec{r})} \int_0^{2\pi} \mathrm{d}\phi_{\varepsilon} \int_0^{\infty} \mathrm{d}\varepsilon \frac{\partial S(\vec{r}+\vec{\varepsilon})}{\partial\varepsilon} J_0\left(\frac{2\pi\rho_0\varepsilon}{cF}\nu_{\max}\right)
\end{aligned} \tag{B.30}$$

From Eq. B.30, we note that the leading expression for the hybrid inverse transform in the case of a bandwidth limited pulse is still proportional to the value of the original object, with a correction term featuring an integration on the amplitude mask spatial derivative over a fast-vaying sign-changing Bessel function of a large argument. The main contribution to this integral comes from averaging the amplitude maks derivative inside a circle of radius $\varepsilon \sim \lambda_{\min} F/\rho_0$. From this, we conclude that the fundamental limit of the spatial resolution in the case of the amplitude mask is set by the finite bandwidth of the probing pulse and is $\sim \lambda_{\min} F/\rho_0$, where $\lambda_{\min}$ is the smallest wavelength probed by the pulse. This result correlates well with the Nyquist theorem for the Fourier transform discussed in the paper.

To confirm this result, we perform numerical simulations using, as an object, a binary mask featuring a pattern of lines of increasing size of ones (full transmittance) and zeros (full absorbance) [Fig. B.3(a)]. In Fig. S3a, the smallest line of "ones" has a width of 400 μm followed by an adjacent line of "zeros" of the same size. The pairs of lines are then repeated with increasing size in increments of 400 μm (i.e. 400 μm, 800 μm, 1200 μm etc.). We then compute the direct transform given by Eq. 5.1 for all the frequencies specified by the THz pulse bandwidth (0.1 - 2 THz with a step of 1 GHz). Then, using the hybrid inverse transform [Eq. 5.12] we reconstruct the original image. In Fig. B.3(b)-(f), we present several

reconstructed images for different values of the maximal THz frequency used in the hybrid inverse transform. In Fig. B.4, we perform the same numerical simulations for a geometrically similar image that feature thinner lines (a minimal width of 100 μm and a step of 200 μm in the width increment between the pairs of the adjacent lines). Just by looking at the images, as expected, we find qualitatively that the resolution improves when the THz bandwidth increases.

From these numerical results, we can estimate the dependence of the spatial resolution of the images obtained using the hybrid inverse transform Eq. 5.12 as a function of the maximal THz frequency used in the reconstruction. To do so, for each line of "zeros" and "ones", we calculate the average reconstructed intensities I_1 and I_0 at the positions where the corresponding lines should be. We then plot these averaged values for each line. If the line of "ones" is resolved, one should thus find an averaged value close to one at the line location. Similarly, if the line of "zeros" is resolved, one should find an averaged value close to zero at the corresponding line location. The adjacent "zero" and "one" lines are considered not resolved if the corresponding averaged values for these lines become comparable, that is $(I_1 - I_0)/(I_1 + I_0) < 0.5$. To illustrate this, in Fig. B.5(a), we present the averaged intensities at the locations of "zeros" and "ones" in the case of $\lambda_{\min} = 600$ μm ($\nu_{\max} = 0.6$ THz). The lines from 400 μm to 1600 μm are not resolvable since "zeros" and "ones" have comparable averaged values. However, starting with a 2000 μm thick line, the lines can be readily resolved according to the condition presented above. From this, we conclude that in the case of $\lambda_{\min} = 600$ μm, the minimal achievable resolution is ~ 2000 μm.

We then perform the same analysis for other values of $\lambda_{\min}$ (various THz pulse bandwidths) and present the results in Fig. B.5(b). The dotted line corresponds to the resolution set by the Nyquist theorem : $\delta x = 0.5\lambda_{\min}F/\rho_0$, while in circles, we present the resolutions found using the approach described above. From this, we confirm that the resolution of the binary amplitude mask indeed follows closely the prediction of the Nyquist theorem. This is further confirmed experimentally in Fig. B.5(c). There, we use three different binary masks in the form of metal plates with cutouts in the shape of lines. Each amplitude mask features three cutouts in the form of lines of 15 mm in length and widths of 2800 μm, 2000 μm and 1200 μm that are separated by the same width from each other.

Then, using our Fourier optics setup and the hybrid inverse algorithm we reconstruct the images of the three lines using different values of the maximal frequency $\nu_{\max}$ in the integral of Eq. 5.12 (different THz bandwidths). The inserts i, ii, iii in the top row of Fig. B.5(c) show images of the three different amplitude masks that were reconstructed using $\lambda_{\min}$ (850 μm, 600 μm, 300 μm respectively). According to the Nyquist theorem, these wavelengths are

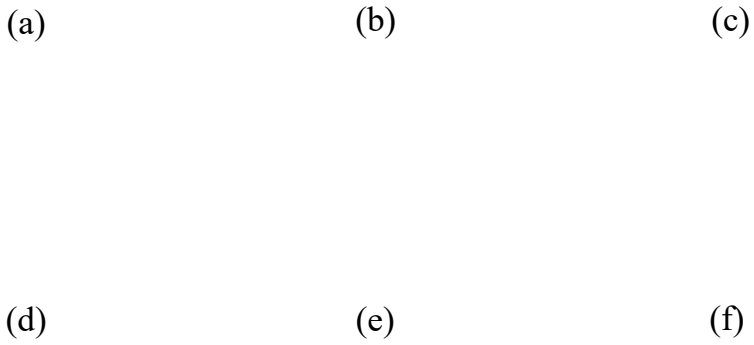

Figure B.3 Numerical reconstruction of a binary mask of 400 μm minimal line width. (a) Target image featuring pairs of "ones" and "zeros" lines of increasing widths. The smallest line is 400 μm, the increment in the line width is also 400 μm. (b) Image reconstruction using hybrid inverse transform [Eq. 5.12] with $\lambda_{\min} = 150$ μm ($\nu_{\max} = 2$ THz), (c) $\lambda_{\min} = 350$ μm ($\nu_{\max} = 0.86$ THz), (d) $\lambda_{\min} = 600$ μm ($\nu_{\max} = 0.5$ THz), (e) $\lambda_{\min} = 800$ μm ($\nu_{\max} = 0.375$ THz) and (f) $\lambda_{\min} = 1000$ μm ($\nu_{\max} = 0.3$ THz)

small enough to correctly resolve the lines in the corresponding amplitude masks, which is indeed what is observed experimentally. At the same time, in the bottom row of Fig. B.5(c) (inserts iv, v, vi), we show images of the same three amplitude masks that were reconstructed using $\lambda_{\min}$ of 1100 μm, 750 μm, and 500 μm respectively. According to the Nyquist theorem, these values of $\lambda_{\min}$ are insufficient to resolve the lines in the corresponding amplitude masks, which is indeed what is confirmed experimentally. From this we conclude that, indeed, our analysis of the image resolution in the case of amplitude masks agrees well with the classical Nyquist theorem applied to the classical Fourier optics systems.

B.3.2 Resolution of the Phase Masks

In the case of phase masks, we have demonstrated earlier that the imaginary part of the hybrid inverse transform is, in some limit, simply proportional to the optical path incurred by the light due to the passage through the phase mask:

$$\Im\{\tilde{S}(\vec{r})\} = -\frac{2\pi}{c}\frac{S(\vec{r})}{\iint \mathrm{d}\vec{r} S(\vec{r})}\mu(\vec{r}) \tag{B.31}$$

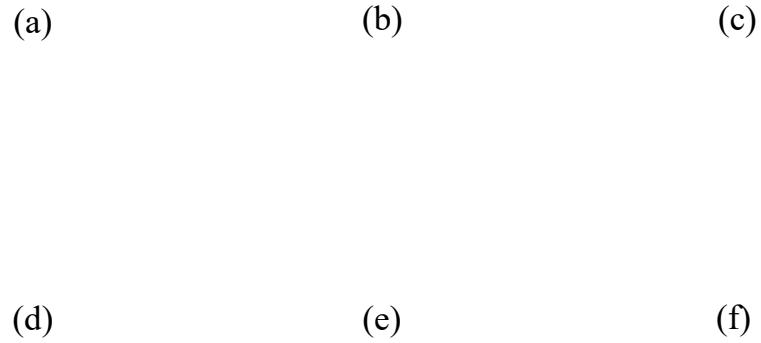

Figure B.4 Numerical reconstruction of a binary mask of 100 μm minimal line width. (a) Target image featuring pairs of "ones" and "zeros" lines of increasing widths. The smallest line is 100 μm, the increment in the line width is also 100 μm. (b) Image reconstruction using hybrid inverse transform [Eq. 5.12] with $\lambda_{\min} = 150$ μm ($\nu_{\max} = 2$ THz), (c) $\lambda_{\min} = 200$ μm ($\nu_{\max} = 1.5$ THz), (d) $\lambda_{\min} = 250$ μm ($\nu_{\max} = 1.2$ THz), (e) $\lambda_{\min} = 300$ μm ($\nu_{\max} = 1$ THz) and (f) $\lambda_{\min} = 350$ μm ($\nu_{\max} = 0.86$ THz)

This result is strictly valid in the case of piecewise constant phase masks if the value of the normalized optical path $\mu_0(\vec{r})$ and the value of the amplitude mask $S(\vec{r})$ are constant within the circle of radius $\varepsilon = \mu_0(\vec{r}+\vec{\varepsilon})$.This result, however, breaks in the vicinity of the boundaries between different optical path regions of the phase mask. We therefore conclude that in the case of the hybrid inverse transform applied to the phase masks, there is a fundamental limit to the resolution of such a transform which is set by the local value of the normalized optical path length $\mu_0(\vec{r}) = \mu(\vec{r})F/\rho_0 = h(\vec{r})(n_m - n_a)$. Therefore, in the case of phase masks, a correction term needs to be added to the resolution given by the Nyquist theorem:

$$\delta x = [0.5\lambda_{\min} + h(n_m - n_a) \cdot \frac{F}{\rho_0}] \tag{B.32}$$

To confirm this prediction, we perform numerical simulations using as target images phase masks featuring geometrical patterns of lines identical to those of amplitude masks presented in Fig. B.3 and Fig. B.4. In the case of phase masks, however, we consider as lines shallow scratches of depth h engraved onto a plastic plate of refractive index $n_m = 1.62$ [Fig. B.6(a)]. For the reconstruction of the engraving pattern we use the hybrid inverse transform [Eq. 5.17]

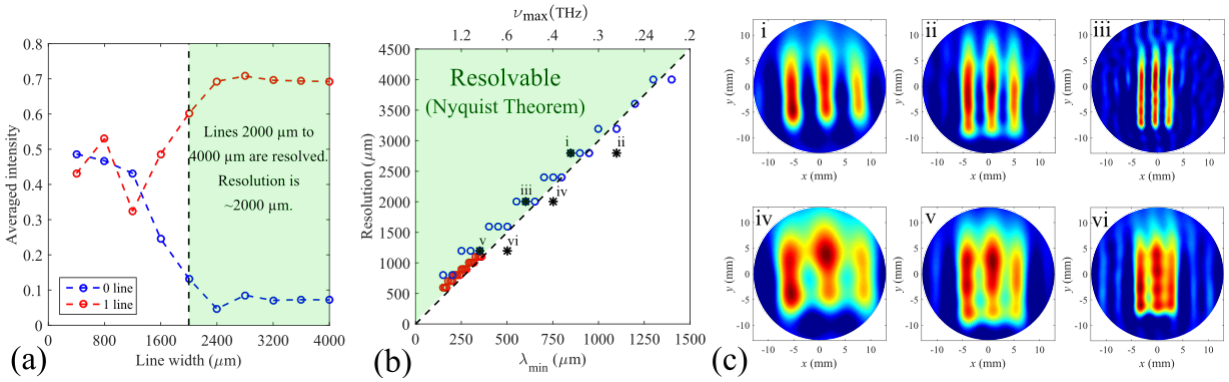

Figure B.5 Image resolution, case of the amplitude masks. (a) Definition of the resolution using averaged values at the location of "ones" and "zeros". (b) Resoltuion of amplitude masks as a function of the THz bandwidth. The green region corresponds to the resolvable region set by the Nyquist theorem. The blue and red circles correspond to Fig. B.3 and Fig. B.4 respectively. (c) Experimental measurements using three different amplitude masks as a function $\lambda_{\min}(\nu_{\max})$. i. Lines of 2800 μm with $\lambda_{\min} = 850$ μm ($\nu_{\max} = 0.35$ THz) and iv. $\lambda_{\min} = 1100$ μm ($\nu_{\max} = 0.27$ THz); ii. Lines of 2000 μm with $\lambda_{\min} = 600$ μm ($\nu_{\max} = 0.5$ THz) and v. $\lambda_{\min} = 750$ μm ($\nu_{\max} = 0.4$ THz); iii. Lines of 1200 μm with $\lambda_{\min} = 300$ μm ($\nu_{\max} = 1$ THz) and vi. $\lambda_{\min} = 500$ μm ($\nu_{\max} = 0.6$ THz).

corresponding to the case of the phase masks. In Fig. B.6(b)-(f), we present the reconstructed optical paths for different values of the line depth h and the same THz bandwidth ($\lambda_{\min}$ fixed to 150 μm). As expected from Eq. B.32, the resolution improves as the scratch depth decreases.

With a definition of the resolution similar to the binary amplitude mask ("ones" are the lines corresponding to engravings, "zeros" are the lines where there is no engraving), we numerically find the resolution for different THz bandwidths and optical thicknesses. In Fig. B.7(a), we plot the resolution as a function of the THz bandwidth for different values of the engraving depth. The dotted line in the figure has the equation $\delta x = 0.5\lambda_{\min}F/\rho_0$ and corresponds to the fundamental limit set by the Nyquist theorem. From the figure, we confirm that the minimal resolution is indeed set by the Nyquist theorem. At the same time, the resolution can be considerably worse than that predicted by the Nyquist theorem due to the contribution proportional to the optical path length of the engraving, which can be significant for deep engravings. Thus, in Fig. B.7(b), we plot this limit as a function of the engraving depths. There, the dotted line follows the equation $\delta x = h(n_m - n_a)F/\rho_0$ and it defines the fundamental limit to the resolution in case of the phase masks in the limit of an infinite pulse bandwidth.

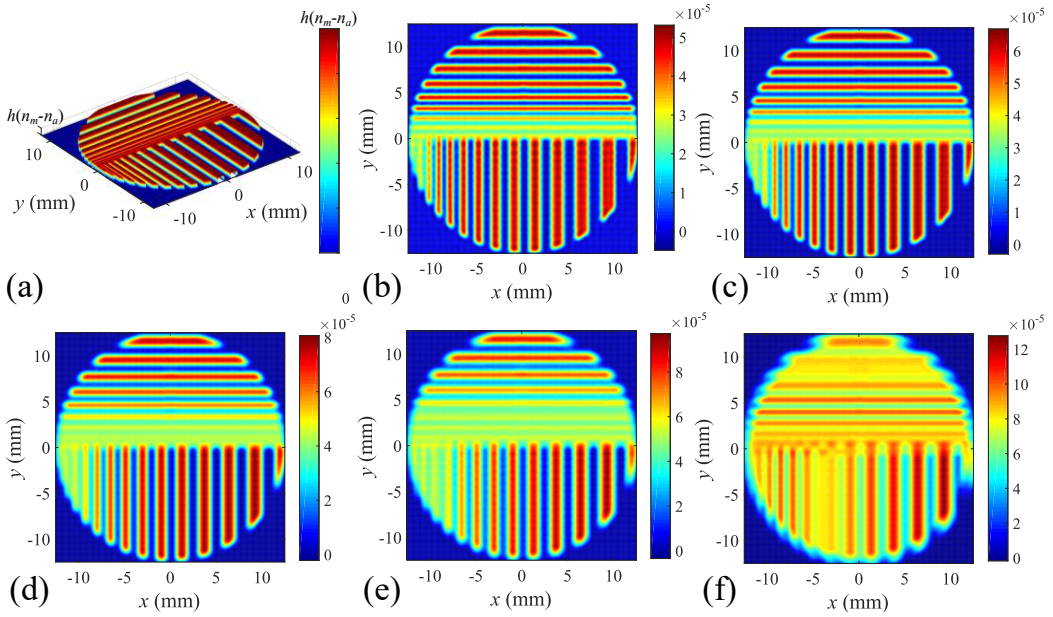

Figure B.6 Numerical reconstruction of a phase mask of 100 μm minimal line width. (a) Target image featuring pairs of "ones" and "zeros" lines of increasing widths. The smallest line is 100 μm, the increment in the line width is also 100 μm. The lines of "ones" are the scratches of depth h, while the lines of "zeros" correspond to unperturbed substrate. Reconstructed optical path variation across the substrate for a fixed bandwidth $\lambda_{\min} = 150$ μm ($\nu_{\max} = 2$ THz) and variable scratch depths (b) $h = 75$ μm, (c) $h = 100$ μm, (d) $h = 125$ μm, (e) $h = 150$ μm and (f) $h = 250$ μm

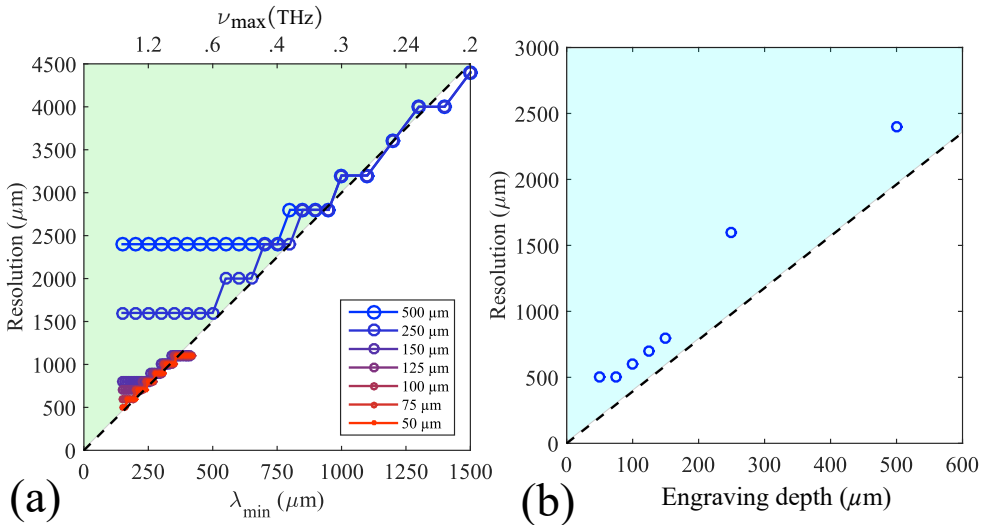

Figure B.7 Image resolution, case of the phase masks. (a) Resolution as a function of the THz bandwidth for different values of the engraving depth h (shown in the legend). The green region corresponds to the resolvable region set by the Nyquist theorem $\delta x > 0.5\lambda_{\text{min}}F/\rho_0$, (b) Resolution as a function of the engraving depth h for a fixed THz bandwidth ($\lambda_{\text{min}} = 150$ μm, $\nu_{\text{max}} = 2$ THz). The blue region corresponds to the resolvable region as defined by the equation $\delta x > h(n_m - n_a)F/\rho_0$.

APPENDIX C SUPPLEMENTARY MATERIAL FOR: TERAHERTZ SUBWAVELENGTH IMAGING USING SUPER-RESOLUTION DETERMINISTIC FLUCTUATIONS

C.1 Super-resolution Reconstruction of Order 4

For a reconstruction of order $n = 4$, the orthogonality condition is defined as:

$$\langle m_i m_j m_k m_l \rangle = \frac{1}{N_t} \mathrm{tr}\left[\mathrm{diag}(m_i)\mathrm{diag}(m_j)\mathrm{diag}(m_k)\mathrm{diag}(m_l)\right] = \begin{cases} \alpha_1 & \text{if } i = j = k = l \\ 0 & \text{else} \end{cases} \tag{C.1}$$

For the simulation result shown in Fig. 4i, we want to construct a basis with $N_p = 16$ pixels. First, we note that the following basis with two pixels respect the orthogonality condition:

$$A_1 = \begin{bmatrix} -1 & -1 \\ 1 & -i \\ 1 & -1 \\ i & -1 \end{bmatrix} \tag{C.2}$$

The following basis respects also the orthogonality condition:

$$A_2 = \begin{bmatrix} -i & -1 \\ -i & -1 \\ -1 & -i \\ -1 & 1 \end{bmatrix} \tag{C.3}$$

One can then verify that the Kronecker product of these two matrices leads to a new matrix that respects the orthogonality condition as well:

$$A_3 = A_1 \otimes A_2 = \begin{bmatrix} i & i & i & i \\ i & 1 & i & 1 \\ 1 & i & 1 & i \\ 1 & -1 & 1 & -1 \\ -i & -1 & -1 & i \\ -1 & -i & i & -1 \\ -1 & -i & i & -1 \\ -1 & 1 & i & -i \\ -i & -i & i & i \\ -i & -1 & i & 1 \\ -1 & -i & 1 & i \\ -1 & 1 & 1 & -1 \\ -1 & 1 & 1 & -1 \\ 1 & -i & i & 1 \\ -i & 1 & 1 & i \\ -i & i & 1 & -1 \end{bmatrix} \tag{C.4}$$

This new matrix is different from the ones above, with dimensions of $N_t = 16$ frames and $N_p = 4$ pixels. By continuing like this, we create a fourth matrix by computing the Kronecker product:

$$A_4 = A_3 \otimes A_1 \tag{C.5}$$

that we do not show here for conciseness reasons, A_4 having now dimensions of $N_t = 64$ frames and $N_p = 8$ pixels. Again, this new matrix respects the orthogonality condition. Finally, we construct a matrix with 16 pixels using the following Kronecker product:

$$A_5 = A_4 \otimes A_2 \tag{C.6}$$

This new matrix has dimensions of $N_t = 256$ frames and $N_p = 16$ pixels. we verified numerically that the new constructed matrix respects the orthogonality condition by computing the 3876 possible non-commutative combinations [following Eq.6.17]. As expected, all of them

are equal to 0, except those when the 4 indices are the same.

Following several numerical experimentations, it seems that the Kronecker product of two matrices that respect the orthogonality condition yields a third matrix that respect the orthogonality as well. This mathematical hypothesis has yet to be rigorously demonstrated.

APPENDIX D FRESNEL DIFFRACTION INTEGRAL

In this appendix, we give the expression of the Fresnel diffraction integral used in the calculations of the Fourier transform of a cylindrical lens in Chapter 7, Section 7.2. As a reminder the Huygens-Fresnel principle states that every point of a wavefront can be seen as the source of a spherical wavefront. Let (x_0, y_0) and (x_1, y_1) be two planes separated by a distance z. For simplicity, we assume here that the two planes are parallel. Mathematically, an aperture $U_0(x_0, y_0)$ positioned in the (x_0, y_0) plane diffracts to $U_1(x_1, y_1)$ following

$$U_1(x_1, y_1) = \frac{z}{i\lambda} \iint U_0(x_0, y_0) \frac{\exp(ik|\vec{r}_{01}|)}{|\vec{r}_{01}|^2} \mathrm{d}x_0 \mathrm{d}y_0 \tag{D.1}$$

where $k = 2\pi/\lambda$ with λ the wavelength, and $\vec{r}_{01}$ is a vector going from the point in the (x_0, y_0) plane to the point in the (x_1, y_1) plane separated by a distance:

$$|\vec{r}_{01}| = \sqrt{z^2 + (x_0 - x_1)^2 + (y_0 - y_1)^2} \tag{D.2}$$

To speed up the computation of Eq. D.1, it is common to consider the Fresnel approximation, where the vector $|\vec{r}_{01}|$ is approximated differently in the denominator and the exponential:

$$|\vec{r}_{01}| \approx \begin{cases} z & \text{in denominator} \\ z\left[1 + \frac{1}{2}\left(\frac{x_0 - x_1}{z}\right)^2 + \frac{1}{2}\left(\frac{y_0 - y_1}{z}\right)^2\right] & \text{in exponential} \end{cases} \tag{D.3}$$

This approximation leads to the following integral:

$$\begin{aligned} U_1(x_1, y_1) = & \frac{\exp(ikz)}{i\lambda z} \exp\left[\frac{ikz}{2z}(x^2 + y^2)\right] \\ & \cdot \iint U_0(x_0, y_0) \exp\left[\frac{ikz}{2z}(x_0^2 + y_0^2)\right] \exp\left[-i\frac{2\pi}{\lambda z}(x_0 x_1 + y_0 y_1)\right] \mathrm{d}x_0 \mathrm{d}y_0 \end{aligned} \tag{D.4}$$

which was used in the calculations of Section 7.2.

APPENDIX E SCIENTIFIC CONTRIBUTIONS

This appendix lists the various scientific contributions resulting of my graduate studies, including peer-reviewed journal articles, published conference proceedings and personnally given oral presentations.

E.1 Peer-reviewed Journal Articles

1. **H. Guerboukha**, K. Nallappan, Y. Cao, M. Seghilani, J. Azana, and M. Skorobogatiy, "Planar porous components for low-loss terahertz optics," Advanced Optical Materials, 7(15), 1900236 (2019). doi.org/10.1002/adom.201900236
2. Y. Cao, K. Nallappan, **H. Guerboukha**, T. Gervais, and M. Skorobogatiy, "Additive manufacturing of resonant fluidic sensors based on photonic bandgap waveguides for terahertz applications," 27(20), 27663-27681, (2019). doi.org/10.1364/OE.27.027663
3. **H. Guerboukha**, K. Nallappan, and M. Skorobogatiy, "Toward real-time terahertz imaging," Advances in Optics and Photonics, 10(4), 843-938 (2018). doi.org/10.1364/AOP.10.000843
4. K. Nallappan, **H. Guerboukha**, C. Nerguizian, and M. Skorobogatiy, "Live streaming of uncompressed HD and 4K videos using terahertz wireless links". IEEE Access, 6, 58030-58042 (2018). doi.org/10.1109/ACCESS.2018.2873986
5. M. Skorobogatiy, J. Sadasivan, and **H. Guerboukha**, "Statistical models for averaging of the pump–probe traces: example of denoising in terahertz time-domain spectroscopy," IEEE Transactions on Terahertz Science and Technology, 8(3), 287-298 (2018). doi.org/10.1109/TTHZ.2018.281482
6. **H. Guerboukha**, K. Nallappan, and M. Skorobogatiy, "Exploiting k-space/frequency duality toward real-time terahertz imaging," Optica, 5(2), 109-116 (2018). doi.org/10.1364/OPTICA.5.000109
7. T. Ma, K. Nallappan, **H. Guerboukha**, and M. Skorobogatiy, "Analog signal processing in the terahertz communication links using waveguide Bragg gratings: example of dispersion compensation," Optics Express, 25(10), 11009-11026 (2017). doi.org/10.1364/OE.25.011009
8. J. Li, K. Nallappan, **H. Guerboukha**, and M. Skorobogatiy, "3D printed hollow core terahertz Bragg waveguides with defect layers for surface sensing applications," Optics express, 25(4), 4126-4144 (2017). doi.org/10.1364/OE.25.004126

9. T. Ma, **H. Guerboukha**, M. Girard, A. D. Squires, R. A. Lewis, and M. Skorobogatiy, "3D printed hollow-core terahertz optical waveguides with hyperuniform disordered dielectric reflectors". Advanced Optical Materials, 4(12), 2085-2094 (2016). doi.org/10.1002/adom.201600171
10. **H. Guerboukha**, A. Markov, H. Qu, and M. Skorobogatiy, "Time resolved dynamic measurements at THz frequencies using a rotary optical delay line," IEEE Transactions on Terahertz Science and Technology, 5(4), 564-572 (2015). doi.org/10.1109/TTHZ.2015.2441701
11. **H. Guerboukha**, G. Yan, O. Skorobogata, and M. Skorobogatiy, "Silk foam terahertz waveguides", Advanced Optical Materials, 2(12), 1181-1192 (2014). doi.org/10.1002/adom.201400228 Highlighted by Nature photonics (N. Horiuchi, "Terahertz optics: Silk foam waveguides", Nature photonics, 2014).
12. A. Markov, **H. Guerboukha**, and M. Skorobogatiy, "Hybrid metal wire–dielectric terahertz waveguides: challenges and opportunities". JOSA B, 31(11), 2587-2600 (2014). doi.org/10.1364/JOSAB.31.002587
13. A. Markov, **H. Guerboukha**, A. Argyros, and M. Skorobogatiy, "A complementary study to "Hybrid hollow core fibers with embedded wires as THz waveguides" and "Two-wire terahertz fibers with porous dielectric support": comment". Optics express, 21(23), 27802-27803 (2013). doi.org/10.1364/OE.21.027802

E.2 Conference Proceedings

1. **H. Guerboukha**, K. Nallappan, Y. Cao, M. Seghilani, J. Azana, and M. Skorobogatiy, "Low-loss planar porous components for terahertz beamforming," IEEE IRMMW-THz, France (2019). doi.org/10.1109/IRMMW-THz.2019.8873875
2. Y. Cao, K. Nallappan **H. Guerboukha**, T. Gervais, and M. Skorobogatiy, "Photonic bandgap Bragg waveguide-based terahertz microfluidic sensor" IEEE IRMMW-THz, France (2019). doi.org/10.1109/IRMMW-THz.2019.8874328
3. **H. Guerboukha**, K. Nallappan, Y. Cao, and M. Skorobogatiy, "Low-loss planar components for THz wireless communications," Radio and Wireless Week 2019, USA (2019). doi.org/10.1109/RWS.2019.8714538
4. K. Nallappan, **H. Guerboukha**, Y. Cao, C. Nerguizian, and M. Skorobogatiy, "Experimental demonstration of 5 Gbps data transmission using long subwavelength fiber at 140 GHz," Radio and Wireless Week 2019, USA (2019). doi.org/10.1109/RWS.2019.8714284
5. K. Nallappan, **H. Guerboukha**, Y. Cao, C. Nerguizian, and M. Skorobogatiy, "High bitrate data transmission using polypropylene fiber in terahertz frequency range," Inter-

national workshop on antenna technology, USA (2019). doi.org/10.1109/IWAT.2019.8730612

6. K. Nallappan, **H. Guerboukha**, and M. Skorobogatiy, "Reconfigurable terahertz array antenna," International workshop on antenna technology, USA (2019). doi.org/10.1109/IWAT.2019.8730646
7. **H. Guerboukha**, K. Nallappan, and M. Skorobogatiy, "Exploiting k-space/frequency duality in Fourier optics toward real-time compression-less terahertz imaging," Paper 106690N, Computational Imaging III, SPIE Commercial + Scientific Sensing and Imaging, USA (2018). doi.org/10.1117/12.2304892
8. K. Nallappan, **H. Guerboukha**, C. Nerguizian, and M. Skorobogatiy, "Live streaming of uncompressed 4K video using terahertz wireless links," Paper I-WCS.01, IEEE ICC Wireless Communications Symposium, USA (2018). doi.org/10.1109/ICC.2018.8422216
9. K. Nallappan, **H. Guerboukha**, C. Nerguizian, and M. Skorobogatiy, "Uncompressed HD and ultra-HD video streaming using terahertz wireless communications," 11th Global Symposium on Millimeter Waves (GSMM) - Sub-Millimeter-Wave and THz Technologies, USA (2018). doi.org/10.1109/GSMM.2018.8439548
10. **H. Guerboukha**, K. Nallappan, and M. Skorobogatiy, "Spectral encoding using k-space/frequency duality," Paper MM2D.6, OSA Imaging and Applied Optics, Mathematics in Imaging, USA (2018). doi.org/10.1364/MATH.2018.MM2D.6
11. **H. Guerboukha**, K. Nallappan, and M. Skorobogatiy, "Spectral encoding using k-space/frequency duality," Paper MM2D.6, OSA Imaging and Applied Optics, Digital Holography and Three-Dimensional Imaging, USA (2018). doi.org/10.1364/3D.2018.JW5E.2
12. K. Nallappan, **H. Guerboukha**, C. Nerguizian, and M. Skorobogatiy, "Practical implementation of live uncompressed 4K video transmission at 140 GHz using photonics technologies," Paper MA1.5, IEEE IRMMW-THz, Mexico (2017). doi.org/10.1109/IRMMW-THz.2017.8066871
13. K. Nallappan, **H. Guerboukha**, M. Seghilani, T. Ma, J. Azaña, C. Nerguizian, and M. Skorobogatiy, "Multiplexing of terahertz wireless communication channels using vortex beams," Paper MB1.2, IEEE IRMMW-THz, Mexico (2017). doi.org/10.1109/IRMMW-THz.2017.8066888
14. T. Ma, K. Nallappan, **H. Guerboukha**, and M. Skorobogatiy, "Metallized 3D printed hollow Core waveguide Bragg grating for dispersion compensation in terahertz range," Paper MC1.2, IEEE IRMMW-THz, Mexico (2017). doi.org/10.1109/IRMMW-THz.2017.8066906
15. J. Li, T. Ma, K. Nallappan, **H. Guerboukha**, and M. Skorobogatiy, "3D printed hollow core terahertz Bragg waveguides with defect layers for surface sensing applications," Pa-

per MC1.4, IEEE IRMMW-THz, Mexico (2017). doi.org/10.1109/IRMMW-THz.2017.8066908

16. **H. Guerboukha**, K. Nallappan, and M. Skorobogatiy, "Fast compressionless reconstruction for terahertz imaging," Paper WC3.6, IEEE IRMMW-THz, Mexico (2017). doi.org/10.1109/IRMMW-THz.2017.8067258
17. T. Ma, K. Nallappan, **H. Guerboukha**, and M. Skorobogatiy, "Dispersion Compensation in Terahertz Communication Links Using Metallized 3D Printed Hollow Core Waveguide Bragg Gratings," Paper SM3J.4, CLEO: Science and Innovations, THz communications, USA (2017). doi.org/10.1364/CLEO_SI.2017.SM3J.4
18. J. Li, K. Nallappan, **H. Guerboukha**, and M. Skorobogatiy, M., "3D printed hollow core terahertz Bragg waveguide for surface sensing applications," Paper JW2A.101, CLEO: Applications and Technology, USA (2017). doi.org/10.1364/CLEO_AT.2017.JW2A.101
19. T. Ma, **H. Guerboukha**, and M. Skorobogatiy, "3D printed hollow core terahertz optical waveguides with hyperuniform disordered dielectric reflectors," Paper JW2A.106, CLEO: Applications and Technology, USA (2017). doi.org/10.1364/CLEO_AT.2017.JW2A.106
20. **H. Guerboukha**, H. Qu, and M. Skorobogatiy, "Linear rotary optical delay lines," Paper 97540C, Photonic Instrumentation Engineering III, SPIE Photonics West OPTO, USA (2016). doi.org/10.1117/12.2216297
21. **H. Guerboukha**, A. Markov, H. Qu, and M. Skorobogatiy, "Dynamic measurements at THz frequencies with a fast rotary delay line," Paper 97470R, Terahertz, RF, Millimeter, and Submillimeter-Wave Technology and Applications IX, SPIE Photonics West OPTO, USA (2016). doi.org/10.1117/12.2216308
22. **H. Guerboukha**, A. Markov, H. Qu, and M. Skorobogatiy, "Dynamic measurements at THz frequencies with a fast rotary delay line," Paper FS-57, IEEE IRMMW-THz, China (2015). doi.org/10.1109/IRMMW-THz.2015.7327465
23. **H. Guerboukha**, G. Yan, O. Skorobogata, and M. Skorobogatiy, "Silk foam terahertz waveguides," Paper MS-49, IEEE IRMMW-THz, China (2015). doi.org/10.1109/IRMMW-THz.2015.7327668
24. **H. Guerboukha**, A. Markov, H. Qu, and M. Skorobogatiy, "Dynamic measurements at terahertz frequencies with a fast rotary delay line," IEEE Photonics North, (2015). doi.org/10.1109/PN.2015.7292506
25. **H. Guerboukha**, G. Yan, O. Skorobogata, and M. Skorobogatiy, "Silk foam terahertz waveguides," IEEE Photonics North (2015). doi.org/10.1109/PN.2015.7292503
26. A. Markov, **H. Guerboukha**, and M. Skorobogatiy, "Hybrid metal wire-dielectric THz fibers: design and perspectives," Paper JW2A.55, CLEO: Applications and Technology, USA (2015) doi.org/10.1364/CLEO_AT.2015.JW2A.55

27. A. Markov, **H. Guerboukha**, and M. Skorobogatiy, "Hybrid metal-dielectric THz fibers: design and perspectives," Paper W2V-21.1. IEEE IRMMW-THz, USA (2014). doi.org/10.1109/IRMMW-THz.2014.6956411

E.3 Oral Presentations

1. **H. Guerboukha**, K. Nallappan, Y. Cao, M. Seghilani, J. Azana, and M. Skorobogatiy, "Low-loss planar porous components for terahertz beamforming," IRMMW-THz – Paris (France), 2019.
2. Y. Cao, K. Nallappan, **H. Guerboukha**, T. Gervais, and M. Skorobogatiy, "Photonic bandgap Bragg waveguide-based terahertz microfluidic sensor," IRMMW-THz – Paris (France), 2019.
3. **H. Guerboukha**, K. Nallappan, and M. Skorobogatiy, "Imagerie térahertz par encodage spectral," Congrès de l'Association francophone pour le savoir – Gatineau (Canada), 2019.
4. **H. Guerboukha**, K. Nallappan, and M. Skorobogatiy, "Terahertz imaging with 45 pixels through spectral encoding of the k-space," Optical Terahertz Science and Technology – Santa Fe (USA), 2019.
5. **H. Guerboukha**, K. Nallappan, M. Seghilani, G. Mangeat G., J. Azaña, and M. Skorobogatiy, "Generation of orbital angular momentum states at terahertz frequencies with metamaterials," Photonics North – Montreal (Canada), 2018.
6. **H. Guerboukha**, K. Nallappan, and M. Skorobogatiy, "Terahertz spectral encoding of the k-space," Photonics North – Montreal (Canada), 2018.
7. M. Skorobogatiy, J. Sadasivan, **H. Guerboukha**, "Averaging of pump-probe traces using statistical models: denoising in THz time-domain spectroscopy," Photonics North – Montreal (Canada), 2018.
8. **H. Guerboukha**, K. Nallappan, and M. Skorobogatiy, "Fast compressionless reconstruction for terahertz imaging," IRMMW-THz – Cancun (Mexico), 2017.
9. J. Li, T. Ma, K. Nallappan, **H. Guerboukha** H. and M. Skorobogatiy, "3D printed hollow core terahertz Bragg waveguides with defect layers for surface sensing applications," IRMMW-THz – Cancun (Mexico), 2017.
10. T. Ma, K. Nallappan, **H. Guerboukha**, and M. Skorobogatiy, "Metallized 3D printed hollow core waveguide Bragg grating for dispersion compensation in terahertz range," IRMMW-THz – Cancun (Mexico), 2017.
11. **H. Guerboukha**, K. Nallappan and M. Skorobogatiy, M. "Extreme compression in THz Fourier imaging," Photonics North – Ottawa (Canada), 2017.

12. J. Li, K. Nallappan, **H. Guerboukha**, and M. Skorobogatiy, "3D printed hollow-core terahertz Bragg waveguides with defect layers for surface sensing applications," Photonics North – Ottawa (Canada), 2017.
13. **H. Guerboukha**, K. Nallappan, and M. Skorobogatiy, "Extreme compression in THz Fourier imaging," Canadian Association of Physicists – Kingston (Canada), 2017.
14. J. Li, K. Nallappan, **H. Guerboukha**, and M. Skorobogatiy M., "3D printed hollow-core terahertz Bragg waveguides with defect layers for surface sensing applications," Canadian Association of Physicists – Kingston (Canada), 2017.
15. **H. Guerboukha**, H. Qu, and M. Skorobogatiy, "Dynamic measurements at THz frequencies with a fast rotary delay line," SPIE OPTO Photonics West – San Francisco (USA), 2016.
16. **H. Guerboukha**, H. Qu, and M. Skorobogatiy, "Linear rotary optical delay lines, " SPIE OPTO Photonics West – San Francisco (USA), 2016.
17. **H. Guerboukha**, H. Qu, and M. Skorobogatiy, "Dynamic measurements at THz frequencies with a fast rotary delay line," Canadian Association of Physicists – Ottawa (Canada), 2016.
18. **H. Guerboukha**, H. Qu, and M. Skorobogatiy, "Contactless dynamic measurements with terahertz waves and a rotary delay line," Canadian Association of Physicists – Ottawa (Canada), 2016.
19. **H. Guerboukha**, G. Yan, O. Skorobogata, and M. Skorobogatiy, "Silk foam terahertz waveguides for biomedical and agri-food applications," Canadian Association of Physicists – Ottawa (Canada), 2016.
20. **H. Guerboukha**, G. Yan, O. Skorobogata, and M. Skorobogatiy, "Silk foam terahertz waveguides," Photonics North – Ottawa (Canada), 2015.
21. **H. Guerboukha**, A. Markov, H. Qu, and M. Skorobogatiy, "Dynamic measurements at terahertz frequencies with a fast rotary delay line," Photonics North – Ottawa (Canada), 2015.
22. Invited talk: A. Markov, **H. Guerboukha**, and M. Skorobogatiy, "Hybrid metal-dielectric THz fibers: design and perspectives," Photonics North – Ottawa (Canada), 2015.
23. Plenary talk: **H. Guerboukha**, and M. Skorobogatiy, "Aux frontières de l'optique: imagerie et spectroscopie térahertz ", Journée de la recherche à Polytechnique – Montreal (Canada), 2015.